LABORATORY OF MECHANICS, MATERIALS AND STRUCTRURES

QUALITATIVE AND QUANTITATIVE SPECTROSCOPIC EVALUATION OF POTASSIUM ADSORPTION ON CARBON NANOTUBES

THESIS

Submitted and defended in Fulfillment of the Requirements for the Degree of Doctor of Philosophy/ Ph.D in Physics

Option: Fundamental Mechanics and Complex Systems

By:

TCHENGUEM KAMTO Camile Rodolphe
Registration number: 17T5822
D.E.A in Physics

Under the co-advising of:

THIODJIO SENDJA Bridinette Epse FANDIO

Associate Professor, University of Yaounde I

MANE MANE Jeannot

Professor, University of Yaounde I

Academic Year 2023

UNIVERSITÉ DE YAOUNDÉ I
THE UNIVERSITY OF YAOUNDE I

FACULTÉ DES SCIENCES
FACULTY OF SCIENCE

DÉPARTEMENT DE PHYSIQUE
DEPARTMENT OF PHYSICS

ATTESTATION DE CORRECTION DE LA THÈSE DE DOCTORAT/Ph.D

Nous, Professeur **HONA Jacques** et Professeur **NDJAKA Jean-Marie Bienvenu**, respectivement Examinateur et Président du jury de la Thèse de Doctorat/Ph.D de Monsieur **TCHENGUEM KAMTO Camile Rodolphe**, Matricule **17T5822**, préparée sous la co-direction du Maître de conférences **THIODJIO SENDJA Bridinette Epse FANDIO** et du professeur **MANE MANE Jeannot**, intitulée : « **Qualitative and quantitative spectroscopic evaluation of potassium adsorption on carbon nanotubes** », soutenue le **Vendredi, 13 Octobre 2023**, en vue de l'obtention du grade de **Docteur/Ph.D** en Physique, Spécialité **Mécanique, Matériaux et Structures**, Option **Mécanique Fondamentale et Systèmes Complexes**, attestons que toutes les corrections demandées par le jury de soutenance ont été effectuées.

En foi de quoi, la présente attestation lui est délivrée pour servir et valoir ce que de droit.

Fait à Yaoundé le......**1 8 OCT 2023**......

Examinateur	Le Chef de Département de Physique	Le Président du jury
Pr HONA Jaques	Pr NDJAKA Jean-Marie Bienvenu	Pr NDJAKA Jean-Marie Bienvenu

Dedication

In loving memory of my Daddy, KAMTO Donatien

Acknowledgements

At the end of the PhD study, I am deeply grateful for the opportunity to have learned from and worked with so many brilliant teachers, collaborators and students. I am happy to express my sincere gratitude to all those from who near or far have accompanied me during these doctoral years and have directly or indirectly contributed to the completion of this document. Nevertheless, I will do my best to condense my thoughts about this.

Firstly, I would like to express my sincere gratitude to almighty God who gave me life, opportunity and knowledge to reach and to end with the PhD study level.

I have furthermore to thank people responsible of the Faculty of sciences, and the Research and postgraduate training unit for physics and applications who allowed to pursue my thesis.

I would like to express my gratitude to my 1st co-advisor Associate Professor THIODJIO SENDJA Bridinette who, despites her multiple academic and family occupations, accepted to guide this work. This thesis would not have been possible without her pernickety vision in nanotechnology physics. I want to thank her for the advices she provided. Her expertise has enabled me to acquire enough knowledge.

I would like to express my sincere gratitude to my 2nd co-advisor Professor MANE MANE Jeannot who, despites his multiple academic, administrative and family occupations, accepted to work as co-advisor of this thesis. I want to thank him for all his teachings and advices.

I would like to deeply thank honorable members of the Jury, who agreed to put aside their multiple occupations so as to evaluate this work. I express to them all my greatest respect.

I would like to thank Professor NDJAKA Jean Marie, Head of the Department of Physics. I am very grateful for his administrative contribution and encouragement.

I would like to thank Professor KOFANE Timoléon Crépin, Head of the Laboratory of Mechanics, Materials and Structures. I am very grateful for his constructive comments.

I am very grateful to Professor NGUENANG Jean-Pierre, Head of the Department of Physics of the University of Douala, for his multiple encouragements and helps.

I am very grateful to: Doctor MEDELIN CASTILLO Nahum of the Autonomous University of San Luis Potosi, Faculty of Engineering, Mexico, Doctor LABRADA DELGADO Gladis Judith of the IPICYT (Instituto Potosino de Investigación Científica y Tecnológica, A.C), Mexico and Mrs NÁJERA-ACEVEDO Margarita Berenice of the Autonomous Uni-

Résumé

Grâce à leur simplicité chimique, et à leurs caractéristiques dimensionnelles associées à des propriétés remarquables, les nanotubes de carbone (CNTs) ouvrent à la nanotechnologie des perspectives innovantes et prometteuses. L'un des principaux défis rencontrés dans le développement des biocapteurs est la stratégie d'immobilisation de l'entité biospécifique sur la surface du capteur, car celle-ci ne doit pas dénaturer l'élément biologique. Dans ce travail, nous avons utilisé les nanotubes de carbone monoparois et multiparois. Les échantillons ont été synthétisés par le procédé de dépôt chimique en phase vapeur (CVD), et par la suite, recuits thermiquement à 550 °C durant deux heures. La spectroscopie XANES utilisée a permis de caracteriser la surface externe des CNTs. Les adsorbats extrinsèques tels que le potassium (K) et intrinsèques tels que les molécules gazeuses (H_2O, O_2, CO_2, CO) ont montré des sensibilités différentes à la géométrie des CNTs, à l'hybridation et au recuit thermique. Le transfert de charge du potassium augmente de 12 % la conductivité des MWCNTs et de 62, 7 % celle des SWCNTs. La désorption est plus importante dans les MWCNTs et s'élève à 70 % pour le potassium. Par contre, elle est moins importante pour les molécules de gaz. Les techniques complémentaires à l'instar de la microscopie électronique en transmission (TEM), la microscopie électronique à balayage (SEM), ou encore la spectroscopie Infrarouge à Transformée de Fourier (FTIR) sont utilisées pour mettre en évidence l'arrangement aléatoire et les particules sphériques comme le fer le long des nanotubes de carbone. Ce qui permet de demontrer que les groupes fonctionnels OH−, C=O and C≡C sont impliqués dans le processus d'adsorption. Et on montre que l'adsorption du potassium dans les solutions aqueuses utilisant les CNTs comme adsorbants se fait par le processus d'échange d'ions.

Mots clés : Nanotubes de carbone, recuit thermique, adsorption, desorption, potassium, spectroscopie XANES.

Abstract

Because of their chemical simplicity and their dimensional characteristics combined with remarkable properties, carbon nanotubes (CNTs) open up innovative and promising prospects for nanotechnology. One of the main challenges encountered in the development of biosensors is the immobilisation strategy of the biospecific entity on the sensor surface, as this must not denature the biological element. In this work we used single walled and multi walled carbon nanotubes (SWCNTs and MWCNTs). The samples were synthesised by chemical vapour deposition (CVD), and then thermally annealed to 550 $^\circ$C for two hours.

The XANES spectroscopy allowed characterizing the external surface of our CNTs. The extrinsic adsorbates such as potassium (K) and the intrinsic like gas molecules (H_2O, O_2, CO_2, CO) showed different sensitivities to CNT geometry, hybridisation and thermal annealing. Potassium charge transfer increased the conductivity of MWCNTs by 12 % and of SWCNTs by 62.7 %. The desorption is 70 % for potassium and more important in MWCNTs. In contrast it is less important for gas molecules. Complementary techniques such as transmission electron microscopy (TEM), scanning electron microscopy (SEM), or Fourier Transform Infrared Spectroscopy (FTIR) are used to highlight the random arrangement and spherical iron particles along the carbon nanotubes. This allowed to demonstrate that the functional groups OH−, C=O and C≡C are involved in the adsorption process. It is shown that the adsorption of potassium in aqueous solutions using CNTs as adsorbants can be done by the ions exchange process.

Keywords : Carbon nanotubes, thermal annealing, adsorption, desorption, potassium, XANES spectroscopy.

Contents

List of Figures

List of Tables

Abbreviations

ATR: Attenuated Total Reflectance

BET: Brunauer Emmett Teller

BSE: Back Scattered Electron

CNTs: Carbon NanoTubes

CVD: Chemical Vapour Deposition

DC-HF-CVD: Direct Current Hot Filament Chemical Vapour Deposition

DFT: Density functional theory

DOS: Density Of States

EA: Electric Arc

ED: Electrodialysis

ECR: Electron Cyclotron Resonance

EDX: Energy Dispersive X-ray spectroscopy

EDS: Energy Dispersive Spectroscopy

EDA: Electron Donor Acceptor

EF: Energy Filtered

ESI: Electron Spectroscopie Imaging

EXAFS: Extended X-ray Absorption Fine Structure

FIB: Focused Ion Beam

FTIR: Fourier Transform Infrared Spectroscopy

FEG: Field Emission Gun

FY: Fluorescence Yield

GI: Grazing Incidence

GIS: Gaz Injection System

HFCVD: Hot Filament Chemical Vapour Deposition

HR-TEM: High Resolution Transmission Electron Microscope

HOPG: Highly Oriented Pyrolytic Graphite

IEMs: Iion-Exchange Membranes

IUPAC: International Union of Pure and Applied Chemistry

IP: Ionization Potentiel

IUPAC: International Union of Pure and Applied Chemistry

LA: Laser Ablation

LURE: *Laboratoire Utilisation du Rayonnement Electromagnétique*

LMIS: Liquid Metal Ion Source

MWCNTs: Multiwalled Carbon Nanotubes

NIR: Near Infrared Radiation

NI: Normal Incidence

NF: Nano Filtration

OMPs: Organic micropolluants

PECVD: Plasma Enhanced Chemical Vapour Deposition

PEY: Partial Electron Yield

pH_{ZPC}: *pH Zero Point Charge*

PL: Photo Luminescence

RO: *Reverse Osmosis*

QED: Quantitative Electron

SEM: Scanning Electron Microscopy

SE: Secondary Electron

SWCNTs: Single-Walled Carbon NanoTube

SACEMOR: Spectre d'Absorption de Céramiques et Molécules Organiques

STM: Scanning Tunneling Microscopy

TPD: Thermal Desorption Spectroscopy

TEY: Total Electron Yield

TGA: *Thermogravimetric Analysis*

TEM: Transmission Electron Microscopy

UNDOS: Unfilled Density Of States

VLS: Vapor Liquid Solid

XANES: X-ray Absorption Near Edge Structure

XPS: X-ray Photoelectron Spectroscopy

ZL: Zero Loss

General Introduction

Currently, there is concern about a global water crisis mainly because about 4 % of water available in the groundwater reserves, which supply about 80 % of the human population [1], is contaminated by agents such as cadmium, chromium, lead, zinc, potassium, fluorides, and pharmaceutical waste, all of which continue to deteriorate water quality. Among those agents, potassium is a very abundant element and is the seventh among all elements of the Earth's crust. As environmental effects, high levels of potassium soluble in water can cause damage to seeds in germination, inhibit the intake of other minerals and reduce the quality of the crop. Furthermore, in damage to health, a side effect of a malfunction of the kidneys can generate a buildup of potassium, thus causing a disturbance in the heart rate. It is clearly understood that it is of great interest to investigate different ways of removing contaminants (K^+) in aqueous solutions. Recent years have seen great advances in the fields of electronics, communication and sensor technology. Significant efforts have been made to understand the fundamental principles leading to the design of ever faster and more compact devices made from innovative functional materials. Officially discovered in 1991 by Iijima [2], carbon nanotubes are defined as a cylinder of nanometric diameter formed by hexagons of carbon atoms and closed at both ends by the insertion of several pentagons. Note that the low-dimensional structures in the nanometer range, are increasingly playing an important role in the fields of biology, chemistry, physics and materials science. Among these applications, the most suitable are: the covalent functionalization (chemical adsorption) of the surface [3,4], the intercalation (doping) of elements for the transfer electric charges (alkalis, halogens) [5]; the physical functionalization (physical adsorption) and encapsulation [6,7]. The possibility for carbon to bind with itself or with another atom of the chains and rings continues to generate remarkable and growing interest at several levels of the scientific community. Obtaining materials with new and predictable properties requires a precise knowledge of their electronic structure.

Since their discovery, many synthesis methods have been developed, allowing access to the carbon nanotubes (CNTs) with various properties. Among these, the decomposition of a hydrocarbon gas under moderated temperature on the surface of an active catalyst is well established. This method, commonly called Chemical Vapour Deposition (CVD), is a suitable one able to synthesize CNTs with a selective control of diameters on a solid substrate at lower temperatures. These characteristics give them enough avantages in comparision with

the existing synthesis routes like: electric arc, laser ablation and solar vaporisation. The CVD-assisted growth methods for the control of CNTs orientation mainly used in this work are PECVD (Plasma Enhanced CVD) and HFCVD (Hot Filament CVD). They allowed to provide CNTs aligned perpendicularly to the substrate surface. Phenomena such as adsorption and desorption on various surfaces have interested scientists for decades. These phenomena are the basis of a certain number of remarkably important processes in the large field of application. Mastering these phenomena on nanomaterials such as CNTs facilitates the manufacture of electronic devices, nano-vectors, chemical or gas sensors, or nano-composites. A certain difficulties must be resolved in order to exploit the full potential of these exceptional materials.

The question then arises as to why few companies incorporate carbon nanotubes in their raw state for various applications? What are the impacts of adsorbates (gaseous molecules) and alkali metal (K) on the effectiveness of CNTs? The objective of this thesis is the study of the adsorption and desorption phenomena on CNTs. An understanding of the process involved in adsorption and their repercussions on its electronic structure is essential to optimize their use. More specifically, the first objective of this work was to characterize the surface and study the effects induced by adsorbates on the electrical and conduction properties of Single-Walled Carbon Nanotubes (SWCNTs) and Multi-Walled Carbon Nanotubes (MWCNTs). For this, we used thermal annealing and XANES spectroscopy. XANES has the advantage of being sensitive to the surfaces chemistry and therefore allows to probe the occupied electronic states, and to obtain information on the unoccupied levels of the CNTs. It should be remembered that Single-Walled Carbon Nanotubes (SWCNTs) have a larger specific surface compared to the others and therefore favouring the adsorption. The second objective is to capture potassium (K) in an aqueous solution using SWCNTs as adsorbent for the application in water treatment and biosensors. To attain our goal, XANES spectroscopy was used in addition with some complementary techniques such as microscopic techniques as transmission electron microscopy (TEM) and scanning electron microscopy (SEM) provide information on the morphology, and texture of CNTs with very high spatial resolution. They can also allow to determine the size and the shape of the elementary grains or agglomerates. The functional groups interfering in the adsorption process of the CNTs can be investigated by the Fourier transform infrared spectroscopy (FTIR), through the characteristic vibrations of the chemical bands. Note that the identification of the functional groups present on the surface of the CNTs is essential, because they determine the conductivity nature of the nanotubes for the improvement of the current tools of diagnosis and biological analysis. This work is organized as follows.

The first chapter presents the basics necessary to understand the experimental and theoretical developments of CNTs. Carbon and its crystalline forms, structure, properties and applications of CNTs are presented. The adsorption phenomenology on CNTs and the formalism of XANES spectroscopy are also described.

The second chapter briefly describes the synthesis methods of carbon nanotubes, the

principle of the microscopic techniques and the experimental conditions used. The principles of FTIR and X-ray Absorption Near Edge Structure (XANES) are also presented.

In the last chapter, we present and discuss the textural properties and morphological characterization of CNTs. Then, the adsorption properties and the functional groups on the surface of CNTs are discussed in addition to the XANES results.

And finally, to end this work, we present the general conclusion, the perspectives and one appendix.

Literature review on carbon nanotubes and characterization techniques

Introduction

In an industrial and increasingly competitive world, nanoscience is a major challenge for the future, both in terms of fundamental and applied research. This emerged in the 1980s with the development of new tools at the atomic scale, such as tunnelling microscopes, which enabled a decisive step forward the observation and movement of atoms. At a very small scale, new phenomena appear (size effects, quantum effects, etc.) and give to materials interesting properties. Carbon nanotubes (CNTs) represent one of the first commercial material for interesting applications in nanotechnology. Since their discovery in the 1990s [2], these nano-objects have attracted considerable interest due to their exceptional intrinsic properties and dimensional characteristics. Carbon nanotubes are formed by winding one or more sheets of a hexagonal network of carbon atoms, called graphene. Thus, this chapter introduces the recalls of carbon and its crystalline forms, structure, properties and applications of CNTs, but also adsorption phenomenology on CNTs and formalism of XANES spectroscopy.

1.1   Carbon and its crystalline forms

Carbon ($Z = 6$) has the particularity to exist under different physical structures called allotropes. It has four electrons on the external layer and has an electronic structure $1s^2 2s^2 2p^2$. Its electronic configuration in the ground state $1s^2 2s^2 2p_x^1 2p_y^1 2p_z^0$ shows that the neutral carbon atom is bivalent, as it has six electrons with four of them occupying the outer orbital and two of them being unpaired [8]. This tetravalence of carbon is due to its ability to hybridize i.e. to go from the ground state to an excited $1s^2 2s^1 2p_x^1 2p_y^1 2p_z^1$. Recall that, hybridization consists in a transition of the atom from a stable state to an excited state ($C^* 1s^2 2s^1 2p^3$), thus very reactive. This excited carbon thus results from the recombination of the electrons of the atomic orbitals $2s$ and $2p$. Note that this recombination can be done in three different ways

allowing the carbon atom to bind to one or more atoms to form molecules. Figure 1.1 shows natural and synthetic allotropes of carbon. Thus, the most common natural allotropes of carbon are diamond and graphite. Diamond, has a three-dimensional (3D) structure generated by sp^3 hybridization and graphite of two-dimensional structure (2D) presents a hybridization of type sp^2, where each atom is connected to the others by in-plane covalent bonds and yields its fourth valence electron to a common background. These planes are connected by Van der Waals type bonds. Graphite is considered in this work, as a reference element. So it will provide a clear signature of the physico-chemical state of sp^2 hybridized carbon. Concerning the synthetic allotropes, we have on the one hand, graphene and carbon nanotubes (CNTs), which are one-dimensional materials (1D), with hybridization sp^2. And on the other hand, the fullerite crystal (fullerene), which is a combination between the two carbon states sp^2 and sp^3 leads to an allotropic variety (0D).
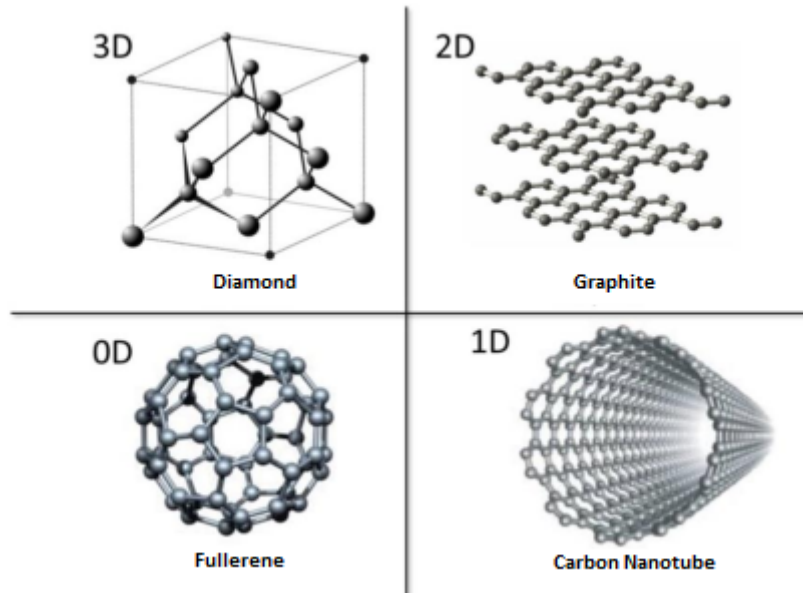
Figure 1.1: Representation of the allotropic forms of carbon and their dimensionality.

1.1.1 Graphite

Natural graphite is a shiny black mineral occurring in flakes and veins, consisting of carbon only. It is an excellent conductor of electricity and heat, and has a high melting point 3500 ˚C. It is a semi-metal, meaning that it has metallic properties but with a very small number of free charges, carriers of electric current, per unit volume. This is due to the fact that the valence band and the conduction band of graphite overlap very little. It is extremely acid resistant, chemically inert and highly refractory. The bonds between graphene layers are weak and produced essentially by the interaction of the electrons of the bonds, they are Van der Waals type interactions.

1.1.2 Graphene

It corresponds to a graphite mono-sheet or monoplane. The graphene sheet corresponds to a hexagonal arrangement, in the shape of honeycomb, of carbon atoms distant of 0.142 nm from each other, confer Figure 1.2. We can thus obtain several types of stacking of the graphene layers [9]:

- AAA (simple hexagonal) 0 % (energetically unfavorable);
- ABA (hexagonal) 85 % (which we will call graphitic contact);
- ABC (rhombohedral) 15 % (energetic).
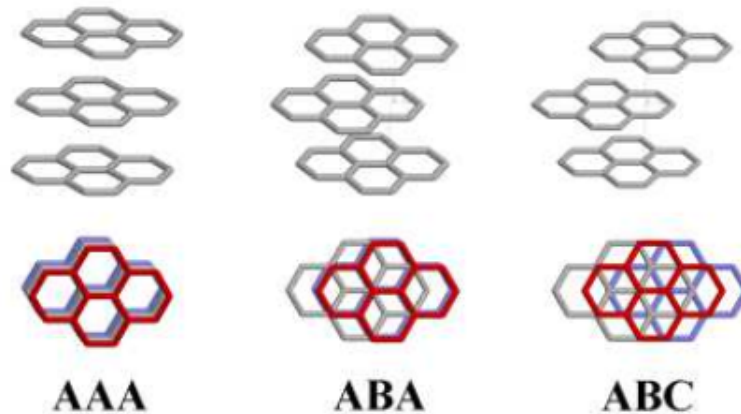
Figure 1.2: Three types of graphene layer stacking [10].

It is a molecule in which the carbon atoms are surrounded by hydrogen atoms whose formula is given by: C_6H_{20} [7]. This molecule is considered theoretically as a perfect two-dimensional (2D) hybridized sp^2 because it consists of a single layer of carbon atoms. The delocalized electrons π that it contains have the same properties as those defined in graphite.
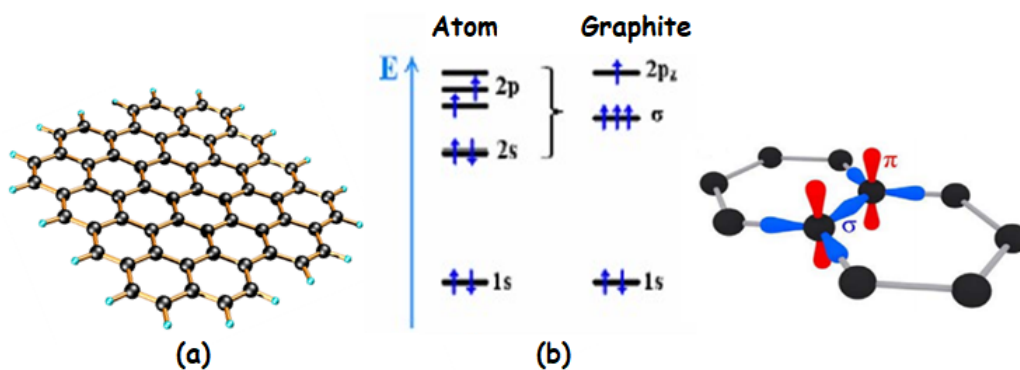
Figure 1.3: (a) Structure of graphene, and (b) structure of carbon molecular orbitals in a graphite plane sp^2 [11].

1.1.3 Fullerenes

Fullerenes constitute the third allotropic form of carbon after graphite and diamond. They are spherical molecules composed of several tens of carbon atoms. They are agenced according

to a mixture of hexagons and pentagons. The molecule of C_{60} molecule was the first fullerene to be discovered in 1985 and to give rise to 3 Nobel prizes: Harold Kroto, Robert Curl and Richard Smalley in 1996 [12]. It is composed, as its name indicates, of 60 carbon atoms arranged in hexagons and pentagons so as to form a spherical structure (Figure 1.4). The introduction of heptagons makes it possible to obtain surfaces with negative curvature, while the introduction of pentagons makes it possible to obtain surfaces with positive curvature. Their chemical formula is $C_{2n}(11 \leqslant n \leqslant 480)$.
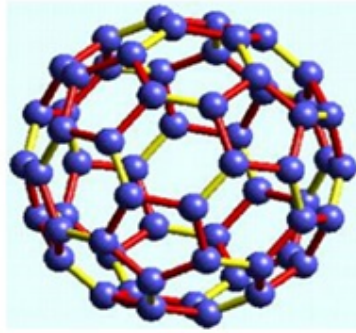
Figure 1.4: Structure of C_{60} the $C-C$ bonds common to a hexagon and a pentagon are represented in red and the bonds common to two hexagons are represented in yellow [13].

1.1.4   Carbon nanotubes

A Carbon NanoTube (CNT) is graphene in cylindrical form. According to Yu et al.[14], the diameter values of SWCNTs are typically around $(1 - 1.5 \text{ nm})$. As for the lengths, they can go up to a few μm . We thus distinguish on the one hand, Single Walled Carbon Nanotubes (SWCNTs), which corresponds to a single layer of graphene forming a cylindrical tube. On the other hand, the Multi Walled Carbon Nanotubes (MWCNTs) which is for several layers of graphene forming several cylindrical tubes all having the same cylindrical axis. These concentric cylinders are linked by Van der Waals forces and spaced by an interplanar distance of 3.4 A°. Between the different cylinders, interactions, called lip - lip interaction take place and contribute to stabilize the final structure [15]. It is very difficult to give a range of dimensions for the MWCNTs, they are variable with respect to the diameter, because it is directly proportional to the number of walls that constitute the CNT.

The principle of bulding the CNTs is based on the graphene sheet. This sheet has two types of edges, named armchair and zigzag because of their appearance. Let's draw a line parallel to the zigzag edge (Figure 1.5), fold the graphene sheet into a roll and connect its two armchair edges to form a tube: we obtain a zigzag SWCNT. And in this case, the hexagons describe circles perpendicular to the axis of the tube. We can also take a graphene sheet where the long edge is the zigzag edge (Figure 1.6, we keep our reference line drawn parallel to the zigzag edge). We fold the sheet and connect its two zigzag edges: we obtain a second type of tube, a SWCNT armchair. And then, the hexagons are aligned parallel to the axis of

the tube. Finally, one edge of the graphene sheet can be translated with respect to the other, parallel to the axis of the tube (Figure 1.7), before connecting the edges to form the tube. A chiral SWCNT is then obtained. The chirality of this object comes from the fact that helicity was introduced by combining two symmetry operations: a translation along the tube axis (the sliding of one edge of the sheet with respect to the other) combined with a rotation around this same axis (the joining of the two edges). The hexagons thus wrap around the axis of the nanotube in a helical manner.
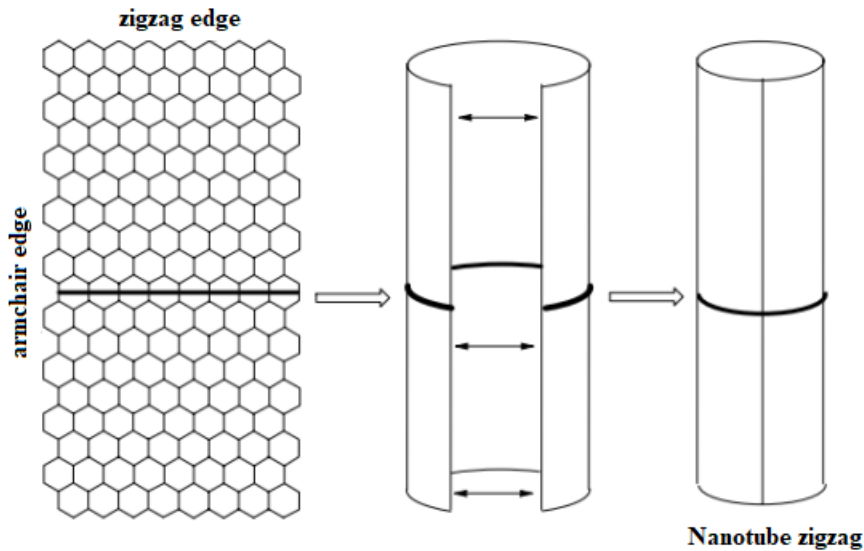
Figure 1.5: Winding of a graphene sheet and connection to form a zigzag SWCNT [13].
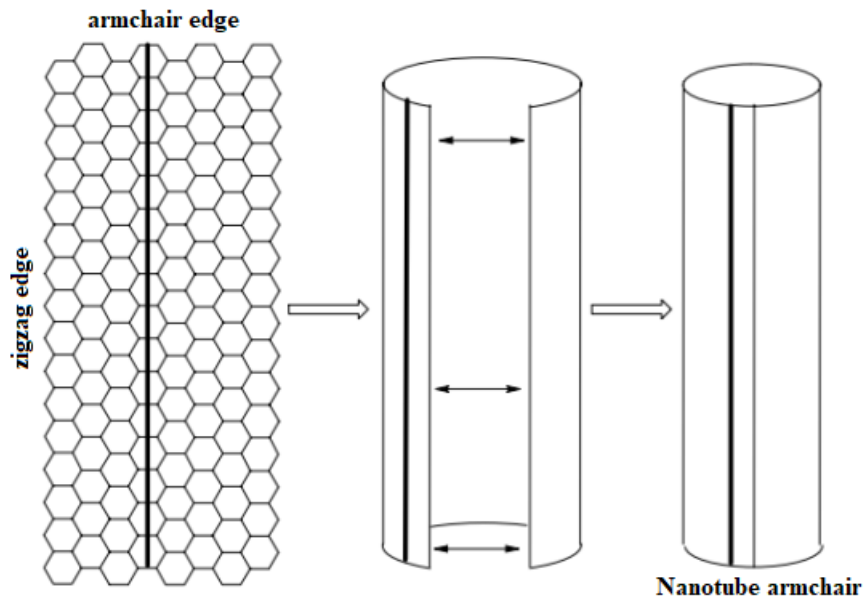
Figure 1.6: Winding of a graphene sheet and connection to form a SWCNT armchair [13].
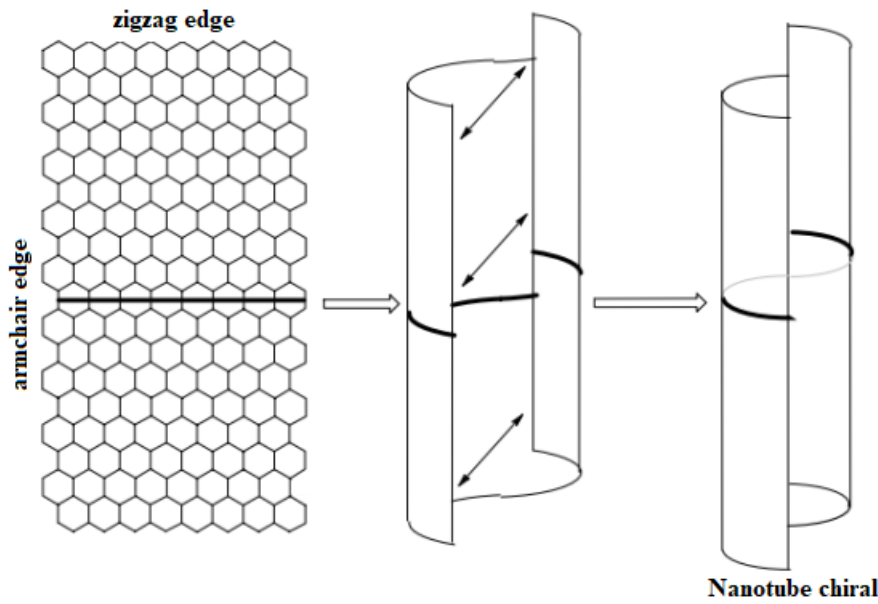
Figure 1.7: Winding of a graphene sheet and connection to form a chiral SWCNT [13].

1.1.5 Orbital Hybridization

Orbital hybridization is the mathematical concept of mixing atomic wave functions into completely new hybrid orbitals, with a new shape and (lower) energy. These new orbitals better explain electrons bonding together in molecules. Consider the element whose bonding is of most interest to us: carbon. Its electronic configuration is $1s^2 2s^2 2p^2$. $2s$ and $2p$ differ very little in energy, therefore, the wave functions can mix when carbon is bonded.

sp^n Hybridization

sp^n is a notation of how the orbitals are hybridized, i.e. a sp^2 has one s (33 %) and two p (66 %) orbitals. Even though several orbitals come together and form new, there are the same number of orbitals available for bonding. How to determine which hybridization a carbon atom has sp^3, sp^2 or sp?

   - 1 triple bond and 1 single bond (or 2 double bonds, in the case of CO_2), then it is sp hybridized (linear);

   - 2 single bonds and 1 double bond, it is sp^2 hybridized (trigonal planar);

   - 4 single bonds, it is sp^3 hybridized (tetrahedral).

(a) s orbital   **(b)** p orbital
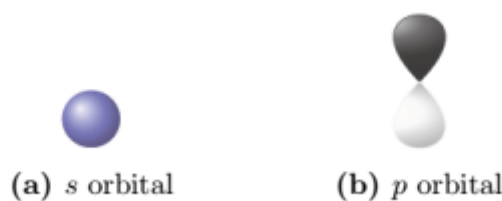
Figure 1.8: s and p orbitals

sp Hybridization (linear)

Mixing one $2s$ and one $2p$ wave functions of carbon, two new hybrids are obtained, called sp orbitals, made up of 50 % s and 50 % p character. The major parts of the orbitals point away from each other at an angle of $180°$. There are two additional minor back lobes (one for each sp hybrid) with opposite sign. The remaining two p orbitals are left unchanged, these two form two π bonds. The $180°$ angle that results from this hybridization scheme minimizes electron repulsion. The oversized front lobes of the hybrid orbitals also overlap better than lobes of unhybridized orbitals; the result is energy reduction due to improved bonding. This is the hybridization that gives rise to Carbyne, one of the materials harder than diamond.

In the sp hybridization, there is linear combination of $2s$ orbital and one of the three $2p$ orbitals sketched in (Figure 1.9), $2p_x$ for example. From these two atomic orbitals, two equivalent orbitals are formed, called hybridized orbitals and, are expressed by linear combination of $2s$ and $2p_x$ and denoted $\mid sp_a >$ and $\mid sp_b >$. Mane et $al.$[8], show that the two hybridized orbitals are expressed by equation (1.1) that follows:

$$\begin{cases} \mid sp_a >= C_1 \mid 2s > + C_2 \mid 2p_x > \\ \mid sp_b >= C_3 \mid 2s > + C_4 \mid 2p_x > \end{cases} \tag{1.1}$$

where the C_i are coefficients expressing the character of $2s$ and $2p$ atomic orbitals in hybridized orbitals. By using the orthogonal and normal conditions requirements

$< sp_a \mid sp_b >= 0$ and $< sp_a \mid sp_a > = < sp_b \mid sp_b > = 1$,

we obtain the relations:

$$\begin{cases} C_1 C_3 + C_2 C_4 = 0 \\ C_3^2 + C_4^2 = 1 \\ C_1^2 + C_2^2 = 1 \\ C_1^2 + C_3^2 = 1 \end{cases} \tag{1.2}$$

The resolution of Equation (1.2) leads to:

$$\begin{cases} \mid sp_a >= \frac{1}{\sqrt{2}} \left(\mid 2s > + \mid 2p_x > \right) \\ \mid sp_b >= \frac{1}{\sqrt{2}} \left(\mid 2s > - \mid 2p_x > \right) \end{cases} \tag{1.3}$$

sp^2 Hybridization (trigonal)

The sp^2 hybridization is the mixing of one $2s$ and two $2p$ atomic orbital, which involves the promotion of one electron in the s orbital to one of the $2p$ atomic orbitals. The combination of these atomic orbitals creates three new hybrid orbitals equal in energy-level. The hybrid orbital is higher in energy than the s orbital but lower in energy than the p orbital, but they are closer in energy to the p orbital. The new set of formed hybrid orbitals creates trigonal structures, creating a molecular geometry of $120°$. The combination of one s orbital, and two

p orbital from the same valence shell provides a set of three equivalent sp^2 hybridized orbital that point in directions separated by $120°$. The directions of these new hybridized orbitals are the dictators of the spatial arrangement for bonding. The sp^2 hybridized orbitals are the same in size, energy shape but different in the spatial orientation. This unique orientation is imperative and is what characterizes a sp^2 hybridized orbital from other hybridized orbitals.
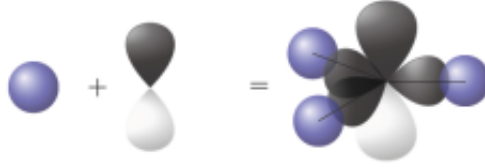
Figure 1.9: sp^2 Hybridization orbitals.

The corresponding sp^2 hybridized orbitals $\mid sp_i>$ $(i = a, b, c)$ are as follows [8]:

$$\begin{cases} \mid sp_a^2 >= C_1 \mid 2s > +\sqrt{1 - C_1^2} \mid 2p_y > \\ \mid sp_b^2 >= C_2 \mid 2s > +\sqrt{1 - C_2^2} \left(\frac{\sqrt{3}}{2} \mid 2p_x > -\frac{1}{2} \mid 2p_y > \right) \\ \mid sp_c^2 >= C_3 \mid 2s > +\sqrt{1 - C_3^2} \left(-\frac{\sqrt{3}}{2} \mid 2p_x > -\frac{1}{2} \mid 2p_y > \right), \end{cases} \tag{1.4}$$

The determination of C_1, C_2 and C_3 is done from the orthonormal requirements of the orbitals and leads to the three following equations:

$$\begin{cases} C_1^2 + C_2^2 + C_3^2 = 1 \\ C_1 C_2 - \frac{1}{2}\sqrt{1 - C_1^2}.\sqrt{1 - C_2^2} = 0 \\ C_1 C_2 + \frac{1}{2}\sqrt{1 - C_1^2}.\sqrt{1 - C_3^2} = 0, \end{cases} \tag{1.5}$$

yielding the solution of Equation (1.5) given by $C_1 = C_2 = C_3 = \frac{1}{\sqrt{3}}$

sp^3 Hybridization (tetrahedral)

To achieve sp^3 bonding, first promotion of one electron from $2s$ to $2p$ results in four singly filled orbitals. Then, the $2s$ orbital is hybridized with all three $2p$ orbitals. This makes four equivalent sp^3 orbitals with tetrahedral symmetry, for electron repulsion minimization. Each has 75 % p and 25 % s character and occupied by one electron. The bond angles of a tetrahedron is $109.58°$. Any combination of atomic and hybrid orbitals may overlap to form $C-C$ bonds which are generated by overlap of hybrid orbitals. The diamond cubic crystal lattice is two tetrahedrally bonded atoms in each primitive cell. Separated by $1/4$ of the width of the unit cell in each dimension. The four directions of tetrahedral bonds from the carbon can be selected as $(1, 1, 1)$, $(-1, -1, 1)$, $(-1, 1, -1)$ and $(1, -1, 1)$. In order to make elongated wave functions to these directions, the $2s$ orbital and the three $2p$ orbitals are mixed, forming an sp^3 hybridization.

The solving of similar equations to equations (1.5) with four unknown coefficients $C_i = (i = 1, 2, 3, 4)$, and orthonormal conditions lead to atomic wave functions. The sp^3 hybrid orbitals obtained in these four directions are as follows [8]:

$$
\begin{cases}
\mid sp_a^3 > = \frac{1}{2}\Big(\mid 2s > + \mid 2p_x > + \mid 2p_y > + \mid 2p_z > \Big) \\
\mid sp_b^3 > = \frac{1}{2}\Big(\mid 2s > - \mid 2p_x > - \mid 2p_y > + \mid 2p_z > \Big) \\
\mid sp_c^3 > = \frac{1}{2}\Big(\mid 2s > - \mid 2p_x > + \mid 2p_y > - \mid 2p_z > \Big) \\
\mid sp_d^3 > = \frac{1}{2}\Big(\mid 2s > + \mid 2p_x > - \mid 2p_y > - \mid 2p_z > \Big)
\end{cases}
\tag{1.6}
$$

In sp^n hybridization, $(n+1)\sigma$ bonds per carbon atom are formed, these σ bonds constitute the skeleton for the local structure of n-dimensional allotrope.

1.2 Electronic band structures of graphene

The problem of electrons in a solid is a multi-electron problem in general, where we have to consider the electron-nucleus interactions as well as the pair potentials describing the electron-electron interactions. We place ourselves in the independent electron approximation where these interactions are represented by an effective potential at one electron. The eigenstates ψ of the one-electron halmitonian where the potential has the periodicity of the Bravais lattice can be chosen as plane waves that are multiplied by a function having the Bravais periodicity, with n called band index and $\overrightarrow{k}$ a given vector:

$$
\psi_{n,k(\overrightarrow{r}+\overrightarrow{R})} = e^{i\overrightarrow{k}.\overrightarrow{r}}.\psi_{n,k}(\overrightarrow{r})
\tag{1.7}
$$

Let us consider an electron moving in a network of periodic atoms. The Hamiltonian that governs its behavior can be decomposed into a kinetic part and a potential part, which will translate the Coulombic interaction between the electron and each of the atoms (nuclei and core and valence electrons). By noting $\overrightarrow{R_n}$ the position, fixed of the n-th atom, and $\overrightarrow{r}$ the position of the electron, the strong bond approximation assumes that in the vicinity of each lattice node, the total Hamiltonian H of the crystal will be written as follows:

$$
H_{at}(\overrightarrow{r} - \overrightarrow{R_n}) = \frac{P2}{2m} + \sum_n V_{at}(\overrightarrow{r} - \overrightarrow{R_n})
\tag{1.8}
$$

This Hamiltonian satisfies the eigenvalue equation :

$$
H_{at}(\overrightarrow{r} - \overrightarrow{R_n}).\Phi(\overrightarrow{r} - \overrightarrow{R_n}) = E_0.\Phi(\overrightarrow{r} - \overrightarrow{R_n})
\tag{1.9}
$$

The wave function of our electron becomes a linear combination of atomic orbitals centered

on the lattice sites and weighted by a phase factor :

$$\psi_{(\vec{r})} = \sum_n e^{i\vec{k}.\vec{r}}.\Phi_{at}(\vec{r} - \vec{R_n}) \tag{1.10}$$

The use of the wave function in the strong bond approximation for graphene uses two atoms per mesh. We will therefore label these atoms A and B, and establish the corresponding functions:

$$\psi^A{}_{k(\vec{r})} = \sum_n e^{i\vec{k}.\vec{R_n}}.\phi(\vec{r} - \vec{R_n}) \tag{1.11}$$

$$\psi^B{}_{k(\vec{r})} = \sum_n e^{i\vec{k}.\vec{R_m}}.\phi(\vec{r} - (\vec{R_m} - \vec{\tau_B})) \tag{1.12}$$

Or $\vec{\tau_B}$ is the translation vector from atom A to atom B. The total electronic wave function in the lattice is written as :

$$\mid \psi > = C_A \mid \psi^A_{\vec{k}} > + C_B \mid \psi^B_{\vec{k}} > \tag{1.13}$$

Determining the energy associated with this Hamiltonian amounts to solving the eigenvalue equation :

$$H \mid \psi > = E \mid \psi > \tag{1.14}$$

$$C_A H \mid \psi^A_k > + C_B H \mid \psi^B_k > = E(C_A \mid \psi^A_{\vec{k}} > + C_B \mid \psi^B_{\vec{k}} >) \tag{1.15}$$

The projection on the states ψ^A_k and ψ^B_k, knowing that $< \psi^i_k \mid H \mid \psi^j_k >$ groups the kinetic and potential energies, and $< \psi^i_k \mid \psi^j_k >$ represents the overlap of the orbitals between close neighbors. The following notations allow us to write:

$$\begin{cases} H_{ij} = < \psi^i_k \mid H \mid \psi^j_k > \\ S_{ij} = < \psi^i_k \mid \psi^j_k > \end{cases} \tag{1.16}$$

$$\begin{cases} C_A(H_{AA} - E) + C_B(H_{AB} - E.S_{AB}) = 0 \\ C_A(H_{BA} - E.S_{BA}) + C_B(H_{BB} - E) = 0 \end{cases} \tag{1.17}$$

Since atoms A and B occupy strictly equivalent sites, their energy terms are identical:

$$H_{BA} = < \psi_B \mid H \mid \psi_A > = < \psi_A \mid H \mid \psi_B >^* = H^*_{AB} \tag{1.18}$$

The same is true for recovery terms:

$$S_{BA} = < \psi_B \mid \psi_A > = < \psi_A \mid \psi_B >^* = S^*_{AB} \tag{1.19}$$

Equations (1.18 and 1.19) are finally used to calculate the determinant of the matrix in

energy, so the result is the following

$$E^2(1- \mid S_{AB} \mid^2) + E(-2H_{AA} + H_{AB}.S^*_{AB} + S_{AB}.H^*_{AB}) + H^2_{AA} - \mid H_{AB} \mid^2 = 0 \qquad (1.20)$$

New shortcuts will allow us to write this expression as a second degree equation in E.

$$\begin{cases} E_0 = H_{AA} \\ E_1 = S_{AB}.H^*_{AB} + H_{AB}.S^*_{AB} \\ E_2 = H^2_{AA} - H_{AB}.H^*_{AB} \\ E_3 = 1 - S_{AB}.S^*_{AB} \end{cases} \qquad (1.21)$$

The two resulting roots of equation (1.21) are the allowed energy values for the electrons p_z of the graphene:

$$E^{\pm}(\vec{k}) = \frac{-(-2E_0 + E_1) \pm \sqrt{(-2E_0 + E_1)^2 - 4E_2E_3}}{2E_3} \qquad (1.22)$$

In the graphene structure, the distance between first neighbors is much smaller than the distance between higher order neighbors. We will restrict the calculations to the first neighbors (Figure 1.10).
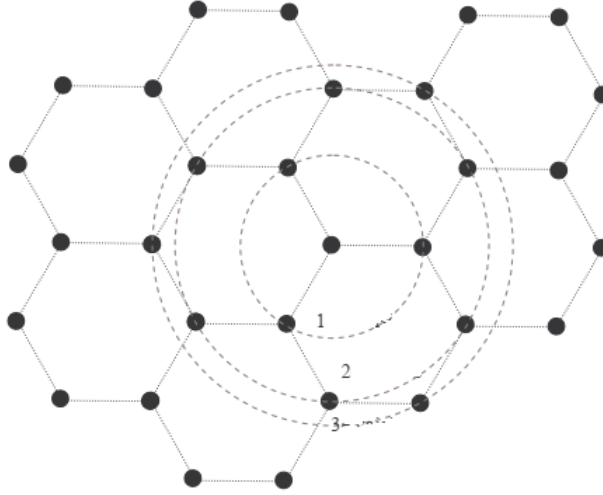
Figure 1.10: Arrangement of the different neighbors in graphene.

This involves the following three approximations. First, the energy H_{AA} becomes a constant, since the first neighbors of an atom A cannot be only atoms B and intervene (N is the number of elementary meshes in the crystal) :

$$H_{AA} = \tfrac{1}{N} \sum_n \sum_{n''} < \phi(\vec{r} - \vec{R_n}) \mid H \mid \phi(\vec{r} - \vec{R_{n''}}) > .e^{i\vec{k}.(\vec{R_{n''}} - \vec{R_n})}$$

$$= \tfrac{1}{N} \sum_n < \phi(\vec{r} - \vec{R_n}) \mid H \mid \phi(\vec{r} - \vec{R_n}) >$$

or

$$H_{AA} = \varepsilon_{2p} \tag{1.23}$$

Then, the interaction between atom A and B is only with the neighboring meshes, located in $-\vec{a_1}, -\vec{a_2}$ and $(-\vec{a_1} - \vec{a_2})$:

$$H_{AB} = \frac{1}{N} \sum_n \sum_m .e^{i\vec{k}.(\overrightarrow{R_B} - \overrightarrow{R_A})} < \phi(\vec{r} - \overrightarrow{R_n}) \mid H \mid \phi(\vec{r} - (\overrightarrow{R_m} - \vec{\tau_B})) >$$

$$H_{AB} = \gamma_0 (e^{-i\vec{k}.\vec{a_1}} + e^{-i\vec{k}.\vec{a_2}} + e^{-i\vec{k}.(\vec{a_1}+\vec{a_2})}) \tag{1.24}$$

With $\gamma_0 = < \phi(\vec{r} - \overrightarrow{R_n}) \mid H \mid \phi(\vec{r} - \overrightarrow{R_n} - \vec{a_i}) >$

And finally, in the same way,

$$S_{AB} = S_0 (e^{-i\vec{k}.\vec{a_1}} + e^{-i\vec{k}.\vec{a_2}} + e^{-i\vec{k}.(\vec{a_1}+\vec{a_2})}) \tag{1.25}$$

With $S_0 = < \phi(\vec{r} - \overrightarrow{R_n}) \mid \phi(\vec{r} - \overrightarrow{R_n} - \vec{a_i}) >$

$$f(\vec{k}) = (e^{-i\vec{k}.\vec{a_1}} + e^{-i\vec{k}.\vec{a_2}} + e^{-i\vec{k}.(\vec{a_1}+\vec{a_2})})(e^{i\vec{k}.\vec{a_1}} + e^{i\vec{k}.\vec{a_2}} + e^{i\vec{k}.(\vec{a_1}+\vec{a_2})})$$

We recalculate the energies E_0, E_1, E_2, E_3, and introducing the function

$$f(\vec{k}) = (3 + 2cos(\vec{k}.\vec{a_1}) + 2cos(\vec{k}.\vec{a_2}) + 2cos(\vec{k}.(\vec{a_1} - \vec{a_2})) \tag{1.26}$$

$$\begin{cases} E_0 = \varepsilon_{2p} \\ E_1 = 2\gamma_0.S_0.f(\vec{k}) \\ E_2 = \varepsilon_{2p}^2 - \gamma_0^2.f(\vec{k}) \\ E_3 = 1 - S_0^2.f(\vec{k}) \end{cases} \tag{1.27}$$

We thus obtain the final expression of the energy of the elections p_z in graphene.

$$E^{\pm}(\vec{k}) = \frac{\varepsilon_{2p} \pm \gamma_0 \sqrt{f(\vec{k})}}{1 \pm S_0 \sqrt{f(\vec{k})}} \tag{1.28}$$
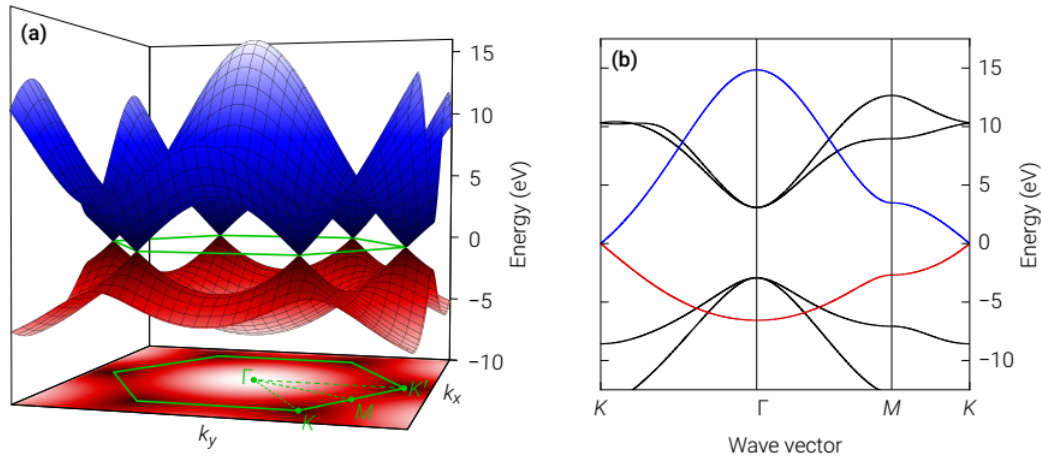
Figure 1.11: Electronic band structure of graphene. (a) Dispersion of the graphene valence (red) and conduction band (blue) formed from the unhybridized carbon $\pi-$orbitals. The hexagonal first BZ featuring the high-symmetry points Γ, M, K , and K' is highlighted in green. (b) Dispersion of the graphene valence band (red), conduction band (blue), and the four lowest-energy $\sigma-$bands along the edges of the triangle ΓMK [16].

Peak	Energy (eV)			Final-state band and Brillouin-zone region
	This work	Ref. 5	Ref. 9^h	
A	285.5	285		π_0 near Q
B	292.5	293	292.4	σ_1, σ_2: Γ→Q
C	295.5			π_0 or π_1 near Γ
D	297.8		296.9	σ_3-σ_6: Q→P
E	303.5	302	303.9	σ_7 near Q
F	307.5		306.9	σ_9 near Q
G	308.5			
H	316.5	316.5		π_4 near Q
I	329	325		
J	333			
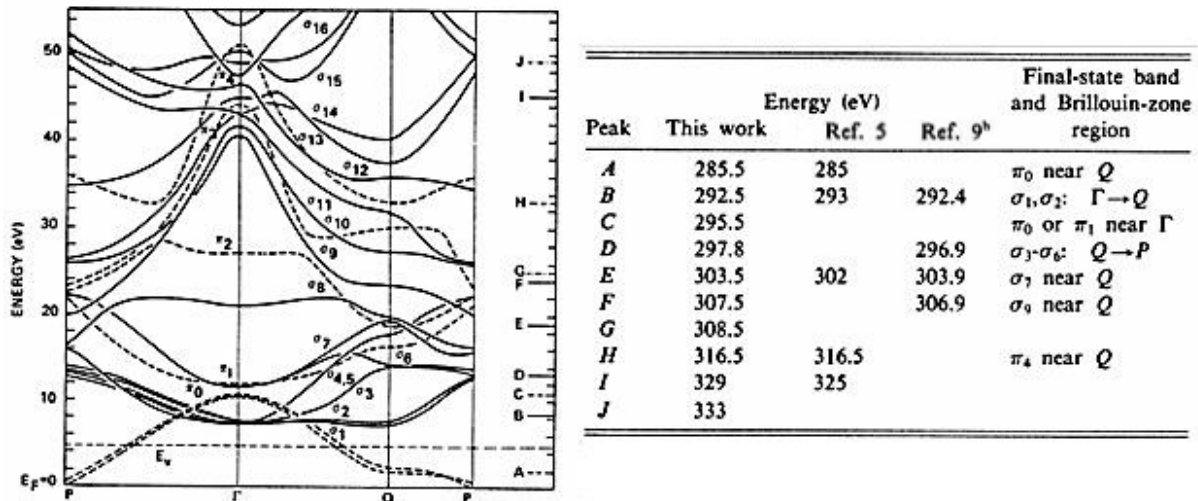
Figure 1.12: Band structure of the graphite (to the left) and graphical representation of peak positions and their symmetries taken from the XAS spectra of monocrystalline graphite (to the right of the band diagram) [17].

The energy scale is aligned so that peak A corresponds to the lowest energy state, of symmetry π, i.e. π_0, in the vicinity of Q in the Brillouin zone, 2 eV above the level by Fermi E_F. The vacuum level is indicated by a dotted line [17]. Different transitions observed in the XAS spectra of graphite, energy positions, symmetry (π or σ) of the transition and the corresponding final state band in the theoretical band structure, and region of the corresponding Brillouin zone [17]. Now that the electronic structure of graphite is specified, it is easy to obtain the electronic properties of carbon nanotubes as we will see in the following.

1.2.1   Direct Lattice Structure of Graphene

These different types of symmetry (armchair, zigzag, chiral) are characterized by the use of two indices (n, m) called indices of chirality. The chirality is a concept that allows to define precisely the geometry, the symmetry and globally to identify the CNT. The different ways of winding the graphene sheet to form a CNT are defined by a vector and an angle of helicity, respectively noted $\overrightarrow{C_h}$ and θ. The chirality vector is defined by the following relation:

$$\overrightarrow{C_h} = n\overrightarrow{a_1} + m\overrightarrow{a_2} = \frac{a}{2} \begin{cases} \sqrt{3}(n+m) \\ (-n+m) \\ 0 \end{cases} \qquad (1.29)$$

With $(n, m)\epsilon \ N^2$ two positive integers characteristic of the tube, $\overrightarrow{a_1}$ and $\overrightarrow{a_2}$ the two unit vectors defining the graphene plane. Knowing that $a = a_{c=c} \ \sqrt{3}$, where $a_{c=c}$ corresponds to the length of the bond between two carbon atoms of a CNT ($a_{c=c} = 1,42 \ \mathring{A}$). The SWCNT consists of a single graphene sheet, illustrated in (Figure 1.13). The diameter values of SWCNTs are, according to Yu et al.[14], between (1-1.5 nm). The lengths can go up to a few μm. These indices are called chiral indices and univocally designate all the structural characteristics of a given nanotube, such as its diameter d, the translation vector $\vec{T}$ (smallest vector belonging to the graphene lattice and orthogonal to $\vec{C_h}$), we have the relation $\overrightarrow{C}.\overrightarrow{T} = 0$.
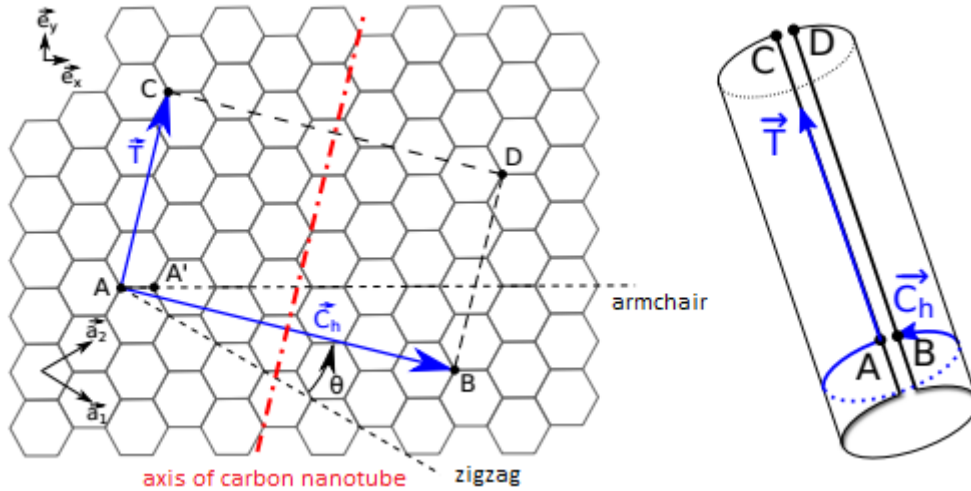
Figure 1.13: Example of bulding of a chiral index nanotube $(n, m)\equiv(5, 2)$. Its elementary mesh can be defined by the vectors $\vec{C_h}$ and $\vec{T}$.

$$\begin{cases} d = \frac{|\overrightarrow{C_h}|}{\pi} = \frac{a}{\pi}\sqrt{n^2 + nm + m^2} \\ \theta = arctan(\frac{m\sqrt{3}}{2n+m}) \qquad\qquad\qquad 0 \le \theta \le 30^\circ \\ \overrightarrow{T} = t_1\overrightarrow{a_1} + t_2\overrightarrow{a_2} = -\frac{n+2m}{d}\overrightarrow{a_1} + \frac{2n+m}{d}\overrightarrow{a_2} \end{cases} \qquad (1.30)$$

Various types of carbon nanotubes are characterized by their respective chiral angles. Two

types of structures are possible, having reflection planes and which are achiral: one named armchair ($\theta = 30°$) whose winding vectors are of type (n, n) and the second one, named zigzag ($\theta = 0°$) whose winding vectors are of type $(n, 0)$. All the other nanotubes $0 < \theta < 30°$ whose parameters (n, m) are independent have a chiral structure with spiral hexagons along the tube axes. The electronic properties of the nanotubes are determined by both their chirality and their diameter.

$\Rightarrow$ For armchair nanotubes (n, m), $\overrightarrow{a_\perp} = n(\overrightarrow{a_1} + \overrightarrow{a_2})$;

$\Rightarrow$ For zigzag nanotubes $(n, 0)$ ou $(0, n)$, $\overrightarrow{a_\perp} = n\overrightarrow{a_1}$.

For n large enough, the zigzag tubes are metallic. If n is a multiple of 3, carbon nanotubes are metallic and semiconductor otherwise

1.2.2 The Reciprocal Lattice of Graphene

The reciprocal lattice is determined according to the usual orthogonality relations with the direct network. Basic vectors $\overrightarrow{K_1}$ and $\overrightarrow{K_2}$ are shown in Figure 1.14. The winding of the nanotube amounts to introducing a condition of periodicity on the functions waves along the circumference of the nanotube. Nanotubes will therefore be systems one-dimensional. Thus, there are $\frac{2\pi}{N}$ vectors $\overrightarrow{k}$ allowed along the circumference. The vector $\overrightarrow{K_2}$ parallel to the axis of the nanotube will be the basic vector of the dispersion curves. Thereby the vectors authorized in any nanotube will be defined by:

$$\frac{-\pi}{|\overrightarrow{T}|} \leq k \leq \frac{\pi}{|\overrightarrow{T}|}; \qquad k_q = k_\perp = \frac{2\pi q}{L} \qquad q \epsilon\, [1 : 2N] \tag{1.31}$$

k is the (scalar) vector defining the first 1D Brillouin zone along the axis of the nanotube and $k_q = k_\perp$ gives the quantization relation related to the confinement according to the circumference. Thus, the armchair nanotubes have for First Brillouin zone and quantification relation (Figure 1.14(a)).

$$\frac{-\pi}{a} \leq k \leq \frac{\pi}{a}; \qquad k_q = k_\perp = \frac{2\pi q}{na\sqrt{3}} \qquad q \epsilon\, [1 : 2n] \tag{1.32}$$

And the zigzags (Figure 1.14(b))

$$\frac{-\pi}{a\sqrt{3}} \leq k \leq \frac{\pi}{a\sqrt{3}}; \qquad k_q = k_\perp = \frac{2\pi q}{na} \qquad q \epsilon\, [1 : 2n] \tag{1.33}$$
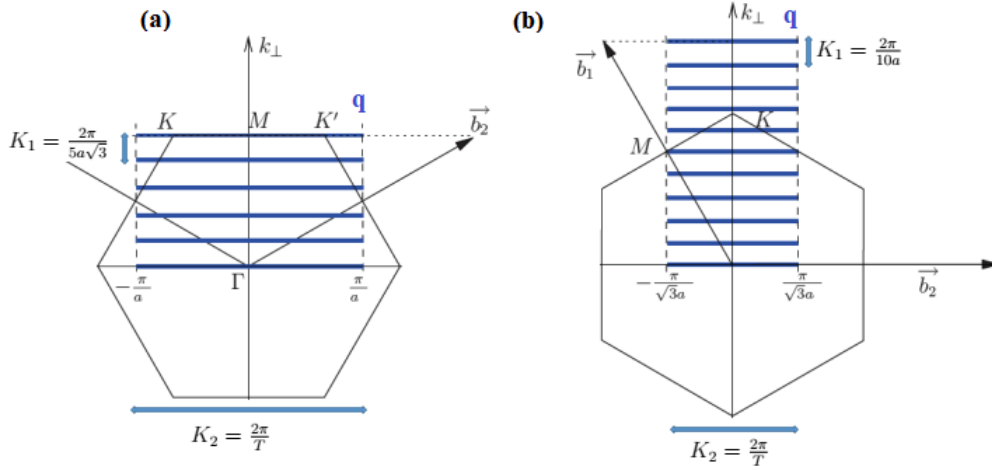
Figure 1.14: First Brillouin zone and quantized vectors (a) armchair nanotube (5,5) (b) zig-zag nanotube (10,0) with the rotation indices q corresponding to the zone folding method [18].

1.3   Electronic band structures of carbon nanotubes

Just like graphite, the carbon nanotubes we study are seen as a sheet of graphene folded on itself along a certain direction defined by a new vector :

$$\vec{a_\perp} = n\vec{a_1} + m\vec{a_2} = \frac{a}{2}\begin{pmatrix} \sqrt{3}(n+m) \\ (-n+m) \\ 0 \end{pmatrix} \tag{1.34}$$

where n, m positive integers defining the nanotube. The norm of $\vec{a_\perp}$ defines the circumference of the nanotube thus : $C_{h(n,m)} =\| \vec{a_\perp} \|= a\sqrt{(n^2 + m^2 + nm)}$. We can easily deduce the radius of the tube : $R_{(n,m)} = \frac{C_{h(n,m)}}{2\pi} = \frac{a}{2\pi}\sqrt{(n^2 + m^2 + nm)}$. The direction orthogonal to $\vec{a_\perp}$ defines the axis of the tube. We thus define a base vector $\vec{a_\parallel}$, which will make it possible to reproduce the unit cell along this axis. This vector must therefore also be a linear combination of $\vec{a_1}$ and $\vec{a_2}$, in addition to its property of orthogonality with $\vec{a_\perp}$:

$$\begin{cases} \vec{a_\parallel} = \quad p\vec{a_1} + q\vec{a_2} = \frac{a}{2}\begin{pmatrix} \sqrt{3}(p+q) \\ (-p+q) \\ 0 \end{pmatrix} \\ \vec{a_\perp}.\vec{a_\parallel} \quad = 0, \end{cases} \tag{1.35}$$

The new integers p and q are obviously related to n and m :
$\frac{3a^2}{4}(n+m)(p+q) + \frac{a^2}{2}(-n+m)(-p+q) = 0$, $4np + 2np + 2mp + 4mp = 0$

$$q = -p\left(\frac{2n+m}{2m+n}\right) \tag{1.36}$$

We introduce the greatest common divisor to $(2n + m)$,

$d = pgdc\left\{(2n+m),(2m+n)\right\}$ and we have the expression of the basic vector along the axis of the tube :

$$\overrightarrow{a_{/\!/}} = \left(\frac{2m+n}{d}\right)\overrightarrow{a_1} - \left(\frac{2n+m}{d}\right)\overrightarrow{a_2} = \frac{a}{2d}\begin{pmatrix} \sqrt{3}(m-n) \\ -3(m+n) \\ 0 \end{pmatrix} \tag{1.37}$$

A nanotube is therefore a one-dimensional structure, with the unique basis vector $\overrightarrow{a_{/\!/}}$. It can be shown that the unit cell contains $\frac{4(n^2+m^2+nm)}{d}$ atoms, which can quickly become enormous when the radius of the tube, either n or m , increasing the basis vectors of the reciprocal lattice can be calculated :

$$\begin{cases} \overrightarrow{b_\perp} &= \frac{\pi}{a(n^2+m^2+nm)}\begin{pmatrix} \sqrt{3}(m+n) \\ (-n+m) \\ 0 \end{pmatrix} \\[6mm] \overrightarrow{b_{/\!/}} &= \frac{\pi d}{a(n^2+m^2+nm)}\begin{pmatrix} \frac{(m-n)}{\sqrt{3}} \\ -(n+m) \\ 0 \end{pmatrix} \end{cases} \tag{1.38}$$
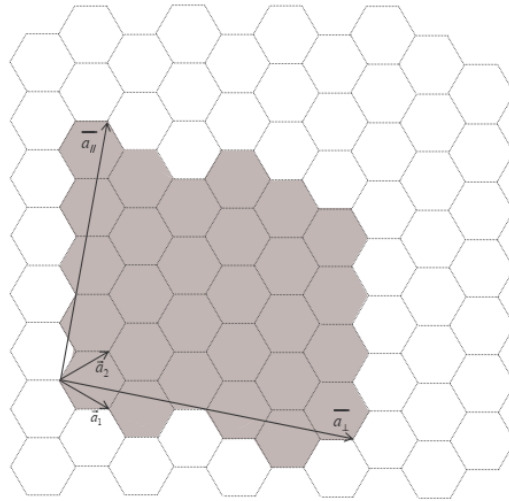
Figure 1.15: The basic carriers of a carbon nanotube $(4,2)$. $\overrightarrow{a_\perp}$ sets the folding direction and $\overrightarrow{a_{/\!/}}$ the translation vector directed along the axis of the tube. The shaded area is the unit cell.

1.3.1   Folding Index

A direct consequence of the folding of the graphene sheet on itself according to $\overrightarrow{a_\perp}$ is the appearance of new periodic boundary conditions, and therefore a quantization of the wave vector $\overrightarrow{k}$ in that direction :

$$k_\perp = \frac{2\pi l}{\sqrt{a(n^2 + m^2 + nm)}} \tag{1.39}$$

where l, takes $2n$ values. The dispersion in energy will only be done along the axis of the tube, the energy will therefore only be a function of $\overrightarrow{k_{\parallel}}$, which further confirms that it has a one-dimensional structure.

1.3.2 Energy calculation using the tight binding method

Using the energy expression already established for graphene, equation (1.28), neglecting orbital overlaps ($s_0 = 0$),

$$E_{(\overrightarrow{k})} = \varepsilon_0 \pm \gamma_0 \left(3 + 2cos(\overrightarrow{k}.\overrightarrow{a_1}) + 2cos(\overrightarrow{k}.\overrightarrow{a_2}) + 2cos(\overrightarrow{k}.(\overrightarrow{a_1} - \overrightarrow{a_2}))\right)^{1/2} \tag{1.40}$$

Then we included the quantization condition equation (1.39) to start we must reexpress the vectors $\overrightarrow{a_1}$ and $\overrightarrow{a_2}$ of the expression of equation (1.34) depending on the vectors $\overrightarrow{a_\perp}$ and $\overrightarrow{a_{\parallel}}$ that we know:

$$\begin{cases} \overrightarrow{a_1} = \frac{d}{(2m+n)+\frac{n}{m}(2n+m)}\overrightarrow{a_{\parallel}} + \frac{\frac{2n+m}{m}}{(2m+n)+\frac{n}{m}(2n+m)}\overrightarrow{a_\perp} \\ \\ \overrightarrow{a_2} = \frac{-d}{(2n+m)+\frac{m}{n}(2m+n)}\overrightarrow{a_{\parallel}} + \frac{\frac{2m+n}{n}}{(2n+m)+\frac{m}{n}(2m+n)}\overrightarrow{a_\perp} \end{cases} \tag{1.41}$$

In writing $\overrightarrow{k} = \overrightarrow{k_\perp} + \overrightarrow{k_{\parallel}}$, and using orthogonality relations :

$$\begin{cases} \overrightarrow{k_\perp}.\overrightarrow{a_{\parallel}} \quad \Longleftrightarrow \quad \overrightarrow{k_\perp}.\overrightarrow{a_{\parallel}} = 0 \\ \\ \overrightarrow{k_{\parallel}} \perp \overrightarrow{a_\perp} \quad \Longleftrightarrow \quad \overrightarrow{k_{\parallel}}.\overrightarrow{a_\perp} = 0 \end{cases}$$

$$\begin{cases} E_k^{(n,n)} = \varepsilon_0 \pm \gamma_0 \left(1 + 4cos^2(\frac{a.k_{\parallel}}{2}) + 4cos(\frac{l\pi}{n})cos(\frac{a.k_{\parallel}}{2})\right)^{1/2} \\ \\ E_k^{(n,0)} = \varepsilon_0 \pm \gamma_0 \left(1 + 4cos^2(\frac{l\pi}{n}) + 4cos(\frac{l\pi}{n})cos(\frac{a\sqrt{3}.k_{\parallel}}{2})\right)^{1/2} \end{cases} \tag{1.42}$$

1.3.3 Energies and origins of optical transitions in carbon nanotubes

As a first approximation, optical transitions in carbon nanotubes can be described as transitions between van Hove singularities. The most likely electronic transitions are those involving energy states associated with pairs of symmetric singularities. They are generally characterized by the nature of the nanotube considered and the pair of singularities involved in the transition. For nanotubes one will find metallic transitions M_{ii} and for semiconductor nanotubes we will have transitions denoted S_{ii} (Figure 1.16). For reasons of symmetry, in the general case, E_{ij} type transitions, with $i \neq j$, are prohibited. In the conical dispersion approximation around point K, the background energies of band with respect to the Fermi

energy can be written, whatever the nanotube, under the form:

$$\varepsilon_i = p\frac{a_{c-c}\gamma_0}{d\sqrt{3}} \tag{1.43}$$

with i a nonzero integer. The value of p depends on the semiconductor or metallic type of the nanotube. It simply comes that the energy separating two even singularities is $2\varepsilon_i$ due to band symmetry from the tight-binding approximation [19]. From where :

$$E_{ii} = 2p\frac{a_{c-c}\gamma_0}{d\sqrt{3}} \tag{1.44}$$

The energies of the different electronic transitions in carbon nanotubes monolayers are usually plotted in a diagram as a function of diameter nanotubes [20,21]. This diagram is commonly called Kataura diagram which was the first to introduce it (Figure 1.16). We find the dependence of energy in function of the inverse of the diameter of the nanotubes. The name of the Kataura diagram is however, remained the energies calculated by the last with a recovery integral $\gamma_0 = 2.75$ eV does not agree perfectly with the experiment.
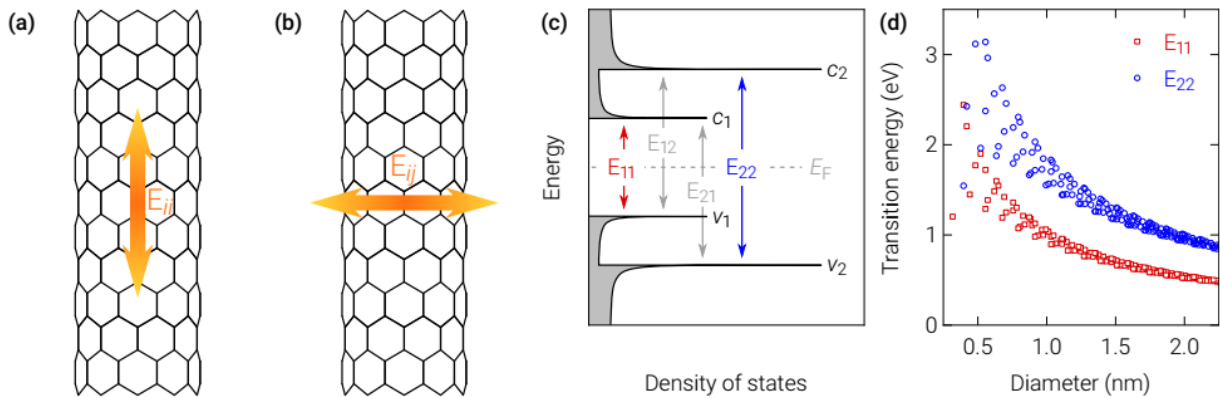
Figure 1.16: Band-to-band transitions of CNTs. (a)–(b) Illustration of electric dipole selection rules for optical transitions with light polarization parallel (left) and orthogonal (right) to the CNT axis, respectively. (c) Optical transitions between the first two valence band (V_1, V_2) and conduction band (C_1, C_2) VHSs, respectively, that are numbered with increasing distance from the Fermi energy E_F. The transitions E_{11} (red) and E_{22} (blue) between valence and conduction band states of equal number are dominant, while the transitions E_{12} and E_{21} (gray) are suppressed. (d) Kataura plot of the transition energies for E_{11} and E_{22} of semiconducting CNTs as a function of the CNT diameter. The data points follow the empirical formulas from [22]. Graphics (a)–(d) are reproduced from [16].

1.4   Properties and Applications of Carbon Nanotubes

1.4.1   Electrical and electronic properties

The peculiarity of the electrical properties of SWCNTs lies in the fact that their metallic or semiconducting nature varies according to the winding of the graphene sheet, i.e., according to their helicity and diameter [23,24]. The combination of size, lightness and electrical properties

of nanotubes has led the scientific community to invest massively in determining potential applications. To this end, single-walled nanotubes can be considered as pure quantum wires in which electrons are confined along the tube axis, behaving as ballistic conductors and thus being able to conduct electrons without heating. An electrical conductivity of 3.104 S.cm^{-1} has been determined for a SWCNTs bundle [25].

The general rules on the character of nanotubes:

⇛ All armchair nanotubes (n, n) are metallic;

⇛ All zigzag nanotubes $(n, 0)$ or $(0, n)$ with n multiples of 3 are metallic, the others are semiconductors;

⇛ All chiral nanotubes (n, m) with $m - n = 3h$ $(h\epsilon Z)$ are metallic, the others are semi-conductors.

The study of the electronic properties of MWCNTs is much more complex. Indeed, each wall having its own helicity, it is difficult to make predictive calculations. However, at high temperature, the conductivity of these materials approaches the semi-classical models used for graphite and carbon fibers, while at low temperature they behave like 2D quantum conductors [26]. CNT electrical properties also depend sensitively on their environment; the adsorption of different chemical species onto the SWCNT and MWCNTs sidewalls can strongly affect the electrical conductivity, making them useful for sensing applications [27]. SWCNT also have potential application in energy production, including in photovoltaics and energy storage. In photovoltaic devices, the conductivity and one dimensional nature of SWCNT allow for increased current mobility of excited electrons, which also reduces the chances of recombination of electrons with lower energy states, or electron holes, leading to improvements in device efficiency [28,29].

1.4.2   Thermal properties

The thermal conductivity of a material results from the exchange of phonons (generated by molecular vibrations) and the displacement of electrons in the material. In the case of CNTs, it is the displacement of electrons that is the main cause of thermal conductivity. As in the case of electrical conductivity, the thermal conductivity of CNTs is linear and is related to the curvature of the CNTs. Chirality is therefore important. The thermal conductivity of CNTs (from 3000 to 6600 W.m^{-1}.K^{-1}) is higher than that of graphite or diamond, the latter being known to be an excellent thermal conductor (from 1000 to 2600 W.m^{-1}.K^{-1}) [30].

1.4.3   Chemical and adsorption properties

Carbon nanotubes are characterized by their high chemical stability. Thanks to the C=C double bond, it is possible to modify their surface properties by joining the functional groups. CNTs have very attractive chemical properties. It is indeed possible to functionalize their

surface by molecular grafting, to intercalate atoms or molecules (doping) between the single-walled nanotubes of a bundle (inter-tubular intercalation) as well as between the different walls of a multi-walled nanotube (inter-planar intercalation). The small dimensions of carbon nanotubes are also associated with large specific surface areas which correspond to the surface area of the samples related to their mass, or to the mass of carbon of the order of $102-103$ m²/g. They therefore have high adsorption capacities [31]. The specific surface area depends closely on the type of nanotube (SWCNTs or MWCNTs), the synthesis method used and the post-synthesis treatments. The specific surface can be described by the following formulation [32]:

$$S = \frac{2}{\rho(R_1 - R_2)} = \frac{2630}{n} \left[m^2/g \right] \tag{1.45}$$

where R_1 and R_2 are the outer and inner radii respectively, and n is equal to the number of walls. With $\rho = 2.26$ g/cm³ and $R_1 - R_2 = 3.36$ A°, these values correspond to those of graphite. This large specific surface area combined with the ease of creating chemical bonds by attachment of functional groups make them promising candidates in the field of catalysis [33]. The increase in the number of walls and to a lesser extent that of the diameter, also leads to a decrease in the specific surface of the CNTs (Figure 1.17).
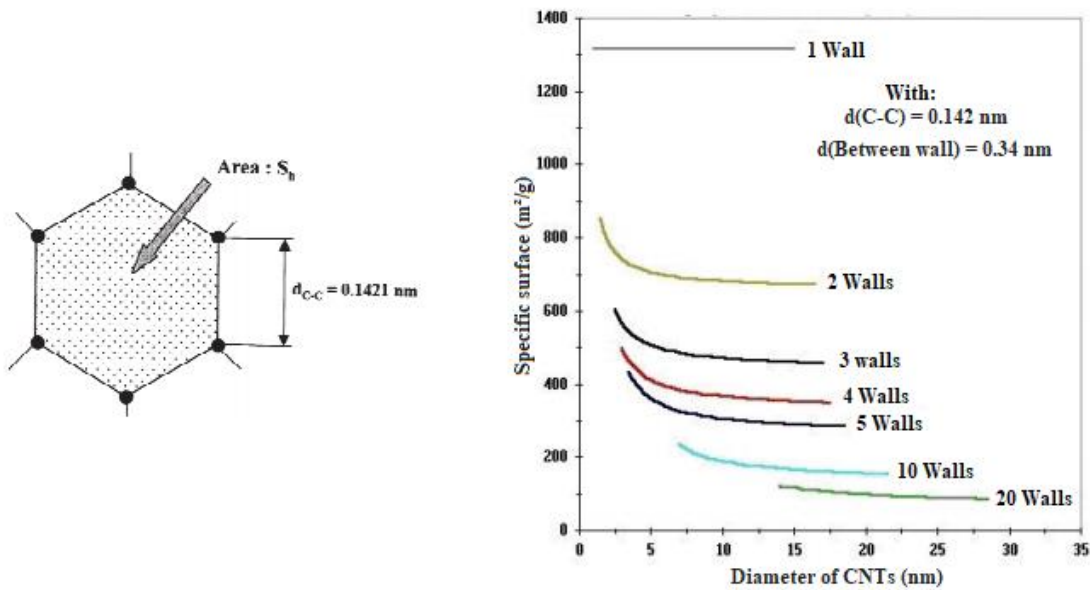
Figure 1.17: The surface area S_h of one hexagon and evolution of the specific surface of CNTs according to the number of walls and the diameter [32].

The convex surface of SWCNT (external) is chemically reactive because the convex arrangement of the sp^2 pyramidal carbon atoms is properly arranged for chemical bonding with reactive species. For the same reason, the concave (inner) surface is expected to be more inert and can resist to the presence of highly reactive species encapsulated in the nanotubes. Thus, the nature and intensity of adsorption are directly correlated to the carbon hybridization.

Furthermore, we now discuss how rehybridization can be observed in Scanning Tunneling Microscopy (STM) experiments. Already without rehybridization, the directions of the π-orbitals in a curved geometry can affect the STM images. If we consider this distortion for the case of a zigzag tube with $\theta = \pi/6$, we see that the hexagons of the graphite sheet will appear compressed in the transverse direction, but stretched around the circumference as shown in (Figure 1.18). For the armchair tubes $\theta = 0°$ on the other hand, there is no deformation along the transverse direction, but the hexagons are still deformed along the circumferential direction as shown in (Figure 1.18) [34].
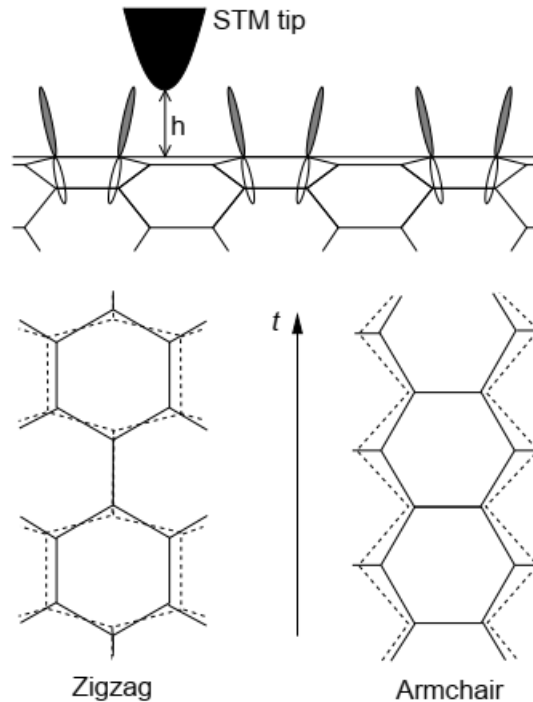
Figure 1.18: Predicted SWCNT deformation viewed by STM image (dashed lines) [34].

For a zigzag tube, we find a pronounced squaring of the hexagons and a change in the lattice constants along the transverse directions. For the armchair tube, the image is only affected along the circumferential direction [34]. These chemical properties are not especially unique, but they facilitate many potential applications. Often, pristine CNTs are oxidized to add sidechains to the nanotube walls, allowing for furhter functionalization. This allows one to personalize the nanotube properties, such as bandgap and solubility, and this also allows for SWCNTs and MWCNTs to be specifically linked to target substrates, which further allows for great control over interactions that can have with other molecules in a given system.

While the discussion so far has lead towards physical science applications, SWCNT also have potential applications in biomedical fields, such as in imaging and drug delivery. Because of some chiralities strong absorbance and emission in the $\sim 700 - 1100$ nm range, SWCNT make good candidates for bioimaging and sensing [35,36]. SWCNT also have potential applications for drug delivery. Due to the ease of functionalizing their sidewalls, SWCNT can be sensitized for interactions with certain biomolecules, allowing one to target specific locations

in an organism. For drug delivery, the SWCNT can be simultaneously loaded with drugs for release upon arrival to the target location [37,38]. Another potential SWCNT application involves photothermal therapy, where SWCNT adsorb Near infrared radiation (NIR), allowing for selective heating and destruction of cancer cells [39].

1.4.4 Curvature and rehybridization

The carbon network on graphene is planar, and thus forms sp^2 hybridization with orthogonal σ and π orbitals (Figure 1.19 (a)). In contrast, the carbon atoms on the CNT surface lie on a curved surface, and thus the σ bonds are pyramidalized, and the π- orbitals bend (Figure 1.19 (b)). Therefore, unlike in planar graphene, the σ and π- orbitals are no longer perpendicular to each other. As a consequence the parts of the π- orbitals outside and inside rearrange due to Coulomb repulsion, and the outer contribution is much larger than the inner one.

These lead to mixing of σ and π- orbitals, which is known as rehybridization, and crucially depends on the nanotube diameter and chirality. The rehybridization leads to bonding which is between sp^2 and sp^3, and can be recognized as $sp^{2+\tau}$. For Fig 1.19 (a), the π- orbital in planar graphene is orthogonal to the σ bonds. And for the Fig 1.19 (b) the π- orbital is no longer perpendicular to the σ bonds on a curved CNT surface, as the π bonds are tilted down by an angle ϑ relative to the tangential direction of the tube, and the π- orbital bending by an angle δ, with respect to the normal drawn on the tube surface.
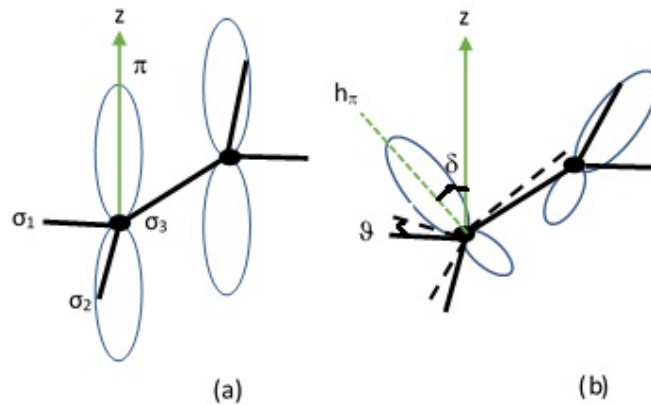
Figure 1.19: Schematic orbitals in graphene and carbon nanotubes [40].

These facts can be mathematically accounted for within π- orbital axis vector construction, where it is assumed that the wave function is still separable in terms of σ and π- orbitals. Assuming the σ bonds are tilted down by an angle ϑ (pyramidalization angle) relative to the tangential direction of the tube, this introduces mixing of p_z orbital with the σ network. Under the orthogonality conditions, the π states on the curved nanotube surface can be written as [41,42]

$$| h_\pi >= \frac{1}{\sqrt{1 + \lambda^2}}(| s > + \lambda | p_z >) \tag{1.46}$$

where λ depends only on the pyramidalization angle ϑ as $\lambda = \frac{1-3sin^2\vartheta}{2sin^2\vartheta}$.

Rehybridizied states have new wave functions, where π- orbital consists of both p and s orbitals. One can estimate the degree of rehybridization τ depending on the tube diameter d, and chirality (n, m). Let δ be the bending angle of π- orbital relative to the normal drawn on the tube surface, and presuming that the angles between the σ bonds and the π- orbitals are equal due to symmetry, one can show that δ depends on tube diameter, and chirality [13,34]. For zigzag and armchair nanotube:

$$\begin{cases} tan\delta = \dfrac{sin^2\frac{\pi}{2n}}{\frac{\pi\sqrt{3}}{6n}+\sqrt{\frac{\pi^2}{12n^2}+sin^2\frac{\pi}{2n}}} & zigzag \\[20pt] tan\delta = \dfrac{tan\frac{\pi}{3n}(2\sqrt{\frac{\pi^2}{12n^2}+sin^2\frac{\pi}{6n}}-tan\frac{\pi}{6n})}{2\sqrt{\frac{\pi^2}{12n^2}+sin^2\frac{\pi}{6n}}+tan\frac{\pi}{3n}} & armchair \end{cases} \tag{1.47}$$

Finally, one can derive an analytical expression for the degree of rehybridization τ in $sp^{2+\tau}$ for both zigzag and armchair nanotubes,

$$\begin{cases} \tau_{zigzag} = \dfrac{4(1+3sin^2\delta)}{3(1+2sin^2\delta)}\dfrac{sin^4\frac{\pi}{2n}}{\frac{\pi^2}{12n^2}+sin^2\frac{\pi}{2n}} & zigzag \\[20pt] \tau_{armchair} = \dfrac{2(1+3sin^2(\delta-\frac{\pi}{3n}))}{3(1+2sin^2(\delta-\frac{\pi}{3n}))}\dfrac{sin^2\frac{\pi}{3n}+2sin^4\frac{\pi}{6n}}{\frac{\pi^2}{12n^2}+sin^2\frac{\pi}{6n}} & armchair \end{cases} \tag{1.48}$$

For both CNTs of type (n, n) and $(n, 0)$ the curvature decreases with diameter and is dominant for zigzag CNTs. This confirming that the curvature effects become dominant in zigzag CNTs. The degree of hybridization (Figure 1.20) is decreasing linearly in the interval $1 \leq n \leq 8$.
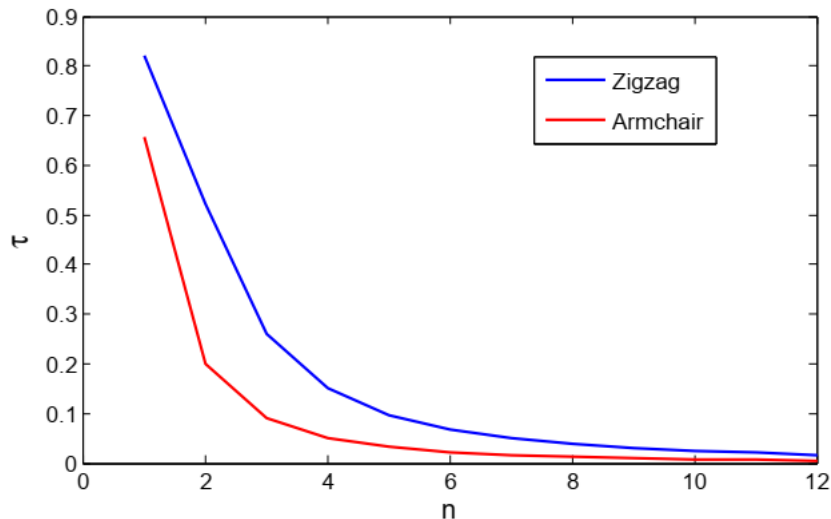
Figure 1.20: Degree of rehybridization as a function of diameter and chirality.

For $n \geq 8$, the degree of hybridization is almost zero for armchair and slightly greater for zigzag. The knowledge of the degree of hybridization allows to have information on the type of

rehybridization and the properties of each type in the CNTs. The degree of pyramidalization allows to get information on the reactivity of each type of CNTs. If a graphene sheet is rolled up into a structure like a CNT, the orbital structure of the carbon is changed, due to the bond length between the carbon atoms decreasing and the changes in bond angles. The s and p orbitals are no longer perpendicular to each other. An overlap of the π- orbitals is introduced. Consequently, the parts of the π- orbitals inside and outside of a nanotube rearrange themselves so that the outside contribution is larger than the inside one (Figure 1.21). The curvature induces a mixed state of the s and p orbitals, called rehybridization.
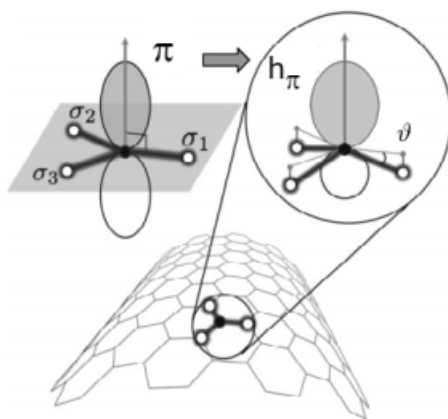
Figure 1.21: Schematic of the π- orbital in the graphene plane and its transformation into h_π in bending as well as the pyramidal angle ϑ [43].

The rehybridization can also be explained by a mixing of the sp^2 and sp^3 orbitals. Although these are saturated, the mixed state contains unsaturated orbitals. The mixing of a tetravalent orbital sp^3 and a trivalent orbital sp^2 leaves one hybrid orbital free for binding. As the sp^3 increases, the more free bonds exist and the more reactivity increases. As an index of the local reactivity, a pyramiding angle ϑ is used, which is sufficient to describe the curvature change induced in the sp^2 hybridization. The degree of $sp^{2+\tau}$ hybridization could be obtained, τ being a number between 0 and 1 [13]. The comparison between the different pyramiding angles allows the comparison of the reactivity, where a higher angle results in a higher reactivity. Thus, the degree of hybridization is strongly dependent on the curvature, so that it is still possible to increase the reactivity alone by folding a CNT.

1.5 X-ray Absorption Spectroscopy theory

1.5.1 Absorption mechanism

The absorption of electromagnetic radiation in matter, whether in solid, liquid or gaseous form, is a very rich phenomenon. This absorption is accompanied by a transfer of energy that will lead to physical, chemical or biological phenomena of great interest. Depending on the

type of material and its thickness, depending on the energy and polarization of the incident radiation, we would have more or less strong absorptions. Three regions, corresponding to three different energy ranges of the incident photon, translate three types of electronic processes sketched on (Figure 1.22). Note that, the absorption depends on the thickness crossed but also on the nature of the material.
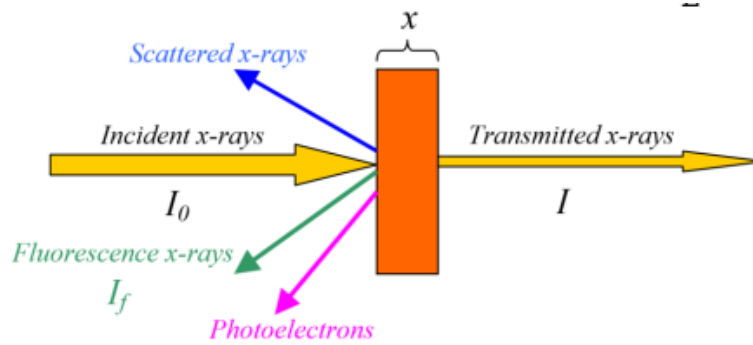
Figure 1.22: Spectrum describing Beer-Lambert law.

It is described by the Beer-Lambert law which gives the transmitted intensity I as a function of the incident intensity I_0 :

$$I = I_0 e^{-\mu x} \tag{1.49}$$

where x is the thickness of the sample, μ the linear absorption coefficient, I_0 the intensity of the incident beam and I the intensity of the transmitted beam.
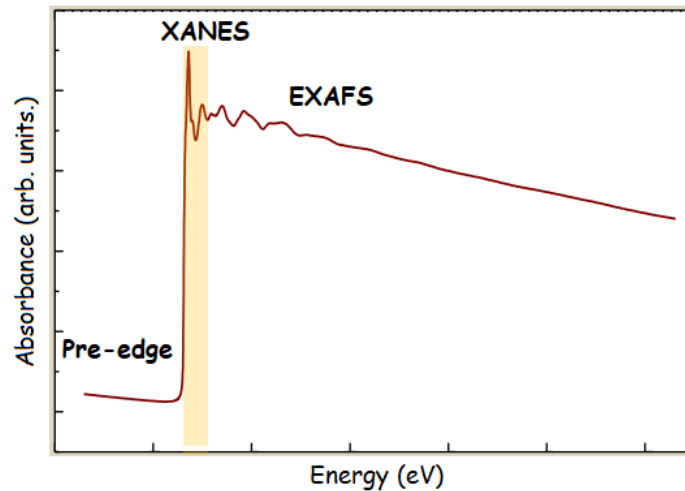
Figure 1.23: Spectrum of an X-ray Absorption showing different regions [44].

1.5.2 X-ray Absorption Near Edge Structure

XANES spectroscopy is a technique that probes the occupied electronic states, and allows to obtain information on the unoccupied levels of the studied system. It is particularly used for the study of light and heavy elements, especially for molecules that may contain such

elements. This spectroscopy is sensitive to chemical shifts. XANES measurements require the use of a polarized monochromatic X-ray beam, at different wavelength. This polarized radiation allows to obtain information on the orientation of the molecular orbitals and to deduce the adsorption mode of the molecule on the surface. For example, K-edge corresponds to the excitation of an electron $1s$.

Pre-edge region

This part of the X-ray absorption spectrum is located in a range of energies below the ionization energy. The X-ray photon is not able to expel a core electron from the absorbing atom from the lowest level, beyond the Fermi level, because its energy is not enough. Therefore, the electronic transition of an electron from the lowest level is not yet possible, but takes place towards the first unoccupied levels. The observed X-ray absorption coefficient then comes from the electronic layers of the atom, or from other elements of the sample, such as impurities. The energy and the intensity of the transitions are then modified by the change of symmetry linked to the presence of the neighboring atoms.

Edge Region : XANES

When the energy of the photon increases without exceeding the binding energy, we observe a rapid increase in the absorption coefficient: this is the edge. When the energy of the photon is slightly higher than the binding energy, transitions to continuum states occur. The photoelectron is then emitted with a low kinetic energy and a large mean free path. It is then involved in multiple scattering phenomena by the neighbors of the absorbing atom. This part of the absorption spectrum extends from a few eV below the edge to about 50 eV above. Therefore the shape of the absorption spectrum bears the imprint of the local environment and the interferences observed on these spectra are the result of two types of scattering: single scattering (Figure 1.24 (a)) and multiple scattering (Figure 1.24 (b)).

It is worth noting that the intensity of the oscillations after the white line are considered as characteristic of the size of the particles. The smaller particles induced weaker oscillations [44]. In the case of single scattering we have a two-legged path, i.e. an absorber-diffuser path followed by a backscattering directly to the absorber atom. For multiple scattering the number of legs will be greater than two. Thus, the XANES part of an X-ray absorption spectrum has several regions or sub-regions. It can present a white line, i.e. a peak of strong intensity just after the edge as illustrated on (Figure 1.23). It includes on the one hand the transitions to the free electronic states of the absorbing atom and on the other hand the multiple scattering towards these neighbors. Finally, the energy at which the edge appears depends on the chemical environment of the selected atom. Moreover, the ionization potential of a core electron varies with the atomic number of the excited atom. It also varies by a few electronvolts depending on its electrical charge.

The position of the absorption edge of a XANES spectrum thus gives information on the

degree of oxidation-reduction within the probed material. Indeed, at these photoelectron energies, the multiple scattering factors have a large amplitude, and on the other hand, the mean free path of the electron is much larger than the inter-atomic distance, which increases the probability of the electron scattering by several atoms before returning to the absorbing atom [45].
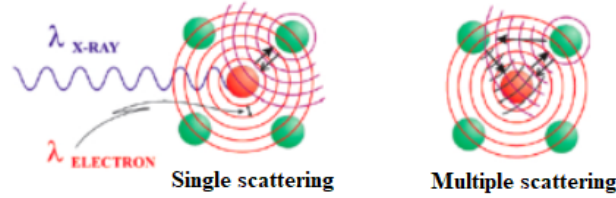
Figure 1.24: (a) Single scattering and (b) Multiple scattering.

EXAFS region

This domain corresponds to a range in energy above the ionization energy, i.e. an energy sufficient to extract an electron from a core level to the continuum of electronic states. Here, contrary to the XANES part, the average free path in the medium is significant. The kinetic energy of the photoelectron is $E_c = E - E_0$, where E is the energy of the incident photon and E_0 is the ionization energy (absorption edge). In this region the absorption coefficient exhibits oscillations that contain structural information about the local arrangement of the absorbing atom. The theory of EXAFS oscillations is based on the duality of wave-corpuscle. Indeed, the photoelectron emitted by the central atom can be considered either as a corpuscle excited from a core level or as a spherical wave propagating in the material.

1.5.3 Formalism of XANES spectroscopy

By scanning the energy of the photons through a tunable source, the various empty levels of the system will be probed, these transitions are governed by the transition probability. This probability of transition from an initial state $< i \mid$ to a final state $\mid f >$ at the K-edge of all elements is given by the Fermi golden rule [46]:

$$P_{if} = \frac{2\pi}{\hbar} \mid < f \mid V \mid i > \mid^2 \rho_f(E) \tag{1.50}$$

where $\rho_f(E)$ is the density of final states, and V is a time-dependent perturbative term.

Within the electrical dipole selection rules and the spherical wave approximations, the expression of the Fermi golden rule is given by:

$$P_{if} = (E_0^2.\pi^2.e^2.N/h.m^2.w^2).(\overrightarrow{e}.\overrightarrow{p}) = I_0^{\pi}.N.(\overrightarrow{e}.\overrightarrow{p}) \tag{1.51}$$

where E_0 is the electric field amplitude, ω the wave number of the electromagnetic field, N the atomic density of carbon atoms and e, h, m have the usual physical meanings. Vectors

$\overrightarrow{e}$ and $\overrightarrow{p}$ are the unit vector of the electric field and the momentum operator which points in the direction of the final state π^*.

1.5.4 Full calculation of the angular dependence of the absorption intensity in the case of carbon nanotubes and carbon nanofibers grown on a flat surface within a geometrical model

We will calculate the last term in the case of carbon nanotubes grown on a flat surface (Figure 1.25). We neglect the contribution of the capped carbons on top of the carbon nanostructures. Let us consider the more general case of carbon nanofibers where the graphitic basal planes (in red) are oriented with a conical polar angle γ relative to the fiber axis AA'. In the case of a carbon nanotube, $\gamma = 0°$, the graphitic basal planes being parallel to the fiber axis AA' [47]. In the case of a carbon nanofiber with a herringbone organization, $\gamma \geq 0°$. The angle with the π- bond direction $\overrightarrow{C}$, that means angle $(\overrightarrow{C}, \overrightarrow{AA'})$ is then $(\frac{\pi}{2} - \gamma)$ whereas the angle with the σ- bond in the graphitic base plane or shell is γ. The XAS signal is integrated over all the π- orbitals along the φ azimuthal angle around the axis of the carbon nanostructure. Now these nanofibers are grown on a flat substrate like SiO_2/Si (100) with a random polar angle θ relative to the normale axis ZZ' to the substrate, meaning that angle $\theta = (\overrightarrow{AA'}, \overrightarrow{ZZ'})$. With a random orientation normal to the surface, $\theta = 0°$. When the tubes are lying within the substrate, $\theta = \pi/2$ rads.

Finally the light impinges the surface at an incidence angle α relative to the (X,Y) plane of the substrate (relative to $\overrightarrow{ZZ'}$ axis) with a Poynting polarisation vector $\overrightarrow{P}$ in the z direction and the electric vector $\overrightarrow{E}$ is within the plane $(x, y, 0)$ of the triedre (x, y, z), with an angle β relative to an horizontal orientation of the electric field in the propagating light, which is generally encountered in synchrotron light.
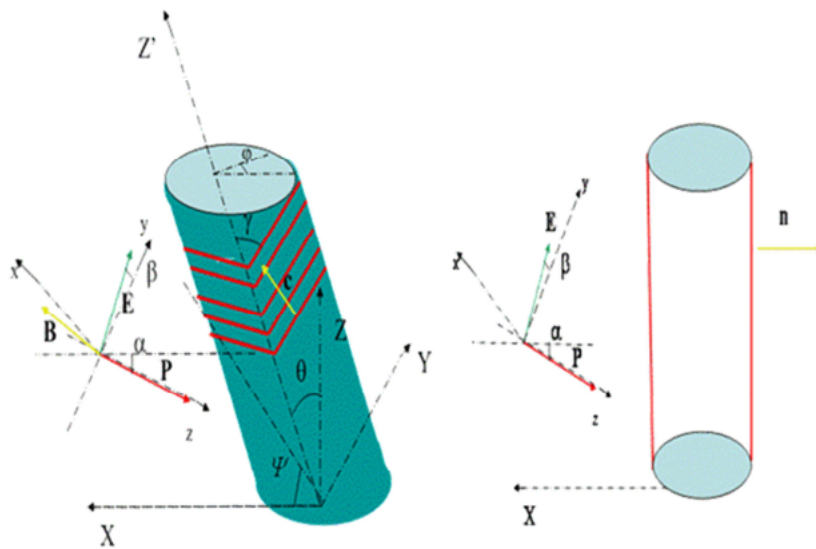
Figure 1.25: Geometrical model of the light irradiation of carbon nanotubes of mean orientation (Left) and high orientation (Right) on a flat surface [47].

Thus $\beta = (\vec{E}, \vec{a_y}) = (\vec{B}, \vec{a_x})$. Thus with $\beta = 0°$ the light is linearly polarized while with $\beta = 45°$ the light is circularly polarized. Assuming a general elliptic polarization of the light $0° \leq \beta \leq 45°$ the intensity of the absorption with transition to π^* states of the carbon nanostructures can be expressed by integrating over all azimuthal angles φ [47]:

$$I_\pi(\alpha, \beta, \gamma, \theta) = \frac{NI_\pi^0}{4}\left\{cos^2\theta\left[(1 - 3sin^2\gamma)(1 - 3cos^2\beta cos^2\alpha)\right] + (1 + cos^2\beta cos^2\alpha) + \right. \quad (1.52)$$

$$\left. + sin^2\gamma(1 - 3cos^2\beta cos^2\alpha)\right\}$$

where N is the atomic density of carbon atoms and I_π^0 is a maximum experimental value of π^* intensity.

Whereas the intensity of the transition to σ^* states, $I_\sigma(\alpha, \beta, \gamma, \theta)$ can be expressed by changing γ by $\gamma + \pi/2$ and multiplying by 3 since there are 3 σ- orbitals for each π symmetry orbital. The result is then:

$$I_\sigma(\alpha, \beta, \gamma, \theta) = \frac{3}{2}\left[1 - I_\pi(\alpha, \beta, \gamma, \theta)\right] \quad (1.53)$$

Case of carbon nanofibers (CNFs)

In the case of a **linearly polarized light** with $\beta = 0°$, the expressions (1.52) and (1.53) reduce to

$$I_\pi(\alpha, 0, \gamma, \theta) = \frac{NI_\pi^0}{4}\left\{cos^2\theta\left[(1 - 3sin^2\gamma)(1 - 3cos^2\alpha)\right] + (1 + cos^2\alpha) + sin^2\gamma(1 - 3cos^2\alpha)\right\} \quad (1.54)$$

and the same as (1.53) for $I_\sigma(\alpha, 0, \gamma, \theta)$,

$$I_\sigma(\alpha, 0, \gamma, \theta) = \frac{3}{2}\left[1 - I_\pi(\alpha, 0, \gamma, \theta)\right] \quad (1.55)$$

In the case of a **circularly polarized light**, $\beta = \frac{\pi}{4}$

$$I_\pi(\alpha, \frac{\pi}{4}, \gamma, \theta) = \frac{NI_\pi^0}{4}\left\{cos^2\theta\left[(1 - 3sin^2\gamma)(1 - \frac{3}{2}cos^2\alpha)\right] + (1 + \frac{1}{2}cos^2\alpha) + sin^2\gamma(1 - \frac{3}{2}cos^2\alpha)\right\} \quad (1.56)$$

$$I_\sigma(\alpha, \frac{\pi}{4}, \gamma, \theta) = \frac{3}{2}\left[1 - I_\pi(\alpha, \frac{\pi}{4}, \gamma, \theta)\right] \quad (1.57)$$

Case of carbon nanotubes ($\gamma = 0°$)

$\Rightarrow$ Linearly polarized light ($\beta = 0°$)

a) **Normal orientation** $(\theta = 0\degree)$; $\beta = 0\degree$, $\gamma = 0\degree$

$$I_\pi(\alpha, 0, 0, 0) = \frac{NI_\pi^0}{2}\left[1 - cos^2\alpha\right] \tag{1.58}$$

$$I_\sigma(\alpha, 0, 0, 0) = \frac{3}{2}\left[1 - I_\pi(\alpha, 0, 0, 0)\right] \tag{1.59}$$

b) **Parallel orientation** $(\theta = \frac{\pi}{2})$; $\beta = 0\degree$, $\gamma = 0\degree$

$$I_\pi(\alpha, 0, 0, \frac{\pi}{2}) = \frac{NI_\pi^0}{4}\left[1 + cos^2\alpha\right] \tag{1.60}$$

$$I_\sigma(\alpha, 0, 0, \frac{\pi}{2}) = \frac{3}{2}\left[1 - I_\pi(\alpha, 0, 0, \frac{\pi}{2})\right] \tag{1.61}$$

$\Rightarrow$ **Circularly polarized light** $(\beta = \frac{\pi}{4})$

a) **Normal orientation** $(\theta = 0\degree)$; $\beta = \frac{\pi}{4}$, $\gamma = 0\degree$

$$I_\pi(\alpha, \frac{\pi}{4}, 0, 0) = \frac{NI_\pi^0}{2}\left[1 - cos^2\alpha\right] \tag{1.62}$$

$$I_\sigma(\alpha, \frac{\pi}{4}, 0, 0) = \frac{3}{2}\left[1 - I_\pi(\alpha, \frac{\pi}{4}, 0, 0)\right] \tag{1.63}$$

b) **Parallel orientation** $(\theta = \frac{\pi}{2})$; $\beta = 0\degree$, $\gamma = 0\degree$

$$I_\pi(\alpha, \frac{\pi}{4}, 0, \frac{\pi}{2}) = \frac{NI_\pi^0}{4}\left[1 + \frac{1}{2}cos^2\alpha\right] \tag{1.64}$$

$$I_\sigma(\alpha, \frac{\pi}{4}, 0, \frac{\pi}{2}) = \frac{3}{2}\left[1 - I_\pi(\alpha, \frac{\pi}{4}, 0, \frac{\pi}{4})\right] \tag{1.65}$$

1.6 States of art

In recent years, nanomaterials have aroused growing interest in improving the sensitivity, selectivity and stability of sensors. These sensors are able to integrate a wide variety of materials such as polymers, composites, semiconductors and carbon nanotubes to detect different contaminants. In this context, carbon nanotubes are nanomaterials that have many advantages thanks in particular to their exceptional intrinsic properties with mechanical resistance, electrical conductivity or even excellent thermal conductivity [48,49]. Research on carbon nanotubes and important advances in chemistry have naturally led to combining the two systems to form innovative materials based on carbon nanotubes. Researchers are developing new sensing technologies that combine microfabrication and nanofabrication to create small, portable, high-precision sensors that can detect alkali metals and biochemical

substances in water. Noted that, Copper who is generally used in applications where high conductivity is required, but it does not retain its apparent conductivity at the dimension scale nanoscale [50]. Work done by Naeemi et *al.*[51] showed that the electrical conductivity of CNTs becomes greater than that of copper (at equivalent diameter), for lengths greater than 10 μm. They really concludes that the electrical conductivity of carbon nanotubes increases with the length of the nanotube, while the conductivity of a copper wire does not increase with the length, but with its diameter. This is due to their one-dimensional electronic structure of CNTs, and whose electronic transport is said to be ballistic [52]. According to these authors, the electron crosses the CNTs (along the axis) without undergoing collisions and without dissipating energy. Theoretically, taking into account ballistic transport, a nanotube would have a minimum resistance of $\frac{h}{4e^2}$ or 6.5 $k\Omega$ (h: Planck's constant, e: charge of an electron), independently of its length [53]. These properties make CNTs promising candidates for the fields of all-optical sensing [48], infrared photodetectors [54], photovoltaic cells [55]. Normally, as-received nanotubes contain few heteroatom functional groups. Adsorption is a very general phenomenon that can be described as the accumulation of a substance occurring at the interface between two phases, most often between a solid and a liquid. The solid is then called adsorbent and the element in the liquid, likely to be retained on the surface of the solid is the adsorbate. The term adsorption has been proposed to indicate that it is a localized phenomenon on a surface and should not be confused with the word absorption which corresponds to the accumulation of a substance in the mass of the solid. A molecule will be adsorbed differently according to the geometry on the surface of the adsorbent. From the point of view of adsorption, the geometrical parameter will affect the cross section of the molecule, which corresponds to the average area occupied by an adsorbed molecule expressed in mm^2. Functionalities affect the electronic properties of CNTs by disrupting the graphitic-like sp^2 network of carbon in the SWCNTs. This disruption produces local sp^3 defects which can introduce an impurity state near the Fermi level [58] and perturb the electronic spectra of these materials [56]. Goldoni and coworkers showed that gas molecules could directly affect the nanotube properties via physisorption or chemisorption, but they could also have an indirect effect by interacting with contaminants bonded to the nanotubes [57]. Jijun et *al.*[58] studied various gas molecules (NO_2, O_2, NH_3, N_2, CO_2, CH_4, H_2O, H_2, Ar) on SWCNTs and bundles using first principles methods. They found that, most molecules can be either charge donors or acceptors to the nanotubes. Charge transfer and gas-induced charge fluctuation might significantly affect the transport properties of SWCNTs. The performance of SWCNTs as adsorbents [59], catalysts [60] and sensors [61] depends on understanding and controlling surface functionalities. The adsorption of heavy metals by nanotubes has been studied by Li group [62,63]. They found that nanotubes show exceptional adsorption capability and high adsorption efficiency for lead removal from water. The adsorption is significantly influenced by the pH value of the solution and the nanotube surface status.

Groundwater moving through sedimentary rocks and soils may pick up a wide range of compounds, such as potassium, magnesium, calcium, and chloride, arsenate, fluoride,

nitrate, and iron; thus, the effect of these natural contaminations depends on their types and concentrations. Potassium is the fourth most abundant element in seawater. With 0.399 g/L concentration, it is next to Na^+, Ca^{2+}, and Mg^{2+} [64]. Potassium is a crucial fertilizer component, the demand of which is ever increasing for reaching the food supply [65,66]. It increases productivity and enhances resistive power in plants toward adverse effect of pests and environment. Human beings and animals acquire this element from plants, which in turn acquire it from soil. Soil should be fortified with potassium as a source to all members of the food chain [67]. Efforts are being made for the recovery of K^+ from water. Reverse osmosis (RO) and electrodialysis (ED) are the two most important membrane technologies for water desalination and treatment [68]. A brief schematic of both methods is presented in Figure 1.26. Water treatment generally refers to the removal of contaminants other than salts, such as organic micropollutants (OMPs), whereas desalination and deionization refer to the removal of salts, thus of ions. RO is a method that uses pressure to drive water through a membrane, retaining on the retentate side most of the ions and other solutes, producing freshwater on the permeate side.
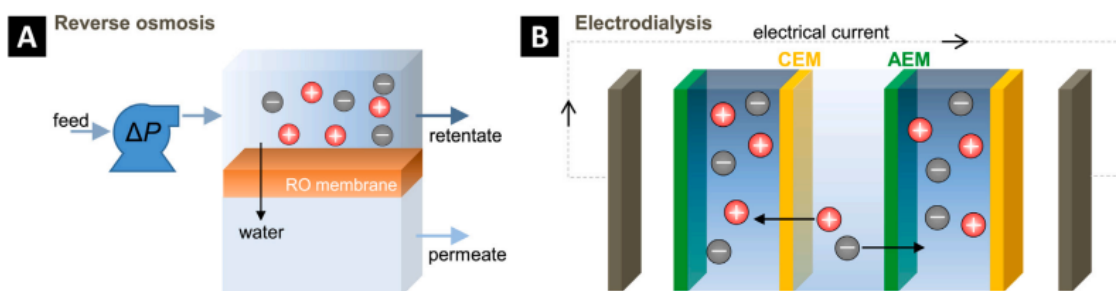
Figure 1.26: Overview of reverse osmosis (RO) and electrodialysis (ED). (A) In RO, pressure is applied to drive water through a membrane, retaining on the retentate side most of the solutes. (B) In ED, electrical current runs across channels and membranes, generated in electrodes placed at both ends of a stack that holds many cell pairs [69].

Nanofiltration (NF) is a companion technology of RO that uses lower pressures, and membranes with larger pore sizes than in RO [70]. In NF, the retention of monovalent ions is much lower than of divalent ions and thus divalent ions can be selectively removed. In ED, water flows through thin channels next to ion-exchange membranes (IEMs) and an applied current pulls the ions from one set of channels through the IEMs to other channels. Though ED and RO are very different methods and use distinctly different physical mechanisms. Reverse osmosis (RO) is a process to remove solutes from water by pushing water through a membrane which largely blocks passage for solutes. This is the general mechanism of all pressure-driven membrane processes, but for water desalination the size of the pores (free volume) in the membrane must be very small, typically well below 1 nm in the selective toplayer of an RO membrane. As part of our research, we will focus on CNTs given their remarkable potential according to the developers of the purification membranes and water desalination. Thus, Kar et *al.*[71] claim that the properties offered by the different types of CNTs will help to

manufacture new generations of high-flux membranes, ensuring high selectivity. Therefore, compared to conventional reverse osmosis and nanofiltration membranes, the smooth and hydrophobic wall of CNTs as well as diameter and close alignment of CNTs, are two important factors that would facilitate the rapid and frictionless circulation of water molecules [72].

The electronic structure of potassium-doped carbon nanotube bundle has been studied by Miyake et *al.*[73] using density-functional theory. It is found that the effect of adsorption is not simple charge-transfer. The nearly free electron state couples with the potassium $4s$ state, and the hybridized state is pulled down to the Fermi level (Figure 1.27). The impurity is a serious obstacle to the characterization of the carbon nanotubes properties due to the interference of impurities and nanotubes.
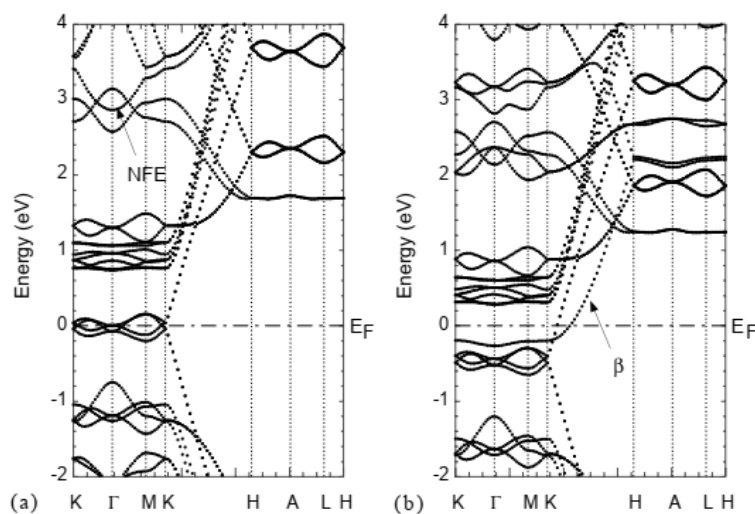
Figure 1.27: Band structures of (a) pristine, and (b) potassium-doped (12,0) carbon nanotube bundle [73].

The first objective of this work is to characterize the surface and study the effects induced by adsorbates on the electrical and conduction properties of Multi-Walled Carbon Nanotubes (MWCNTs). The second objective is to capture potassium (K) in an aqueous solution using SWCNTs for the application in water treatment and biosensors.

To date, various models have been applied to describe the adsorption of organic molecules on CNTs in aqueous phases, such as Freundlich [74], Langmuir [75], BET [76], and Polanyi-Manes models [77]. Several methods have been applied to detect and quantify functional groups on carbon surfaces [78]. Infrared spectroscopy (IR) [79], X-ray photoelectron spectroscopy (XPS) [79], thermal desorption spectroscopy (TPD)[80], elemental analysis [80] and Boehm titration [79] are the most frequently used methods. Although the Boehm titration is a valuable technique, it is limited to special functional groups [78]. TPD does not provide detailed information about the type of functionality as it only probes the products of their decomposition. Quantitative analysis of XPS and IR is not straightforward [78]. In the time-consuming titration [81], the difficulty resides in assigning the peaks, and the influence of experimental parameters (such as the heating rate in TPD) highlight the need

for new methods. Identification and quantification of those functional groups have become key issues for the field of CNTs materials topic. Scientists try to develop new methods as Scanning electron microscopy (SEM) [82] and transmission electron microscopy (TEM) [83] which are both qualitative methods to detect functional groups more effectively. We have also, potentiometric titration [84] which determines the acidic and basic properties of adsorbents and the nature of their functional groups. FTIR determine the presence of certain chemical functions via the absorption of vibrations characteristic of chemical bonds. XANES technique is a powerful tool, it is sensitive to the chemical adsorption, impurities, and orbital rehybridization [85]. Novel monitoring technologies and devices are needed for pollutants and microbial detection. Protection of human health and ecosystem requires rapid, precise sensors capable of detecting pollutants at the molecular level.

1.6.1 Functionalization of carbon nanotubes

We will focus on techniques used to functionalize carbon nanotubes. The chemical functionalization of carbon nanotubes has aroused great interest since the beginning of their use, in particular in order to be able to solubilize them and/or couple them to molecules of biological interest. Many functionalization methods have been developed. This part presents the outline of the different types of functionalization that are used today. They can be classified into four major categories described in the (Figure 1.28).
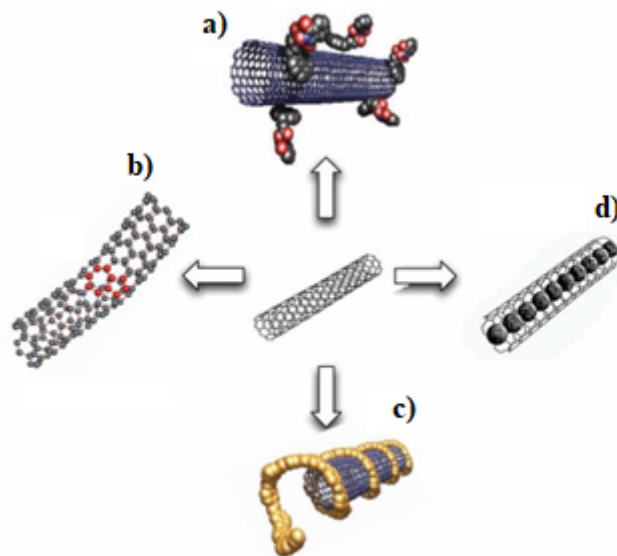
Figure 1.28: Diagram describing the different ways of functionalizing carbon nanotubes [86].

a) Covalent functionalization

This is the creation of a covalent chemical bond between the network of the nanotube and the molecule that we want to graft onto its surface. This link can be created first by fluorination of carbon nanotubes [86]. The main advantage of the fluorination of nanotubes is that the

fluorine atoms can then be easily substituted by reaction with various classes of compounds [86]. Thus, the fluorinated nanotubes constitute a basic material to then easily adapt the desired derivatization of the nanotubes. Finally, it can be noted that the covalent functionalization of the tubes achieved by this route is reversible [87] by heating the functionalized tubes in air. This reversibility makes it possible in particular to determine the degree of functionalization by thermogravimetric analysis (TGA). The covalent functionalization can finally be carried out by the addition of radicals.

b) The use of defects present on the surface of nanotubes for functionalization

Despite their high resistance to oxidation, the nanotubes present in the treated sample are also partially oxidized by exposure to acid. Thus are generated on the surface of the tubes and particularly at the level of the ends (rich in defective zones) oxygenated functions. Insofar as the tubular structure is preserved despite these network alterations, the creation of these anchor points on the surface of the tubes was used for their functionalization. This last type of functionalization with biological molecules makes it possible to envisage the design of sensors.

c) Non-covalent functionalization

These are interactions between molecules and carbon nanotubes without formation of covalent bonds. The first type of non-covalent functionalization concerns the interaction of carbon nanotubes with polymers. Certain polymers have a favored interaction with the tubes; these are semi-conjugated polymers which spontaneously organize themselves into a helix whose pitch is compatible with the diameter nanotubes. A second category of non-covalent interactions concerns molecules of interest biological as proteins [88]. The third category corresponds to the non-covalent interaction that exists between the graphitic network of carbon nanotubes and the aromatic and polyaromatic molecules, called aromatic stacking or π-stacking.

d) Endohedral functionalization

This involves the encapsulation of molecules or crystals inside carbon nanotubes. Two major classes can be cited; on the one hand, the encapsulation of fullerenes and the consequent formation of peapods [89] and on the other hand the encapsulation of biological molecules.

1.6.2 Toxicity of carbon nanotubes

The applications and industrial production of CNTs are constantly growing. The consequences of their production, their use, as well as their impact on human health and the environment must be assessed. The history of health, technological and environmental risks shows that their management a posteriori refers to the importance of risk assessment as early

as possible. It is therefore a question of identifying the technological, economic and social issues associated with the development of these technologies while evaluating a priori the risks generated by their production, their uses and their applications. The three most common routes of exposure are: the respiratory tract (airborne particles), the dermal route (contact) and the digestive tract (although inhalation and ingestion are partially mechanically linked). Several in vitro studies [90] have shown that carbon nanotubes would be able to cross the cell membrane to enter the cell, accumulate there and cause cytotoxicity. On this last point, Jia et al.[90] have sought to compare the toxicity of different carbon nanostructures: fullerenes (C_{60}), SWCNTs and MWCNTs. First of all, they note that the fullerenes do not cause any inflammation of the cells, unlike carbon nanotubes, for which it would seem that at equal mass concentration, SWCNTs are more cytotoxic. However, the toxicological properties of carbon nanotubes are directly correlated to their physico-chemical characteristics [91]. On the one hand, catalytic residues (metallic nanoparticles) can also be toxic to the body. Indeed, iron residues can lead to formation of free radicals (OH^{*}) and thus damage proteins, lipids and genetic material contained in the cells. Cobalt residues can also lead to defects in the chromosomes [92]. On the other hand, the tendency of CNTs to agglomerate, due to their composition and their structure, in aqueous and therefore biological media, could quickly become problematic, making their elimination difficult. The chemical modification of the walls of CNTs (type and rate of functionalization) can strongly influence their potential toxicity [93], the walls being what is directly in contact with the environment. They are the ones who go condition the integration of CNTs in biological media and interactions with cells and tissues. In general, the more CNTs have a functionalization rate high, the more they are dispersed and individualized in solution and the more easily they are eliminated through the kidneys [94]. Conversely, CNTs with no or little functionalization tend to form aggregates which then accumulate in the organs (liver, spleen, lungs) [95]. Furthermore, it was also shown that the diameter and the length of the CNTs had influence on their toxicity. Indeed, the longer the CNTs are, the more the responses are important [95]. In terms of diameter, SWNTs cause more toxic effects than DWCNTs [93] and MWCNTs [90]. The functionalization of the CNTs therefore plays a crucial role in the toxicity of the CNTs: first, it is essential in order to best eliminate all the residual metallic nanoparticles which can lead to a loss of the integrity of the genetic information, and second, it makes it possible to individualize and to shorten the CNTs thus able it possible to eliminate them more easily.

Conclusion

In this first chapter, we have presented the versatility of carbon by its different allotropic forms. It appears from this that, there are two different forms of carbon nanotubes. The first forms are related to graphite, diamond and amorphous carbons. The second are new forms (nanostructures of carbon) such as: fullerenes, graphene and carbon nanotubes. Adsorption of the molecules and functionalization of covalent sidewall onto carbon nanotube (CNT)

constitute another method of doping CNT nanomaterial. The main interactions between carbon nanotubes and adsorbate molecules are Van der Waals, hydrophobic, π-π interaction, and, in special cases, also H-bonding. XANES spectroscopy gives a relationship between the curvature, the carbon atoms hybridization and the sidewall adsorption of contaminants on carbon nanostructures. The use of tools such as microscopy methods and X-ray absorption spectroscopy for characterization can give informations on the electronic structure of the carbon nanotube materials. The key point to realize these applications remains the characterization. Thus, the second part will consist in exploring the structure of the matter with experimental and synthesis techniques. This is the subject of the next chapter.

Experimental Techniques and Methods

Introduction

Obtaining materials with new and predictable properties requires an increasingly precise knowledge of their electronic structure. Many techniques allow to characterize carbon nanotubes and to highlight processes such as adsorption and desorption of molecules, atoms or radicals on their surfaces. In reality, in a crystalline solid, even at zero temperature, each atom oscillates around an equilibrium position and oscillates more when the temperature of the system is high. It is through this mechanism of perturbation that the carriers exchange energy with the system. In the following, we will describes the synthesis methods of carbon nanotubes, the principle of the microscopic characterization techniques and the experimental conditions used in each. Thus, Transmission Electron Microscopy (TEM), Scanning Electron Microscopy (SEM), Fourier Transform Infrared Spectroscopy (FTIR) and X-ray Absorption Near Edge Structure (XANES) will be presented. These complementary techniques will allow us to have the maximum information on the various involved processes. Synchrotron radiation proving to be a powerful tool for surface studies will be exploited for that purpose.

2.1 Theoretical model to describe the CNT growth mechanism

To express the theory of CNT growth by CVD, we use a model based on phonon vibration [96]. According to this model, CNT growth occurs through nanotube vibration on the catalyst particle and addition of a new carbon atom to the nanotube structure. In the CNT growth by CCVD, catalyst particles are produced on a suitable substrate. After making the appropriate temperature conditions in the growth chamber, the carbon feedstock is flowed into the chamber. The feedstock molecules are adsorbed on catalyst surface and decomposed to carbon and hydrogen molecules (Figure 2.1(a)) The carbon atoms diffuse in the catalyst particle and place in the nanotube growth area on the catalyst surface (Figure 2.1(b)). After a while of growth process, a carbon layer is formed on the surface of catalyst particle and

prevents feedstock molecules contact to the catalyst surface, so that actually stops the growth process (Figure 2.1(c)).
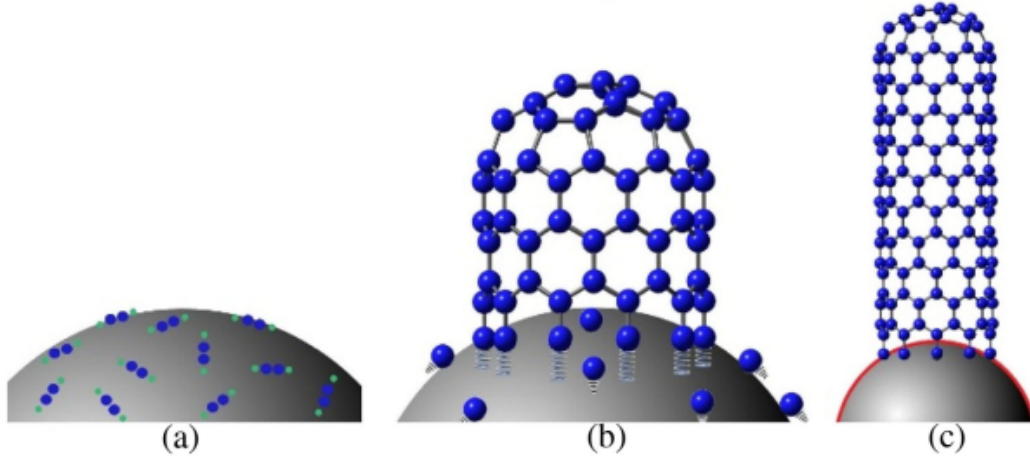
Figure 2.1: Schematic diagram of CNT growth by CCVD. (a) Surface adsorption of C_2H_2 feedstock molecules on catalyst and carbon production. (b) Diffusion of produced carbon atoms to form the nanotube. (c) Formation a carbon layer on catalyst surface (showed by red line), that stops the growth process [97].

The interaction between CNT and its catalyst is provided by Van der Waals force. When the van der Waals force minimizes, a carbon may place between the catalyst and tube. It should be emphasized that for an optimized growth mechanism, the phonon vibration amplitude (catalyst-tube distance) must be equal to a carbon atom diameter. If the vibration amplitude reduces or increases from a carbon atom diameter, the optimized growth will be perturbed. The phonon vibration amplitude is affected by temperature, so the optimized growth will be obtained at a specific temperature. It is common to simulate phonon vibration by a spring. In this system, longitudinal vibrations play principle role and transversal vibrations do not have any contribution in the growth. The equivalent spring between two loops is shown in (Figure 2.3). It should be emphasized that all forces between two loops are in the same direction and the net force is $-nkz$, where n is the number of carbon atoms in one loop. The equivalent spring coefficient is considered $K = nk$. Also this equivalent form, for $N(t)$ loops of the CNT, is shown in (Figure 2.3(a)), where M is the mass of one loop, $M = nm_c$, and m_c is the mass of one carbon atom. It is possible to simplify the equivalent form in (Figure 2.3(a)); as shown in (Figure 2.3(b)). In this illustration M_T is the total mass of carbon nanotube, $l(t)$ is the length of the growing nanotube and K_T is the total spring coefficient [89]: $M_T = N(t)M$; $K_T = N(t)K$ and $l(t) = N(t)\bar{l} = N(t)l_c$.

By considering these circumstances the Hamiltonian of the system could be written like [98]:

$$H = \frac{P^2}{2M} + \frac{P_T^2}{2M_T} + V(z) \simeq \frac{P^2}{2M} + V(z) \tag{2.1}$$
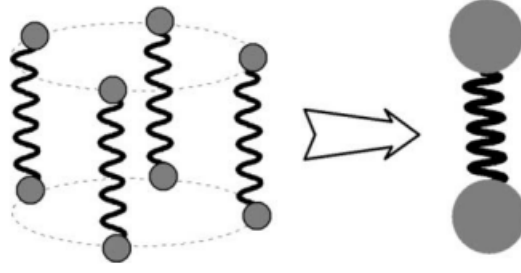
Figure 2.2: Schematic illustration of two carbons loops and its equivalent form [98].

The thermal energy of the system for one degree of freedom is $\frac{1}{2}k_BT$. It is divided between kinetic and potential part of the Hamiltonian. It is possible to simplify the equivalent form in (Figure 2.3(a)); as shown in (Figure 2.3(b)).
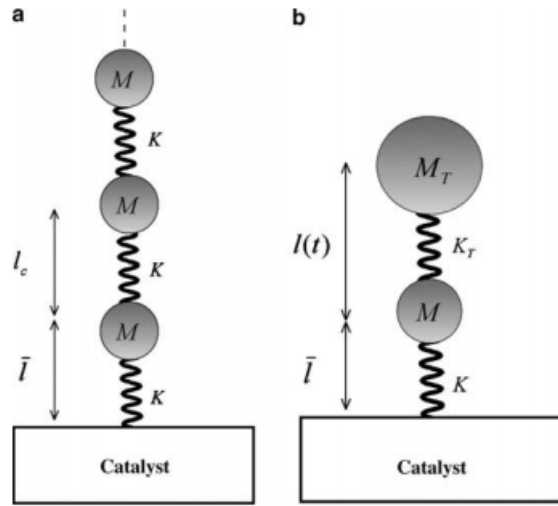
Figure 2.3: Schematic illustration of carbon nanotube growth system: (a) loop equivalent form; (b) growth equivalent form [98].

$$\frac{1}{2}k_BT = \frac{1}{2}K(l - \bar{l})^2 + \frac{1}{2}K_T(l' - l(t))^2 \tag{2.2}$$

where l is the unequilibrium length of the spring between the carbon and catalyst and l' is the unequilibrium length of the equivalent spring in the (Figure 2.3). If the potential energy maximizes, damping due to atmosphere and any other loss in the system are considered. The CNT growth equation as a function of time will be [98]:

$$\left[l(t)e^{\gamma t}\right]^5 + \frac{l_c}{n}\left[l(t)e^{\gamma t}\right]^4 - \frac{k_BTl_c^5}{4\pi^2n^4m_cz_{max}^2}t^2 = 0 \tag{2.3}$$

It is possible to investigate the growth behavior for tubes of different diameters [98]:

$$\left[l(t)e^{\gamma t}\right]^5 + \frac{l_cd_{c-c}}{\pi D}\left[l(t)e^{\gamma t}\right]^4 - \frac{k_BTl_c^5d_{c-c}}{4\pi^6D^4m_cz_{max}^2}t^2 = 0 \tag{2.4}$$

As it is observed in (Figure 2.4), for the large diameter sized tubes, growth curve saturates more rapidly than small sized ones. This fact is due to the reduction of the phonon vibrations by increasing the inertia of the CNT. In this system, longitudinal vibrations play principle role and transversal vibrations do not have any contribution in the growth. The interaction between CNT and its catalyst is provided by van der Waals force. Due to this interaction, the CNT vibrates with a definite frequency. When the van der Waals force minimizes, a carbon may place between the catalyst and tube.
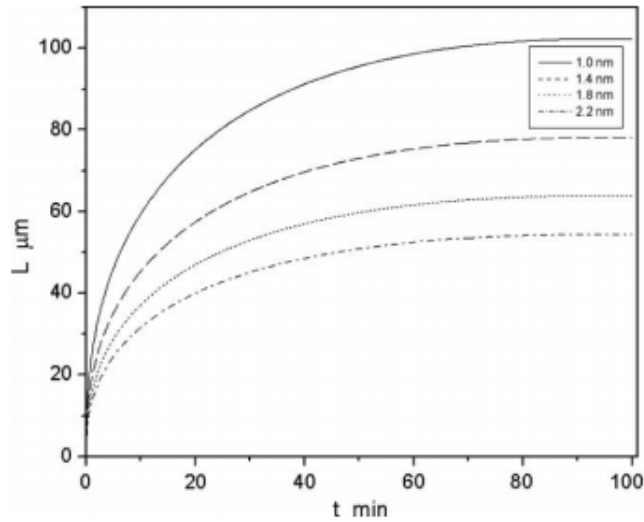
Figure 2.4: CNT length as a function of growth duration at $700°C$ for tubes of different diameters [98].

2.1.1 Comparison Between Catalysts

Time dependence curves of nanotube length for these catalysts are shown in Figure 2.5. A Comparison between these results shows that the carbon production performance of nickel is better than that of cobalt, and as well as the cobalt performance is better than that of iron. Diagrams of thermal dependence of nanotube length for three desired catalysts are shown in Figure 2.5. Different substrates have different Van der Waals coefficients. Changing the substrate alters the phonon vibration amplitude and affects the growth mechanism. So the optimized temperature must be changed to obtain the carbon atom diameter sized phonon vibration amplitude (carbon atom diameter sized catalyst-tube distance). Also different substrates may change the CNT diameter and as it was shown in (Figure 2.6), changing the CNT diameter affects directly the growth mechanism.
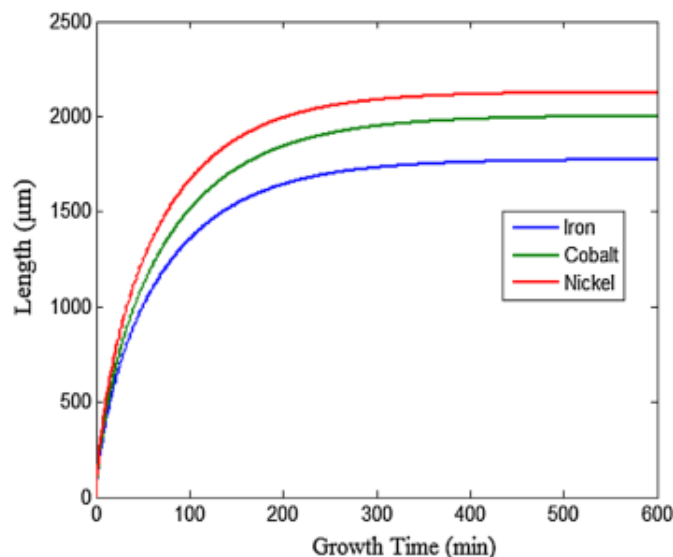
Figure 2.5: Time dependence curves of nanotube length for desired catalysts. Blue: iron (Fe); green: cobalt (Co); red: nickel (Ni) [97].
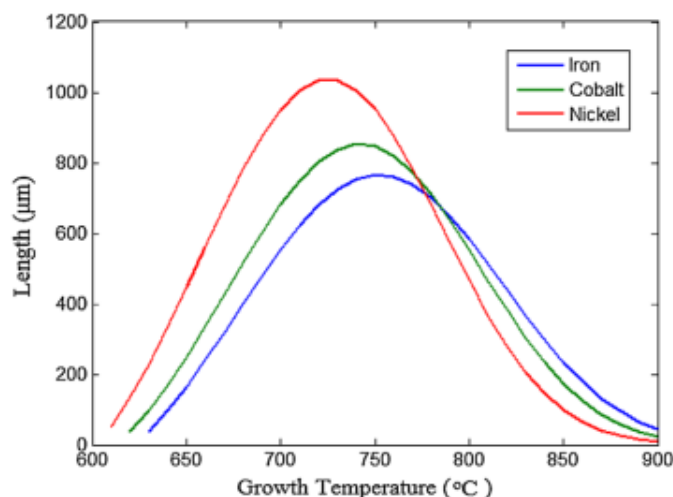
Figure 2.6: Thermal dependence of nanotube length for desired catalysts. Blue: iron (Fe); green: cobalt (Co); red: nickel (Ni) [97].

2.1.2 Effect of Feedstock Flow Rate on Nanotube Growth

Flow rate of feedstock indicates the availability of carbon, so changing this parameter leads to change in nanotube growth. Both the chemical composition (type) and flow rate of feedstock are effective in the nanotube growth process. Here the theoretical results for comparing different carbon feedstocks are presented. The results show that among the four types of the feedstock, acetylene has the best efficiency, which compared to ethylene (in second place) has a much better performance. After ethylene, methane and ethane are located, by less difference. Methane and ethane have almost the same performance.
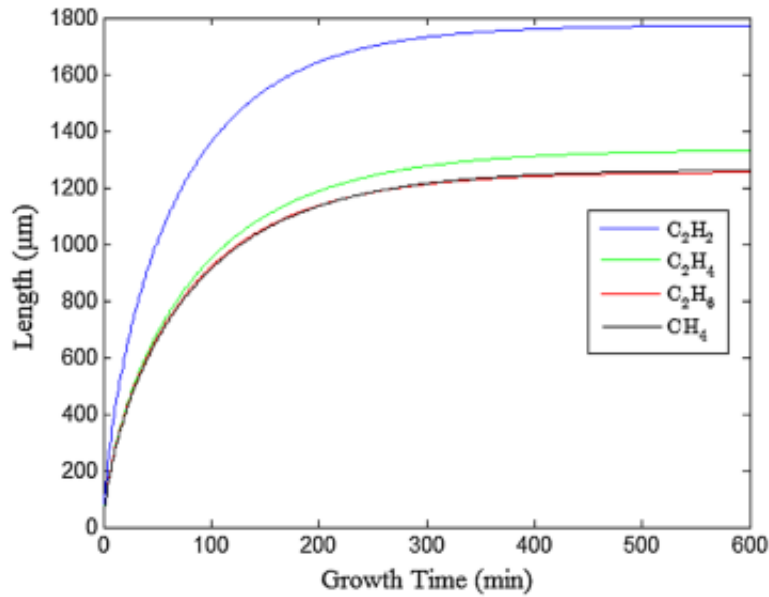
Figure 2.7: Thermal dependence of nanotube length for desired catalysts. Blue: iron (Fe); green: cobalt (Co); red: nickel (Ni) [97].

2.2 Synthesis methods of Carbon Nanotubes

The different methods of synthesis of carbon nanotubes fall into two main categories: high temperature (Electric Arc, Laser Ablation and solar vaporization) and low temperature methods (CVD: Chemical Vapor Deposition). The Electric Arc, Laser Ablation and CVD methods are the most widely used because they allow the production of large quantities and good quality of carbon nanotubes.

2.2.1 High Temperature Synthesis

This first family is based on the sublimation of carbon in an inert atmosphere. These techniques require that the temperature of the target be at least 3000 °C for the carbon to vaporize, the energy being supplied by Joule effect or laser irradiation. When metallic catalysts are used, they are vaporized at the same time as the carbon. The nanoparticles are then formed by condensation of the metal atoms in the zones of lower temperature.

a) Electric Arc

The electric arc method was introduced in the early 1960s to produce carbon fibers and was then used for the production of fullerenes, before allowing the synthesis of carbon nanotubes. It consists in establishing a strong electric discharge between two electrodes. In a reactor, the arc is generated under an inert helium atmosphere between the two electrodes [99]. The cathode consists of a fixed graphite bar cooled with water, while the anode, also consisting of a graphite bar, is mobile on a translation axis (Figure 2.8). The arc is created by progressively

approaching the anode to the cathode until the distance between the two is small enough to allow a high current of 100 A to flow. A voltage of 30 V between the electrodes is maintained by continuously moving the anode towards the cathode in order to keep a constant distance between the two during synthesis. The temperature in the inter-electrode area causes the carbon to sublimate and the positive electrode (the anode) is consumed. Synthesis times are typically 2 minutes. The main advantage of the electric arc is that it is a simple and inexpensive technique for the fabrication of fullerenes, single and multi-leaf nanotubes. It allows to produce nanotubes of very good structural quality. Nevertheless, the very high temperatures generated during the synthesis prevent any possibility of direct growth on lithographed substrates for electronic applications.
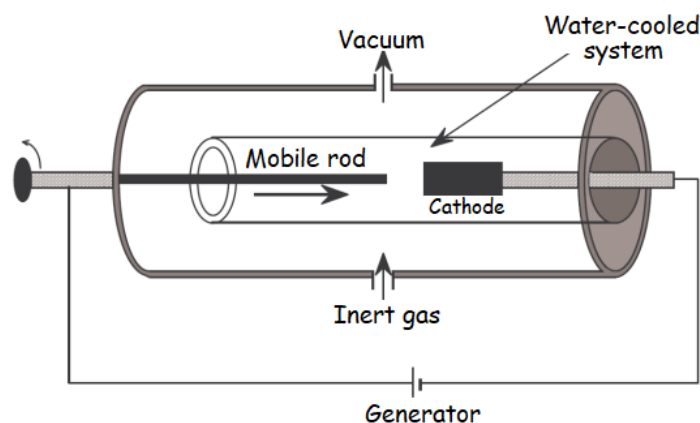
Figure 2.8: Schematic representation of an electric arc reactor [100].

b) Laser Ablation

Laser ablation (Figure 2.9) was historically the first technique allowing the synthesis of fullerenes. It is based on the evaporation of a graphite target by a laser beam. The target is placed in an oven whose temperature is maintained fixed during the experiment. The products are driven by a flow of neutral gases towards a cooled zone where they are collected. The MWCNTs obtained are relatively short (300 nm in length) compared to those obtained by the electric arc. This technique is generally used for the synthesis of SWCNT when the target is impregnated with a small quantity of catalysts (transition metals). The tubes obtained form bundles which diameter 5 to 20 nm, contained between 100 and 500 tubes. This technique has the advantage of producing large quantities of nanotubes of regular structure and well crystallized, but it is very expensive and the products are not really pure.
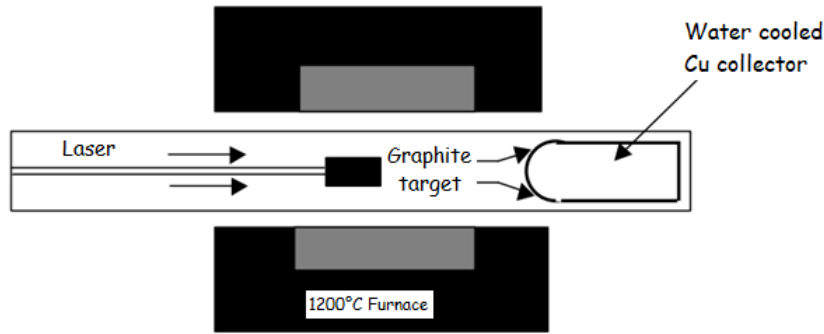
Figure 2.9: Schematic representation of the laser ablation method [100].

The parameters influencing this production method are essentially the nature of the substrate, the size of the catalytic particles or the reaction time. Thus, the diameter (the number of concentric layers for MWCNTs) and the length of nanotubes can be adjusted by changing the nature of the catalytic particles or the reaction time. This technique allows the production of single and multi-layered carbon nanotubes.

2.2.2 Low Temperature Synthesis of CNTs by CVD

Most synthetic CVD techniques use as a source carbon and different hydrocarbon gases such as methane (CH_4), acetylene (C_2H_2), for the production of single or multi-walled carbon nanotubes. The growth takes place by the decomposition of the hydrocarbons on the surface of the catalytic nanoparticles made of transition metals like cobalt (Co), nickel (Ni) or iron (Fe). There are several methods for synthesizing CNTs [101]. The most numerous are the high temperature methods. These methods do not lead to the material consisting only of CNTs. They are always mixed with amorphous carbons and catalytic metal particles, because very high temperatures ($> 1000 \,^{\circ}C$) favor catalyst-substrate interactions. Under such conditions, a purification step (oxidation) of the obtained nanotubes is necessary. The challenge is therefore to develop synthesis methods allowing to control both quantitatively and qualitatively the CNTs. Among these processes, the most appropriated are the Chemical Vapor Deposition (CVD) processes on a planar substrate of $SiO_2/Si(100)$.

1) Synthesis by Plasma Enchanced CVD (PECVD)

Here, we deal in details with substrate preparation and growth of carbon nanotubes. Like CVD from which it is derived, it is a dry deposition technique, i.e. from a gaseous phase. Generally, the technique of chemical vapor deposition consists of activating a mixture of gas to create reactive entities which will deposit, react and form new compounds at the surface of a substrate. In the PECVD method [102], the chemical reaction is assisted by an electric discharge created generally by a radio frequency electromagnetic wave (frequency of the order of 13 Mhz) which ionizes the gases and forms a plasma (i.e. a globally neutral mixture made up of ions and electrons). The plasma promotes the dissociation of gases and activates

the chemical reaction in the vapor phase. In the case of ECR-PECVD reactions (ECR for Electron Cyclotron Resonance) a microwave source (of the order of 2.4 Ghz) is injected into the reaction chamber. The resonance is obtained when the frequency of this source and the frequency of the electron cyclotron are equal. The energetic coupling between the electrons of the plasma and the microwave source is then optimal, which increases the degree of ionization of the plasma and makes it possible to carry out deposits while maintaining the substrate at temperatures lower than ($500\,°C$). Finally, the electrical discharge can be initiated by coupling the CVD reactor with a DC voltage applied between the sample surface and a counter electrode, which results in a planar plasma. The nanotubes are then oriented using the preferred direction imposed by the plasma and straight tubes of variable length and perpendicularity to the surface are reproducibly produced.

2) Synthesis by Hot Filament CVD (HFCVD)

The CVD method assisted by hot filament is a variant of conventional CVD. It consists of adding a metallic filament heated to a very high temperature ($2000\,°C$) in the oven which will cause cracking of the hydrocarbon. The gas decomposes thermally in contact with the resistively heated filament before decomposing on the substrate at room temperature. The success of HFCVD [102] is due to the fact that the gases are very efficiently cracked into atomic radicals on the surface of the hot filament (tungsten, or tantalum) if it is maintained at a temperature above ($1700\,°C$). HFCVD has been used for many years to produce diamond nanocrystal films. In the case of the growth of carbon nanotubes, a mixture of methane (CH_4) and dihydrogen (H_2) is introduced in the reactor with a ratio of 80 % of (H_2) and 20 % of (CH_4). The main purpose of the hot filament is to dissociate molecular hydrogen into atomic hydrogen. This atomic hydrogen reacts with (CH_4), and deposits solid carbon on the substrate.

3) Direct Curent Hot Filament CVD (DC-HF-CVD)

A new chemical vapor deposition method using hot filament with direct current plasma has been designed for nucleation and subsequent growth of diamond films on Si (100). The growth process as well as the current-voltage characteristics ($I = f(V)$) of DC discharge are reported [103]. The gas-phase constituents were obtained by activating a stable glow discharge between two gate electrodes coupled to two sets of hot parallel filaments installed between them and biased at the corresponding plasma potential. The sample is negatively biased by a small pull-down potential of 10 - 15 V relative to the cathode grid. Such a design makes possible to create a high density of both ions and radicals which are extracted and focused on the surface of the sample. The current density on the sample can be fine tuned independently of the primary plasma. A homogeneous plasma completely covering the surface of the sample is visualized. Consequently, a high nucleation density ($\geq 10^{10}\ cm^{-2}$) occurs [104].

4) Synthesis of oriented CNTs on plain SiO$_2$/Si (100) substrates by a catalytically enhanced CVD process (DC HF CCVD)

a) Substrate Preparation: SiO$_2$/Si (100)

Silicon (Si) is one of the substrates that has the particularity of having a crystal structure identical to that of diamond, with respective interatomic distances of 2.35 A° for Silicon and 1.55 A° for carbon so exhibiting a mismatch parameter. Between the closest atoms, bonds are established, made by the atomic orbitals hybridized sp^3. Similarly, between the atoms of carbon and silicon are established covalent bonds. The substrate SiO$_2$/Si (100) are prepared by depositing a layer of SiO$_2$ of thickness 8 nm on a layer of Si (100) (n doped by Sb: $\rho = 3$ m.Ω.cm; size 8.5x6x0.245 mm^3). The thickness of the SiO$_2$ layer is evaluated by recording the ratio of the SiO$_2$/Si at the Si_{2p} level in XPS.

The choice of depositing a SiO$_2$ on Si (100) preceding the deposition of Co is subject to three conditions [105]:

- Prevent interdiffusion of Si and Co to form cobalt silicides;

- Obtain the easy agglomeration or coalescence of Co atoms in the form of a fine distribution of Co islands, thanks to the large difference in surface energies between Co and SiO$_2$;

- To provide, however, via tunneling electron transport through the oxide layer, suitable samples for field emission measurements, which are reported elsewhere [105].

The SiO$_2$/Si (100) substrate is then transferred to preparation chambers under ultra-high vacuum (base pressure of 10^{-10} mbar) where the evaporation of Co and CNT growth are subsequently performed. The Co (99.995 % purity) is evaporated with an OMICRON EFM3 source under a pressure of 7.10^{-10} - 2.10^{-9} mbar on the sample heated to 925 K $\pm$ 20 K for 30 minutes. But, the thickness of the SiO$_2$ layer must remain thin enough to allow electronic emission measurements.
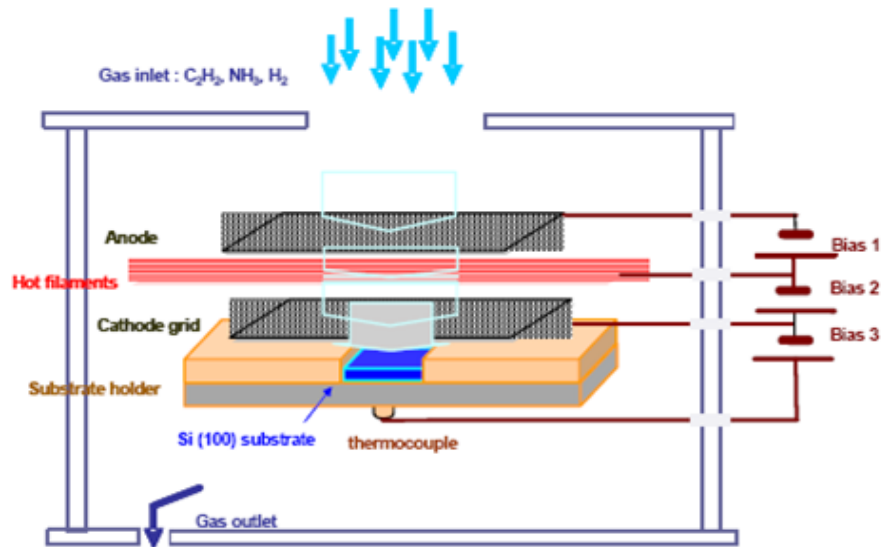
Figure 2.10: Ultra-high vacuum chamber for CNT growth [106].

b) Growth of carbon nanotubes

After substrate preparation, the samples are transferred to an ultrahigh vacuum chamber prepared for CNT growth by chemical vapor deposition (Figure 2.11). The pressure in the ultra-high vacuum chamber is less than 10^{-9} mbar. The gas mixture ($C_2H_2+ H_2$) and sometimes ($C_2H_2+ H_2+ NH_3$) is thermally activated by hot filaments (up to a power of $P = 150$ W), and accelerated by polarization between an anode and a cathode (polarization voltage = 310 ± 10 V) (Bias 1). The potential (voltage) of the filaments is fixed so that the electronic emission is compensated by the positive ions that hit the filaments. The first plasma stabilized by the filament emission ensures a high concentration of both activated neutral and ionic species (bias 2). The low extraction voltage creates a discharge plasma and allows the extraction of a controlled current density of ionic species (bias 3). The temperature is controlled and regulated by an independent infrared heating system, installed behind the sample. A Pt/PtRh thermocouple is in contact with the backside of the sample during the temperature rise. This thermocouple is disconnected when the bias is activated and the contact is then used to record the electrical current density flowing through the sample.

The different steps of preparation of the substrate and the growth of the CNTs can be summarized on the (Figure 2.11).
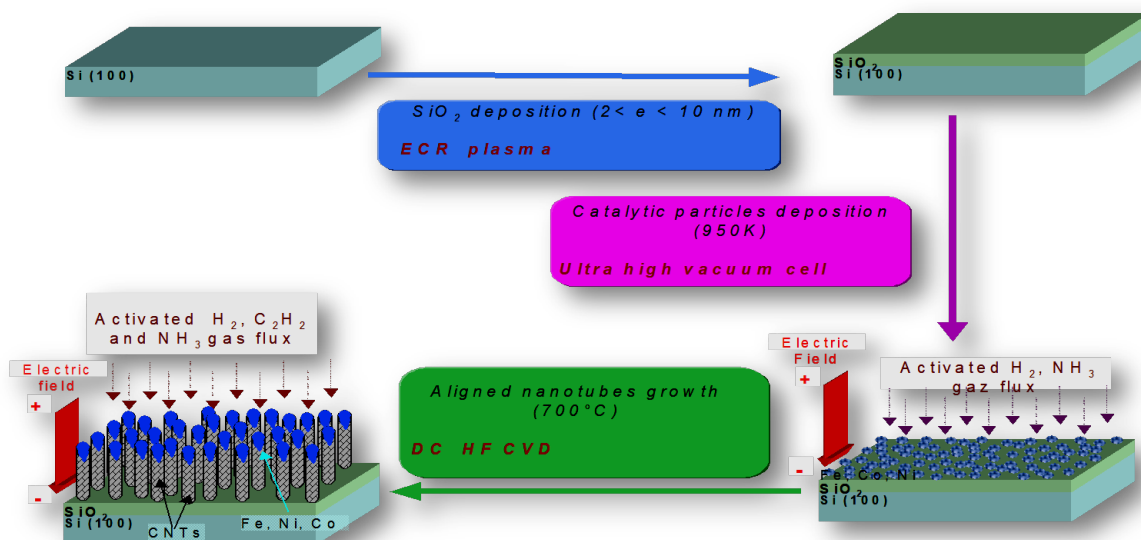
Figure 2.11: Steps of preparation and growth of the CNTs [103].

The sequences of the deposits are as follows:

- The sample is first heated under vacuum (10 K/min, 573 K, 10 min);

- It is heated to 973 K (10 K/min; 40 min) in the presence of H_2;

- Acetylene (sometimes acetylene + ammonia mixture) is introduced into the chamber;

- The plasma and the extraction discharge on the sample are adjusted to the desired values.

The extraction current is kept constant and bias voltage varies slightly around 310 V. The growth of the CNTs itself goes through a process in three steps, namely:

- An adsorption and decomposition hydrocarbon species (such as C_2H_2, H_2) on the reactive facets of the catalyst particles;

- A diffusion of carbon through the metallic particle (that rises to the top of the growing tube);

- An extrusion to obtain graphitic walls (shells).

2.3   Nucleation mechanisms

Since their discovery, a lot of theoretical work has been done to understand the growth mechanisms of nanotubes. Thus, the understanding of the nucleation mechanisms still remains a real challenge in the race to produce mass of nanotubes of denial chirality. Several models have been proposed to explain the growth mechanisms of MWCNT or SWCNT with or without the presence of catalytic particles. These models are mainly divided into two distinct areas: a phenomenological model based on Vapor-Liquid-Solid (VLS) transitions [107] or another model based on atomic scale simulations [108]. The process of nanotube growth

by CVD can be broadly explained as follows: there is first a decomposition and a chemical adsorption of the carbonaceous molecules on the surface of the catalytic particle. Then the carbon dissolves and diffuses inside the catalyst. It ends up segregating and graphitizing parallel to the surface of the particle once it is saturated with carbon atoms. It then forms the cap of the nanotube on the top of the catalytic particle which leads to a decrease of the surface energy. Then, either the carbonaceous cap continues to grow and ends up covering all the particle by deactivating it to form a carbon nanocapsule, or it is expelled from the catalytic particle by adding carbon dimers forming the cylindrical shape of a SWCNT. In the latter case, a second carbonaceous cap can also form under the first one before being expelled forming the structure of a MWCNT [109].

The carbon concentration gradient between the surface and the volume of the particle ensures the continuity of the growth process as long as the temperature and the concentration of hydrocarbon gases are maintained at values that prevent the poisoning of the catalytic particles [110]. The diameter of the emerging tubes is then determined by the size of the catalytic particle which, during growth, can either be rejected at the tip of the nanotube ("top-growth") or maintained at its base by remaining attached to the substrate ("base-growth"). Nevertheless, the synthesis of the multiple carbon forms derived from carbon nanotubes is far from being explained by a common mechanism. Numerous models exist nevertheless based on the one proposed by Baker in 1988 to explain the growth of carbon nanofibers [110]. In this model, the carbon is dissolved within the catalyst and then diffuses through the particle before being extruded. The dehydrogenation reaction being exothermic, Baker postulates the existence of a temperature gradient within the catalyst. The extrusion of the carbon therefore takes place in the coldest zone of the particle, where the nanofiber grows [111]. Baker's model has since been contradicted in some of its assumptions; the gradient in carbon concentration seems to be preferred to the temperature gradient to explain the driving force responsible for nanotube growth [112]. Also, many nanotubes are synthesized in a (CH_4) atmosphere which is an endothermic gas. Still, this model has laid a solid foundation in understanding the mechanisms of nanotube nucleation and formation. For example, the state of the catalytic particle considered as solid in this model has been experimentally verified by HRTEM in-situ measurements [113]. The catalyst retains its crystalline character while being very mobile and capable of changing its morphology (elongation, shrinkage). This catalytic state seems surprising in first approximation when one knows that CVD takes place at temperatures of the order of $600 - 700\,^{\circ}C$ and in view of the nanometric shape of the catalyst which could be considered as liquid. To summarize, depending on the size of the catalyst and thus on the type of nanotube obtained (SWCNT, MWCNT) as well as on the synthesis temperature, the microscopic mechanisms to be taken into account, in particular carbon diffusion, are different. This leads to multiple models that are not universal but only adapted to narrow windows of synthesis conditions. Beyond these models, two growth modes are empirically observed, depending on the position of the catalyst at the end of the growth:

$\Rightarrow$ Root-growth or Base-growth: The particle remains attached to the substrate during

the synthesis of the carbon nanotube (Figure 2.12 (a));

$\Rightarrow$ Top-growth: The particle detaches itself on the substrate during the growth of the CNT, it is found at the end of the synthesis at the top of the nanotube (Figure 2.12 (b)).

In the literature, both modes are encountered in CVD, PECVD and HFCVD. The appearance of one mode or the other depends essentially on the interaction between the catalyst particle and the substrate. In the case of a silicon substrate, for example, the formation of a silicide favors the "base-growth" mode [114]. On the contrary, when using a dielectric or refractory material as a substrate (SiO_2, TiN, Cr), the interactions are weak and the "top-growth" mechanism is generally observed [115].
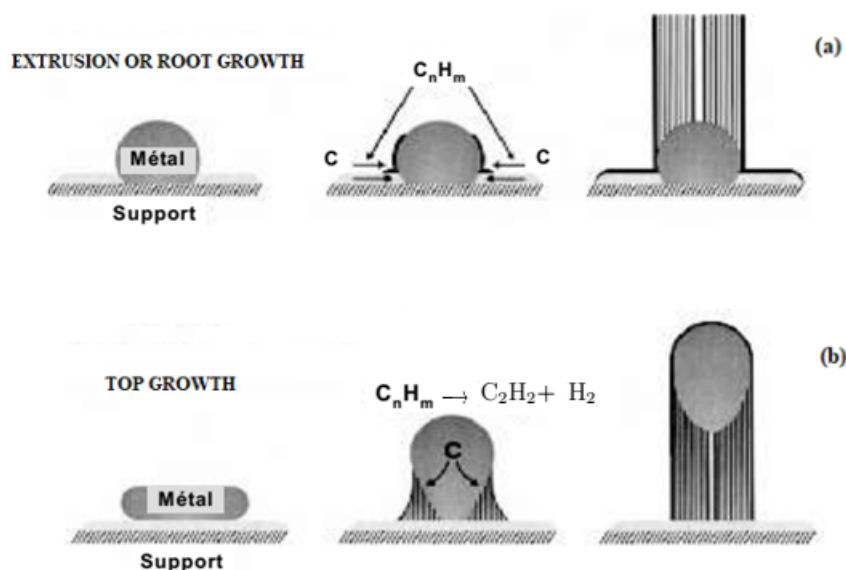
Figure 2.12: Simplified diagram of the "Top Growth" (b) and "Root Growth" (a) models for the formation of carbon nanotubes [111].

Moreover, it should be noted that, independently of the criteria explained above (substrate/catalyst interaction), the growth of SWCNTs (and more generally of small diameter CNTs) follows, with very rare exceptions, the "base-growth" mode [116]. At present, many questions remain unanswered, notably in the understanding of the microscopic mechanisms and in the search for optimal conditions leading to the formation of nanotubes of perfectly controlled chirality. The key role played by the catalytic particle is crucial to understand the formation of such tubes. Although it has been shown that armchair chirality nanotubes can be the most energetically stable structures [117], no experimental protocol has been able to systematically reproduce the formation of such tubes.

2.4   Potentiometric Titration

This technique allows the determination of the acidic and basic properties of the adsorbents and the nature of their functional groups. Acidic and basic sites on carbon nanotubes were determined by the acid-base titration method proposed by Boehm. The Boehm titration (BT) is one of few methods that enables a quantification of specific oxygen-containing surface groups on carbon materials. It provides absolute values based on a chemical reaction. The acid sites were neutralized with a 0.1 N NaOH solution and the basic sites with a 0.1 N HCl solution. The acidic and basic sites were determined by adding 50 mL of 0.1 N titrating solution and 0.01 g of SWCNTs to a 50 mL volumetric flask. The flask was partially immersed in a constant temperature water bath set at 298 K, and it was left there for 5 days. The flask was agitated manually twice a day. Afterward, a sample of 10 mL was taken and titrated with 0.1 N HCl or NaOH solution. The titration was carried out by triplicate using a potentiometer, Orion, model EA940.
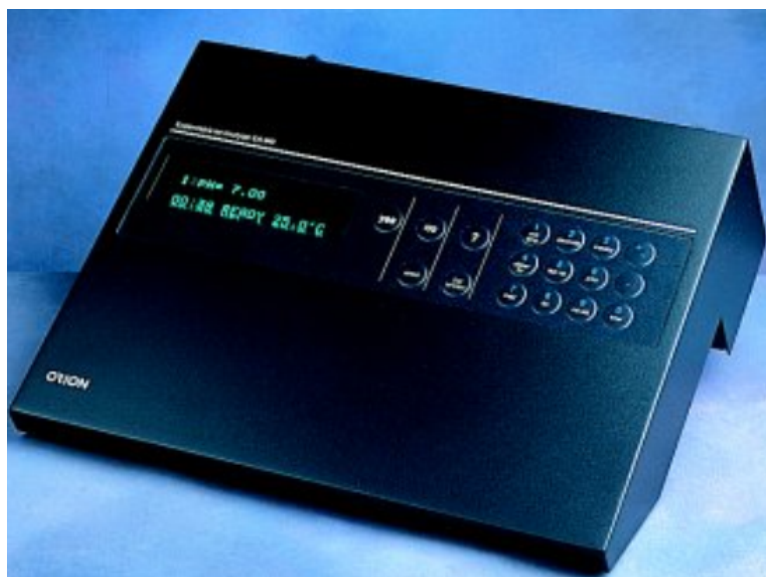
Figure 2.13: Potentiometer, Orion, model EA940.

Batch equilibrium method for determination of the point of zero charge (PZC)

Accordingly, the samples of SWCNTs (0.01 g) were shaken in PVC vials, for 24 h, with 40 ml of 0.01 or 0.1 mol/dm^3 KNO$_3$, at different pH values. Initial pH values were obtained by adding an amount of KOH or HNO$_3$ solution (0.1 mol/dm^3), keeping the ionic strength constant. The amount of H$^+$ or OH$^-$ ions adsorbed by SWCNTs was calculated from the difference between the initial and the final concentration of H$^+$ or OH$^-$ ions. Surface charge densities of SWCNTs, in aqueous solutions of KNO$_3$, were determined by potentiometric titration. The titration started from pH corresponding to PZC of SWCNTs. Two runs were carried out: (a) in the presence of SWCNTs (0.01 g of SWCNTs into 200 ml of 0.001, 0.01 or 0.1 mol/dm^3 KNO$_3$), (b) in the same electrolyte in the absence of SWCNTs (blank). A 0.1 mol/dm solution of HNO$_3$ or NaOH was used as a titrant in the pH range below or

above that of PZC, respectively. A dose of titrant, 0.05 - 0.5 ml, dependent on the solution pH and the electrolyte concentration, was added successively every 10 min. During the titration, solutions were stirred with a magnetic stirrer and purified N_2 was bubbled through the system, preventing any CO_2 or O_2 adsorption from the air. Experiments were carried out at 298 ± 0.2 K. The difference in acid or base quantities, used to reach the same pH in solutions with SWCNTs and the blank, was taken to represent the association or dissociation of H^+ ions from SWCNTs surface. Experimental results of the pH determination are PZC illustrated in (Figure 3.1). They are given as pH values of filtered solutions after equilibration (pH) with SWCNTs as a function f of initial pH values (pH) of solution.

2.5 Batch adsorption experiments

Single-walled carbon nanotubes grown by the chemical vapor deposition (CVD) method were purchased from Sigma-Aldrich and used for batch adsorption experiments. The characteristics given by de supplier are carbon content (> 85 %), carbon nanotubes (> 75 % +/-5 %), diameter (1.4 +/- 0.1 nm) length (> 5 mm) and specific surface area ($450 - 550$ m^2/g). Reagent grade (> 98 %) potassium nitrate (KNO_3) was supplied by CTR (in Mexico) and also used for the adsorption experiments. Data on the adsorption balance of pollutants described on single-walled carbon nanotubes were obtained in batch adsorbents according to the following methodology : In 50 ml vials, an initial volume (V_0) of 40 ml of an initial concentration (C_0) of 100 mgl^{-1} of potassium (K), was adjusted to different pH with solutions 0.01 and 0.1 N of HNO_3 and NaOH. A mass (m) of 0.01 g of SWCNTs was added. Each sample was made in triplicate.
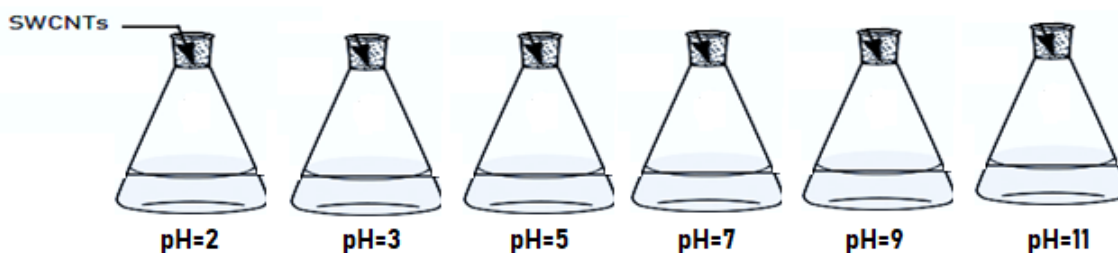
Figure 2.14: Preparation of SWCNTs at different pH.

The vials were placed inside a bath at a constant temperature of 25 ˚C for 3 days, regulating the pH and registering for a final volume (V_f), until the balance was reached. After that, the equilibrium concentration of K (C_f) was determined as well as the adsorption capacity.
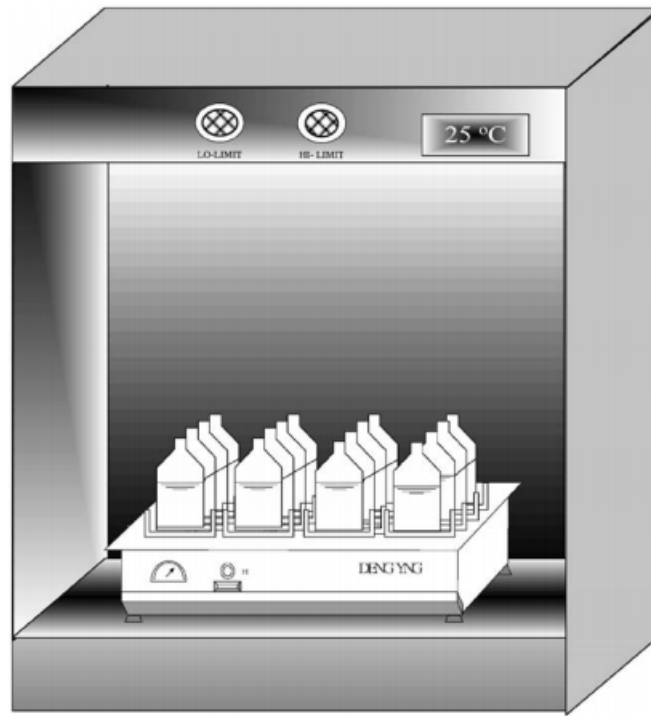
Figure 2.15: Experimental setup of the batch system [118].

The adsorption capacity (q) was calculated by means of a mass balance according to the following equation:

$$q = \frac{V_0 C_0 - V_f C_f}{m} \tag{2.5}$$

where: C_0 is an initial concentration of pollutant in mgl^{-1}, C_f is a final concentration of pollutant also in mgl^{-1}, m is a mass of adsorbent material in g, q is a mass of pollutant adsorbed per unit mass of adsorbent in mgg^{-1}, V_0 is an initial volume in L and V_f is a final volume in L. The surface charge and zero point charge pH (pH$_{ZPC}$) were evaluated using a potentiometric titration method proposed by Castillo et *al.*[119].

2.6   Electron Microscopy

Electron microscopy is an essential tool for characterizing any nanomaterial since it allows direct observation of size, shape and structure. The local structure of the carbon nano-structures (CNSs) can be investigated at the nanometer level by TEM (Tramission Electron Microscopy) and SEM (Scanning Electron Microscopy). TEM and SEM use electron beam, the electrons from the primary beam are scattered in the material and, before being absorbed, they spread in a region called the volume of primary excitation (Figure 2.16).
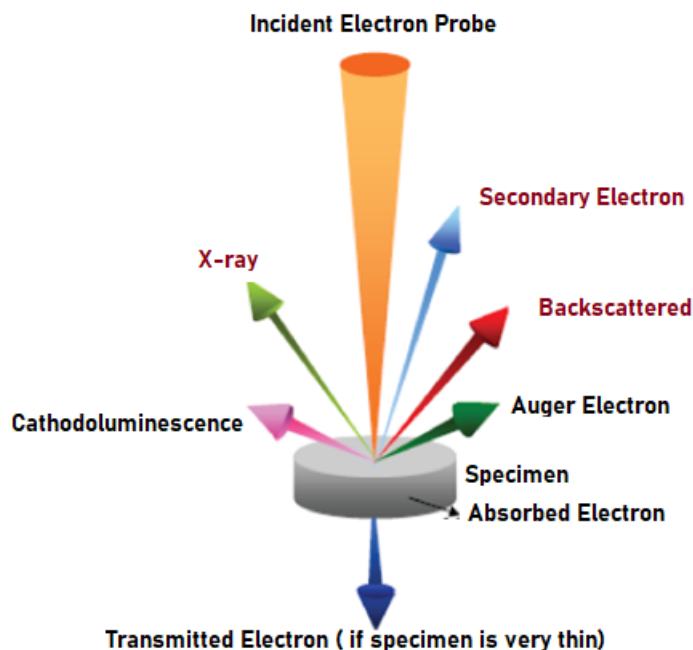
Figure 2.16: Schematic drawing of possible signals created when an incident electron beam interacts with a solid sample.

The characteristic length of this region depends on the material density and on the primary electron energy but is in the order of some microns. The electron-matter interaction in this volume causes the emission of several different signals and several information can thus be obtained by detecting different signals (Figure 2.16). In particular:

- In the primary region **Secondary Electrons** (SE) are emitted by ionization of atoms in the specimen by the primary beam. The secondary electrons have a small energy thus their absorption length is in the order of some nanometers the exact value depends on specimen density and incident beam energy. As a consequence only the secondary electrons emitted in the upper part of the excitation volume get off the specimen to be collected by the SE detector. The detection of secondary electrons can be used to obtain information on a layer with a thickness of some nanometers located just below the surface of the specimen. SE electrons are generally used to obtain 3D information on the specimen surfaces because their emission intensity is proportional to the cosinus of the angle between the surface normal and the SE detector. This is the same dependence followed by the intensity of light reflected by a surface, which depends on the angle between the reflecting surface and the optical detector (or the eye of the observer). The obtained image can thus be used to visualize the surface reliefs by just looking at the image as we would look at a 3D object illuminated by light. More sophisticated techniques can be used to obtain additional information on the surface (composition, electric potential ...) by using the SE signal.

- **Back-scattered Electrons** (BSE) can also be collected using a specic detector. Since they have larger energy than SE, BSE are originated from deeper regions of the interaction volumes (characteristic lengths of the order of 10 to 100 nm). Since they come from regions farther away form primary electron beam, BSE imaging has lesser resolution than SE imaging.

On the other hand, since the intensity of back-scattering strongly depends on the local specimen density, it can be used to obtain direct information on the specimen composition. As a rule of thumb it can be considered that high density regions in the specimen correspond to brighter regions in the BSE image. This is only applicable to the specimens since on irregular surfaces some region of specimen can be located between the emission point and the detector. This shadowing effects, together with a careful design of the detector can be used to obtain topographic contrast with BSE.

- Electrons from the primary beam also cause the emission of X-rays. Since the absorption length of the emitted X-rays is of the order of some microns, the resolution of EDS techniques in the SEM is micrometric.

In Electron microscopy, electrons are used to obtain high resolution imaging. In general, it can be considered that the spatial resolution δ of a wave-optical device, is given by the the Rayleigh formula [120]:

$$\delta = 0.6x\frac{\lambda}{NA} \tag{2.6}$$

where λ is the wavelength of the electron and NA is the numeric aperture of the magnifying lens. The numeric aperture depends on the refractive index of the medium (a refractive index analog can be dened for electron waves [121] and on the angular aperture of the lens. It can be shown that its value is approximately equal to 1. For an optical microscope using green light, the resolution amounts to 300 nm (NA= 1, and $l = 550$ nm). This same formula can be applied to electrons since the waveparticle duality principle tells us that electrons behave, statistically, as waves. The idea behind electron microscopy is to obtain a high resolution by exploiting electrons. In 1925, Louis De Broglie [122] postulated that the wavelength of an electron depends on its energy according to the following law:

$$\lambda = \frac{h}{p} \tag{2.7}$$

where p, is the momentum of the electron and h is the Planck constant. By using relativistic dynamics the following expression can be obtained for the electron wavelength:

$$\lambda = \frac{hc}{\sqrt{(eV)^2 + 2eVmc^2}} \tag{2.8}$$

where m and e are the electron mass and charge, respectively, c the speed of light and V is the acceleration voltage. With this formula it can be shown that a resolution of the order of the picometer can be obtained with a 200 kV acceleration voltage. This is obliviously a considerable improvement when compared with light optics.

In practice, the theoretical resolution is not really achievable because of the presence of aberrations in the imaging system. Nevertheless, at present, a resolution of some Angstroms can be obtained with standard commercial devices and a sub-Angstrom resolution can be obtained by using aberration corrected microscopes. There are two main kind of electron

microscopes, the Scanning Electron Microscope (SEM) and the Transmission Electron Microscope (TEM), both exploiting electrons but with a very different operation mode.

2.6.1 Transmission Electron Microscope (TEM)

The main instrument used for the experiments described in this dissertation was a TEM, is a microscope which uses electrons (as opposed to a "normal" optical microscope which uses light, i.e. photons) to form an image of a sample specimen. Electrons are extracted from a filament and accelerated by applying a high voltage towards the specimen in the part of the TEM called the electron gun. A series of magnetic lenses and apertures are used to control this electron beam, with the intention to make all electrons travel parallel to each other. The electron beam hits the specimen, going through it, making some of the electrons scatter. The electrons coming out on the other side now contain information about the specimen stored in their trajectories. See Figure 2.17 for a schematic of a TEM and the electron beam path.
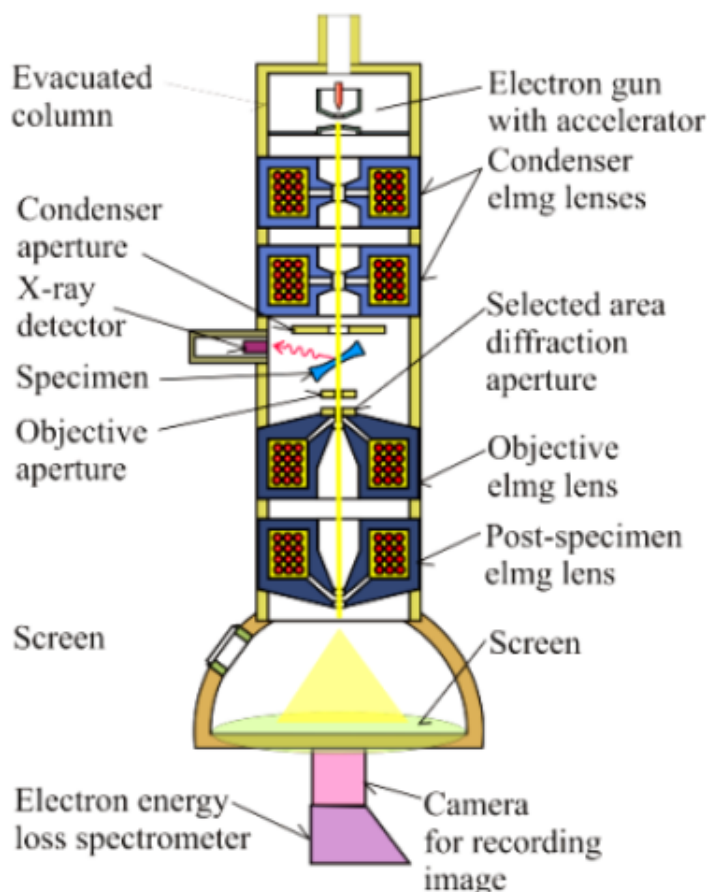
Figure 2.17: Schematic of a TEM. The imaging systems and beam paths are highly simplified, as most TEM have more lenses and apertures. [123].

Following the beam path past the specimen, another series of electromagnetic lenses work together to collect this information and present it to the TEM operator. These latter objective lenses are used to form a focal plane and an image plane of the scattered electrons, and finally

to magnify and project an image onto a fluorescent screen or a camera detector, where the focused rays of electrons prepared by the objective lenses can be detected and converted into a viewable image. By controlling the intermediate lenses the operator of the TEM can choose to project either the focal plane or the image plane onto the screen. The focal plane is where all rays scattered with the same angle converge at the same point creating what is called a "diffraction image" of the specimen. Conversely, the image plane is the point in space where electron rays originating from the same point in the specimen converge, thus creating a "real image" of the specimen. Furthermore, by inserting an aperture in the image plane, a so called "selected area aperture", it is also possible to select a specific region of the specimen. If one instead inserts an aperture in the focal plane one can remove electrons scattered with a larger angle to improve diffraction focus, or to single out a certain diffracted angle for imaging to create a so called "dark field" image of the specimen. It is also possible to single out only the "central beam" in the focal plane, creating a "bright field" image. The wide selection of operating modes in a TEM makes it extremely versatile when it comes to extracting information about the specimen from the scattered electrons.

⇒ Beam-specimen interaction and acceleration voltage

A TEM can be operated at a large range of accelerating voltages, normally between about 100 - 300 kV but can also be higher or lower. The accelerating voltage determines the speed and energy of the electrons in the beam, which in turn determines scattering angles and influences the resolution of the final image. However, there is also a risk of damaging the carbon nanostructure of graphene or CNT by inducing so called "knock-on" damage, where scattering electrons transmit too much energy to a carbon atom, knocking it out of position or removing it completely. In the experiments leading to this dissertation, an accelerating voltage of 90 kV was predominantly used, as this was found to be a balanced option offering slightly more contrast in the resulting images than for 80 kV, while significantly reducing the risk for knock-on damage seen at 100 kV.

⇒ Specific instrument information

The measurements described in this dissertation were performed at room temperature using a JEOL (JEM 2100) transmission electron microscope equipped with a LaB6 cathode and a digital camera from Gatan (SC1000 Orius). The main column is pumped with a turbo pump and with the anti-contamination device cooled with liquid nitrogen, the base pressure was around 7×10^{-8} mbar.

2.6.2 Scanning Electron Microscope

In SEM [124], a condensed beam is used to obtain information on a particular area of the specimen and the electrons forming the beam are characterized by an energy ranging between a fraction of a keV and 30 keV. As its name suggests, in a SEM, a specific area can be observed

by scanning the specimen surfaces with the electron beam. In a All measurements described in this dissertation were made inside a TEM, but it should be noted that before the final experimental setup was decided upon, an alternative setup inside a SEM was also attempted. SEM is the most widely used type of electron microscope. The image is formed by a focused electron beam that scans over the surface area of a specimen, and not formed by instantaneous illumination of a whole field as with the TEM.
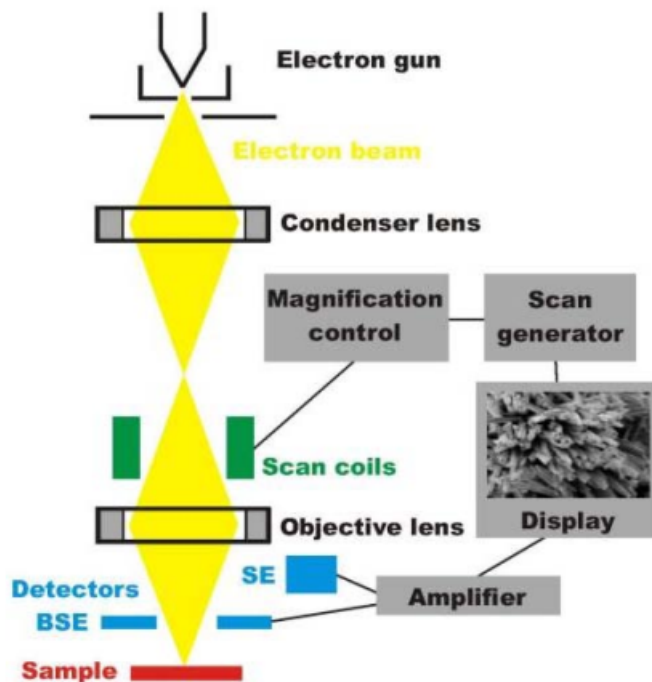
Figure 2.18: Basic construction of SEM [124].

2.6.3   Energy Dispersive X-ray Spectroscopy (EDS)

Energy Dispersive X-Ray Spectroscopy (EDS) is an analytical technique to qualitatively and quantitatively identify the elemental composition of materials analyzed in an SEM. EDS analyzes the top few microns of the sample with a spatial resolution as small as one micron. A detector converts X-rays into voltage signals; which feed a pulse processor, to measure the signals and pass them to data analyzer for display and investigation. Si(Li) detector cooled at cryogenic temperatures by liquid nitrogen is often employed; additionally, some modern systems come with silicon drift detectors (SDD) employing Peltier cooling systems. To produce characteristic X-rays from an object, it is bombarded by either a highly energetic beam of charge carriers (electrons or protons) or X-rays. The atoms of the sample contain ground state (unexcited) electrons in discrete energy levels or electron shells bound to the nucleus. An electron from an inner shell may be excited by an incident beam, thereby removing it from its shell and generating a hole where electron was present before excitation. This hole can be occupied by an electron of a higher-energy shell. The difference in energies of the higher- and lower- energy shells is emitted as an X-ray. Quantitative measurement

of the energy and number of these X-rays can be done with energy-dispersive analysis of Xrays. Since the energy of these X-rays is characteristic feature of energy difference between two shells and atomic structure of discharging element, EDS can be employed to identify the elemental composition of an object.
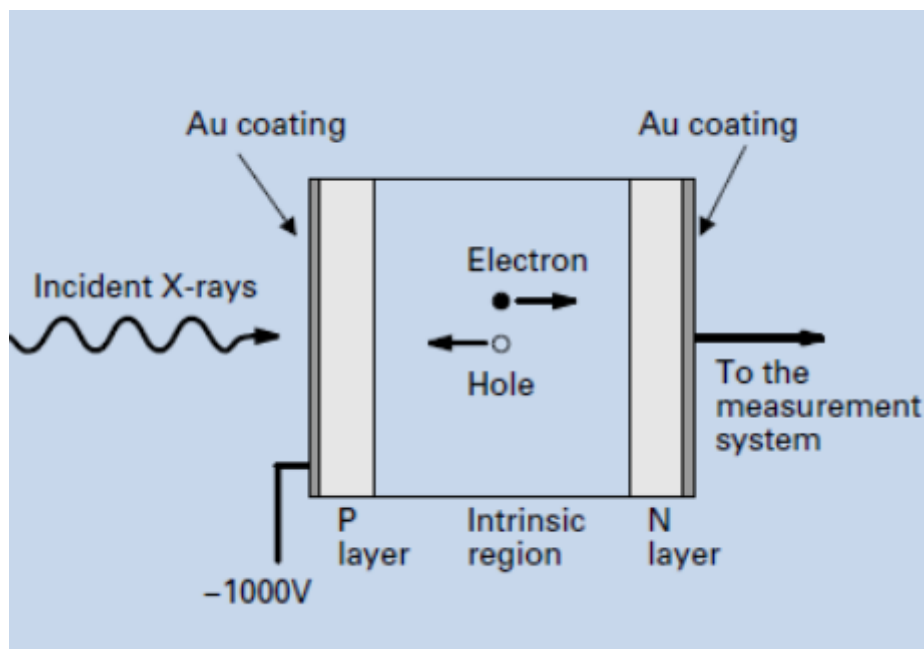
Figure 2.19: EDS semiconductor detector assembly [125].

When a sample is irradiated with highly energetic beam of electrons then a characteristic X-ray is generated. Due to irradiation when an electron is excited from the inner shell of its parent atom, the vacant place is occupied by the higher energy electron from the outer shell and the energy difference between the two shells is emitted as an X-ray. The joule of energy liberated in electron transfer is dependent upon from which shell it is transferring to which shell. Emitted X-rays energy as well as number through specimen is obtainable by an energy dispersive spectrometer. These emitted X-rays are known as characteristic X-rays because their energies (wavelength) are specific to the element from which it is emitted. Thus, this technique can be used for elemental analysis. When K shell electrons are excited, they emit characteristic X-rays which are termed as "K Lines" and those emitted from L and M shells are called "L Lines" and "M Lines" respectively. When the element is heavy then its characteristics X-rays energies are also higher, therefore incident electrons of higher energy are required. Different types of X-rays are emitted when incident electrons strike the atomic nucleus and these are known as "continuous X-rays", "white X-rays" and "background X-rays".
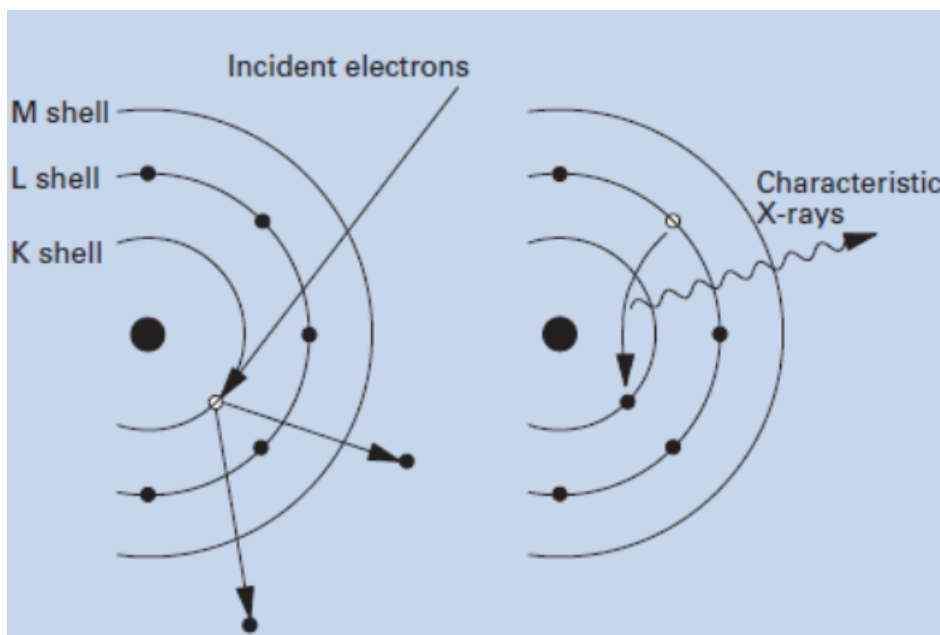
Figure 2.20: Principle of characteristic X-Rays Generation [125].

Sample's qualitative compositional data can be known from the respective peak positions with appropriate energies. The X−ray quantanumber measures the concentration of the elements, i.e., the height of the peak, but there is no linear connection between quantum numbers and elemental concentration portions. The concentration calculation requires the net count rates and characteristic X-ray energy of a specimen is the marker of the specimen atomic number.

2.6.4 Instrumentation of the EDS

Figure 2.21 shows the working arrangement of EDS with SEM. This instrument is mainly composed of four components : Electron beam source ; X−ray Detector ; Pulse Processor ; Analyzer.
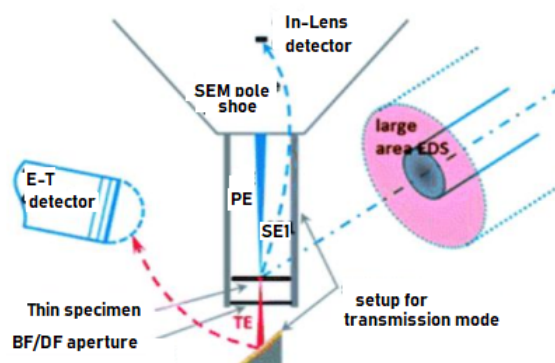
Figure 2.21: Working arrangement of Energy dispersive analysis of X−rays [125].

Electron beam source : As EDS is employed with the scanning electron microscope therefore the same electron gun (Field Emission) is used as the incident electron source and to focus the beam lenses are used along with aperture. The energy of the electron beam has to be carefully selected to overcome the compromise between the resolution requirements and the production efficiency of Xrays. The produced X-rays are detected by two crystal spectrometers.

X-ray Detector : The X-rays counts (which is the abundance of emitted X-rays) versus X-rays energies are measured by the EDS detector. Detector, a solid state device which is based on lithium drifted silicon. As X−rays strike the surface of the detector, a charge pulse is created. This charge pulse is directly proportional to theenergy of the incident X−ray.

Pulse Processor : A charge sensitive preamplifier is employed to convert the charge pulse to a voltage pulse.

Analyzer Multi-channel analyser is used to sort pulses by voltage in the signals which are received by the analyser. The energy of the X-ray can be obtained by measuring the voltage of the charge pulses. This energy is then sent for display and data processing. Here, data is displayed as histogram of intensity vs voltage.

X-rays generated EDS spectrum helps to carry out qualitative analysis to identify whatever elements are present in the sample when it is irradiated with high energy beam of electron. There are 3 methods of examination :

X-Ray Mapping

It is used to study particular elemental distribution. For analysis purpose, electron beam is scanned over a particular area and the related characteristics X-rays are acquired. If the peak to background ratio is very low then X-ray Map does not show the distribution of desired element, i.e., it shows the distribution of continuous X-rays. Sometimes X-Ray Map may not show the distribution of elements which are not of interest because characteristics X-Rays of elements of interest are close to those of not desired. It happens when energy difference between the desired element and undesired element is equal to the spectrometer energy resolution. It takes more time to acquire one X-ray picture as intensities of X-rays are less in comparison to that of secondary and backscattered electrons. The resolution of X-Ray Mapping is limited by "Area Analysis"

Analysis Area

Incident electrons when strike the specimen surface, get diffused and lose their energy by generating characteristic X-rays. This X-ray generation is spread over an area of around a few micrometers under standard operating condition. Thus, a larger area needs to be analyzed in order to examine the particle of the order of few nm range in a SEM image. The analysis area can be decreased by reducing the accelerating voltage. However, accelerating voltage cannot be reduced below a certain level, since the generation of X-rays requires high

accelerating voltages.Another strategy to reduce the analysis area is by reducing the thickness of the sample under investigation.

Quantitative Analysis

As characteristic X-rays intensities are proportional to the particular element's concentration, therefore quantitative analysis can be performed. The concentrations of unknown elements in a sample can be obtained by matching the intensities of characteristic X-ray of standard sample with that of the unknown sample. However, X-Ray generated in the sample may be either absorbed within the sample or excite the X-rays from other elements before being emitted in vacuum. Therefore, correction is required in this analysis method for which the following requirements are prerequisite.

Non-Conductive specimen analysis

For non-conducting sample, metal coating is required in order to prevent the charging but if requirement is to detect light element then it is suggested to use thin coating film, as heavy metal coating can block the X-ray emission through the sample because the X-ray intensities are less in comparison to secondary and backscattered electrons. Figure 2.22 and 2.23 show Helios nanolab 600 computers and control panel.
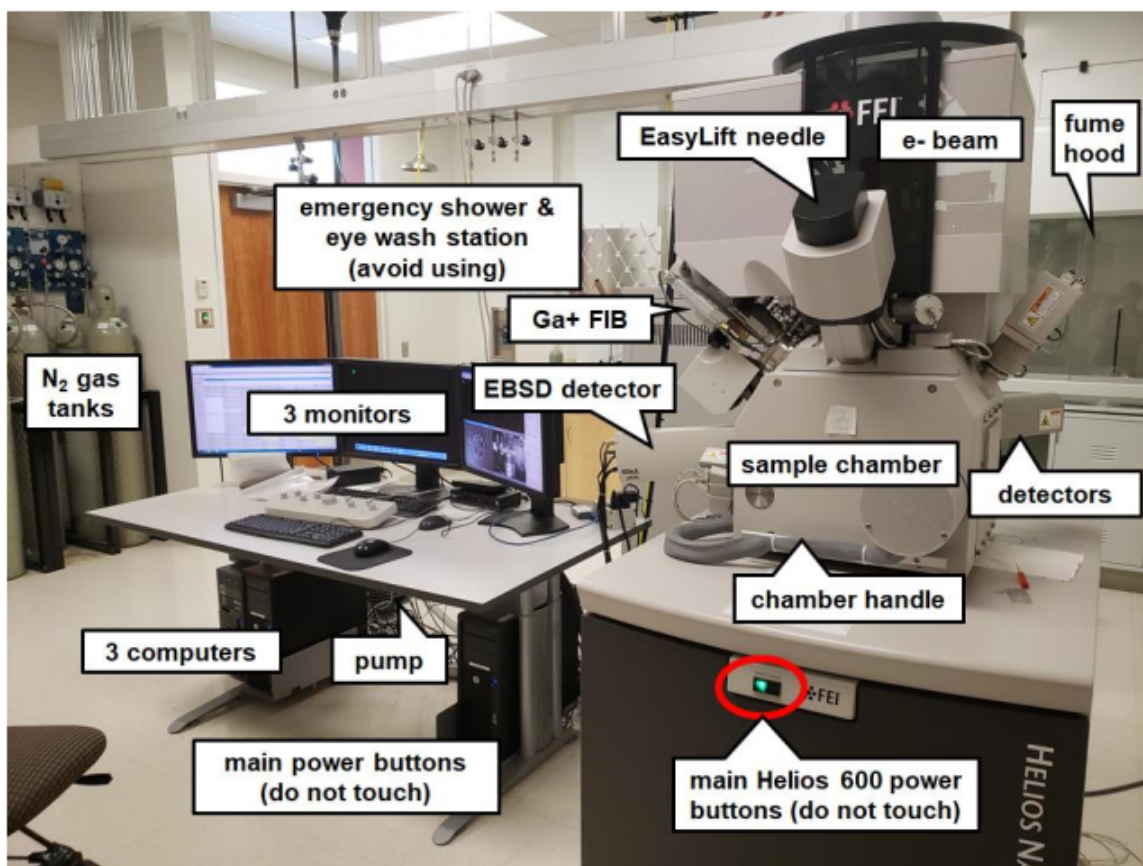
Figure 2.22: Helios Nanolab 600 [126].
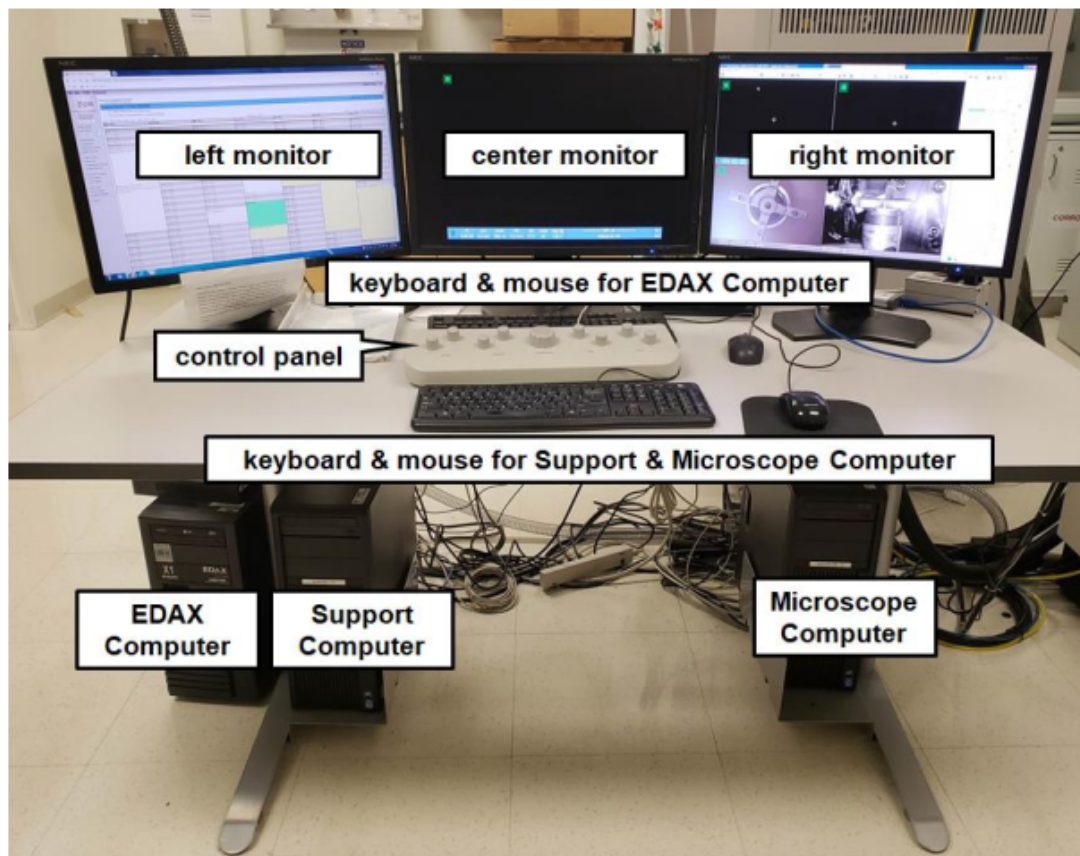
Figure 2.23: Helios 600 computers and control panel [126].

2.6.5 TEM microscopic samples

The Transmission Electron Microscope is generally used to characterize the microstructure or nanostructure of materials with very high spatial resolution. Information on morphology, crystal structure and defects, crystal phases, and composition can be obtained by combining optical electron imaging, electron diffraction, and small probe capabilities [82].

Preparation

Initial specimen preparation must be performed before the sample is placed into the FIB using the conventional TEM specimen preparation method. An area of interest is located and cut to < 3 mm in length. The sample is then mechanically polished as thin as possible (< 50 μm) to reduce the FIB time preparing thin sections of brittle materials for FIB thinning. Samples may also be cut to size using a wire saw. The sample is then positioned into the FIB so that sputtering may begin. A metal line is usually deposited on the area of interest to prevent damage and spurious sputtering of the top portion of the specimen and to also delineate the location of the area of interest. Typical dimensions of the metal line are ~ 1 μm wide x 2 mm high x 30 mm long. Large trenches are sputtered on either side of the area of interest using a high Ga$^+$ beam current. The beam current is reduced and milling is performed on alternate sides of the specimen to reduce redeposition of sprayed material onto

the surface of the specimen. Milling is continued until the membrane is thinned to ~ 100 mm or less (the final thickness of the specimen will depend on the information sought and the density of the material(s)). A finished electron transparent portion of the sample is usually $\sim 5 \mu$m x 20 mm. FIB sample preparation is performed using JEM-2100-Jeol microscope with an Oxford brand EDS probe.

Feature of JEM-2100-Jeol microscope

The Jeol JEM-2100 is a computer-controlled high-resolution transmission electron microscope (HR-TEM) with excellent analytical performance for daily use in a multi-user environment. The configuration of the instrument combines ease-of-use with capabilities for routine atomic resolution imaging of crystal lattices by coherent electron scattering or phase contrast (TEM); or by incoherent electron scattering of Z-contrast in the scanning transmission electron microscopy (STEM) mode. It offers routinely local spatial resolution at 2 nm or better for analytical TEM, i.e., analysis of elemental composition and chemistry (electronic bonding) by X-ray energy dispersive spectroscopy (XEDS), diffraction for crystal structure determination and crystallographic studies, and electron energy-loss spectroscopy (EELS). The JEM-2100 (Figure 2.24) is equipped with attachments for XEDS analysis from Oxfrod Instruments (Inca platform) and a GIF TRIDIEM post-column energy filter (Gatan Inc.) for acquisition of energy-filtered images and diffraction. The JEM-2100 operates with a Schottky field-emission electron gun (FEG) at 120 kV up to 200 kV, offers large sample tilt ($\geq 30^{\circ}$ X- & Y-tilt) combined with superior XEDS sensitivity without significantly affecting image resolution, achieving 0.22 mm point resolution and information limit of about 0.16 mm in TEM mode. Extension of image resolution towards the information limit by exit-plane wave function reconstruction from combined beam-tilt and through focal-series is available, and is greatly aided by improved beam and stage stability. In TEM and STEM mode the field emission gun (FEG) produces intense electron point probes with diameters of 0.5 mm and down to 0.16 mm, respectively, carrying sufficient current to provide for local diffraction, compositional and chemical analysis with sub-nanometer resolution. The post-column energy-filter is a very powerful component of the system, facilitating energy-filtered (EF) TEM and EELS. Forcing the electrons scattered by the specimen onto an energy-dispersive path and onto a CCD-camera facilitates EELS with resolution of 1.05 eV ($1s$ acquisition, 200 kV, 180 μA emission current) and 0.63 eV ($1s$ acquisition, 200 kV, 40 μA emission current). Use of the energy-selecting slit allows zero-loss (ZL) filtering for imaging and diffraction with only elastically scattered electrons, which increases contrast in phase contrast (HREM) and diffraction contrast images, and facilitates use of thicker specimens and quantitative electron diffraction (QED), especially useful in combination with convergent beam ED (CBED). Electron spectroscopic imaging (ESI) in TEM mode is accomplished by use of the energy-selecting slit to form images of element specific energy-loss and enables rapid elemental mapping directly in the EF-TEM images, which has great advantages over XEDS mapping with respect to speed of acquisition.
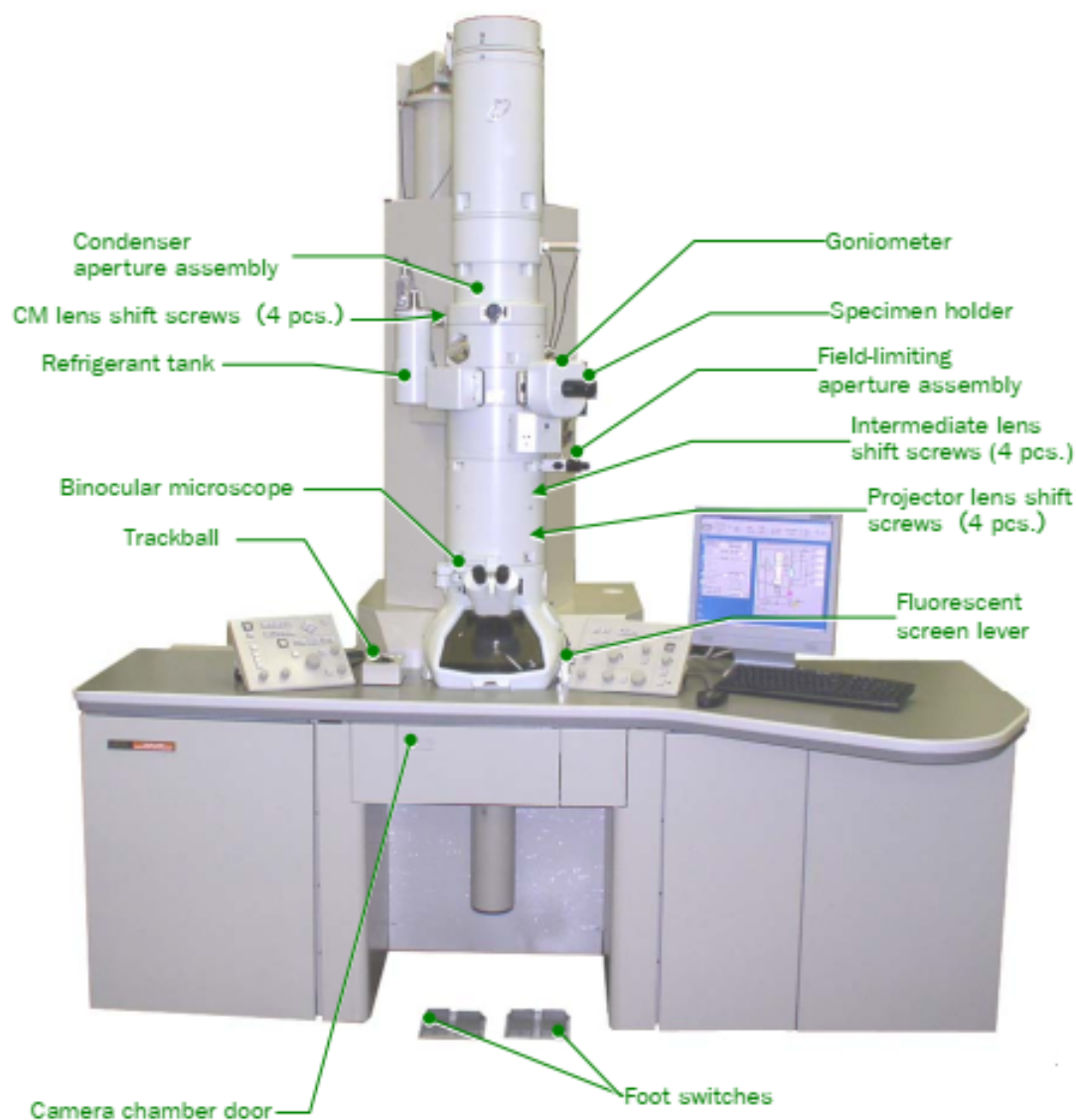
Figure 2.24: The external appearance of JEM-2100 microscope [127].

2.6.6 Fourier Transform Infrared Spectroscopy (FTIR)

Spectroscopy is the study of the interaction between matter and electromagnetic radiations. Dependent on electromagnetic wave sources and relative detectors, a series of spectroscopy can be realized for different applications in material research. Fourier transform infrared (FTIR) is one of the important analytical techniques for researchers. This type of analysis can be used for characterizing samples in the forms of liquids, solutions, pastes, powders, films, fibers, and gases. This analysis is also possible for analyzing material on the surfaces of substrate. In the FTIR analysis procedure, samples are subjected to contact with infrared (IR) radiation. The IR radiations then have impacts on the atomic vibrations of a molecule in the sample, resulting the specific absorption and/or transmission of energy. This makes the FTIR useful for determining specific molecular vibrations contained in the sample.

Principles of FTIR Spectroscopy

In FTIR analyses, Infrared light from the light source passes through a Michelson interferometer along the optical path. The Michelson interferometer comprises a beam splitter, moving mirror, and fixed mirror. The light beam split into two by the beam splitter is reflected from the moving mirror and fixed mirror, before being recombined by the beam splitter. As the moving mirror makes reciprocating movements, the optical path difference or retardation to the fixed mirror changes, such that the phase difference changes with time. The light beams are recombined in the Michelson interferometer to produce interference light. The intensity of the interference light is recorded in an interferogram, with the optical path difference recorded along the horizontal axis. The signal is at maximum at zero retardation where all wavelengths have constructive interference. The zero retardation is also found with the total constructive feedback.
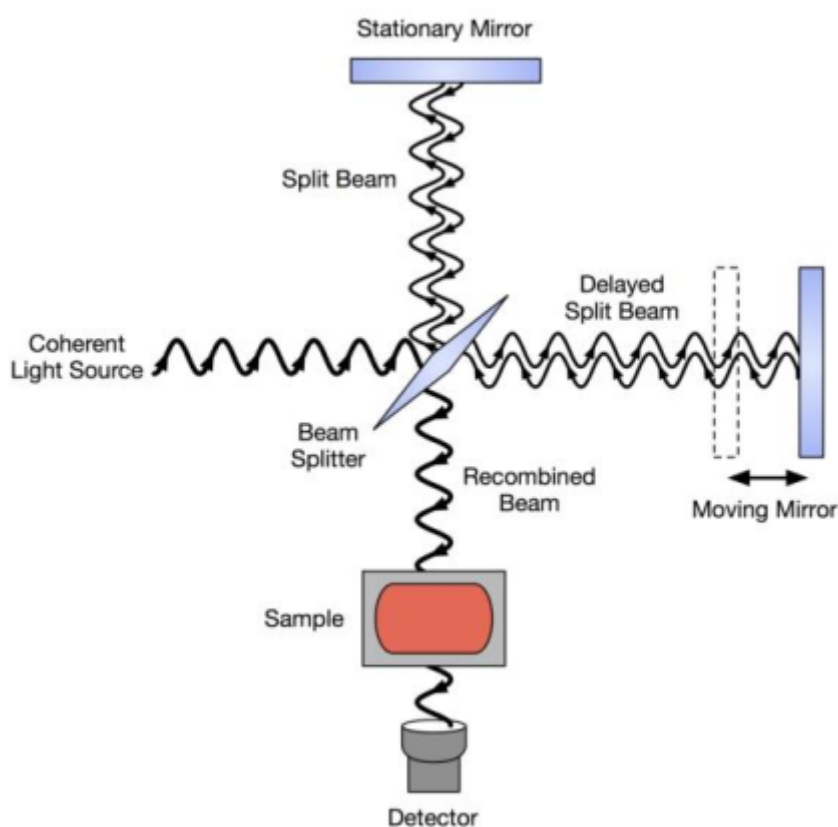
Figure 2.25: Operating diagram of the FTIR device [128].

The Figure 2.26 shows the schematic diagram of FTIR for detailed analysis process of the sample which is exposed to the infrared radiation. Firstly, a glowing black-body light source emits infrared energy beam. Then the infrared beam enters the interferometer where the interferogram signal creates. After then, the beam enters the sample compartment where it is transmitted through or reflected off of the surface of the sample. When materials are exposed to infrared radiation, molecules of the sample absorb radiation of definite wavelengths that results in the change of dipole moment of molecules. Some of the infrared radiation is

transmitted by the sample and some of it is absorbed. As a consequence, the vibrational energy levels of the sample molecules transfer from the ground state to the excited state. The resulting spectrum demonstrates the transmission and absorption of the sample molecules, and creates the sample's molecular fingerprint. The absorption peak frequency determines the vibrational energy gap of sample molecules and the number of the absorption peak is corresponding to the number of molecule's vibrational freedom. The magnitude of absorption peak is determined by the possibility of the transition of energy levels and the change of dipole moment. Finally the infrared beam enters to the detector for final measurement. The measured signal is digitized and sent to the computer for the Fourier transformation. The final infrared spectrum is then presented to the user for interpretation and any further manipulation.
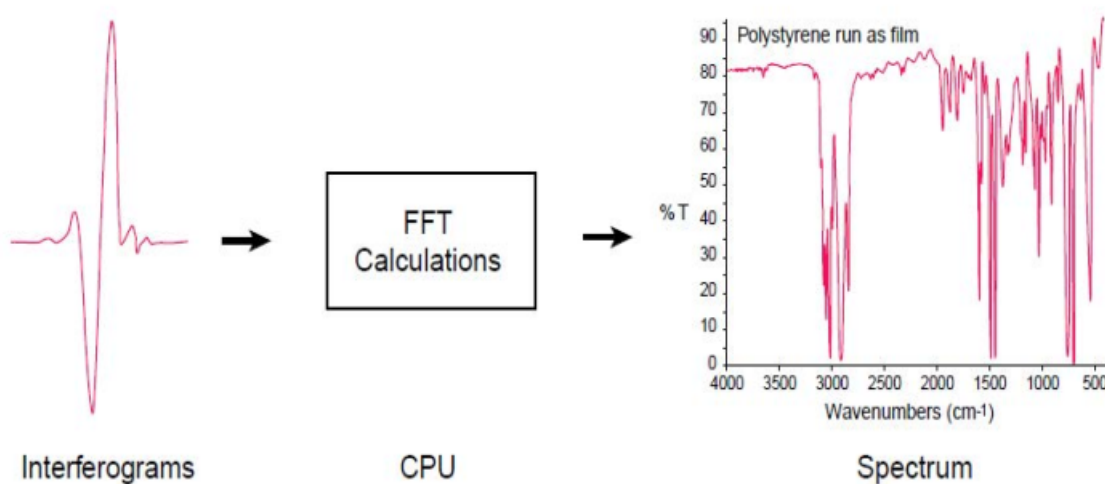
Figure 2.26: Schematic diagram of FTIR for analysis process of the sample [129].

The signal collected by the spectrophotometer is then transformed into an absorption spectrum using a mathematical treatment called Fourier transform. By scanning the mirror over a large range δ, we obtain an interferogram of the source. For this monofrequency source, the intensity $I(\delta)$ at the detector, $I(\delta) = B(\sigma)cos(2\pi\delta\sigma)$. If the two mirrors (F and M) are exactly at the same distance from the blade, the relative phase δ between the two waves is zero, the two waves are in phase, the interference is constructive and the intensity is maximum. If the mobile mirror is moved by a distance of $\lambda/4$, the additional phase will be $\delta = \lambda/2$. In this case, the interference is destructive and the intensity is zero. In the limit where the frequency spectrum is continuous, it is more convenient to work with an integral.

$$I(\delta) = \int\limits_{-\infty}^{+\infty} B(\sigma)cos(2\pi\delta\sigma)d\sigma \qquad (2.9)$$

This last equation reveals that the interferogram $I(\delta)$ is simply the cosine Fourier transform of the source spectrum, $B(\sigma)$. The information contained in this interferogram is equivalent to that of the $B(\sigma)$ spectrum of a blackbody. Of course, it is difficult to interpret

this interferogram. We therefore prefer to calculate $B(\sigma)$ from it. It is then a question of calculating the inverse Fourier transform. It is important to note that the integral over δ is calculated over the interval $]-\infty; +\infty[$, while the integral over σ is only calculated over the interval $[0; +\infty[$, i.e. on positive frequencies.

$$B(\sigma) = \int\limits_{-\infty}^{+\infty} I(\delta)cos(2\pi\delta\sigma)d\delta \tag{2.10}$$

Experimental Considerations

The spectrometer used in this work is a Thermo scientific Nicolet iS10 in Figure 2.27. The observable range for our system is between wavenumbers from 4000 to 500 cm^{-1}. When a spectrum is taken the detected voltage as function of the wavenumber is measured. But this function indicates not only the properties of the sample, but also of everything in the beam path and more importantly the sensitivity function of the detector and the radiation properties of the source.

Figure 2.27: Nicolet iS10 FT-IR spectrometer equipped with Smart iTR ATR [130].

For sample preparation, 200 mg of KBr was mixed with approximately 2 mg of the samples to collect the FTIR spectra. KBr is used because it transmits 100 % in the recorded wavenumber range and because it does not show an absorption spectrum in the IR region. FTIR is based on the absorption of infrared radiation by the sample to be analyzed when the beam energy is equal to the vibrational energy of the molecule. This sample can be in a gaseous, solid or liquid state. It allows via the absorption of vibrations characteristic of chemical bonds, to determine the presence of certain chemical functions present in the material. The elements present on the surface were identified according to the spectral positions of their characteristic peaks. This allowed the determination of the point elemental chemical composition of the surface of the adsorbent particles.

Step-by-step Analysis Procedure

Step 1 : Identification of number of absorption bands in the entire IR spectrum. If the sample has a simple spectrum (has less than 5 absorption bands, the compounds analyzed

are simple organic compounds, small mass molecular weight, or inorganic compounds (such as simple salts). But, if the FTIR spectrum has more than 5 absorption bands, the sample can be a complex molecule.

Step 2 : Identifying single bond area (2500 - 4000 cm^{-1}).

Step 3 : Identifying the triple bond region (2000 - 2500 cm^{-1})

Step 4 : Identifying the double bond region (1500 - 2000 cm^{-1})

Step 5 : Identifying the fingerprint region (600 - 1500 cm^{-1})

2.7 Production of synchrotron radiation

Synchrotron radiation facilities are high-brilliance light sources that offer unique possibilities for investigating nature. They provide outstanding tools for both fundamental and applied research and support technology in a wide range of areas. Indeed, synchrotron radiation research has become a major factor in the progress of science and technology in all industrially developed countries. A general overview of the electromagnetic spectrum is presented in Figure 2.28. Synchrotron radiation light covers the spectrum from infrared and visible through ultraviolet to X-rays.
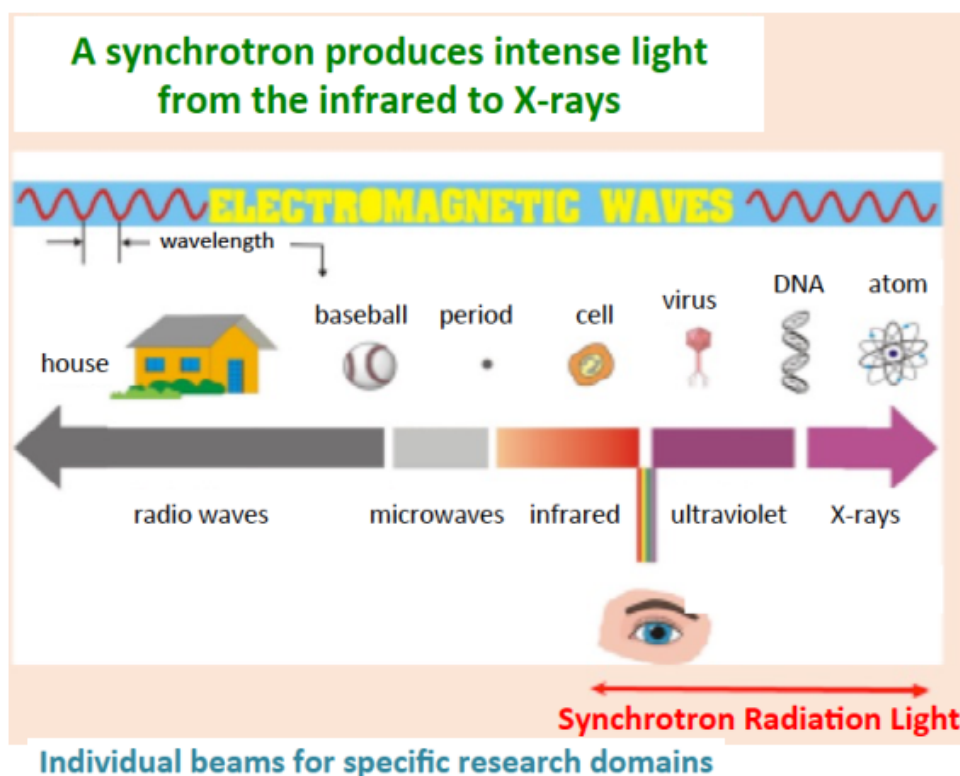
Figure 2.28: The electromagnetic spectrum from radio waves to X-rays [131].

The X-ray spectroscopy technique uses two main sources of radiation: the radiation source produced by the conventional X-ray tubes [132] and the radiation source produced in the synchrotron storage rings.

2.7.1 Production of X-rays by conventional sources

These X-rays are produced following a heating of the metal target (anode) by electrons coming from the cathode, then accelerated in a vacuum by an intense electric field. Let us consider the Crookes tube of Figure 2.29 also called gas discharge or cold cathode tube. It is made using a glass bulb containing a concave-shaped metal (aluminum) cathode and an anode or target in which a vacuum is created with a remaining residual air pressure of approximately 100 Pa or 1 Torr [133]. The shape of the cathode makes it possible to condense the flow of electrons which causes the induction coil to provide an accelerating voltage. The ionization of the residual air is produced in the form of a discharge causing a flow of electrons from the cathode towards the anode. This tube was improved in 1913 by William Coolidge and Crookes [133].
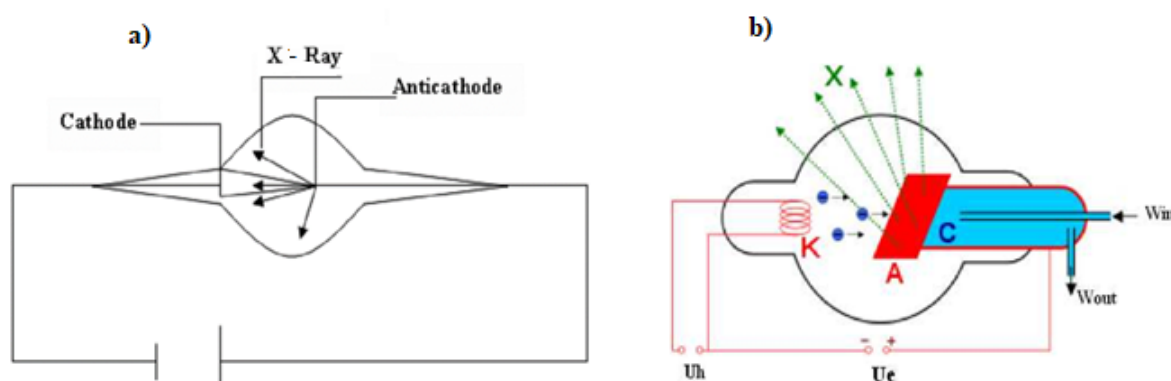
Figure 2.29: Production of X-rays: (a) Crookes tube and (b) Coolidge tube [133].

2.7.2 Synchrotron light production

The principle of synchrotron radiation is based on the fact that when a charged particle is accelerated and undergoes a curvature, it emits electromagnetic radiations. In a storage ring, the electrons move at considerable speeds, the radiation then emitted depends on the speed of the electrons and covers a very wide range of electromagnetic spectrum from infrared to X-rays. Figure 2.30 of a synchrotron showing the linear accelerator, the booster, the storage ring and the beamlines. Indeed, the electrons are accelerated in a linear accelerator (linac) through an electron gun until their energy is of the order of several million electron volts (MeV). Then, they enter in the booster whose role is to increase their energies up to the order of GeV. They are then transferred to a circular accelerator called a storage ring as shown in Figure 2.30, where they are forced to move along a circular trajectory under the action of a magnetic field produced by the magnets placed along the circumference. The displacement of these electrons at the relativistic speed following the circular trajectory is done by emission of electromagnetic radiation in its direction: This is Synchrotron radiation. It is presented in Figure 2.30, which consists of optical and experiment cabins and workstations that allow experiments to be conducted according to the given applications.
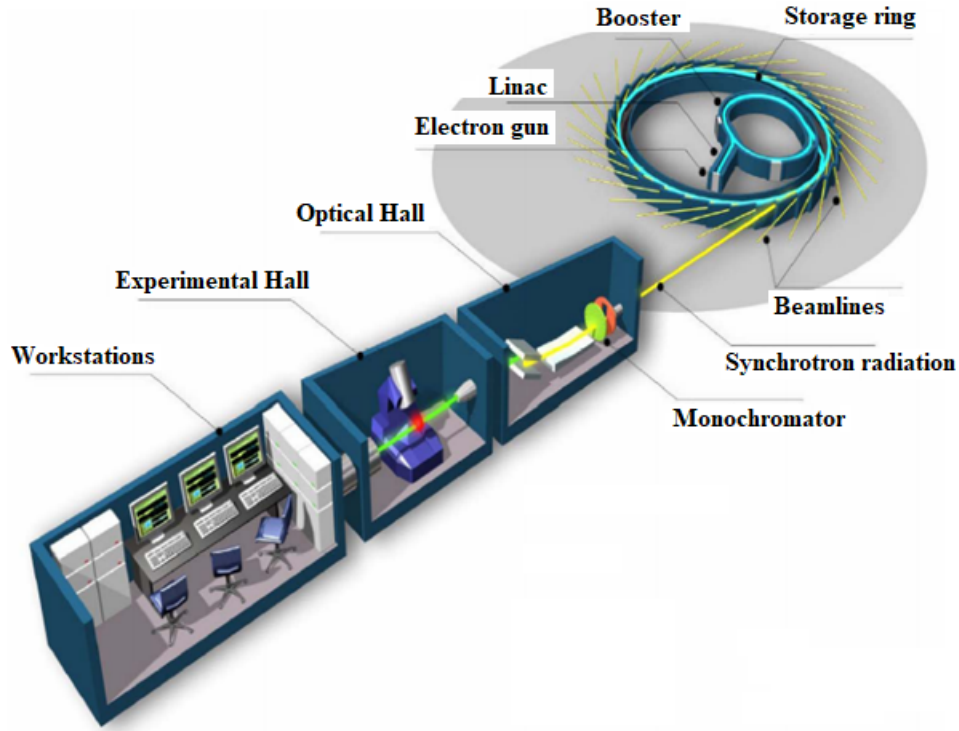
Figure 2.30: Production of the synchrotron light source [131].

2.8   Acquisition process of XANES spectra of CNTs

Starting from HOPG (Highly Oriented Pyrolytic Graphite) as a reference model, the UNDOS (Unfilled States Density of States) are explored as a function of the energy of incoming X-ray beam at fixed incidence angle $\alpha = (\overrightarrow{P}, \overrightarrow{C})$; $\overrightarrow{P} = \overrightarrow{E} \wedge \overrightarrow{H}$ being the Poynting vector of X-ray beam and $\overrightarrow{C}$, the normal to the surface plane (Figure 2.31). Thus, one is near Normal Incidence (NI) when α approaches $0°$ ($\overrightarrow{P}$ anti parallel to $\overrightarrow{C}$) and the electric field vector $\overrightarrow{E}$ lies almost in the substrate plane. In the other hand, one is near Grazing Incidence (GI) when α approaches $90°$, with $\overrightarrow{P}$ nearly parallel to the surface plane and $\overrightarrow{E}$ nearly normal to the surface plane ($\overrightarrow{E}$ nearly parallel to $\overrightarrow{C}$). For a pure CNT (Figure 2.31), it is obvious that the components of the electric field vector $\overrightarrow{E}$, along $\overrightarrow{a_r}$ and $\overrightarrow{a_z}$ in cylindrical coordinates are respectively:

$$\overrightarrow{E_r} = \overrightarrow{E_\pi} = E_0 sin(\frac{\pi}{2} - \alpha).\overrightarrow{a_r} = E_0 cos\alpha.\overrightarrow{a_r} \tag{2.11}$$

$$\overrightarrow{E_z} = \overrightarrow{E_\sigma} = E_0 cos(\frac{\pi}{2} - \alpha).\overrightarrow{a_z} = E_0 sin\alpha.\overrightarrow{a_z} \tag{2.12}$$
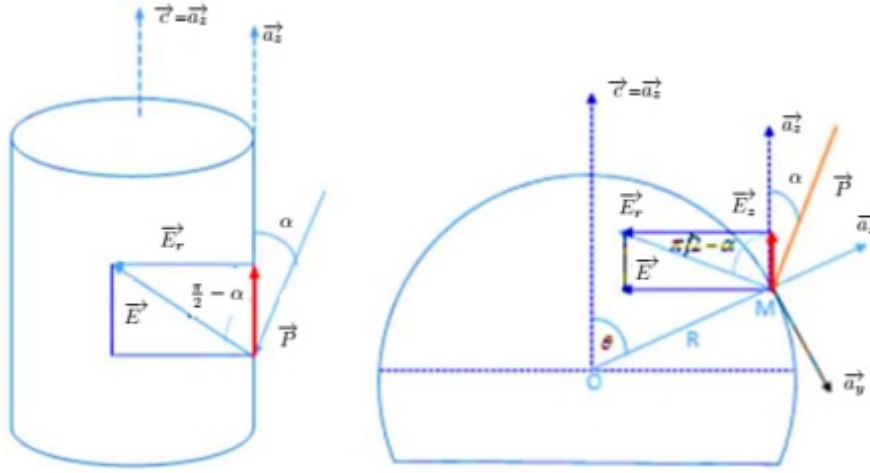
Figure 2.31: (Left) Polarized light irradiation of the tubular part of a pure CNT and (Right) Polarized light impinging the half spherical (cap) part of the CNT [8].

$\overrightarrow{E_\pi}$ and $\overrightarrow{E_\sigma}$ are the components of the electric field directed towards the final orbital states of the π- and σ symmetries respectively. The XAS signal strength is then proportional to:

$$I_\pi = \overrightarrow{E_\pi}.\overrightarrow{E_\pi^*} = I_r = I_0 cos^2\alpha \tag{2.13}$$

$$I_\sigma = \overrightarrow{E_\sigma}.\overrightarrow{E_\sigma^*} = I_z = I_0 sin^2\alpha \tag{2.14}$$

These intensities correspond respectively to the maxima at normal and grazing incidence angles [8]. Thus, this short development predicts the angular variation of the absorption spectra. In the CNT, σ- orbitals lie along the shells (vertical side-walls) while the π- orbitales are directed perpendicular to this $\overrightarrow{C}$ axis. By adjusting the angle of incidence of the synchrotron radiation on the sample, it is possible to excite final states of specific symmetry at the K-edge of carbon. According to Fermi's golden rule and the electric dipole selection rules, when the electric field vector is located in the ground plane (i.e. $\overrightarrow{E}$ perpendicular to the $\overrightarrow{C}$ axis ($\overrightarrow{E} \perp \overrightarrow{C}$)), then the final π^* states are selected. When the $\overrightarrow{E}$ vector is perpendicular to the plane (i.e. $\overrightarrow{E}$ parallel to the $\overrightarrow{C}$ axis ($\overrightarrow{E}//\overrightarrow{C}$)), then the σ- symmetry states are excited. Therefore, the intensity of each of the transitions will depend strongly on the angle α between the Poynting vector, then electric field vector $\overrightarrow{E}$ and $\overrightarrow{C}$ axis.

2.8.1   XAS data collection methods

There are experimental techniques for determining the absorption coefficient, or alternatively quantities proportional to it. These different procedures have advantages and limitations, depending on the type of sample studied (thin films, solid materials, etc.), the information sought (sensitivity to volume or surface) and the experimental environment (presence or

absence of the magnetic field) [105]. In the case of thin films or solid materials, the most commonly used methods are :

- Transmission mode detection;
- Current mode detection (TEY, PEY);
- Fluorescence mode detection.

a) Transmission detection mode

Transmission detection is the most direct method for absorption coefficient measurements. It simply involves measuring the number of photons of radiation before and after passing through the sample. It is rarely used for "soft" X-rays with energies below 2 KeV, as the penetration depth is very shallow (a few tens of nanometers). This method is effective for relatively thin samples deposited on X-ray transparent substrates, a condition achieved at high energy (energy above 12 KeV). For thin films deposited on absorbing substrates, other methods do not directly measure the absorption process but rather the processes that result from it. This is the case of the current detection method.

b) Current detection mode

This method is based on the measurement of the number of electrons emitted following the absorption process. These are either photoelectrons or Auger electrons (electrons emitted during the non-radiative de-excitation of core holes). It is possible to determine the effective absorption cross-section by choosing the kinetic energy of the electrons that reach a surface. This method suffers from many limitations, for example, when varying the kinetic energy of the incident photons, the Auger electron peak and the photoelectron peak can interfere. By measuring all the electrons arriving on the surface, regardless of their energies, a more widely used current detection technique has been developed: Total Electron Yield (TEY) [105]. Here, the XAS signal is dominated by low energy electrons (below 20 eV), which have undergone inelastic shocks (secondary electrons). Some of these electrons are produced by photoelectrons, others by Auger electrons. Like the Auger electrons themselves, the later part is proportional to the effective absorption cross section.

This method is very sensitive to the surface and magnetic field applied to the material. A major difficulty in current detection is the saturation phenomenon. It is observed at grazing incidence, and is characterized by the absorption of electrons over a distance much smaller than the escape depth (average depth characteristic of the electrons in a material and which is independent of the kinetic energy of the incident photons) and the signal saturates. And the measured signal is no longer proportional to the absorption coefficient. Moreover, as before, being interested in all the electrons arriving on a surface independently of their energy, the other method of current detection consists of taking into account only the electrons with an energy greater than a threshold value, the method used is the partial detection of electrons or PEY (Partial Electron Yield).

c) Fluorescence detection mode

The depth of penetration of electrons is small, so current detection measurements do not capture volume properties sufficiently (below 3 nanometres). Fluorescence detection or FY (Fluorescence Yield) is suitable for volume, since photons interact less with the material than electrons (inertia). In addition, the application of an intense magnetic field does not disturb the signal. However, the signal measured in FY is only proportional to the absorption coefficient in specific cases. The relationship between the fluorescence intensity and the absorption coefficient is very complex. At grazing incidence angles, the fluorescence signal is rounded up to be proportional to the absorption coefficient. This is similar to the phenomenon encountered in TEY detection and is known as self-absorption. Experimentally, the effects of self-absorption are so great that measurements are usually made at normal incidence.

One of the advantages of the XAS technique is that it is possible to select an element by choosing one of its absorption edges and to study its local environment. It constitutes a local probe. This method can be applied to all crystalline, amorphous or liquid materials. Among the materials currently in the spotlight are carbon nanotubes (CNTs), which are the basis of several electronic devices, more specifically those emitting electric fields, whose design requires CNTs arranged perpendicular to the flat surface of a substrate. These CNTs are preferably obtained by chemical vapour deposition or CVD methods, catalysed by transition metals (Fe, Co, Ni) and possibly by current discharge plasma. Here, we present the use of synchrotron X-ray polarisation, in the framework of electric dipolar selection rules, by exploiting the intensity variations of the different types of transitions ($1s\rightarrow\pi^*$ and $1s\rightarrow\sigma^*$) observed in XAS, to complete these CNT orientation studies with greater precision and finesse. It is the exploitation of these electrical dipole selection rules that are exploited within the framework of the geometrical model [47] to characterise the orientation of all or any of the nanostructures that can be obtained with the growth methods currently available.

2.8.2   Carbon nanotube XAS spectra

XANES measurements were performed at Carbon K-edge on the SWCNTs in the SACEMOR beamline [102], at the Laboratoire pour l'Utilisation du Rayonnement Electromagnétique (LURE, ORSAY, France). A TGM monochromator with a resolution better than 0.2 eV at the carbon K-edge was used. The spectra were recorded in total electron yield (TEY) and partial electron yield (PEY) detection with an energy step of 0.1 eV and normalized to the spectrum of a freshly gold-coated copper grid. Calibration of the spectra was performed using the carbon ionization potential. The residual pressure in the ultra high vacuum chamber was 10^{-9} mbar. The contamination of the carbon surface by the beamline optics does not exceed 1 % of the total signal and can therefore be neglected for materials with a high carbon concentration. The experiments were conducted in two configurations with respect to the angle $\alpha = (\overrightarrow{p}, \overrightarrow{c})$ between the normal to the sample surface and the incident direction of the radiation (Poynting vector). The first configuration is at normal incidence ($\alpha = 0^\circ$)

with $\vec{E}$ perpendicular to the surface (Figure 2.32), and the second is at grazing incidence ($\alpha = 90°$) with $\vec{E}$ parallel to the surface (Figure 2.32). The angular variations in the intensity of transitions at the K-edge of carbon to the unpopulated σ^* and π^* states were recorded at these values of the incidence angle, respectively. The step size was 0.1 eV. The prepared samples were then examined and introduced into the XAS analysis chamber and subsequently cleaned by heating at 550 °C for two hours.
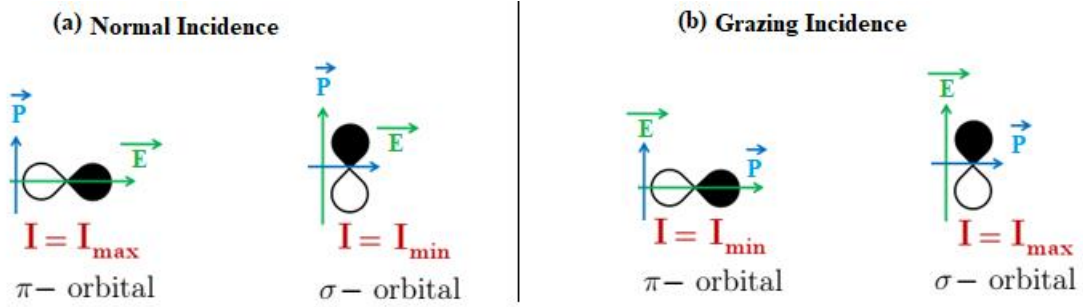
Figure 2.32: Schematic representation of the Poynting vector $\vec{P}$ and of the electric field vector $\vec{E}$.

2.8.3 Data Analysis of XANES Spectra

The obtained spectra are normalized to that of a fresh gold-coated copper grid. The energies are calibrated against the carbon ionization potential (IP). With this calibration procedure, the error at the carbon K-edge is expected to be less than 0.2 eV. The background signal is substracted from the low energy side before the pre-edge using a linear contribution from the background. The spectra are then normalized to the pre-edge intensity on one side μ_0, and to the absorption intensity at $\mu(320)$ at 320 eV on the other side, according to the relation:

$$I = \frac{\mu(E) - \mu_0}{\mu(320) - \mu_0} \tag{2.15}$$

Where I is the relative intensity, $\mu(E)$ is the absorption coefficient corresponding to the energy E, and μ_0 is the absorption coefficient at pre-edge. Above this energy range (above 320 eV), oscillations due to EXAFS occur. Multiple scattering and single scattering interfere with these transitions (EXAFS) and the analysis was not continued beyond 320 eV. Using density of states (DOS) calculations, it has been made possible to assign the K-edge absorption structures of carbon in XAS to specific Brillioun zone states in the theoretical band structure of graphite [108]. In addition, by recording the angular dependence of the carbon edge lines, the symmetries and final states were determined. Thus, in single-crystal graphite, it is shown that the intensity of a pure $1s \rightarrow \pi^*$ transition located at 285 eV is proportional to $sin^2\alpha$ [8] (with its maximum at grazing incidence), while the intensity of a transition $1s \rightarrow \sigma^*$ is proportional to $cos^2\alpha$ (with its maximum at normal incidence) [8]. The line shape analyses of the individual transitions were conducted using the GAXPS software developed at the IPCMS in Strasbourg. This software allows to deconvolute XAS spectrum

into several elementary peaks. The calculation used in the solftware is based on the model of Doniah and Sunjic. An experimental spectrum can thus be parameterized with values that have a physical meaning and can be controlled at each moment. These parameters can be adjusted in an automatic way, and there are two types: parameters common to all peaks and parameters specific to each elementary peak.

The common parameters are: the experimental Gaussian (eV), the pivots (X (eV) and Y (counts)) which are the baseline levels and the slope (counts/eV). They are defined once at the beginning of the analysis. The parameters of each elementary peak are: energies (E, E_0, E_c), area or intensity (shot/s), Lorentzian (eV), asymmetry (unitless), background (1/eV) and Gaussian (eV). The correct values are obtained by successfuly superimposing the experimental and theoretical curves. The XAS data acquisition methods used are the total current detection (TEY) and partial current detection (PEY). The later is not sensitive enough to the surfaces. All spectra obtained are first corrected to substract the background noise.

Conclusion

In this chapter, CNTs growth was studied theoretically and experimentally to investigate its dependence on parameters such as the catalyst, the growth temperature and carbon feedstock. Some of the parameters, including catalyst particle and growth temperature are the main effective parameters in the decomposition process and carbon diffusion. So the effect of the type and the diameter of the catalyst, the temperature of the growth environment, and the type and flow rate of the carbon feedstock, are assumed in the growth process analysis. The properties and the behaviour of the CNTs depend strongly on the synthesis, adsorption, purification and post-processing methods. The use of microscopy and spectroscopy tools for the characterization of materials brings new and complementary solutions. By studying the fine structures present in the absorption edge of the elements in the X-ray domain, we have obtained information on the electronic structure of the CNTs. The measurement and XAS data of the absorption spectrum of a monolayer of chemisorbed molecules should not take into account the contribution of the substrate. Because the later could distort the analysis of the results.

Results and Discussions

Introduction

The knowledge of the structure of a system is required to elucidate new materials with novel properties. CNTs have intensively undergone theoretical and experimental studies because of their versatilities. CNTs are mostly characterized by SEM and TEM, which are both qualitative methods. These techniques can deepen the morphology of the system, but are not able to give enough information on the electronic and structural properties. The XANES technique on the contrary is a powerful tool that provides the structural and electronic information on the local environment around the absorber atom in the medium range order due to its angular dependence of the absorption transition [27]. It is sensitive to the chemical adsorption and impurities, defects, and orbital rehybridization [27]. To functionalize nanotubes and fullerenes, the chemical reactivity of carbon atoms needs to be understood with quantitative accuracy. Our work is oriented towards surface phenomena, so we have correlated and cross-checked the information provided by XANES to obtain a detailed knowledge of the structure of our samples. An original approach was adopted, combining high-resolution XANES experiments and microscopic investigations, the later aimed to highlight the adsorption and desorption properties of CNTs for applications such as increasing electrical conductivity and water purification. Study of the morphology of CNTs, the metal-support interaction and the coverage rate was thus made possible by the combination of different experimental methods.

3.1   Textural properties of CNTs

CNTs have selective adsorptive properties suitable for the separation and purification of gas mixture as well as the treatment of contaminated water. The use of CNTs as adsorbates requires a sufficient knowledge on their textural properties, such as the size and the volume of their pores, in addition to their surface area. These caracterize the portions of the surface of the material which are likely to the adsorption phenomena. These parameters were determined using Brunauer, Emmett and Teller (BET) method which allows to evaluate gas adsorption data and consequently give a specific surface area of the investigated material. The textural properties of SWCNTs determined in this study, which include specific surface area, pore volume, and average pore diameter, are presented in Table 3.1.

Table 3.1: Textural properties of SWCNTs compared with values of [133].

Material	Surface area BET ($m^2.g^{-1}$)	Pore volume ($cm^3.g^{-1}$)	Pore size (mm)
SWCNTs	582	1.625	1.18
SWCNTs [134]	700	/	/

Our BET specific surface area value $582 \ m^2.g^{-1}$ is smaller than that reported by Dehghani *et al.*[134], the difference can be justified by the growth, preparation or functionalization conditions of CNTs. Figure 3.1 presents the trend of the adsorption capacity of hydrogen ion q_{H+} on the surface of SWCNTs.
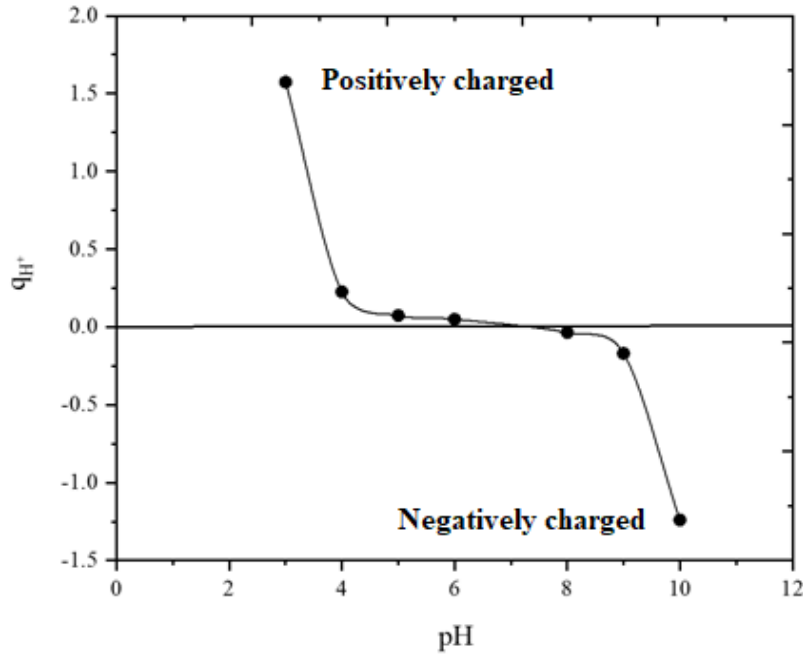
Figure 3.1: Charge distribution of SWCNTs [133].

The distribution of charges on the surface is generally not homogeneous in sign. In the case where H^+ and OH^- are the only ionic species determining the surface charge. The pH_{ZPC} was defined as the pH at which the net surface charge of an adsorbent in an aqueous solution is neutral. At this value, the active acidic or basic groups do no longer contribute to the pH of the solution. The surface charge and zero point charge pH (pH_{ZPC}) of SWCNTs are evaluated using a potentiometric titration method proposed by Castillo *et al.*[84]. This technique allows the determination of the acidic and basic properties of the adsorbents and the nature of their functional groups. This characterizes the load charge distribution of SWCNTs. It is observed that the surface of SWCNTs is almost neutral with a pH $\simeq 6.79$. On the other hand, at pH $<$ pH_{ZPC}, q_{H+} is decreasing from 1.7 to almost zero. In this $q_{H+} = 0$ region, the surface of SWCNTs is positively charged and attractive to anions in solution. Then, attractive electrostatic interaction with anions is predominant on the surface of the adsorbent leading to the competition between H^+ and anions. For pH $>$ pH_{ZPC} , the

surface is negatively charged with greater attraction to cations, because the q_{H^+} becomes negative with its minimum at -1.25. The region corresponding to a basic region where the surface of the adsorbent is negatively charged favoring the attraction or the repulsion of respectively the positive and negative charges from the adsorbates. $-OH$ groups attract or release protons depending on the pH of the solution. The value of pH_{ZPC} [133] which is equal to 6.79 was determined by the graph of Figure 3.1 and Table 3.2 along with data from another work in which SWCNTs were spiked with NO, and COOH molecules shows the values of pH_{ZPC}.

Table 3.2: Zero point loading of SWCNTs compared with other CNTs materials.

Material	SWCNTs	NO-SWCNTs	COOH-SWCNTs
pH_{ZPC}	6.79	7.5	1.2
Ref	This study, [133]	[135]	[135]

Note that the introduction of carboxylic groups in CNTs made them electron acceptors [135], increasing the adsorption of electron donors and decreasing the adsorption of electron acceptors. The difference between the pH_{ZPC} values and those reported by other authors is mainly due to the synthesis preparation and functionalization conditions. For ionizable organic chemicals, variation of pH can lead to a change in chemical speciation, thus changing their adsorption characteristics [135]. Increasing pH generally leads to an increase in ionization, solubility, and hydrophilicity, and thus a decrease in the adsorption of natural organics on CNTs [136,137].

From the results in Figure 3.1, it can be concluded that for pH < 6.79, the surface of SWCNTs is positively charged and the attraction phenomenon with anions is dominant. Likewise, for pH > 6.79 the surface is negatively charged and the attraction phenomenon with cations is dominant [84,138]. Indeed, the more positive the surface charge, the less the surface hydroxyls have the power to capture protons from the solution. Conversely, surface hydroxyls relegate fewer protons to solution in the case of a negatively charged surface. Then, depending on the nature of the charges in the solutions one can get the electrostatic attraction, or ion exchange mecanism which are involved in the adsorption process.

3.2 Morphological characterization of CNTs

3.2.1 Case of SWCNTs

The surface and morphology of the single-walled carbon nanotubes were observed by TEM and SEM. Figures 3.2 and 3.3 show the TEM micrographs of the carbon nanotubes which confirm that they are single-walled type (SWCNTs) and particles on their surface can be observed.
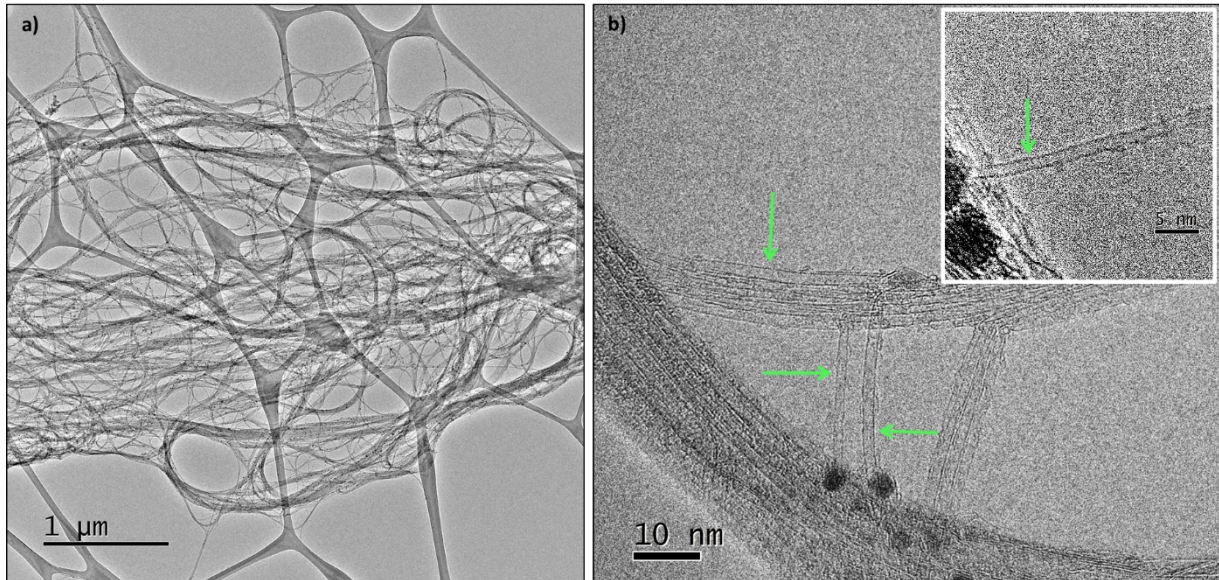
Figure 3.2: TEM micrographs of SWCNTs: (a) the distorted distribution and (b) the single walled carbon nanotubes graph [133].

The samples show rough surfaces and elongated and straight tubular or cylindrical filaments of a few nanometers (1.3 - 1.8 nm), with a distorted distribution. The diameter given by TEM is in good agreement with the value (1.4 nm) given by the supplier. Figure 3.3 (b), shows the spherical particles with a significantly short size (3.0 - 10.0 nm) observed on the tubes. These particles can be attributed to the metal catalyst particles used to synthesize the SWCNTs by the CVD method. In addition, the elemental analysis of the chemical composition of the SWCNTs surface was determined by using energy dispersive spectroscopy (EDS) coupled with TEM. Figure 3 (a) shows the EDS microanalysis in SWCNTs of the region marked by the green square in Figure 3.3 (b). The chemical analysis revealed elements like carbon (89.87 %), followed by oxygen (5.81 %), and in small proportions iron (4.15 %) and sulfur (0.21 %).
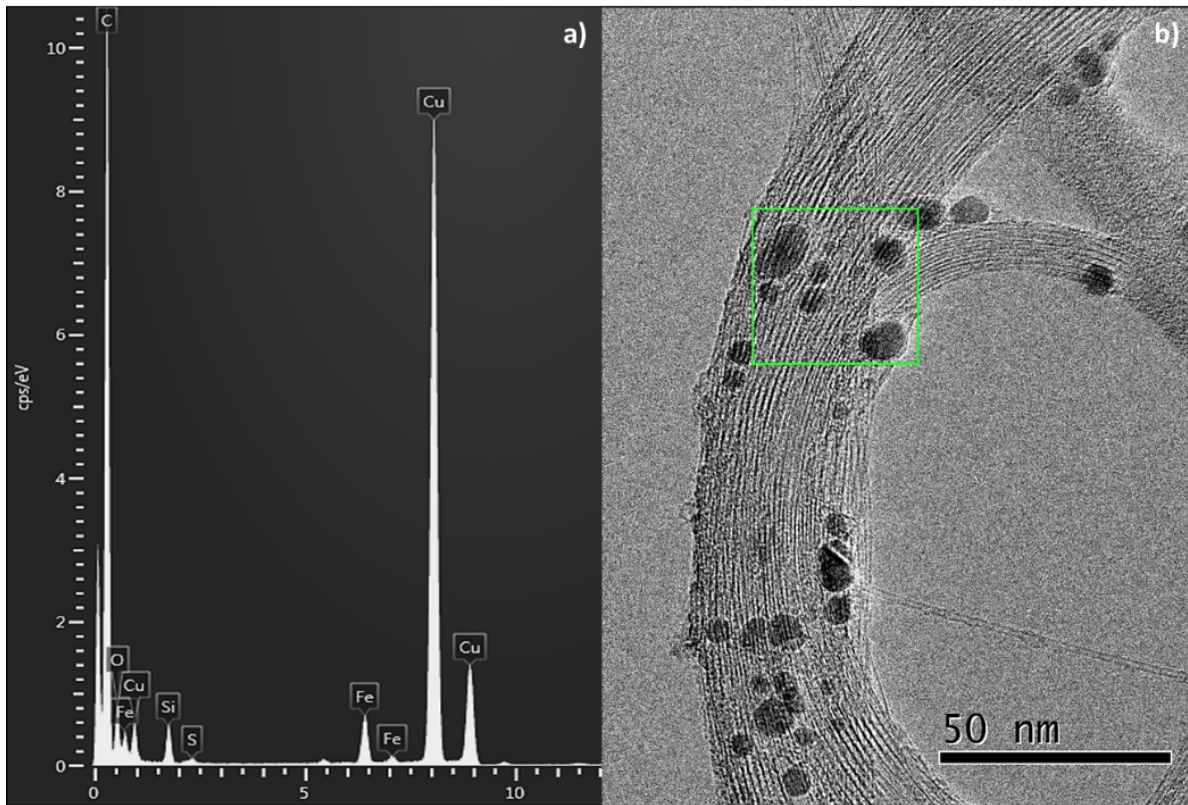
Figure 3.3: (a) EDS microanalysis of the (b) selected region in TEM micrograph of SWCNTs [133].

SEM was performed as well to enrich the SWCNTs surface characterization, Figure 3.4 shows a general area of the sample using Secondary Electrons (SE) and Backscattered electrons (BSE). In Figure 3.4 (a), a random arrangement can be observed as well as the presence of spherical iron particles along the carbon nanotubes. Figure 3.4 (b) was acquired with the BSE detector where one can appreciate the high contrast of the iron particles, denoting a homogeneous iron distribution. We note that, (SE) mode of electrons allows to obtain images giving an account of the shape of the surface and to inform on the size of the grains and agglomerates. It is also an appropriate technique to identify defects such as porosities or cracks even if the information acquired does not reflect the volume extent of the defects under the surface studied. Besides, (BSE) mode of electrons allows to obtain images in chemical contrast. The heavier elements appear bright and the lighter ones dark. This makes it possible to identify the distribution of the various phases in the composite materials but the information on the shape of the surface can be lost.
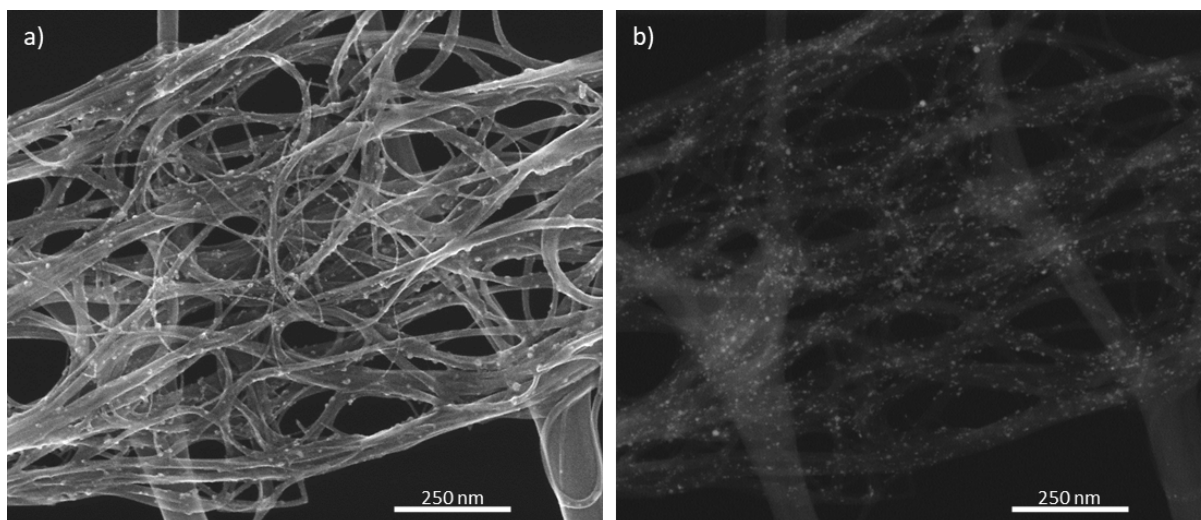
Figure 3.4: SEM micrographs of SWCNTs by (a) SE detector showing morphological details and (b) BSE detector, evidencing Iron homogeneous presence [133].

The microanalysis spectrum of the region marked with the green rectangle of Figure 3.5 allows to determine the composition and distribution of chemical elements in the analyzed sample. According to the chosen mode, it is possible to carry out an elementary analysis on a precise point or on average on a surface, to constitute a profile of concentrations on a given distance or to carry out the elementary cartography of a surface.
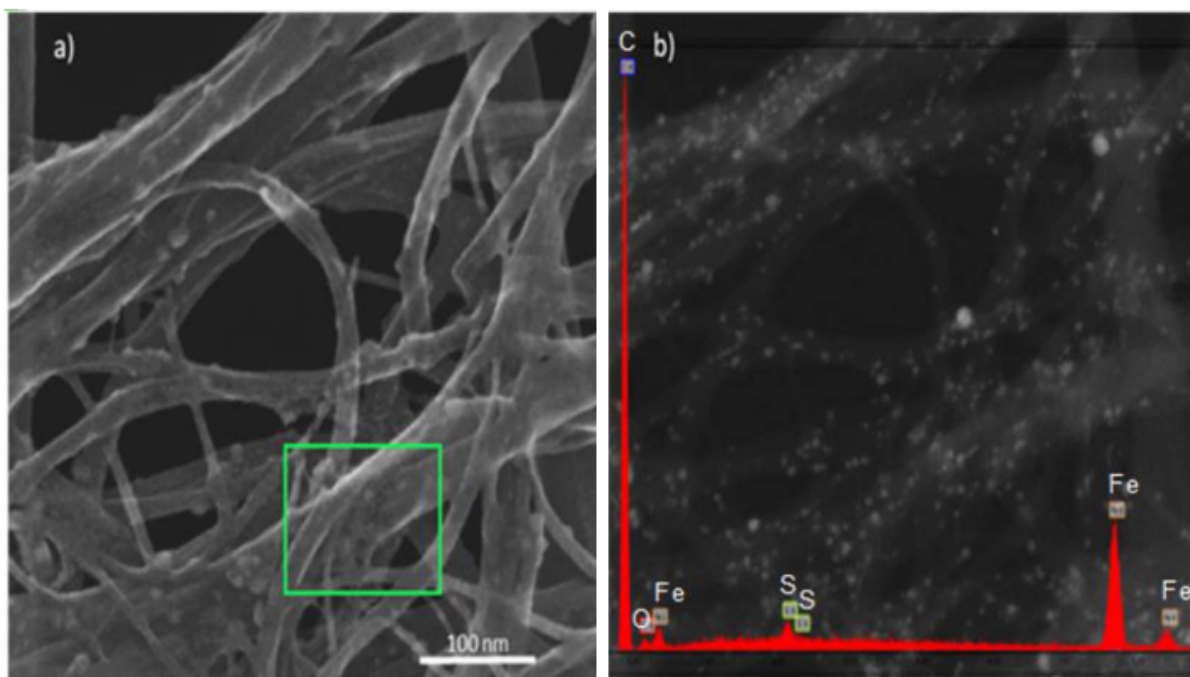
Figure 3.5: SEM micrographs of SWCNTs by (a) SE detector, indicating in the green rectangle the distribution of chemical elements (b) EDS microanalysis of the area and the respective BSE micrograph [133].

The analyses repeated five times revealed the same elements reported previously: Carbon (87.89 %), Oxygen (6.72 %), Iron (5.15 %) and Sulphur (0.24 %), averaged values.

It can be seen that these values have undergone a slight difference compared to those previously observed. This difference varies respectively by: Carbon (1.98 %), Oxygen (0.91 %), Iron (1 %) and Sulphur (0.03 %). This is associated with the choice of the electron modes, in our case the BSE. The presence of copper and silicon is attributed to the secondary signals generated by the grid used to support the sample. The Figures 3.3 (a) and 3.5 (b) show that the intensity of the sulfur peak is relatively too low (almost not visible) in the EDS spectrum due to its very low concentration. This can be explained by the weaker interaction between the wall of SWCNTs with sulfur. Our findings are in agreement with the results of Li *et al.*[139] who reported that, for SWCNTs synthesized by Electric Arc, the Raman spectrum response to the presence of encapsulated sulfur is relatively modest. Thus, to provide the effect of sulfur incorporation on the electronic structure of SWCNTs, Li *et al.*[139] also examined the near-infrared and visible Raman spectra. The (NIR/VIS) results show that, the features due to the interband electronic transition regions of SWCNTs changed little in the NIR/VIS spectrum of SWCNTs synthesized by Electric Arc. Based on the interband electronic transitions, sulfur encapsulation has a large effect on the electronic structure of the SWCNTs. And the observed increase in the SWCNT diameters of about 10 % can be correlated to a change in its geometry [139].

The presence of iron can be justified by the CVD growth method used to produce SW-CNTs. In this method, metal particles such as iron, cobalt, copper, etc. are usually used as catalysts during the synthesis procedure. Thus, some residues may remain on the surface or inside the tubes during the growth of SWCNTs. The electronic properties of CNTs are very sensitive to their environment, in particular to the adsorbed molecules, which cause significant variations in the value of the conduction gap, and therefore in the electrical conductivity. This high sensitivity is therefore advantageous for the development of chemical or biological sensors. It should also be remembered that knowing the composition of the CNTs surface makes it possible to better select the molecules whose electrons/orbitals can interact with those of the CNTs.

3.2.2 Case of MWCNTs

SEM images (Figure 3.6) invariably present a collection of tight and vertical CNTs, evenly distributed on the flat surface of the substrate with varying density, depending on the concentration of ammonia in the gas phase [8]. However, the diameter of the nanotubes is invariably around 20 ± 5 nm. It is essentially dictated by the diameter of the catalytic metal particles which are found at the tops of the tubes (top growth mechanism) whatever the sample.
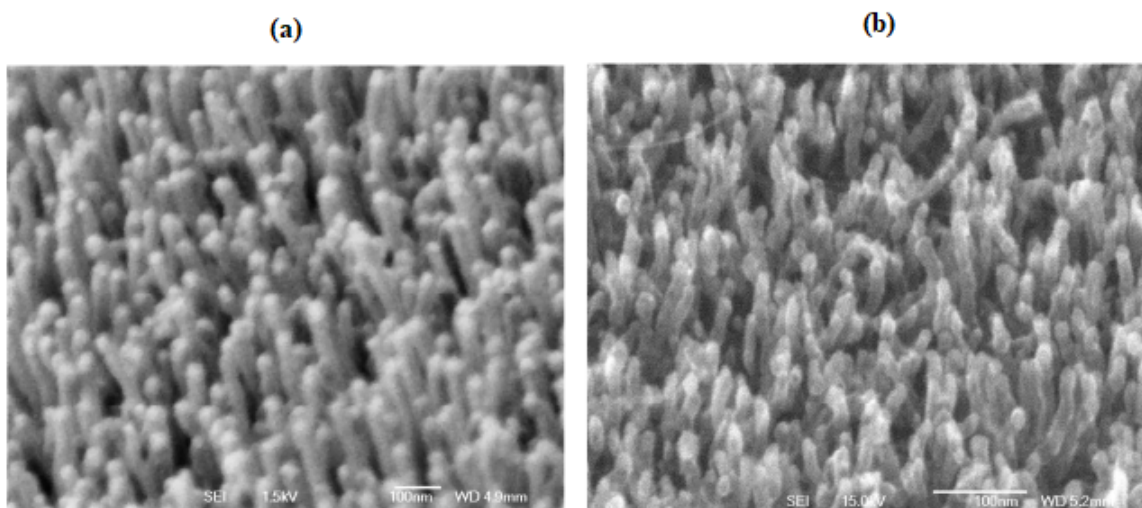
Figure 3.6: SEM images of CNTs: (a) Medium Oriented and (b) Highly Oriented [8].

On the other hand, TEM images present, in addition to an overview, details of isolated nanotubes detached from the substrate by the preparation procedure. Figure 3.7 shows such an isolated CNT, with a needle-shaped Co particle at one end.
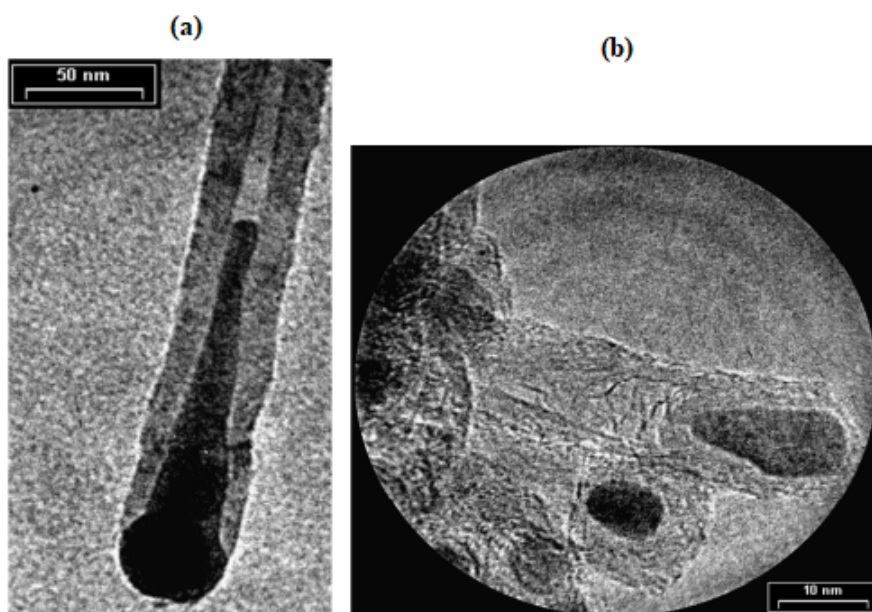
Figure 3.7: TEM images of CNTs: (a) Medium Oriented and (b) Highly Oriented [8].

The metallic particles of Co, whose single-crystal structure has been confirmed by electron diffraction (on selected domains), uniformly exhibit very anisotropic shapes of plug or pinhole type at zero or low ammonia concentration. Images highlight both ends of isolated CNTs and detached from the substrate with the graphite structure for attachment to the substrate on one side, and on the other, the metal particle inserted into the tube. One can however clearly realize that metallic particles of very contrasting shapes are distributed through the nanotube (Figures 3.6 and 3.7). This presence of metallic particles through the CNT, as well

as the anisotropic shape of the particle which is hoisted to the top of the CNTs, was explained by the fusion of the later followed by the pulsed release (clearing) of the fragments of this particle at the top of the CNTs during growth. TEM analyzes also show better crystallization of CNTs and a decrease in the number and size of the internal walls of CNTs with increasing ammonia concentration. This may be correlated to the rate (yield) of growth increasing and supplanting the growth of closed graphene sidewalls. However, the outer diameter (0D) of the nanotubes is mainly dictated by the initial size of the metal particles serving as catalysts.

3.3 Adsorption properties of potassium adsorbed SW-CNTs and functionnal groups

3.3.1 Adsorption properties

The adsorption capacities of the contaminants studied at C_o =100 mgl^{-1}, and 0.01 g of SWCNTs adsorbent at different pH (2, 3, 5, 7, 9, 10, and 11) obtained from three samples we considered were identic and are shown in Figure 3.9. The results revealed that the experiments using potassium as a contaminant lead to a considerable adsorption capacity at the lowest and highest pH taken from the acidic and basic regions. The highest value of 10.35 mgg^{-1} is obtained at pH =2. On the contrary, the adsorption capacity corresponding to neutral region was minimal. These results suggest that SWCNTs have a great capacity to remove potassium in the lower acidic and basic regions. It is worth reminding that the surface is known to be positively charged at pH < pH$_{ZPC}$ [136,137], favoring electrostatic attraction with anions on the adsorbent surface. In contrast, the electrostatic repulsion of anions is dominant at pH > pH$_{ZPC}$, where the adsorbent surface is negatively charged. Potassium in an aqueous solution is a cation (K$^+$) and its adsorption on SWCNTs could have decreased at pH < pH$_{ZPC}$ if the dominant mechanism was the electrostatic attraction; however, the maximum adsorption capacity is obtained at pH = 2. This can be explained by considering that K$^+$ could have exchanged with another cation such as Fe^{2+}, Cu^{2+} on the surface of SWCNTs and the adsorption of cations is accompanied by the release of protons. This means that, in the presence of other cations and anions capable of adsorbing specifically on the surface, the H$^+$ and OH$^-$ species are no longer the only ions determining the charge of the surface of the CNTs.

The EDS analysis shown in Figures 3.3 (a) and 3.5 (b) reveals the presence of Iron (Fe), Copper (Cu) on the surface of SWCNTs. Thus the ion exchange process can be considered as a main adsorption mechanism. According to Yueh *et al.*[141], Fe in carbon nanotubes is exited in the forms of clusters and a thin layer. It can present two kinds of Fe−C bonds. The bonding between the Fe cluster and the C atoms on the tube wall will be more like that of iron carbide with strong chemical bonds. While the bonding between the Fe thin layer and the graphite sheet is more like bonding between two metallic layers. Thus, the Fe cluster should interact strongly with the carbon tube. On the other hand, the increase of

K^+ adsorption capacity at pH > pH_{ZPC} can be attributed to the increase of the negative charges on the surface of SWCNTs. In that region where exist negative charges, the increase of the adsorption capacity can be justified by an electrostatic attraction between K^+ ions and negative charges like S^{2-} ions and carboxylic groups. The introduction of carboxylic groups ($-COOH$) to CNTs made CNTs electron acceptors [135]. Thus, one can conclude that potassium is adsorbed by a double mechanism depending on the region around the pH_{ZPC}. The pH of the solution has a strong effect on the adsorption of potassium on the carbon nanotube. The involved mechanisms are then, the ion exchange (chemisorption) in the acidic region and the electrostatic attraction (physisorption) in the basic region. With increasing pH, the positive charge of the SWCNTs surface decreases, decreasing by this causes the repulsive Coulomb force imposed on the adsorbed cation. In addition, the low concentration of sulfur shown by EDS (Figure 3.5 (b)) can allow us to declare that the ion exchange mechanism is the dominant one since ion concentration was found to be significant compared to sulfur just taken as an example. CNTs, especially SWCNTs, have shown to be more efficient adsorbents with higher adsorption capacity. In addition, CNTs have potential applications in water treatment due to their adsorption characteristics. Previous reports showed that chemical modifications easily affected the atomic and electronic structures of SWCNTs [135].
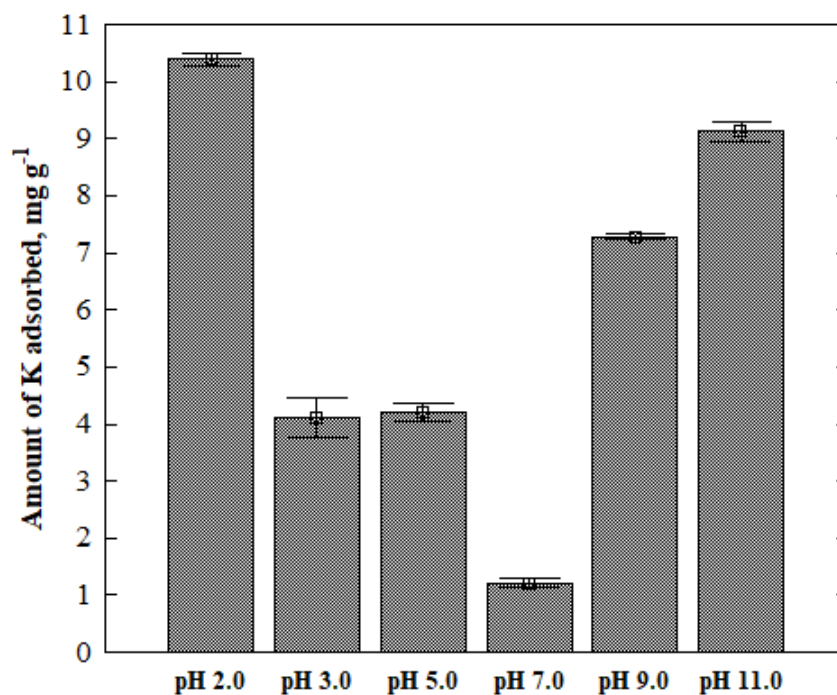
Figure 3.8: Adsorption capacity of SWCNTs for K^+ removal from aqueous solutions [133].

3.3.2 Functional groups

Each carbon atom in a CNT has a π- electron orbital perpendicular to CNT surface along the sidewall.

Therefore, organic molecules containing π electrons can form π-π bonds with CNTs, such as organic molecules with C=C double bonds. The most widely recognized influence of functional groups on CNT interactions is on the electron-donor-acceptor (EDA) π-π interaction, i.e., the strength of π-π bond is greatly dependent on the functional groups attached to the benzene rings for organic chemicals [140]. The identification of the functional groups involved in the adsorption process can be done by FTIR. This technique is a suitable one able to reveal chemical bonds that are present and can interact with isolated particles from aqueous solutions. Figure 3.9 shows the infrared spectra of SWCNTs samples compared to the potassium adsorbed SWCNTs spectra (SWCNTs -K). In these spectra, are distinguished the specific peaks corresponding to the vibrations of the O−H (hydroxy group) which are between the bands 2475 to 2625 cm^{-1} [142]. The Li$^+$ ion solvation structures in the electrolytes were characterized with electrospray ionization mass spectrometry (ESI-MS) [143]. The authors show that the small peaks in the spectra can be attributed to the small amount of impurities with one −OH group instead of H in the solvent molecules. In addition, the peaks of 1980, 2015, 2040, 2175, and 2190 cm^{-1} bands are attributed to C≡C. As well, the peak 1730 cm^{-1} is assigned to the C=O band.
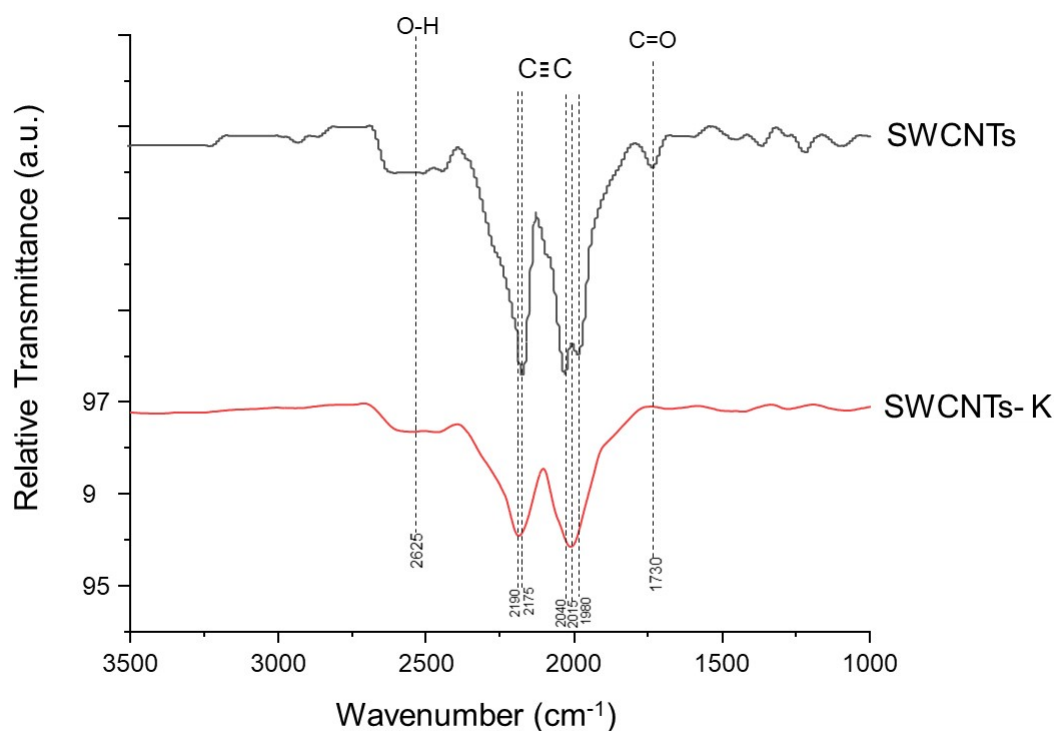
Figure 3.9: Infrared spectrum of SWCNTs and potassium adsorbed SWCNTs [133].

It can be observed that in the adsorbed samples, the bands corresponding to carbonyl group C=O and alkyne group C≡C are attenuated while that of OH− is almost identical. This may suggest that the bands C=O and C≡C are those mostly interfering in the adsorption process. The ex situ $C1s$ XPS spectra of the lithiated and delithiated synthesized by Electric Arc of the pristine indicate the existence of C−C bond, C−O, and isolated carbonyl C=O

bonds [143]. The later two may arise from the impurity of the pristine SWCNTs or impurities introduced during the sulfur encapsulation. During lithiation, both C−O and C=O peaks become much more pronounced [143].

Functional groups also greatly determine organic chemical polarity. Because the predominant mechanisms are different for polar and nonpolar chemicals, predictions of their adsorption on CNTs require different models. For example, for polar organic chemicals, the adsorption tends to increase with increased CNT oxygen content because of the enhanced H-bond or EDA interaction. However, for nonpolar chemicals, the adsorption may decrease with increased CNT oxygen content because of the depressed hydrophobic interaction [135]. For example, if CNTs are to be used in water treatment, chemical-specific modification may be needed to improve treatment performance. For the same reason, chemical-specific models may also be needed to predict organic chemical-CNT interactions [135].

3.4 Adsorption evaluation of potassium adsorbed SW-CNTs by XANES spectroscopy

X-ray absorption spectroscopy (XAS), photoemission spectroscopy, electron energy-loss spectroscopy are all very important methods for characterizing the electronic properties of materials. In particular, XAS, which is a core electron excitation process, provides information not only about the core-electron energy, but also about the unoccupied electronic states in materials. When an x-ray is incident on a material, the x-ray photons excite the core electrons, such as the $1s$ and $2s$ electrons to unoccupied states above the Fermi level. At a certain energy, the absorption increases drastically and gives rise to an absorption edge that occurs when the incident photon energy and the absorption edge energy are both matched to each other to cause the excitation of a $1s$ electron to the unoccupied states. Generally, if an electron is excited from the $1s$ ($2s$) orbital, the process is called K (L)-edge absorption. The XAS technique provides information about the density of states (DOS) of the unoccupied states since the DOS of the $1s$ energy band has a small bandwidth compared with that of the unoccupied electronic band.

3.4.1 Graphite XAS spectra

To ascertain the reliability of the analysis of CNTs XAS spectra, the XAS spectra of HOPG sample is first recorded. Graphite, with its layered structure and large interlayer separation, is often modelled as a two-dimensional solid. In addition, the knowledge of the properties of graphite is a starting point for understanding the structure and properties of many new carbon nanostructures like nanotubes. Using calculations of density of states (DOS), it has been possible to assign the features of the C(K) absorption spectrum (XAS) to specific states of the Brillouin zone in the theoretical band structure of graphite, Figure 3.10.
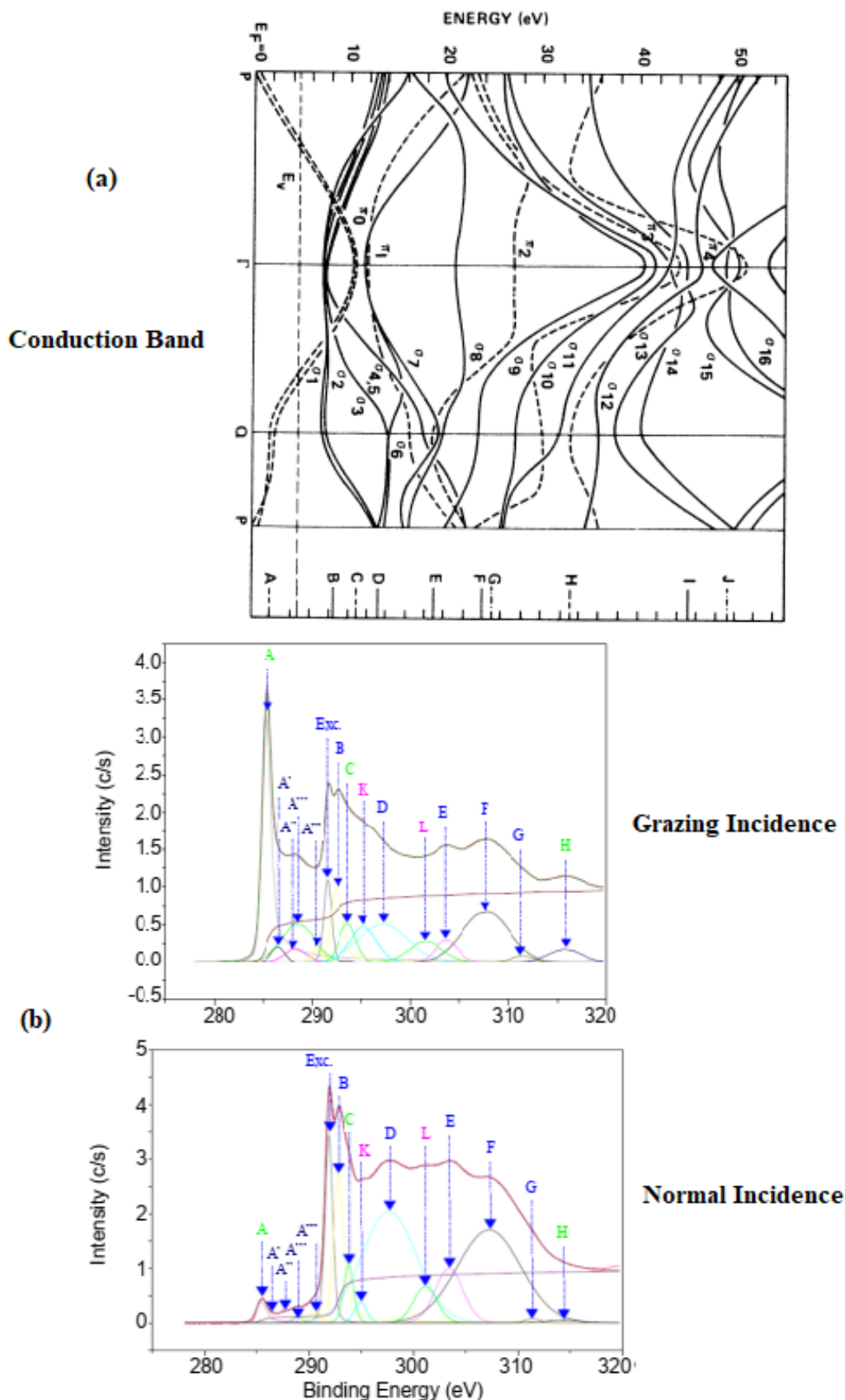
Figure 3.10: (a) Theoretical band structure of graphite obtained from density of states (DOS) calculations and (b) XAS (carbon K-edge) of HOPG at grazing (GI) and normal (NI) incidences, respectively. HOPG was preliminary in situ treated at 500 °C [47].

The two-dimensional nature of graphite results in a strong directionality of the orbitals: σ- orbitals lie within the basal plane, while π- orbitals are directed perpendicular to this basal plane along the C axis. By tuning the incidence angle of the polarized synchrotron light on the sample α, it is possible to excite final states of specific symmetry at the carbon K-edge. According to the Fermi gold rule and the dipole selection rules, when the electric field vector $\vec{E}$ lies within the basal plane (i.e. perpendicular to the $\vec{C}$ axis ($\vec{E} \perp \vec{C}$), then σ^* final states are selected. When the $\vec{E}$ vector is perpendicular to the plane (i.e. parallel to the $\vec{C}$ axis ($\vec{E} \parallel \vec{C}$), then final states of π- symmetry are excited. Thus the intensity of each transition will strongly depend on the angle α between the electric field vector $\vec{E}$ and the $\vec{C}$ axis.

Moreover, by monitoring the angular dependence of the spectral features of the carbon K-edge, the symmetries of the final states were determined. This model allowed us to assign all the spectra of carbon nanotube this work. The features of the XAS spectra are analyzed with regard to the more probable energy level of the UDOS states given on the bottom of the band diagram. The features of the XAS spectra are analyzed with regard to the more probable energy level of the UDOS states given on the bottom of the band diagram. Nevertheless it is clear that the full absorption spectra can be divided into three regions. At 285.5 eV the peak named A corresponds to the transition towards unoccupied π_0 states near Q in the Brillouin zone at 2 eV above the Fermi level and strongly dependent on the incident angle. The vacuum level is indicated by a dashed line. The second region namaled A', A", A"', A"" within 286.5 - 292.5 eV corresponds to the free electron like interlayer states and adsorbed or chemisorbed molecular states. They are strongly dependent on the chemical treatment of the sample. In this energy range the contributions of $1s \longrightarrow \pi^*$ and $1s \longrightarrow \sigma^*$ transitions are due to adsorbed functionalized states such as C-O-, C-H, C=O, C-OH,... The XAS spectra exhibit a σ^* exciton at 291.6 eV corresponding to a C-H* bond resonance. Moreover the small shoulder at 286 - 287 eV may also be attributed to a singularity in the DOS of graphite. The third region above 277.54 eV corresponds to the transitions to empty σ^* symmetry states and π^* symmetry states.

3.4.2 Case of non adsorbed SWCNTs

The full absorption spectra of SWCNT (Figure 3.10) can be divided into three regions. The first region located at 265.94 eV with the peak named A is attributed to the transition to the empty π^* band states, consistent with the final π_0 band states in the vicinity of Q. The second region located between 269.69 eV and 271.34 eV corresponds to the interlayer states of almost free electrons and adsorbed molecular states, and named A', A", commonly encountered in graphite spectra [85]. These states are deeply dependent on the chemical treatment of the sample. The contributions of the transitions are due to the existence of the functional groups such as C−OH, C−O, C−H..., which result from the adsorption of the molecules such as H_2O, CO_2, CO or hydrocarbons [85].
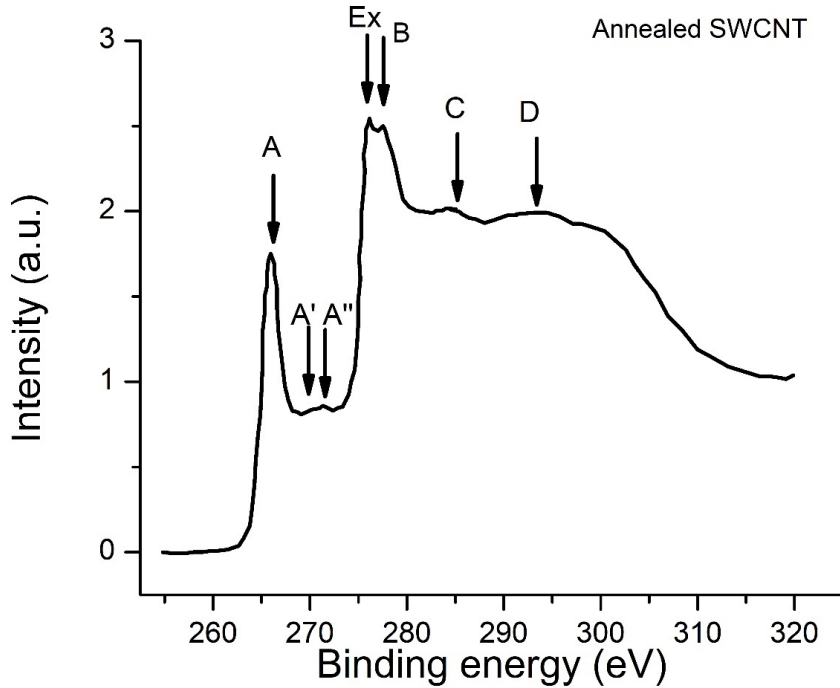
Figure 3.11: Experimental XANES spectrum of annealed and non adsorbed SWCNTs [133].

The third region above 277.54 eV corresponds to the transitions to empty σ^* symmetry states and π^* symmetry states. The features corresponding to C and D respectively at 284,43 eV and 293.05 eV were associated with σ-symmetry while Ex. at 276.14 eV was correlated to σ^* exciton (C$-$H* bond resonance). The large feature D has been assigned to the superposition of multiple-scattering resonances. The energies and assignments of the main peaks in the carbon K-edge of annealed non adsorbed SWCNTs are summarized in table 3.3.

Table 3.3: XANES adsorbates parameters of annealed and non adsorbed SWCNTs [133].

Peaks	BE (eV)	Intensity (c/s)	Final-states band and Brillouin-zone
Adsorbates			
A'	269.69	0.82	π^*C=C$-$OH / $-$(C=C$-\pi^*$C=O)
A"	271.34	0.86	π^*C=O
Non adsorbates			
A	265.94	1.75	π_0 near Q
EX	276.14	2.54	Exciton
B	277.54	2.50	$\sigma_1, \sigma_2 : \Gamma \rightarrow Q$
C	284.43	2.01	π_0 or π_1 near Γ
D	293.05	1.99	/

The effect of the gaseous environment on the electronic properties of CNTs has recently attracted a lot of attention [138,139]. Because the adsorption of molecules constitutes another type of doping of CNTs it can be reminding that the identified intrinsic adsorbates

H_2O, O_2, CO_2, CO are impurities specific to the surface of the CNTs [68]. Most molecules adsorb weakly on SWCNTs and can be either charge donors or acceptors [141]. Charge donor molecules (H_2O, CO_2) interaction between the nanotubes is weak and does not have a significant influence on the electronic structures of SWCNTs [141]. Santucci *et al.*[144] have proven both by theoretical and experimental methods that CO adsorbs weakly on the tube wall with essentially no charge transfer between the tube and molecule. Moreover, Sankar *et al.*[145] performed first-principle density functional theory (DFT) studies on the adsorption of gas molecules on (10,0) SWCNT. Their results showed that for the adsorbed molecules (H_2O and CO), no charge transfer exists between the tube and molecule. The adsorbate A' in Figure 3.10 corresponds to the final states $\pi^*C= C-OH$ or $-(C = C-\pi^*C=O)$ and is due to water molecules. It is not also sensitive enough to the thermal treatment suggesting the negligible charge transfer between the surface of CNTs and water molecules. The charge transfer is not negligible for O_2 and NO_2 which are both charge acceptors [141].

The bond length of $C-C$ after adsorption of oxygen molecule on the external surface of nanotube increases since oxygen is more electronegative than carbon [146]. The interaction between O_2 molecules and SWCNT is much more pronounced, and SWCNT can be turned into a $p-$type conductor after NO_2 or O_2 adsorption [141] as it can be observed for the adsorbate A" ($\pi^*C=O$) affected mainly by thermal annealing. This suggests that the curvature affects the physical, electronic, and chemical properties of the CNTs and has a significant effect on the desorption process [141]. It is revealed that the contribution of gas molecules is 23.7 % in SWCNTs. This observation can be assigned to the electronic behavior of gas molecules and especially to the strong interaction of O_2 with the surface of CNTs. This can be correlated with some results, including nuclear magnetic resonance (NMR), which proved the increase of density of states at the Fermi level of SWCNTs after exposure to oxygen [145]. More to that, Collins *et al.*[146] found that oxygen gas has dramatic effects on conductivity. The FTIR also showed that the functional groups at the surface of SWCNTs are principally $OH-$, $C=O$ and $C\equiv C$.

3.4.3   Case of Potassium adsorbed SWCNTs

We note the presence of peaks named P' and P" resulting from the potassium adsorbed on SWCNT. Compared to our previous results [8,147], we note that the peaks A"', A"" and P are not observed in our present spectra (Figure 3.11 and 3.12) due to their extremely low resolution. Thus, we will focus only on the visible peaks in the following. And in agreement with our previous works [8], the two dominant peaks near 266.02 eV (A) and 277.61 eV (B) were associated with an unoccupied π^* and σ^* band, respectively. Similar dominant peaks (A) and (B) are observed in the work of Zhong *et al.*[147] on a SWCNT treated with the LiOH water. After a fitting process of their data (using the Igor package), they obtained two other picks like A' and A" of the present work. According to the reported XANES data, the first one A' has been assigned to π^* ($C-OH$) and the second one A" to $\pi^*(C=O)$.

Zhong *et al.*[147] have also found a third peak attributed to $\sigma^*(C-O)$ when the SWCNT material was treated by immersion in a 1 M LiOH water solution at pH = 12 for five days. Of all the above, the appearance of the peaks A' and A'' clearly demonstrates the involvement of functional groups in the adsorption process; which will affect the atomic and electronic structures of SWCNTs. The enhancement of A'' peak indicates the possible oxidation which is also consistent with the XANES result. Let us stress that the heat exchange through the annealed process has been shown to cause changes in the binding energy and the intensity of the adsorbates. The shift of the peak indicates the weakening of Van der Waals interaction between the potassium and the wall of the SWCNTs.
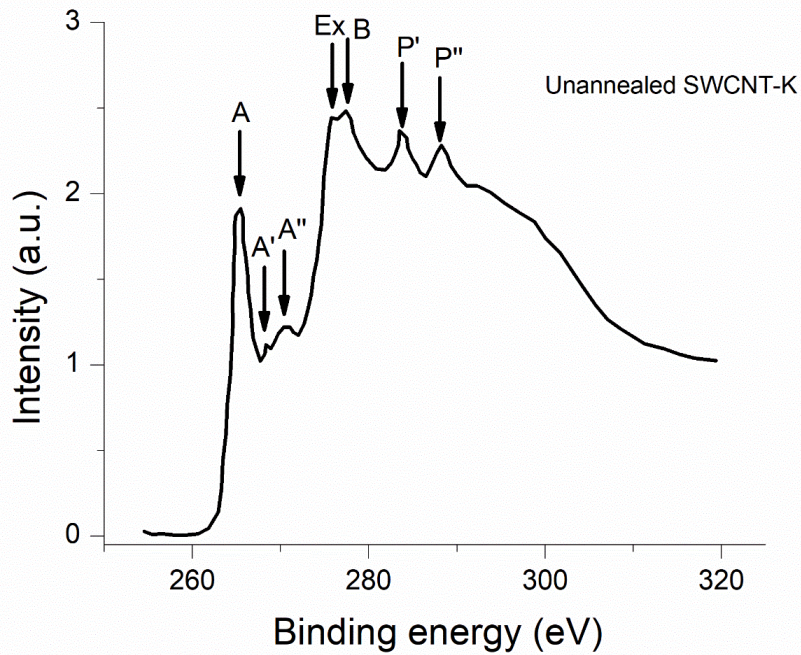
Figure 3.12: Experimental XANES spectrum of unannealed and potassium adsorbed SW-CNTs [133].

Table 3.4: XANES adsorbates parameters of unannealed and potassium adsorbed SWCNTs [133].

Peaks	BE (eV)	Intensity (c/s)	Final-states band and Brillouin-zone
Adsorbates			
A'	268.36	1.12	$\pi^*C=C-OH$ / $-(C=C-\pi^*C=O)$
A''	270.37	1.22	$\pi^*C=O$
P'	283.48	2.37	Potassium L_2-L_1
P''	288.21	2.28	Potassium L_2
Non adsorbates			
A	265.45	1.91	π_0 near Q
EX	275.79	2.44	Exciton
B	277.40	2.48	$\sigma_1, \sigma_2 : \Gamma \to Q$

The energies and assignments of the main peaks in the carbon K-edge of both cases of unannealed and annealed SWCNTs with potassium adsorbed are summarized in tables 3.4 and 3.5. It is observed that the intensities of different adsorbates are higher for the annealed samples suggesting that the thermal treatment can affect the adsorbates whatever their origin. For annealed samples, the disappearance of peak A' and the resolution of peak A" can be noticed. The increase in the peaks P' and P" can also be seen. However, no change is seen in the shape of the peaks P' and P". These results showed that in the SWCNTs, the intrinsic adsorbates are less sensitive than the extrinsic adsorbates. Thus, the hybridization of the nanotubes can be affected. Concerning the non adsorbed (Figure 3.10 and table 3.3) and the adsorbed annealed samples (Figure 3.11 and table 3.5), one can observe that the labeled main peaks in the spectrum of the latter are better resolved. Peak A' is sharper and peak A" is more intense in the adsorbed annealed samples (Figure 3.11). The two intense peaks P' and P" which are due to potassium are in the position of peaks C and D in the non adsorbed spectrum. The adsorption process has brought a great change in the spectrum suggesting that the electronic properties of the samples as well as the hybridization, can be modified by means of adsorption or doping. They can vary depending on the nature and the type of adsorbates utilized to remove the pollutants when using SWCNTs. Our results also show that the conductivity of the SWCNTs is first modified and then improved by 75 %. After thermal annealing, 41 % of gas molecules are still adsorbed against 75 % of potassium. In addition, for 75 % of the potassium adsorbates on the surface of SWCNTs, the contribution of the adsorbates gas molecules increases by 17.3 %.
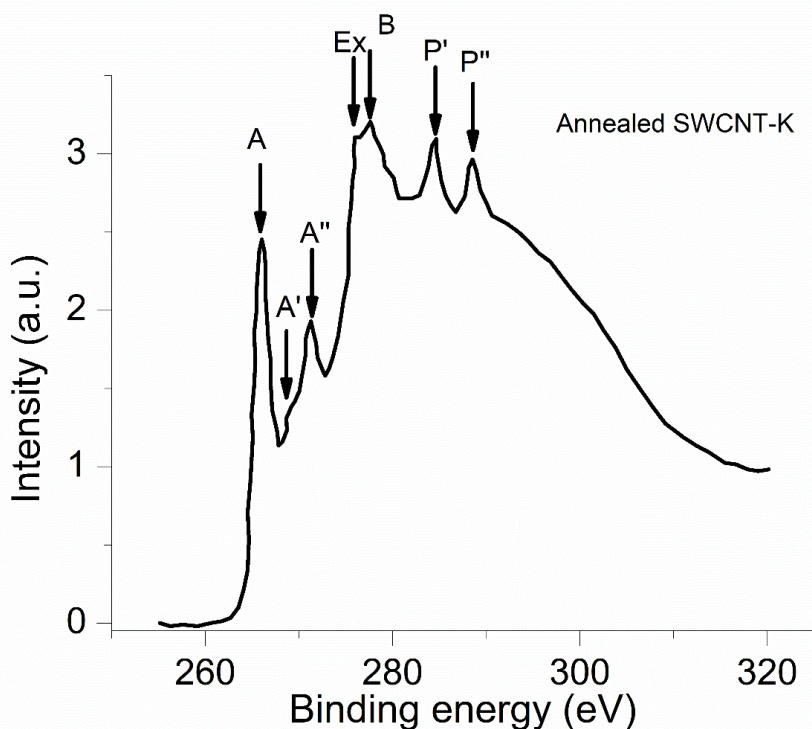
Figure 3.13: Experimental XANES spectra of annealed and potassium adsorbed SWCNTs [133].

Thus, the performance of SWCNTs depends on a better understanding of the functionalities at the CNTs surface. The tube molecules interaction may substantially affect the carbon nanotubes and lead to the applications like chemical sensors. Intensities of adsorbates are directly correlated to carbon hybridization since the reactivity is connected to the diameter and type of hybridization in CNTs. It is seen that the values of the binding energy change from unannealed to annealed samples due to the thermal annealing treatment. The intensities of all adsorbates are increasing from unannealed to annealed samples in SWCNTs. These results suggest that the binding energy, as well as the intensity of the intrinsic adsorbates, strongly depend on the diameter (curvature) of the CNTs. It can be understood that the adsorbates bonding can be affected by the thermal annealing process. They can either be shrunk or lengthened depending on the degree of thermal treatment. This could somehow affect the hybridization of the CNTs. Indeed, the great chemical reactivity of the SWCNTs is the consequence of the external arrangement of the pyramidized carbon atoms sp^2 arranged correctly for the formation of chemical bonds with the reactive species.

Table 3.5: XANES adsorbates parameters of annealed and potassium adsorbed SWCNTs [133].

Peaks	BE (eV)	Intensity (c/s)	Final-states band and Brillouin-zone
Adsorbates			
A'	268.64	1.31	π^*C=C$-$OH / $-($C=C$-\pi^*$C=O$)$
A"	271.26	1.93	π^*C=O
P'	283.66	3.09	Potassium L_2-L_1
P"	288.52	2.97	Potassium L_2
Non adsorbates			
A	266.02	2.45	π_0 near Q
EX	275.93	3.11	Exciton
B	277.61	3.21	$\sigma_1, \sigma_2 : \Gamma \to Q$

Thus, CNTs having large curvature require less geometric deformation and hybridization change to accept an adsorbate. In addition, the effects of heat exchange have been shown to cause changes in the binding energy and the intensity of the adsorbates. As shown earlier, the adsorbates are more sensitive in SWCNTs. The intensity of adsorbates A' corresponding to the final states π*C=O is strongly affected in SWCNTs by thermal annealing treatment, as well as that of peaks P' and P" which are assigned to the final potassium states L_2 - L_1 and L_2. This suggests that the height of these adsorbates can be considerably reduced by heat treatment. This can be explained since it is known that one of the main objectives of thermal annealing is to minimize impurities. Other adsorbates are less sensitive to thermal treatment. All adsorbates are affected differently by interaction with each CNT's surface, creating a different environment that can alter molecular reactivity. These results show that the adsorbates are influenced by thermal annealing leading to the changes in the curvature and hybridization in SWCNTs nanomaterials.

3.5 Adsorption evaluation of MWCNTs by XANES spectroscopy

Using density of states (DOS) calculations, it has been made possible to attribute the K-edge absorption structures of carbon in XAS to specific Brillioun zone states in the theoretical band structure of graphite [148]. The XANES reveals that the electronic transitions in the carbon atoms of CNTs are similar to that of the carbon atoms in graphite [148]. Figures 3.16 to 3.21 show XANES spectra and tables 3.8 to 3.13 give final-states band and Brillouin-zones of MWCNTs. In this case, all XANES spectra of MWCNTs can also be divided into three regions as for the SWCNTs. The structural properties are almost similar for the first two regions. The third region above 291.8 eV corresponds to the transitions to empty σ^* symmetry states and π^* symmetry states. These peaks are localized in B, E, C, H, K, and L. In the present case, our MWCNTs were not contaminated with potassium. So adsorption takes place only by non-intrinsic contaminants named A', A", A"', A"". It is observed that the adsorbates A"' and A"" are not detectable or do not exist, because they have no chemical bonds present on the surface. We can say that these adsorption sites do not interact with the surface and therefore their absence contributes to increasing the level of the material purity. This can be also explained by the fact that thermal annealing favors the total desorption of these peaks.
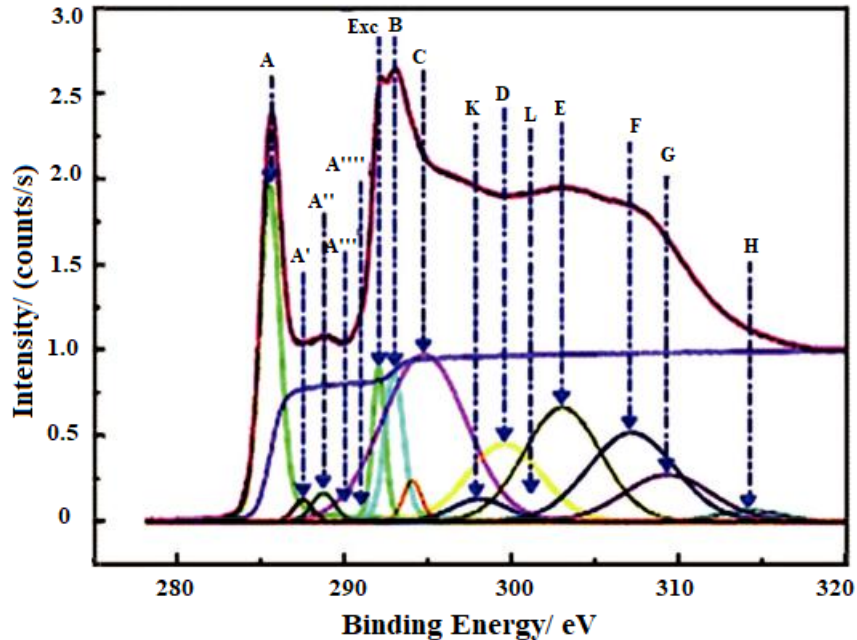
Figure 3.14: Experimental (red) and calculated (blue) spectra of annealed and uncontaminated MWCNTs at normal incidence [27].
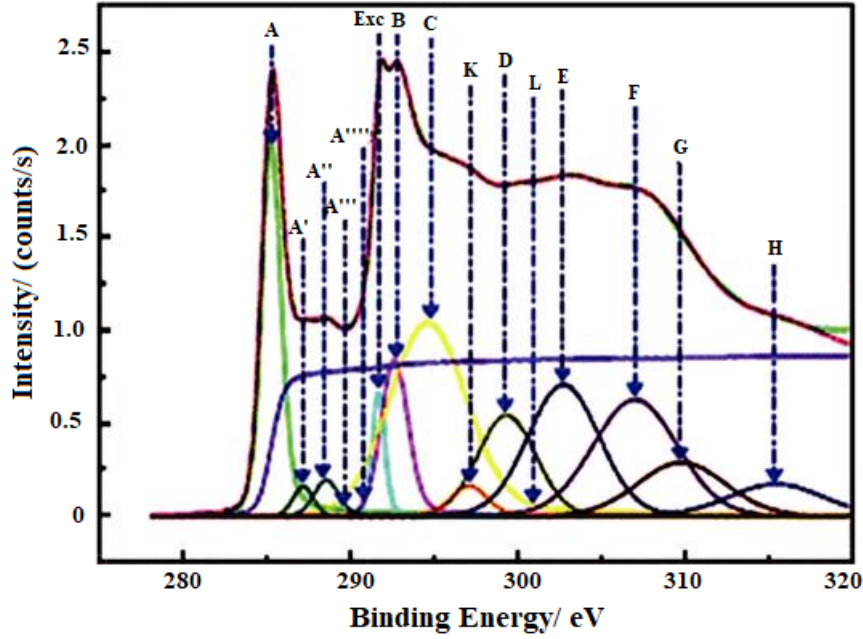
Figure 3.15: Experimental (red) and calculated (blue) spectra of annealed and uncontaminated MWCNTs at grazing incidence [27].

Table 3.6: XANES adsorbates parameters of annealed and uncontaminated MWCNTs at normal incidence values from Fig 3.13 [27].

Peaks	BE /(eV)	Intensity (c/s)	Final-states band and Brillouin-zone
Adsorbates			
A'	287.54	0.19	Free-electron + interlayer states+adsorption
A"	288.65	0.30	Free-electron + interlayer states+adsorption
A"'	/	/	Free-electron + interlayer states+adsorption
A""	/	/	Free-electron + interlayer states+adsorption
Non Adsorbates			
A	285.43	3.44	π_0 near Q
C-H Exc.	291.96	0.92	Exciton
B	292.86	1.40	$\sigma_1, \sigma_2 : \Gamma \rightarrow Q$
C	294.68	6.20	π_0 or π_1 near Γ
D	299.10	0.55	$\sigma_3 - \sigma_6 : Q \rightarrow P$
E	302.95	3.88	σ_7 near Q
F	307.10	3.40	σ_9 near Q
G	309.25	1.80	π_4 near Q
H	314.20	0.30	/
K	297.05	0.00	π_0 or π_1 near Γ
L	299.50	2.54	$\sigma_6 - \sigma_7$: near Q

In Figures 3.15 and 3.16 we observed that, adsorbates A"' and A"" only appear when potassium is adsorbed. This suggests that these adsorbates are the results of interactions between the functional groups present on the surface and potassium. This is true for the two incidences. Here our samples are also annealed and contain not only intrinsic contaminants

but also potassium contaminants. The total disappearance of the adsorbates A"' and P"
is observed in the two incidences, (tables 3.8 and 3.9). This suggests that they are more
sensitive to thermal annealing.

Table 3.7: XANES adsorbates parameters of annealed and uncontaminated MWCNTs at
grazing incidence values from Fig 3.14 [27].

Peaks	BE (eV)	Intensity (c/s)	Final-states band and Brillouin-zone
Adsorbates			
A'	287.14	0.24	Free-electron + interlayer states+adsorption
A"	288.50	0.40	Free-electron + interlayer states+adsorption
A"'	/	/	Free-electron + interlayer states+adsorption
A""	/	/	Free-electron + interlayer states+adsorption
Non adsorbates			
A	285.20	3.55	π_0 near Q
C-H Exc.	291.65	0.68	Exciton
B	292.57	1.93	$\sigma_1, \sigma_2 : \Gamma \to Q$
C	294.50	6.54	π_0 or π_1 near Γ
D	297.06	0.45	$\sigma_3 - \sigma_6 : Q \to P$
E	302.70	3.83	σ_7 near Q
F	306.97	4.00	σ_9 near Q
G	309.75	1.90	/
H	315.40	1.20	π_4 near Q
K	297.05	0.00	π_0 or π_1 near Γ
L	299.30	2.40	$\sigma_6 - \sigma_7 :$ near Q
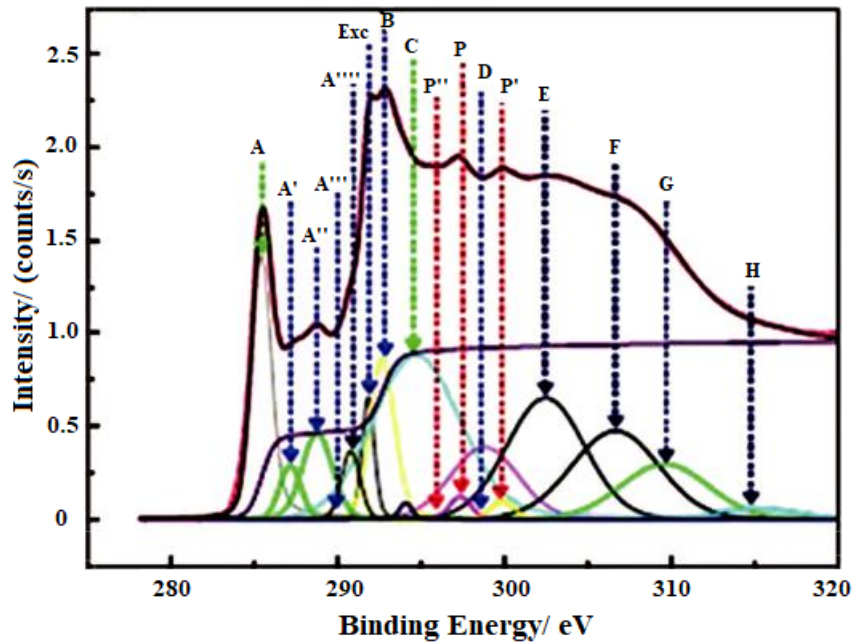
Figure 3.16: Experimental (red) and calculated (blue) spectra of annealed and contaminated
MWCNTs at normal incidence [27].
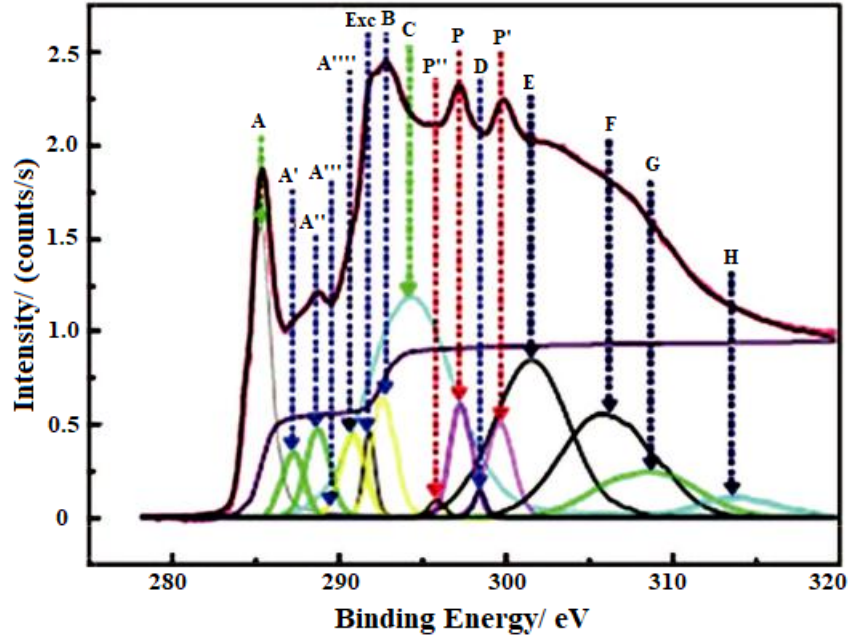
Figure 3.17: Experimental (red) and calculated (blue) spectra of annealed and contaminated MWCNTs at grazing incidence [27].

Table 3.8: XANES adsorbates parameters of annealed and contaminated MWCNTs at normal incidence values from Fig 3.15 [27].

Peaks	BE /(eV)	Intensity (c/s)	Final-states band and Brillouin-zone
Adsorbates			
A'	287.10	0.46	Free-electron-like-interlayer states+adsorption
A"	288.72	1.10	Free-electron-like-interlayer states+adsorption
A'''	289.94	0.0	Free-electron-like-interlayer states+adsorption
A''''	290.72	0.52	Free-electron-like-interlayer states+adsorption
P"	297.51	0.0	Potassium L_2 level
P	297.30	0.19	Potassium L_2, L_3 level
P'	299.81	0.17	Potassium $L_2 - L_1$ levels
Non adsorbates			
A	285.35	2.56	π_0 near Q
C-H Exc.	291.77	0.67	Exciton
B	292.60	1.82	$\sigma_1, \sigma_2 : \Gamma \to Q$
C	294.55	6.23	π_0 or π_1 near Γ
D	298.75	2.00	/
E	301.42	3.86	σ_7 near Q
F	306.60	3.15	σ_9 near Q
G	309.55	1.97	/
H	315.20	0.33	π_4 near Q
I	329.00	/	/
J	333.00	/	/

Table 3.9: XANES adsorbates parameters of annealed and contaminated MWCNTs at grazing incidence values from Fig 3.16 [27].

Peaks	BE (eV)	Intensity (c/s)	Final-states band and Brillouin-zone
Adsorbates			
A'	287.10	0.46	Free-electron-like-interlayer states+adsorption
A''	288.72	1.02	Free-electron-like-interlayer states+adsorption
A'''	289.94	0.0	Free-electron-like-interlayer states+adsorption
A''''	290.72	0.63	Free-electron-like-interlayer states+adsorption
P''	297.51	0.0	Potassium L_2 level
P	297.30	0.17	Potassium L_2, L_3 level
P'	299.81	0.20	Potassium $L_2 - L_1$ levels
Non adsorbates			
A	285.35	2.56	π_0 near Q
C-H Exc.	291.77	0.674	Exciton
B	292.60	1.82	$\sigma_1, \sigma_2 : \Gamma \rightarrow Q$
C	294.55	6.40	π_0 or π_1 near Γ
D	298.75	2.00	/
E	301.42	3.88	σ_7 near Q
F	306.60	3.26	σ_9 near Q
G	309.55	2.00	/
H	315.20	0.50	π_4 near Q
I	329.00	/	/
J	333.00	/	/
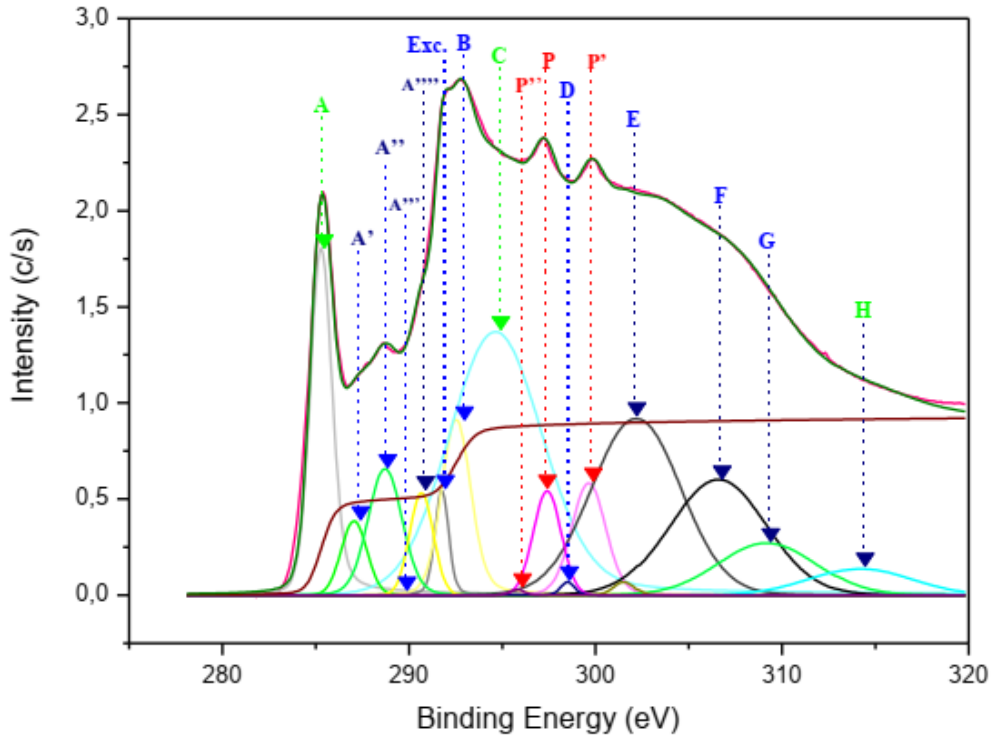
Figure 3.18: Experimental (red) and calculated (blue) spectra of unannealed and contaminated MWCNTs at normal incidence [27].
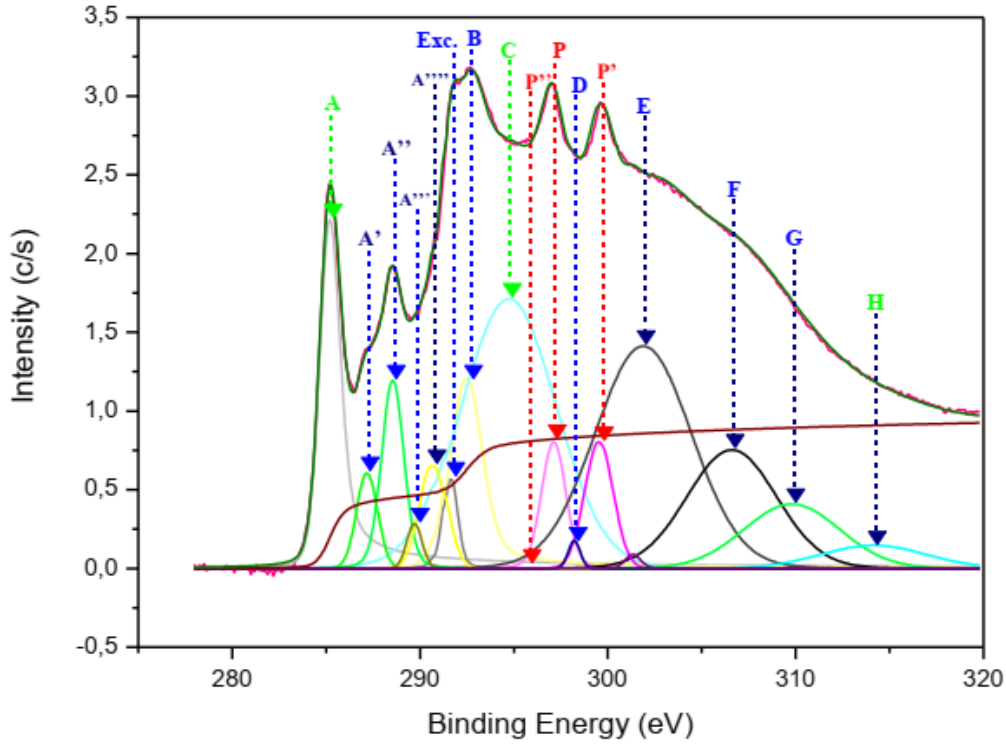
Figure 3.19: Experimental (red) and calculated (blue) spectra of unannealed and contaminated MWCNTs at grazing incidence [27].

Table 3.10: XANES adsorbates parameters of unannealed and contaminated MWCNTs at normal incidence values from Fig 3.17 [27].

Peaks	BE /(eV)	Intensity (c/s)	Final-states band and Brillouin-zone
Adsorbates			
A'	287.10	0.67	Free-electron-like-interlayer states+adsorption
A''	288.77	1.57	Free-electron-like-interlayer states+adsorption
A'''	289.94	0.0	Free-electron-like-interlayer states+adsorption
A''''	290.33	0.85	Free-electron-like-interlayer states+adsorption
P''	297.90	0.03	Potassium L_2 level
P	297.40	1.02	Potassium L_2, L_3 level
P'	299.76	1.39	Potassium $L_2 - L_1$ levels
Non adsorbates			
A	285.35	3.18	π_0 near Q
C-H Exc.	291.82	0.56	Exciton
B	292.57	2.05	$\sigma_1, \sigma_2 : \Gamma \to Q$
C	294.62	9.30	π_0 or π_1 near Γ
D	298.60	1.39	/
E	302.25	5.50	σ_7 near Q
F	306.63	3.93	σ_9 near Q
G	309.22	1.80	/
H	314.20	0.95	π_4 near Q
I	329.00	/	/
J	333.00	/	/

Table 3.11: XANES adsorbates parameters of unannealed and contaminated MWCNTs at grazing incidence values from Fig 3.18 [27].

Peaks	BE (eV)	Intensity (c/s)	Final-states band and Brillouin-zone
Adsorbates			
A'	287.10	0.86	Free-electron-like-interlayer states+adsorption
A''	288.77	1.90	Free-electron-like-interlayer states+adsorption
A'''	289.94	0.29	Free-electron-like-interlayer states+adsorption
A''''	290.33	1.10	Free-electron-like-interlayer states+adsorption
P''	297.90	0.03	Potassium L_2 level
P	297.40	1.39	Potassium L_2, L_3 level
P'	299.76	1.55	Potassium $L_2 - L_1$ levels
Non adsorbates			
A	285.35	5.56	π_0 near Q
C-H Exc.	291.82	0.58	Exciton
B	292.57	3.73	$\sigma_1, \sigma_2 : \Gamma \rightarrow Q$
C	294.62	11.00	π_0 or π_1 near Γ
D	298.60	0.14	/
E	302.25	9.30	σ_7 near Q
F	306.63	4.60	σ_9 near Q
G	309.22	2.67	/
H	314.20	1.05	π_4 near Q
I	329.00	/	/
J	333.00	/	/

We observed for both incidences angles corresponding to our annealed and unannealed contaminated samples that, finals states and bands in the Brillouin zones are identical. This suggests that thermal annealing does not destroy the structural properties of our samples, but improves its degree of graphitisation. Each adsorbate corresponds to a specific electronic transition that is assigned to peaks A', A'', A''', and A'''' or P, P'and P''. These peaks are strongly related to the height of the adsorbates. In addition, the probability of a chemical species to be adsorbed depends on the nature of the surface. The types of bonds and associated physical properties depend considerably on the types of atoms adsorbed [149]. The amount of adsorbates on the surface varies with the radius of curvature of the CNTs since adsorption depends strongly on the specific surface area [150]. Our samples show significant differences on intensities of all adsorbates at normal and grazing incidence angles. During the adsorption process, a rehybridization can occur in which the sp^2 and sp^3 orbitals are mixed, leading to two free hybrid orbitals. So that, if the contribution of sp^3 increases, this will lead to the presence of more free bonds, resulting in the increase of reactivity. Figure 3.19 shows a comparison of the intensities of unannealed and annealed contaminated MWCNTs for different adsorbates at normal and grazing incidence angles, respectively.
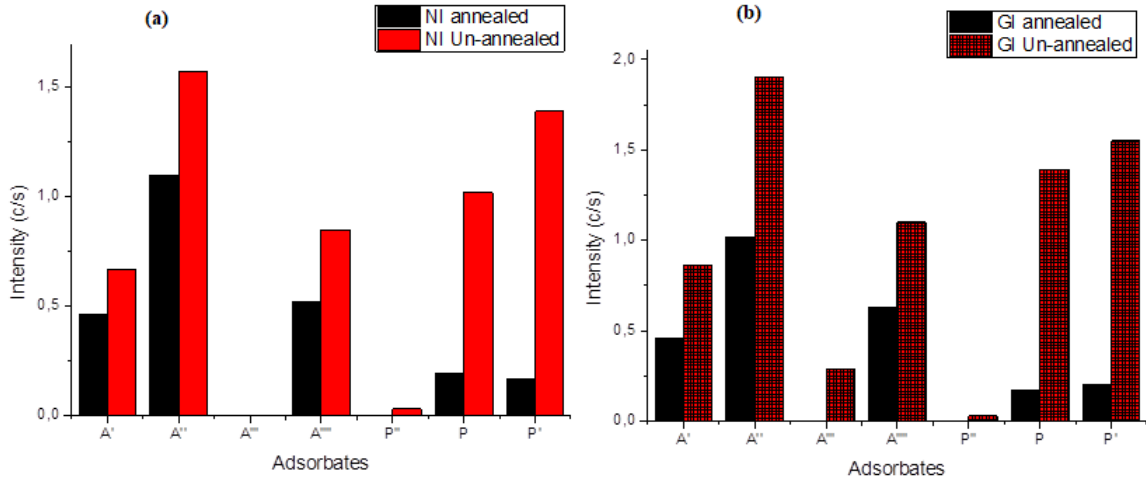
Figure 3.20: The trend of adsorbate intensities for unannealed and annealed contaminated MWCNTs in both incidences.

Comparison of the intensities of annealed and non-annealed contaminated MWCNTs shows that in both studied angles, the amount of all adsorbates decreases significantly after the thermal annealing process. However, it is shown that when potassium is adsorbed at 12 %, the intrinsic adsorbates increase by 2.12 and 1.64 times at normal and grazing incidence angles, respectively. At normal incidence, the electric field vector $\overrightarrow{E}$ is parallel to the sample surface, so the π-states are excited to π^* and some adsorbed chemical species are masked by others. In contrast, at grazing incidence where the $\overrightarrow{E}$ vector is perpendicular to the surface, the σ-states are excited to σ^*. These results show that the adsorption process is also affected by the direction of the X-ray beam, as demonstrated Huang *et al.*[145]. It can be understood that the adsorbates are either affected or desorbed with different sensitivities. This can be explained by the types of bonds that are formed on the surface and/or the temperature of the annealing process (which might not be sufficient). This is why thermal annealing is a powerful technique, as it allows us to highlight the adsorbates that can camouflate the functions present on the surface of CNTs, and thus modify their distribution and their interaction with their environment. Quantifying the sensitivity of the adsorbates can provide information about the purification method. Thus, the desorption efficiency of the adsorbates can be expressed as follows:

$$Rdt = \frac{I_{initial} - I_{final}}{I_{initial}} x 100\% \tag{3.1}$$

where $I_{initial}$ and I_{final} are the adsorbate intensities before and after thermal annealing, respectively.

The histogram representing the adsorbate desorption efficiency evaluated from the XANES results is shown in Figure 3.20 for normal and grazing incidence angles. For spectra recorded at normal incidence, the intensities of the peaks are lower than those observed at grazing incidence. Several factors may be responsible for this variation. Indeed, this change may be

linked to a greater state of structural disorder. In addition, a change in the type of atom involved in the neighbouring atomic layer can also have a strong influence on the intensity of the peaks, particularly when the differences between the atomic numbers are important.
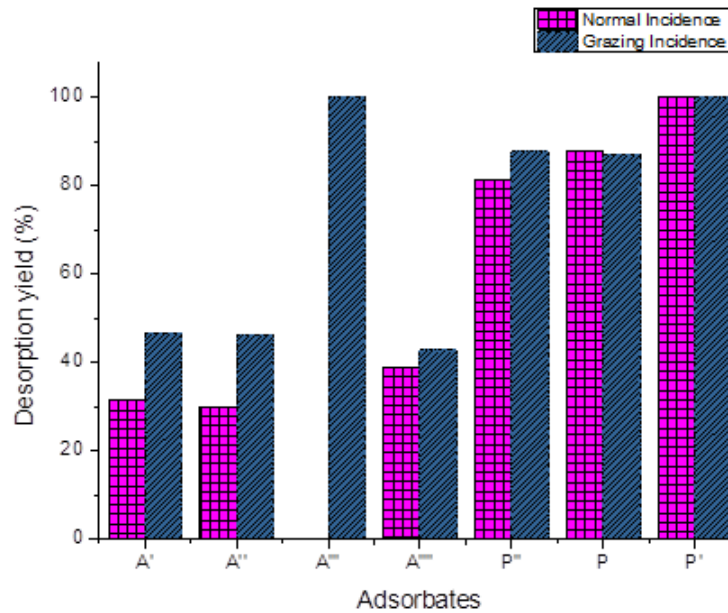
Figure 3.21: Desorption efficiency of adsorbates at normal and grazing incidence angles.

On the other hand, potassium donor species can easily be used to dope MWCNTs. Ding *et al.*[146] and Dresselhaus *et al.*[147] have shown that doping MWCNTs with potassium can improve the conductivity and Fermi energy. The conductivity of MWCNTs is modified in the presence of potassium and is increased by about 12 % after thermal annealing. Figure 3.21 shows the comparison of the intensities of annealed and non-annealed contaminated SWCNTs and MWCNTs.
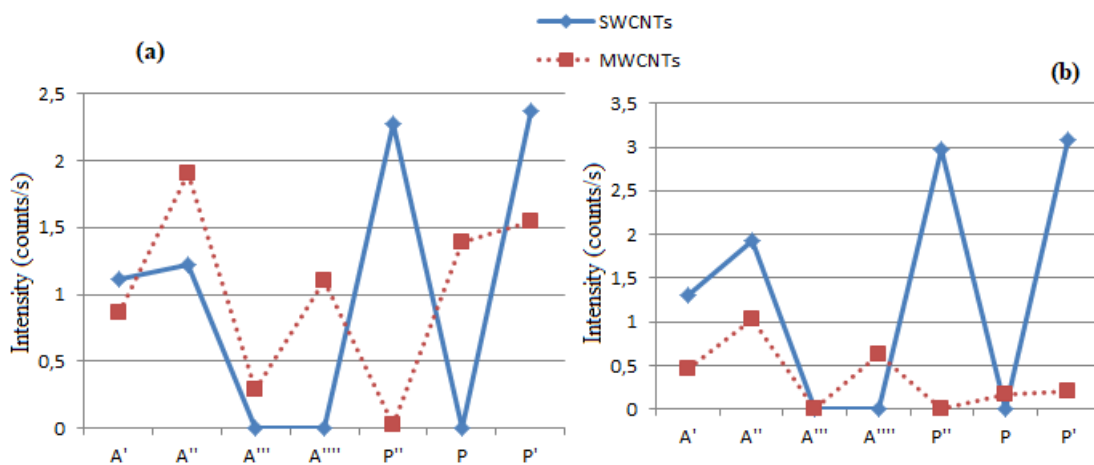
Figure 3.22: Comparison of the intensities of SWCNTs and MWCNTs contaminated (a) unannealed and (b) annealed.

Moreover, the grazing incidence angle geometry is favorable to the desorption process.

The remarkable electronic and transport properties of doped carbon nanotubes make them important building blocks in nanoelectronics. In particular, the controlled p/n doping and reversible adsorption/desorption of gas molecules strongly coupled with nanotube electronic states, are key issues in obtaining nanotube-based devices with desirable properties. It can be observed that non-intrinsic adsorbates (P, P', and P") are more sensitive to thermal annealing compared to intrinsic adsorbates (A', A", A"', and A""). On the one hand, the high sensitivity of potassium adsorbates to thermal annealing demonstrates that physical bonds are established on the surface, leading to the physisorption mechanism. On the other hand, since intrinsic adsorbates are not sensitive enough to thermal annealing, suggesting the existence of chemical bonds on the surface, the chemisorption mechanism can be attributed to these types of adsorbates. Chemical bonds are more difficult to break. The presence of competitive species reduces the capacity of adsorprion of each species on the adsorbent. After the thermal annealing, it is observed that the intensities of the adsorbates present on the SWCNTs are greater than those of the MWCNTs. This therefore provides information on the type of chemical bond involved between the different adsorbates and the surface of the CNTs. Moreover, in the presence of potassium, a slight decrease in the binding energy of different adsorbates is observed for the SWCNTs and MWCNTs. Phenomenon that we have attributed to the loss of sp^2 hybridization contained in the π- orbital and at the same time to the increase of sp^3 hybridization of CNTs.

Conclusion

The characterization of the CNTs after synthesis is mandatory since the properties of these materials can be well understood for applications related to adsorption and desorption. First of all, XANES spectroscopy was used to qualitatively and quantitatively evaluate the adsorbed species on the CNTs. We observed that the quantity adsorbed on the surface is proportional to the diameter of the MWCNTs and SWCNTs. It is seen that the adsorption of potassium increases the conductivity of both CNTs after thermal treatment. Moreover, thermal annealing is one of the efficient methods for the purification and controlling conductivity. We noticed that, the highest adsorption capacity for the removal of potassium by SWCNTs is obtained at pH = 2 suggesting that the ion exchange can be assigned to the adsorption mechanism. TEM and SEM micrographs confirmed the single wall type of carbon nanotubes and a random arrangement of SWCNTs, as well as the presence of the spherical iron particles along carbon nanotubes. The Carbon, Oxygen, Iron, and Sulphur elements are detected on its surface and Iron may be attributed to the metal catalysts particles used during the synthesis. It should be noted that the adsorbates present on the surface of CNTs are useful for non-covalent functionalization with potential applications in biology, water treatment and environmental protection.

General Conclusion

In this work, we have presented the versatility of carbon by its different allotropic forms. We described the hybridization of carbon, which gave information on the electronic structure of graphite and carbon nanotubes. Our attention was then turned to the presentation of the particular structure of CNTs, their exceptional physico-chemical properties and their potential applications. A comparative study of the synthesis methods was done. It showed that lot of the characteristics of the carbon nanotubes result from the synthesis conditions. The use of microscopy and spectroscopy tools for the characterization can give informations on the electronic and structural properties of the carbon nanotube materials. The effet of thermal treatment was described aiming to improve the characteristics of CNTs samples. The investigated CNTs were synthesized by Chemical Vapour Deposition (CVD) method, on a planar $SiO_2/Si(100)$ substrate catalytically assisted by transition metals (Ni, Fe, Co). A qualitative and quantitative evaluation of the adsorbates present on the surface were also investigated. The treatment used was chosen with the aim of presenting a good efficiency and preserving the structure of the CNTs, as well guaranteeing the properties that these materials can offer for later applications. To be well used in various applications, their characterization is necessary to understand their related properties. One of the suitable characterization techniques is X-ray Absorption Spectroscopy coupled with microscopy. To obtain valuable information, the synchrotron radiation is needed because of its high brightness, tunable energy, high flux, low divergence and high ratio of signal to noise.

The XAS technique which uses synchrotron radiation allows to probe matter by means of a phenomenological study. The use of X-ray polarisation in the characterization was also examined as well as the different methods of collecting XAS signal. Concerning the characterization of the orientation of CNTs by the developed geometrical model [47], it is well known that at the K edge of graphitic carbon, the transitions are strongly dependent on the incidence angle θ between the Poynting vector of the polarised X-rays and the surface normal. In particular, the 1s→π^* transition is very sensitive to variations in the incidence angle θ and for the case of an electric dipolar transition, the intensity of the transition varies in $sin^2\theta$. The use of such tools for the characterization of materials is a multidisciplinary field that closely associates experimentalists and theoricians, because it brings new and complementary answers to those provided by the techniques used daily in the laboratory. TEM and SEM micrographs confirmed the single wall type of carbon nanotubes and a random arrangement

of SWCNTs, as well as the presence of the spherical iron particles along carbon nanotubes. The Carbon, Oxygen, Iron, and Sulphur elements are detected at the surface of SWCNTs and Iron may be attributed to the metal catalysts particles used during the synthesis. We noticed that, the highest adsorption capacity for the removal of potassium by SWCNTs is obtained at pH=2 suggesting that the ion exchange can be assigned to the adsorption mechanism. Including other methods, the infrared spectroscopy shows that the functional groups involved in the adsorption process are $OH-$, $C=O$ and $C\equiv C$. XANES spectroscopy has identified two intrinsic peaks corresponding, respectively to the adsorbates associated to the $\pi^*C=C-OH$ or $-(C=C-\pi^*C=O)$ and $\pi^*C=O$. Our results also show that adsorbates were found to have different sensitivities to the thermal annealing. The desorption of potassium on MWCNTs was almost 70 % greater after the thermal annealing, and for SWCNTs, 41 % of gas molecules still adsorbed against 75 % of potassium. In addition, for 75 % of the potassium adsorbates on the surface of SWCNTs, the contribution of the adsorbates gas molecules increases by 17.3 %. The studies carried out on the annealed samples also showed that, thermal annealing during the purification process favoured the reaction between the species of intrinsic origin and the potassium contaminants, and controlled the conductivity with the desorption process. The performance of these depends on the good knowledge of the types of adsorbates or functional groups present on the surface. Our studies have shown that, depending on the type of adsorbates and the functions present on the surface, the impacts are different. We first observed the increase in electrical conductivity in the presence of potassium. Then, we found that these adsorbates interacted with each other through several mechanisms. We also showed that SWCNTs could be used as an adsorbent for applications in the field of water purification. In practice, carbon nanotubes can be doped in different ways, including intercalation of electron donors like alkali-metal or acceptors like halogen, subtitutional doping, molecular adsorption, covalent sidewall functionalization. The characterization of carbon nanostructures after synthesis is mandatory because the properties of these materials must be well understood to optimize their use in various applications.

Perspectives

Designing nanotubes-based nanoscale materials and devices requires the control of physical properties of carbon nanotubes. In particular, it is desirable to design the electronic band structures of the nanotubes. As part of our future works, we will focus on the photophysics of excitons in SWCNTs. Understanding exciton dynamics in carbon nanotubes is essential to unlocking the many potential applications of these materials. From a fundamental point of view, studies of exciton diffusion can provide valuable information on microscopic interactions between excitons and their environment in nanotubes [154]. Noted that, excitons are essential for explaining optical processes in SWCNTs, such as optical absorption, photoluminescence (PL), and resonance Raman spectroscopy [155]. The performance of CNTs needs for a deep understanding of excited states and their dynamics.

Bibliography

[1] Statistics on Water in Mexico, (2010) edition published by National Water Commission of Mexico Edited by Ministry of Environment and Natural Resources, Mexico www.conagua.gob.mx

[2] Iijima, S. (1991) Helical microtubules of graphitic carbon. Nature, 354, 56-58 . https://doi.org/10.1038/354056a0

[3] Bahr, J.L. and Tour, J.M. (2002) Covalent chemistry of single-wall carbon nanotubes. J. Mater. Chem.,12: 1952-1958. https://doi.org/10.1039/B201013P

[4] Sun, Y.P., Fu, K., Lin, Y., and Huang, W. (2002) Functionalized carbon nanotubes : properties and applications. Accounts of Chemical Research, 35, 1096-1104. https://doi.org/10.1021/ar010160v

[5] Rao, A.M., Eklund, P.C., Shunji Bandowet al., (1997) Evidence for charge transfer in doped carbon nanotube bundles from raman scattering. Nature, 388, 257-259. DOI: 10.1038/40827

[6] Yan-Li Zhao and Fraser Stoddart, J. (2009) Noncovalent functionalization of single-walled carbon nanotubes. Accounts of chemical research, 42, 1161–1171. https://doi.org/10.1021/ar900056z

[7] Cyrielle, R. (2012) Transfert d'énergie dans des composés nanotube de carbone/porphyrine, Thèse de doctorat, École normale supérieure de Cachan-ENS Cachan.

[8] Mane, M. J., Thiodjio, S. B., Eb, M. R., (2015) Contribution of Carbon Nanotubes Cap to XAS Signal: A Review. Journal of Materials Sciences and Applications,1,195-220. (http://www.aascit.org/journal/jmsa)

[9] Simonis, P., (2003) Etude de surfaces de graphite et de nanotubes de carbone par microscopie à force atomique et par microscopie à force atomique et par microscopie et spectroscopie à éffet tunnel, Thèse de doctorat, Facultés des Universitaires Notre Dames de la Paix.

[10] Aïssa, A., (2005) Comportement mécanique et électrique des enchevêtrements de nanotubes de carbone, Thèse de doctorat, école centrale Paris.

[11] Michael, B. (2007) Modification des surfaces des nanotubes de carbone par un polymère conducteur électrogénéré pour la réalisation des nanocomposites multifonctionnels, Thèse de doctorat, école centrale Paris.

[12] Morel, D. L., Ghosh, A. K., Feng, T.J., Stogrin, E. L., Purwin, P.E., Fishman, C. (1978) High-efficiency organic solar cells, Appl. Phys. Lett., 32, 495. https://doi.org/10.1063/1.90099

[13] Pierre, M. (2002) Réactivité et manipulation de nanotubes de carbone monocouches : fonctionnalisation de surface par greffage covalent et mise en œuvre comme agent structurant Matériaux, Thèse de Doctorat, Université d'Angers.

[14] Yu, O., Jing-Cui, P., Hui, W., Zhi-Hua, P. (2008) The Rehybridization of Electronic Orbitals in Carbon Nanotubes. Chin. Phys. B , 17, 3123. DOI: 10.1088/1674-1056/17/8/059

[15] Jia, G., Wang, H., et al., (2005) Cytotoxicity of carbon nanomaterials : single-wall nanotube, multi-wall nanotube, and fullerene. Environ Sci Technol, 39, 1378-1383. https://doi.org/10.1021/es048729l

[16] Hofmann, M. S. (2016) Spectroscopy of localized excitons in carbon nanotubes. Dissertation, Ludwig-Maximilians-Universität, München. URN: urn:nbn:de:bvb:19-202117.

[17] Rosenberg, R. A., Love, P. J., Rehn, V. (1986) Polarization-dependent C(K) near-edge x-ray-absorption fine structure of graphite, Phys. Rev. B,33, 4034-4037

[18] Bertrand Bourlon (2005) Physique interfeuillet dans les nanotubes de carbone multifeuillets. PhD thesis, Université Paris VI.

[19] Roquelet, C., Jean-Sébastien, L., Alain-Rizzo, V., Voisin, C., Roussignol, et al., (2010) p-stacking functionalization of carbon nanotubes through micelle swelling. ChemPhysChem,11,1667–1672. doi: 10.1002/cphc.201000067.

[20] Kataura, H., Kumazawa, Y., Maniwa, Y., Umezu, I., Suzuki, S., Yo Ohtsuka, and Y Achiba, (1999) Optical properties of single-wall carbon nanotubes. Synthetic Metals, 103,2555–2558. DOI 10.1016/S0379-6779(98)00278-1

[21] Mintmire, JW and White, CT, (1995) Electronic and structural properties of carbon nanotubes. Carbon, 33, 893– 902. doi.org/10.1016/0008-6223(95)00018-9

[22] Weisman, R. B. and Bachilo, S. M. (2003) Dependence of Optical Transition Energies on Structure for Single-Walled Carbon Nanotubes in Aqueous Suspension: An Empirical Kataura Plot. Nano Lett. 3, 9 . DOI: 10.1021/nl034428i.

[23] Bethune, D. S., Klang, C. H., Vries, M. S. D., Gorman, J. (1993) Cobalt-catalysed growth of carbon nanotubes with single-atomic-layer walls.Nature 363, 605-607. https://doi.org/10.1038/363605a0

[24] Saito, R., Fujita, M., Dresselhaus, G., et al. (1992) Carbon fibers based on C 60 and their symmetry. Phys. Rev. B 45, 6234- 6242. https://doi.org/10.1103/PhysRevB.45.6234

[25] White, T., Todorov, T. N. (1998) Carbon nanotubes as long ballistic conductors. Nature 393, 240-242. https://doi.org/10.1038/30420

[26] Ouyang, M., Huang, J. L., Lieber, C.M. (2002) Fundamental Electronic Properties and Applications of Single-Walled Carbon Nanotubes,Acc. Chem. Res. 35, 1018-1025. https://doi.org/10.1021/ar0101685

[27] Tchenguem Kamto, C. R., Thiodjio Sendja. B., and Mane Mane, J. (2019) Adsorption and desorption phenomena on thermally annealed multi-walled carbon nanotubes by XANES study Chin.Phys. B, 28, 093-101. DOI : 10.1088/1674-1056/ab3437

[28] Jariwala, D., Sangwan, V. K., Lauhon, L. J., Marks, T. J., Hersam, M. C. (2013) Carbon Nanomaterials for Electronics, Optoelectronics, Photovoltaics, and Sensing. Chem Soc Rev , 42 (7), 2824–2860. https://doi.org/10.1039/C2CS35335K

[29] Dai, L., Chang, D. W., Baek, J.-B., Lu, W. (2012) Carbon Nanomaterials for Advanced Energy Conversion and Storage. Small , 8 (8), 1130–1166. DOI: 10.1002/smll.201101594

[30] Itkis, M. E., Borondics, F., Yu, A., Haddon, R. C. (2006) Bolometric infrared photoresponse of suspended single-walled carbon nanotube films. Science,312, 413-416. DOI : 10.1126/science.1125695

[31] Dupont-Pavlovsky, N., (2000) Matériaux carbonés et adsorption, cours DEA, Université Henri-Poincaré, Nancy-1

[32] Peigney, A., Laurent, C., Flahaut, E., Bacsa, R. R. and Rousset, A. (2001) Specific surface area of carbon nanotubes and bundles of carbon nanotubes, Carbon, 39, 507. https://doi.org/10.1016/S0008-6223(00)00155-X

[33] Serp, P., (2003) Carbon nanotubes and nanofibers in catalysis. Applied Catalysis A: General, 253, 337–358. https://doi.org/10.1016/S0926-860X(03)00549-0

[34] Kleiner, A., Eggert, S. (2001) Curvature, Hybridization, and STM Images of Carbon Nanotubes. Phys. Rev. B, 64, 113-402. DOI : https://doi.org/10.1103/PhysRevB.64.113402

[35] Liu, Z., Tabakman, S., et al., (2009) Carbon Nanotubes in Biology and Medicine: In Vitro and in Vivo Detection, Imaging and Drug Delivery. Nano Res, 85–120. https://doi.org/10.1007/s12274-009-9009-8

[36] Yang, W., Ratinac, K. R., Ringer, S. P., Thordarson, P., Gooding, J. J., Braet, F. (2010) Carbon Nanomaterials in Biosensors: Should You Use Nanotubes or Graphene ? Angew. Chem. Int. Ed. 2010, 49 (12), 2114–2138. DOI : 10.1002/anie.200903463

[37] Bianco, A., Kostarelos, K., Partidos, C. D., Prato, M. (2005) Biomedical Applications of Functionalised Carbon Nanotubes. Chem. Commun, 5, 571. https://doi.org/10.1039/B410943K

[38] Bianco, A., Kostarelos, K., Prato, M. (2005) Applications of Carbon Nanotubes in Drug Delivery, Curr. Opin. Chem. Biol, 9 (6), 674–679. doi: 10.1016/j.cbpa.2005.10.005.

[39] Kam, N. W. S., O'Connell, M., Wisdom, J. A., Dai, H. (2005) Carbon Nanotubes as Multifunctional Biological Transporters and Near-Infrared Agents for Selective Cancer Cell Destruction. Proc. Natl. Acad. Sci. U. S. A, 102 (33), 11600 – 11605. https://doi.org/10.1073/pnas.0502680102

[40] Kabir, M., Van Vliet, K. J. (2016) Kinetics of Topological Stone-Wales Defect Formation in Single Walled Carbon Nanotubes. arXiv,1, 1601-1169 [cond-mat.mes-hall], DOI: https://doi.org/10.1021/acs.jpcc.5b11682

[41] Haddon, R. C. (1993) Chemistry of the Fullerenes: The Manifestation of Strain in a Class of Continuous Aromatic Molecules. Science , 261, 1545-1550. DOI: 10.1126/science.261.5128.1545

[42] Dumitricˇa, T., Landis, C. M., and Yakobson, B. I. (2002). Curvature-induced polarization in carbon nanoshells. Chemical Physics Letters, 360, 182-188. https://doi.org/10.1016/S0009-2614(02)00820-5

[43] Spitalsky, Z., Tasis, D., Papagelis, K., Galiotis, C. (2010) Carbon Nanotube-polymer Composites: Chemistry, Processing, Mechanical and Electrical Properties. Prog. Polym. Sci, 35 (3), 357−401. https://doi.org/10.1016/j.progpolymsci.2009.09.003

[44] Ankudinov, A. L., Rehr, J. J., Low, J. J., Bare, S. R. (2002) Sensitivity of Pt x-ray absorption near edge structure to the morphology of small Pt clusters. J. Chem. Phys, 116, 1911-1919. https://doi.org/10.1063/1.1432688

[45] Vlaic, G., and Olivi, L. (2004) EXAFS Spectroscopy: a Brief Introduction. Croat. Chem, Acta. 77, 427-433. ISSN-0011-1643

[46] Stöhr, J. (1992) NEXAFS Spectroscopy, Springer, Berlin. ISBN : 978-3-662-02853-7.

[47] Mane, M. J., Le Normand, F., Eba, M. E., Cojocaru, C.S., Ersen, O., Senger, A., Laffon, C., Tchiodjio, S. B., et al (2014) Alignment of Vertically Grown Carbon Nanostructures Studied by X-Ray Absorption Spectroscopy. Materials Sciences and Applications, 5, 966-983. http://dx.doi.org/10.4236/msa.2014.513098

[48] Jorio, A., Dresselhaus, G., and Dresselhaus, M. S. (eds.): Carbon Nanotubes: Advanced Topics in the Synthesis, Structure, Properties and Applications. Top. Appl. Phys. Springer-Verlag, Berlin, Heidelberg 2008. DOI: 10.1007/978-3-540-72865-8.

[49] Volder, M. F. L. D., Tawfick, S. H., Baughman, R. H., and Hart, A. J. (2013) Carbon Nanotubes: Present and Future Commercial Applications. Science, 339, 6119 . DOI: 10.1126/science.1222453.

[50] Steinhögl, W., Schindler, G., Steinlesberger, G., Traving, M. and Engelhardt, M. (2005) Comprehensive study of the resistivity of copper wires with lateral dimensions of 100 nm and smaller Journal of Applied Physics,97, 023706; https://doi.org/10.1063/1.1834982

[51] Naeemi, A., Huang, G., Meindl, J.D. (2007) Electronic Component and Technology Conference. ECTC '07. Proceedings, 420–428.

[52] Chiu,H.-Y., Deshpande, V.V., Postma, H.W. Ch., Forro, L. and M. Bockrath. (2005) Ballistic Phonon Thermal Transport in Multiwalled Carbon Nanotubes, PRL, 95, 226-241. DOI: 10.1103/PhysRevLett.95.226101

[53] Z. Yao, C. Dekker et P. Avouris : Top. Appl. Phys., 80, 147–171, 2001.

[54] Wang, S., Zhang, L., Zhang, Z., Ding, L., Zeng, Q., Wang, Z., Liang, X., Gao, M., Shen, J., Xu, H., Chen, Q., Cui, R., Li, Y., and Peng, L.-M. (2009) Photovoltaic Effects in Asymmetrically Contacted CNT Barrier-Free Bipolar Diode. J. Phys. Chem. C, 113, 17 . DOI: 10.1021/jp901282h.

[55] Zhao, J.J., Park, H.K., Han, J., and Lu, J.P. (2004) Electronic properties of carbon nanotubes with covalent sidewall functionalization. J. Phys. Chem. B, 108 (14), 4227-4230. https://doi.org/10.1021/jp036814u

[56] Boul, P.J., Liu, J., Mickelson, E.T., Huffman, C.B., Ericson, L.M., Chiang, I.W., Smith, K.A., Colbert, D.T., et al (1999) Reversible sidewall functionalization of buckytubes. Chem. Phys. Lett., 1999, 367-372. https://doi.org/10.1016/S0009- 2614(99)00713-7

[57] Goldoni, A., Larciprete, R., Petaccia, L., and Lizzit, S. (2003) Single-wall carbon nanotube interaction with gases: Sample contaminants and environmental monitoring. Journal of the American Chemical Society,125 (37), 11329-11333. https://doi.org/10.1021/ja034898e

[58] Jijun, Z., Alper, B., Jie, H., and Jian, P.Lu. (2002) Gas molecule adsorption in carbon nanotubes and nanotube bundles. Nanotechnology, 13, 195–200. DOI:10.1088/0957-4484/13/2/312

[59] Yang, C.M., Kanoh, H., Kaneko, K., Yudasaka, M., and Iijima, S. (2002) Adsorption behaviors of HiPco single-walled carbon nanotube aggregates for alcohol vapors. J. Phys. Chem. B, 106(35), 8994-8999. https://doi.org/10.1021/jp025767n

[60] Toebes, M.L., Prinsloo, F.F., Bitter, J.H., van Dillen, A.J., and de Jong, K.P. (2003) Influence of oxygen-containing surface groups on the activity and selectivity of carbon nanofiber supported ruthenium catalysts in the hydrogenation of cinnamaldehyde. J.Cataly, 214(1), 78-87. DOI:10.1016/S0021-9517(02)00081-7

[61] Nguyen, C.V., Delzeit, L., Cassell, A.M., Li, J., Han, J., and Meyyappan, M. (2002) Preparation of nucleic acid functionalized carbon nanotube Arrays. Nano Letters, 2(10), 1079- 1081. https://doi.org/10.1021/nl025689f

[62] Li, Y.H., Wang, S.G., Wei, J.Q., Zhang, X.F., Xu, C.L., Luan, Z.K., Wu, D.H., and Wei, B.Q. (2002) Lead adsorption on carbon nanotubes. Chemical Physics Letters, 357(3-4), 263-266. DOI:10.1016/S0009-2614(02)00502-X

[63] Li, Y.H., Wang, S.G., Luan, Z.K., Ding, J., Xu, C.L., and Wu, D.H. (2003) Adsorption of cadmium(II) from aqueous solution by surface oxidized carbon nanotubes. Carbon, 41(5), 1057-1062. https://doi.org/10.1016/S0008-6223(02)00440-2

[64] Zhang, N.; Kawamoto, T.; Watanabe, H.; Jiang, Y.; Zhang, Z.; Lei, Z.; Parajuli, D. Selective Adsorption of Potassium in Seawater by CoHCF Thin Film Electrode and Its Electrochemical Desorption/Regeneration. Materials 2021, 14, 3592. https://doi.org/10.3390/ma14133592

[65] Ciceri, D.; De Oliveira, M.; Allanore, A. Potassium fertilizer via hydrothermal alteration of K-feldspar ore. Green Chem. 2017, 19, 5187–5202.

[66] Hou, J.; Yuan, J.; Xu, J.; Sun, L. Synthesis and characterization of K-phillipsite (K-PHI) membrane for potassium extraction from seawater. Microporous Mesoporous Mater, 172, 217–221.

[67] Kinekar, B. K. Potassium Fertilizer Situation in India : Current Use and Perspectives. Karnataka J. Agric. Sci. 2011, 24, 1-6.

[68] A. Campoine, L. Gurreri, M. Ciofalo, G. Micale, A. Tamburini, A. Cipollina, Electrodialysis for water desalination: A critical assessment of recent developments on process fundamentals, models and applications, Desalination 434 (2018) 121–160.

[69] P.M.Biesheuvel,S.Porada,M.Elimelech, J.E. Dykstra (2022) Tutorial review of reverse osmosis and electrodialysis. Journal of Membrane Science 647-120221https://doi.org/10.1016/j.memsci.2021.120221

[70] A. Yaroshchuk, M.L. Bruening, E. Zholkovskiy, Modelling nanofiltration of electrolyte solutions, Adv. Colloid Interface Sci, 268 (2019) 39–63.

[71] Kar, Soumitra, R.C. Bindal et P.K. Tewari. 2012. «Carbon Nanotube Membranes for Desalination and Water Purification: Challenges and Opportunities». Nana Today, 7, 385-389.

[72] Thomas, John A. et Alan J.H. McGaughey. 2008. «Reassessing Fast Water Transport through Carbon Nanotubes». Nana Letters, 8, 2788-2793.

[73] Miyake, T., Saito, S. (2002) Electronic structure of potassium-doped carbon nanotubes. Physica B, 323, 219–221. https://doi.org/10.1016/S0921-4526(02)00963-8

[74] Liu, G. H., Wang, J. L., Zhu, Y. F., Zhang, X. R. (2004) Application of multiwalled carbon nanotubes as a solid-phase extraction sorbent for chlorobenzenes. Anal. Lett, 37, 3085–3104. https://doi.org/10.1081/AL-200035912

[75] Su, F. S.; Lu, C. S. (2007) Adsorption kinetics, thermodynamics and desorption of natural dissolved organic matter by multiwalled carbon nanotubes. J. Environ. Sci. Health Part A, 42, 1543– 1552. https://doi.org/10.1080/10934520701513381

[76] Hilding, J., Grulke, E. A., Sinnott, S. B., Qian, D. L., Andrews, R., Jagtoyen, M. (2001) Sorption of butane on carbon multiwall nanotubes at room temperature. Langmuir, 17, 7540–7544. https://doi.org/10.1021/la010131t

[77] Yan, X. M., Shi, B. Y., Lu, J. J., Feng, C. H., Wang, D. S., Tang, H. X. (2008) Adsorption and desorption of atrazine on carbon nanotubes. J. Colloid Interface Sci, 321, 30–38. https://doi.org/10.1016/j.jcis.2008.01.047

[78] Salame, I. and Bandosz, T. (2001) Surface chemistry of activated carbons: Combining the results of temperature-programmed desorption, boehm, and potentiometric titrations. J. Colloid Interface Sci., 240 (1) 252-258. https://doi.org/10.1006/jcis.2001.7596

[79] Wang, Z., Kanoh, H., Kaneko, K., Lu, G., and Do, D. (2002) Structural and surface property changes of macadamia nut-shell char upon activation and high temperature treatment. Carbon, 40(8), 1231-1239. https://doi.org/10.1016/S0008- 6223(01)00286-X

[80] Peng, X. J., Li, Y. H., Luan, Z. K., Di, Z. C., Wang, H. Y., Tian, B. H., Jia, Z. P. (2003) Adsorptionof 1,2-dichlorobenzenefromwaterto carbon nanotubes. Chem. Phys. Lett, 376, 154–158. https://doi.org/10.1016/S0009-2614(03)00960-6

[81] Gotovac, S., Honda, H., Hattori, Y., Takahashi, K., Kanoh, H., Kaneko, K. (2007) Effect of nanoscale curvature of single-walled carbon nanotubes on adsorption of polycyclic aromatic hydrocarbons. Nano Lett, 7, 583–587. https://doi.org/10.1021/nl0622597

[82] Cojocaru, C. S., and Le Normand, F. (2006) On the role of activation mode in the plasma- and hot filaments-enhanced catalytic chemical vapour deposition of vertically aligned carbon nanotubes. Thin Solid Films , Elsevier, 515-53. DOI: http://dx.doi.org/10.1016/j.tsf.2005.12.137

[83] Taschner, C., Pacal, F., Leonhardt, A., Spatenka, P., Bartsch, K., Graff, A., and Kaltofen, R. (2003) Synthèse de nanotubes de carbone alignés par CVD à filament chaud assisté par plasma DC. Surf. Coat. Technol, 81, 174–175. doi: 10.1016/S0257-8972(03)00712-6.

[84] Medellin-Castillo, N. A., et al. (2007) Adsorption of fluoride from water solution on bone char Ind. Eng. Chem. Res, 46, 9205. https://doi.org/10.1021/ie070023n

[85] Eba Medjo, R., Thiodjio, S. B., Mane, M. J., and Owono, A. P. (2009) A study of carbon nanotube contamination by XANES spectroscopy. Phys. Scr, 80, 045-601. doi:10.1088/0031-8949/80/04/045601

[86] Khabashesku V.N., Billups W.E., Margrave J.L.(2002) « Fluorination of single-wall carbon nanotubes and subsequent derivatization reactions »Acc. Chem. Res, 35, 1087.

[87] Boul P.J., Mickelson E.T., Huffman C.B., Ericson L.M., Chiang I.W., Smith K.A., Colbert D.T., Hauge R.H., Margrave J.L., Smalley R.E «Reversible sidewall functionnalization of buckytubes» Chem. Phys. Lett, 1999, 310-367.

[88] Balavoine F., Schultz P., Richard C., Mallouh V., Ebbesen T., Mioskowski C. « Helical crystallization of proteins on carbon nanotubes : a first step towards the development of biosensors » Angew. Chem., Int. Ed,1999 38 (13-14), 1912.

[89] Luzzi, D.E., Smith B.W. « Carbon cage structures in single wall carbon nanotubes : a new class of materials » Carbon 2000 38, 1751.

[90] Jia,Q. (2008) Research progress of novel adsorption processes in water purification: a review. J Environ Sci (China), 20 (1), 1–13

[91] K. Donaldson, R. Aitken, L. Tran, V. Stone, R. Duffin, G. Forrest, A. Alexander, Toxicol. Sci., 2006, 92, 5.

[92] Firme III CP and Bandaru PR, Toxicity issues in the application of carbon nanotubes to biological systems. Nanomedicine, 2010, 6 (2) 245-256.

[93] Yan L, Zhao F, Li S, Hu Z and Zhao Y, Low-toxic and safe nanomaterials by sur-facechemical design, carbon nanotubes, fullerenes, metallofullerenes, and graphenes. Nanoscale, 2011, 3, 362-382.

[94] Lacerda L, Soundararajan A, Singh R, Pastorin G, Al-Jamal KT, Turton J, Frederik P, Herrero MA, Li S, Bao A, Emfietzoglou D, Mather S, Phillips WT, Prato M, Bianco A, Goins B et Kostarelos K, Dynamic imaging of functionalised multi-walled carbon nanotube systemic circulation and urinary excretion. Adv Mater, 2008, 20, 225-230.

[95] Ménard-Moyon C and Bianco A, Atténuation de la toxicité des nanotubes de carbone grâce à la fonctionnalisation chimique. Techniques de l'ingénieur, 2014, in 167.

[96] M. Vaezzadeh, E. Noruzifar, S. F. Atashzar, M. Vaezzadeh, M. Ahmadi, Chem. Phys. Lett. 2006, 419, 154.

[97] Shahivandi,H., Vaezzadeh, M., and Saeidi, M.(2017)Theoretical Study of Effective Parameters in Catalytic Growth of Carbon Nanotubes. Phys. Status Solidi A, 00, 1700101 DOI: 10.1002/pssa.201700101

[98] Vaezzadeh, M., Noruzifar, E., Farokh Atashzar, S., Vaezzadeh, M., Ahmadi, M. (2005) Simulation of carbon nanotube growth at optimized temperature. Chemical Physics Letters 419, 154–157

[99] Journet, C., Maser, W., Bernier, P. et al. (1997) Large-scale production of single-walled carbon nanotubes by the electric-arc technique. Nature 388, 756–758. https://doi.org/10.1038/41972

[100] Journet, C., Bernier, P. (1998) Production of carbon nanotubes. Applied Physics A: Materials Science & Processing 67, 1–9. https://doi.org/10.1007/s003390050731

[101] Briois, V., Brouder, Ch., Sainctavit, Ph., Itié, J. P., Polian, A., San Miguel, A. (1997) Structure, structural phase transitions, mechanical properties, defects, etc. Phys. Rev. B, vol. 56, p.5866.

[102] Eba Medjo, R. (2011) Structural and morphological characterization of carbon nano-structures synthesized by chemical vapour deposition using spectroscopic techniques and electron microscopies, Thèse de doctorat université de yaounde I.

[103] Rey, S. (2000) Thèse de doctorat. Université Strasbourg.

[104] Cojocaru, C. S. (2003) Thèse, Université Louis Pasteur, Strasbourg I.

[105] Mane Mane, J. (1993) Thèse, Université de Nancy I.

[106] Thiodjio Sendja, B., Eba Medjo, R., Mane Mane, J., Ben-Bolie, G. and Ateba, P. (2015) Theoretical Investigation of X-Ray Absorption near Edge Spectroscopy (XANES) Angular Dependence of Aligned Carbon Nanotubes Grown by DC HF CVD Process. Materials Sciences and Applications, 6, 373-390. doi: 10.4236/msa.2015.65043.

[107] Saito, Y. (1995) Nanoparticles and lled nanocapsules. Carbon ,33, p. 979988. https://doi.org/10.1155/2012/613746

[108] Amara, H., Roussel, J.M., Bichara, C., Gaspard, J.P. and Ducastelle, F. (2009) Tightbinding potential for atomistic simulations of carbon interacting with transition metals: Application to the Ni-C system. Physical Review B, 79, p. 014109014126. DOI:https://doi.org/10.1103/PhysRevB.79.014109

[109] Nagy, J. B., Bister, G., Fonseca, A., Méhn, D., Kónya, Z., Kiricsi, I., Horváth, Z.E., and Biró, L.P. (2004) On the Growth Mechanism of Single-Walled Carbon Nanotubes by Catalytic Carbon Vapor Deposition on Supported Metal Catalysts , dans : Journal of Nanoscience and Nanotechnology 4, 326-345. DOI: https://doi.org/10.1166/jnn.2004.069

[110] Baker, R.T.K. (1988) Catalytic growth of carbon filaments. Carbon 4, 315-323. https://doi.org/10.1016/0008-6223(89)90062-6

[111] Ducati, C., Alexandrou, I., Chhowalla, M., Robertson, J. and Amaratunga, G.A.J. (2004) The role of the catalytic particle in the growth of carbon nanotubes by plasma enhanced chemical vapor deposition. Journal of Applied Physics, 95, 6387-6391. https://doi.org/10.1063/1.1515126

[112] Helveg, S., Lopez-Cartes, C., Sehested, J., Hansen, P.L., Clausen, B.S., RostrupNielsen, J.R., Abild-Pedersen, F. and Nørskov, J.K. (2004) Atomic-scale imaging of carbon nanobre growth. Nature, 427, 426-429. doi: 10.1038/nature02278.

[113] Choi, G.S., Cho, Y.S., Hong, S.Y., Park, J.B., Son, K.H. and Kim, D.J. (2002) Carbon nanotubes synthesized by Ni-assisted atmospheric pressure thermal CVD. Journal of Applied Physics ,91, 3847-3854.

[114] Park, J.B., Cho, Y.S., Hong, S.Y., Choi, K.S., Kim, D., Choi, S.Y., Ahn, S.D., Song, Y.H., Lee, J.H. and Cho, K.I. (2002) Cross-sectional transmission electron microscopy of carbon nanotubes catalyst substrate heterostructure using a novel method for specimen preparation. Thin Solid Films ,415, 7882. DOI : 10.1016/S0040-6090(02)00507-2

[115] Choi, J.H., Lee, T.Y., Choi, S.H., Han, J.H., Yoo, J.B., Park, C.Y., Jung, T., Yu, S., Yi, W., Han, I.T. and Kim, J.M. (2003) Density control of CNTs using NH3 plasma treatment of Ni catalyst layer. Thin Solid Fims ,435, p. 318-323. DOI : 10.1016/S0040-6090(03)00341-9

[116] Hata K., Futaba D.N., Mizuno K., Namai T., Yumura M. et Iijima S. (2004) Water Assisted Highly Effcient Synthesis of Impurity-Free Single-Walled Carbon Nanotubes. Science ,306,1362-1364. doi: 10.1126/science.1104962.

[117] Ding, F., Harutyunyan, A.R. and Yakobson, B.I. (2009) Dislocation theory of chirality controlled nanotube growth. Proceedings of the National Academy of Sciences,106,2506-2509. doi: 10.1073/pnas.0811946106

[118] Lu, C., Chiu, H. (2006) Adsorption of zinc(II) from water with purified carbon nanotubesChemical Engineering Science, 61, 1138–1145 doi:10.1016/j.ces.2005.08.007

[119] Medellin-Castillo, N A et al. (2007) Adsorption of fluoride from water solution on bone char Ind. Eng. Chem. Res. 46, 920-512. https://doi.org/10.1021/ie070023n

[120] David B. Williams and C. Barry Carter. Transmission Electron Microscopy: A Textbook for Materials Science. Springer Science & Business Media, August 2009.

[121] M. Lentzen. The refractive index in electron microscopy and the errors of its approximations. Ultramicroscopy, 176:139-145, May 2017.

[122] Louis de Broglie. Recherches sur la théorie des Quanta. November 1924.

[123] Lixin, G., Nian, W., Xu, T., et al (2020) Application of FIB-SEM Techniques for the Advanced Characterization of Earth and Planetary Materials. https://doi.org/10.1155/2020/8406917

[124] SU, D.S. (2010) Transmission Electron Microcopy.

[125] Russ, J. C. (1984) Fundamentals of Energy Dispersive X-ray Analysis, Butterworths. London.

[126] Standard Operating Procedure for FEI Helios 660 NanoLab.

[127] JEM-2100 Electron Microscope

[128] Xiang, Junjie, "Foutier Transform Infrared Spectroscopy Instrumentation and Integration with Thermogravimetry" (2018). Masters Theses & Specialist Projects. Paper 2572.

[129] Dilhumar Abdurazik (2016), Thesis, School of Natural and Applied Sciences of İstanbul Şehir University

[130] Garry, R., Michael, B., et al. Powerful New Identification Tools with OMNIC Specta Software. Thermo Fisher Scientific, Madison, WI, USA

[131] SEE-LS: A 4th Generation Synchrotron Light Source for Science and Technology, Dieter Einfeld (ed.) CERN Yellow Reports: Monographs, CERN-2020-001 (CERN, Geneva, 2020) https://doi.org/10.23731/CYRM-2020-001

[132] Lee, P. A., et al. (1981) Extended x-ray absorption fine structure its strengths and limitations as a structural tool. Rev. Mod. Phys. 53,805. https://doi.org/10.1103/RevModPhys.53;769

[133] Tchenguem Kamto, C. R. et al (2021) X-ray absorption near edge spectroscopy of the electronic structure of potassium adsorbed single walled carbon nanotubes Phys. Scr. 96 105803. https://doi.org/10.1088/1402-4896/ac0b86

[134] Dehghani, M. H., et al. (2015) Removal of noxious Cr (VI) ions using singlewalled carbon nanotubes and multi-walled carbon nanotubes Chem. Eng. J. 279 34452. DOI : 10.1016/J.CEJ.2015.04.151

[135] Pan, B. and Xing, B. (2008) Adsorption mechanisms of organic chemicals oncarbon nanotubes Environ. Sci. Technol 42 900513. https://doi.org/10.1021/es801777n

[136] Wang, S. G., Liu, X. W., Gong, W. X., Nie, W., Gao, B. Y. and Yue, Q. Y. (2007) Adsorption of fulvic acids from aqueous solutions by carbon nanotubes J. Chem. Technol. Biotechnol. 82 698704. https://doi.org/10.1002/jctb.1708

[137] Lu, C. Y. and Su, F. S. (2007) Adsorption of natural organic matter by carbon nanotubes Sep. Purif. Technol. 58 11321. DOI : 10.1016/j.seppur.2007.07.036

[138] Medellin-Castillo, N. A., Leyva-Ramos, R., Padilla-Ortega, E., Ocampo, P. R., Flores, C. J. V. and Berber-Mendoza, M. S. (2014) Adsorption capacity of bone char for removing fluoride from water solution. Role of hydroxyapatite content, adsorption mechanism and competing anions J. Ind. Eng. Chem. 20 401421. https://doi.org/10.1016/j.jiec.2013.12.105.

[139] Li, G et al. (2015) Giant raman response to the encapsulation of sulfur in narrow diameter single-walled carbon nanotubes. J. Am. Chem.Soc. 138 403. https://doi.org/10.1021/jacs.5b10598

[140] Blasé, X., Benedict, L. X., Shirley, E. L. and Louie, S. G. (1994) Hybridization effects and metallicity in small radius carbon nanotubes Phys. Rev.Lett. 72 1878. DOI : https://doi.org/10.1103/PhysRevLett.72.1878

[141] Yueh, C. L. et al. (2001) Electronic structure of the Fe-layercatalyzed carbon nanotubesstudied by xray-absorption spectroscopy Appl. Phys.Lett. 79 3179. https://doi.org/10.1063/1.1416165

[142] McPhail, M. R., Sells, J. A., He, Z. and Chusuei, C.C. (2009) Charging nanowalls: adjusting the carbon nanotube isoelectric point via surface functionalization. J. Phys. Chem. C 113 141029. https://doi.org/10.1021/jp901439g

[143] Fu, C. et al. (2018) Confined lithium-sulfur reactions in narrow-diameter carbon nanotubes reveal enhanced electrochemical reactivity. ACS. Nano. 12 977584. https://doi.org/10.1021/acsnano.7b08778

[144] Santucci, S., Picozzi, S., Di Gregorie, F., Lozzi, L., Cantalini, C., Valentini, J. M. L. and Delley, B. K. (2003) NO2 and CO gas adsorption on carbon nanotubes; Experiment and theory. J. Chem. Phys. 119 1090410. https://doi.org/10.1063/1.1619948

[145] Sankar, P., Srivastava, D., Cho, K. (2001) External Chemical Reactivity of Fullerenes and Nanotubes. Mat. Res. Soc. Symp. Proc. 675. DOI:10.1557/PROC-675-W1.5.1

[146] Collins, P. G., Bradley, K., Ishigami, M. and Zettl A (1801) Extreme oxygen sensitivity of electronic properties of carbon nanotubes Sci. 2871801–4. DOI:10.1126/science.287.5459.1801

[147] Zhong, J., Song, L., Chiou, J., Dong, C., Liang, X,. and Wu, Z., (2010) Electronic structure study of modified single-walled carbon nanotubes by soft-x-ray absorption and resonant emission spectroscopy Appl. Phys. Lett. 96 213112. DOI:10.1063/1.3441027

[148] Rosenberg, R. A., Love, P. J., Rehn, V., (1986) Polarization-dependent C(K) nearedge x-ray-absorption fine structure of graphite. Phys. Rev. B, vol. 33, pp. 4034-4037. https://doi.org/10.1103/PhysRevB.33.4034

[149] Durgun, E., Dag, S., Bagci, V.M.K., et al. (2003). Systematic study of adsorption of single atoms on a carbon nanotube. Phys. Rev. B, 67, 201401. 123. 124. https://doi.org/10.1103/PhysRevB.67.201401

[150] Zhong, J., Liu, C., Wu, ZY., Mamatimin, A., Kurash, I., Cheng, HM.,Gao, B. and Liu, L. (2005) Study of Carbon Based Nanotubes. High Energy Phys. Nucl. Phys.29 97

[151] Huang, W., Wang, Y., Luo, G., Wei, F. (2003) 99.9% purity multi-walled carbon nanotubes by vacuum high-temperature annealing. Carbon , 41, 2585–2590. https://doi.org/10.1016/S0008-6223(03)00330-0

[152] Ding, Y., Yang, X. B. and Ni, J. (2006) Adsorption on the carbon nanotubes Front. Phys. Chin. 1 317. https://doi.org/10.1007/s11467-006-0019-7

[153] Dresselhaus, M. S., Williams, K. A., and Eklund, P. C. (1999) Hydrogen storage in single-walled carbon nanotubes, MRS Bull. 24 45.https://doi.org/10.1063/1.126503

[154] Amanda R. Amori, Zhentao Hou, and Todd D. Krauss, Excitons in Single-Walled Carbon Nanotubes and Their Dynamics, Annu. Rev. Phys. Chem. 2018. 69:81-99. DOI: 10.1146/annurev-physchem-050317-014241

[155] Mildred S. Dresselhaus, Gene Dresselhaus,Riichiro Saito, and Ado Jorio, Exciton Photophysics of Carbon Nanotubes, Annu. Rev. Phys. Chem. 2007. 58:719-47. DOI: 10.1146/annurev.physchem.58.032806.104628

Appendix

1. **Camile Rodolphe Tchenguem Kamto**, Bridinette Thiodjio Sendja , Marius Silenou Mengoue, Nahum Medelin Castillo, Gladis Judith Labrada Delgado, Margarita Berenice Nájera-Acevedo and Jeannot Mane Mane ; X-ray absorption near edge spectroscopy of the electronic structure of potassium adsorbed single walled carbon nanotubes. Phys. Scr. 96 (2021) 105803. **Impact Factor : 3.081**

2. **Camile Rodolphe Tchenguem Kamto**, Bridinette Thiodjio Sendja, and Jeannot Mane Mane ; Adsorption and desorption phenomena on thermally annealed multi-walled carbon nanotubes by XANES study. Chin. Phys. B Vol. 28, No. 9 (2019) 093101. **Impact Factor : 1.652**

Physica Scripta

PAPER

X-ray absorption near edge spectroscopy of the electronic structure of potassium adsorbed single walled carbon nanotubes

Camile Rodolphe Tchenguem Kamto[1]**, Bridinette Thiodjio Sendja**[2] **, Marius Silenou Mengoue**[3] **, Nahum Medelin Castillo**[4]**, Gladis Judith Labrada Delgado**[5]**, Margarita Berenice Nájera-Acevedo**[4] **and Jeannot Mane Mane**[2,6]

1   University of Yaoundé I, Faculty of Science, Department of Physics, Yaoundé, Cameroon
2   University of Yaounde I, National Advanced School of Engineering, Department of Mathematics and Physical Science, Po Box 8390 Yaounde, Cameroon
3   Centre for Atomic, Molecular Physics and Quantum Optics, Faculty of Science, University of Douala, PO Box 8580, Douala, Cameroon
4   Autonomous University of San Luis Potosi, Faculty of Engineering, San Luis Potosí, S.L.P., Mexico
5   IPICYT (Instituto Potosino de Investigación Científica y Tecnológica, A.C), San Luis Potosi, S.L.P., Mexico
6   University of Dschang, Dschang, Cameroon

E-mail: sbridine@yahoo.fr

Abstract

Carbon nanotubes (CNTs) show exceptional properties which make them extremely attractive for many applications. The electronic structure of potassium adsorbed single-walled carbon nanotubes (SWCNTs) is investigated by x-ray near edge structure (XANES) spectroscopy. Gas molecules (H_2O, O_2, CO_2, CO) and potassium (K) adsorbates showed non negligible sensitivity to the geometry, thermal annealing treatment, and hybridization. The SWCNT type is shown by transmission electron microscopy (TEM) whereas an aleatory arrangement of SWCNTs and the spherical iron particles along carbon nanotubes are observed by scanning electron microscopy (SEM). XANES shows that the charge transfer effect in K-doping SWCNTs increases the conductivity to 62.7%. The adsorption study demonstrates that the adsorption mechanism to remove potassium from aqueous solutions using SWCNTs is assimilated to the ion exchange process. The functional groups OH^-, C=O and C≡C are involved in the adsorption process. They are correlated to the assignment of the adsorbates given by XANES.

1. Introduction

The ever-growing demand for portable, compact, and energy efficient technologies has driven scientists to challenge the boundaries of bulk material science. Small scale devices can be created with the existing material and utilized for various applications. Since the discovery of carbon nanotubes (CNTs) in 1991 by Iijima [1], the intensive research activity around carbon nanotubes is favored by their unique combination of physical and chemical properties, which originates from their molecular structure. They exhibit excellent mechanical and electronic properties [2].

Recent studies on possible nanodevice applications have recognized that the surface functionalization of nanotubes and fullerenes would play an important role in nanodevice development [3]. To functionalize nanotubes and fullerenes, the chemical reactivity of carbon atoms needs to be understood with quantitative accuracy. One significant way in which carbon materials differ from other materials is that carbon atoms have many possible electron states by hybridization of an atomic orbital. In carbon, there are three possible hybridizations: sp, sp^2 and sp^3. The bonding in the CNTs is primarily of sp^2 and may sometimes be sp^3 when the curvature is high [4, 5]. The rehybridization between the π orbitals and σ bonds can occur when the graphite sheet rolls into CNTs since the π orbitals are no more orthogonal to the surface [5]. The curvature of the CNTs is affected by the hybridization. As a result, the bandgap of the tubes can be reduced, and the energies of the

electronic states modified. The properties of carbon nanotubes are highly dependent on the morphology, size, and diameter [6].

The remarkable electronic and transport properties of doped carbon nanotubes make them important building blocks in nanoelectronics, which may speed up the development of molecular circuits and related devices. In particular, the controlled p/n doping and reversible adsorption/desorption of gas molecules strongly coupled with nanotube electronic states, are key issues in obtaining nanotube-based devices with desirable and tunable conductance.

In the past decades, the sorption behavior of carbon nanotubes has been intensively studied [7–10]. Adsorption of the molecules and functionalization of covalent sidewall onto carbon nanotube (CNT) constitute another method of doping CNT nanomaterial. The molecules can be adsorbed on the CNT either by weak Van der Waals-like interaction or a covalent bond formed between molecules and nanotubes. Many works have been focused on the chemical modification of CNTs surface, which can facilitate the manipulation by improving the solubility in an aqueous solvent and can give the possibility to control the nature of binding between CNTs and adsorbed molecules [11]. In addition, carbon nanotubes are also a potential adsorbent for the removal of pollutants in aqueous solutions such as contaminated water. Currently, there is concern about a global water crisis mainly because about 4% of water available in the groundwater reserves, which supply about 80% of the human population [12], is contaminated by agents such as cadmium, chromium, lead, zinc, potassium, fluorides, and pharmaceutical waste, all of which continue to deteriorate water quality. Among those agents, potassium is a very abundant element and is the seventh among all elements of the Earth's crust. As environmental effects, high levels of potassium soluble in water can cause damage to seeds in germination, inhibit the intake of other minerals and reduce the quality of the crop. Furthermore, in damage to health, a side effect of a malfunction of the kidneys can generate a buildup of potassium, thus causing a disturbance in the heart rate. It is clearly understood that it is of great interest to investigate different ways of removing contaminants in aqueous solutions. It was shown that potassium doping brings superconductivity in single walled CNTs (SWCNTs) [13, 14].

In the previous works, the investigation of binding energies, the intensity of CNTs annealed and unannealed in grazing incidence angle obtained by x-ray absorption near edge structure (XANES) show two categories of adsorbates [10, 15]. On the one hand, the intrinsic adsorbates A', A'', A''', A'''' corresponding to gas molecules (H_2O, CO, CO_2, O_2), and on the other hand the extrinsic adsorbates named P, P' and P' which are assigned to potassium (K) element [10, 15]. These results are at the origin of our curiosity consisting of studying the adsorption capability of the SWCNTs to adsorb potassium and the electronic properties of the SWCNTs adsorbent materials. Then, we performed the adsorption measurements in aqueous solutions with the potassium as adsorbate and SWCNTs as an adsorbent in addition to XANES experiments on SWCNTs and potassium adsorbed SWCNTs. The hybridization is first investigated through thermal annealing treatment onto the adsorbates on the surface of CNTs using XANES spectroscopy. The potassium adsorption behavior of SWCNTs is also studied.

2. Methodology

2.1. Materials

Single-walled carbon nanotubes grown by chemical vapor deposition (CVD) method were purchased from Sigma-Aldrich company and used as received. The characteristics are carbon content ($>$85%), carbon nanotubes ($>$75% + /−5%), diameter (1.4 + /−0.1 nm) length ($>$5 mm) and specific surface (450–550 $m^2\,g^{-1}$). The potassium nitrate (KNO_3) reagent grade ($>$98%) was supplied by CTR company (in Mexico) and used for adsorption experiments.

2.2. Adsorption experiments and characterization procedure

Data on the adsorption balance of pollutants described on single-walled carbon nanotubes were obtained in batch adsorbents according to the following methodology: In 50 ml vials, an initial volume (V_0) of 40 ml of an initial concentration (C_0) of 100 mg l^{-1} of potassium (K), was adjusted to different pH with solutions 0.01 and 0.1 N of HNO_3 and NaOH. A mass (m) of 0.01 g of SWCNTs was added. Each sample was made in triplicate. The vials were placed inside a bath at a constant temperature of 25 °C for 3 days, regulating the pH and registering for a final volume (V_f), until the balance was reached. After that, the equilibrium concentration of K (C_f) was determined as well as the adsorption capacity. The adsorption capacity (q) was calculated by means of a mass balance according to the following equation:

Figure 1. Charge distribution of SWCNTs.
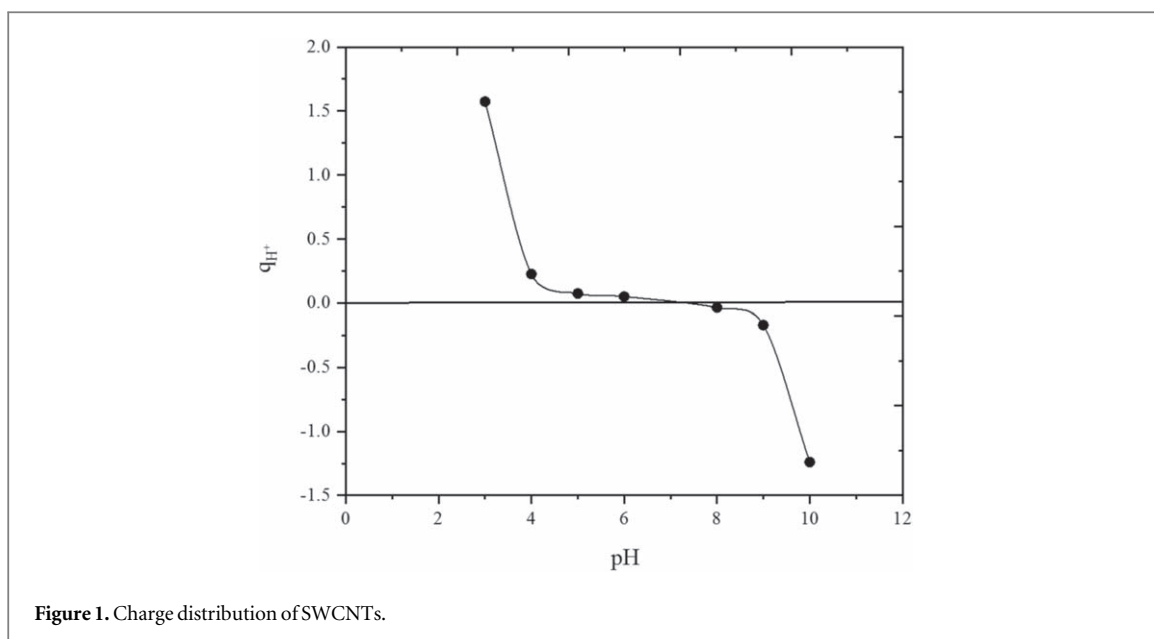
Table 1. Textural properties of SWCNTs.

Material	Surface area BET ($m^2\,g^{-1}$)	Pore volume ($cm^3\,g^{-1}$)	Pore size (nm)
SWCNTs	582	1.625	1.18
SWCNTs [18]	700	ND	ND

$$q = \frac{V_0 C_0 - V_f C_f}{m} \tag{1}$$

where:

C_0 is an initial pollutant concentration in $mg\,l^{-1}$, C_f is a final pollutant concentration also in $mg\,l^{-1}$, m is a mass of adsorbent material in g, q is an adsorbed pollutant mass per unit of adsorbent mass in $mg\,g^{-1}$, V_0 is an initial volume in L and V_f is a final volume in L.

The surface charge and zero point charge pH (pH_{ZPC}) were assessed using a potentiometric titration method proposed by Castillo *et al* [16]. This technique makes it possible to determine the acidic and basic properties of adsorbents and the nature of their functional groups.

SWCNT was analyzed by Transmission Electron Microscopy (TEM) using a JEM-2100-Jeol microscope with Oxford brand EDS probe. The surface of the carbon nanotubes was analyzed by Scanning Electron Microscopy (SEM) using a FIB/SEM FEI Helios Nanolab 600-FEI scanning electron microscope with EDAX brand EDS probe equipped with a dispersed energy micro-analysis system for elemental qualitative analysis of the surface. The elements present on the surface were identified according to the spectral positions of their characteristic peaks. This determined the point elemental chemical composition of the surface of the adsorbent particles. Surface details of SWCNTs were observed using secondary electrons (SE). Backscattered electrons (BSE) were used to visualize contrasts of shades of gray due to differences in chemical composition on the surface of particles.

The identification of the functional groups in the VA samples has been investigated by Fourier transform Infrared (FTIR) spectroscopy. The FTIR measurements were performed using OMNIC smart ITR diamond ATR (Thermo scientific Nicolet iSIO) spectrophotometer in a frequency range of 4000 to 500 cm^{-1}. For sample preparation, 200 mg of KBr has been mixed with about 2 mg of the samples to collect the FTIR spectra. KBr is used because it transmits 100% in the recorded wavenumber range and the fact that it does not show any absorption spectrum in the IR region.

2.3. XANES experiments

XANES measurements were performed at Carbon K-edge on the SWCNTs in the SACEMOR beamline [17] at the Laboratoire pour l′ Utilisation du Rayonnement Electromagnétique (LURE, ORSAY, France). A high-energy
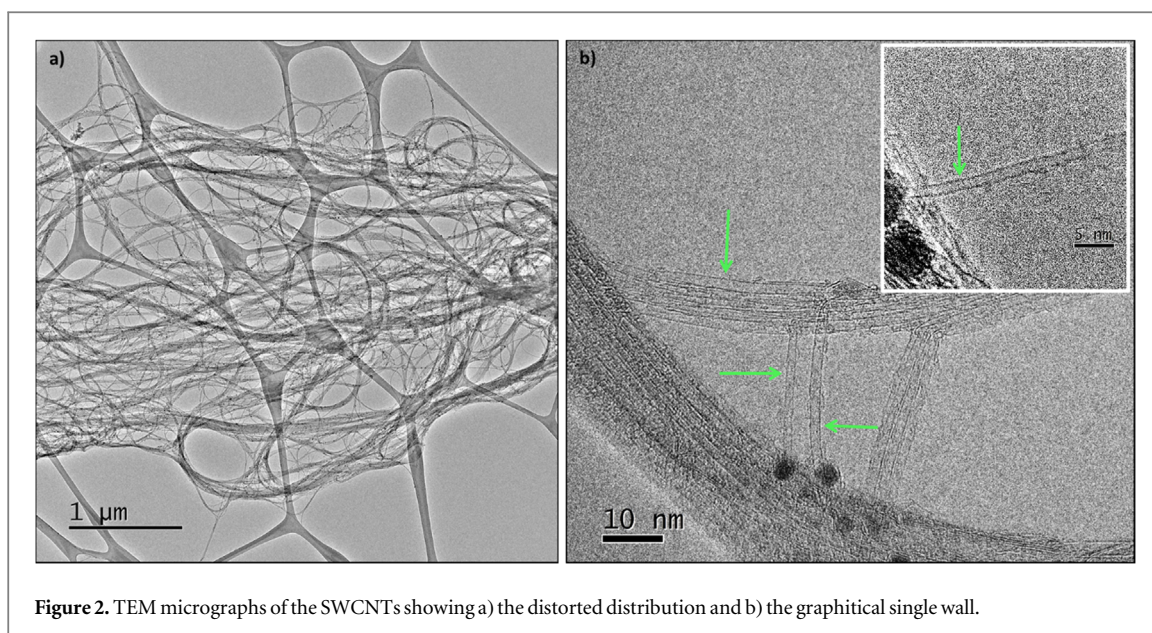
Figure 2. TEM micrographs of the SWCNTs showing a) the distorted distribution and b) the graphitical single wall.

Table 2. SWCNTs point zero charge.

Material	pH_{ZPC}
SWCNTs	6.79
NO-SWCNTs [19]	7.5
COOH-SWCNTs [19]	1.2

TGM monochromator with a resolution greater than 0.2 eV at the carbon K-edge was used. The spectra were recorded in the total-electron-yield (TEY) detection and partial-electron-yield (PEY) with the energy step of 0.1 eV and normalized to the spectrum of a copper grid freshly coated with gold. The calibration of the spectra was done using the carbon ionization potential.

3. Results and discussions

3.1. Textural properties of SWCNTs

The textural properties of single-walled carbon nanotubes determined in this study, which include the specific area, pore volume, and average pore diameter, are shown in table 1. The value of our specific area BET 582 m^2 g^{-1} is smaller than the reported by Dehghani *et al* [18], the difference can be justified by the CNTs growth, preparation, or functionalization conditions.

The pH_{ZPC} has been defined as pH, to which the net surface charge of an adsorbent in an aqueous solution is neutral. At this value, acidic or basic active groups are no longer contribute to the pH of the solution. The pH_{ZPC} value was determined by the graph in figure 1 and is mentioned in table 2 along with data from another work in which the SWCNTs were doped with NO and COOH molecules. Its surface is almost neutral. Note that the introduction of carboxylic groups to CNTs made CNTs electron acceptors [19], by increasing the adsorption of electron donors and decreasing the adsorption of electron acceptors. The difference in pH_{ZPC} values from those reported by other authors is mainly due to the origin of the material and preparation or functionalization conditions. For ionizable organic chemicals, the variation in pH can result in a change in chemical speciation, consequently altering their adsorption characteristics [19]. Increased pH generally leads to increased ionization, solubility, and hydrophilicity, and thus decreased adsorption of natural organic matter on CNTs [20, 21]. According to the results of figure 1, it is observed that its surface is almost neutral (6.79). On the other hand, at pH < pH_{ZPC}, the surface of the SWCNTs is positive and attractive to the anions in solution, and at pH > pH_{ZPC} the surface is negative with greater attraction to the cations.
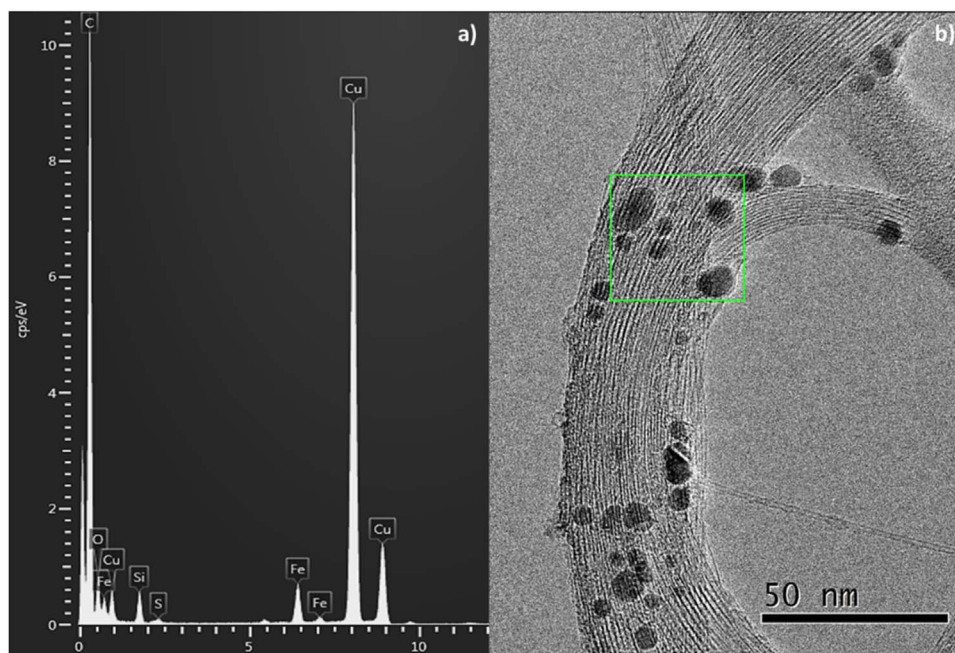
Figure 3. (a) EDS microanalysis of the (b) selected region in the SWCNTs.
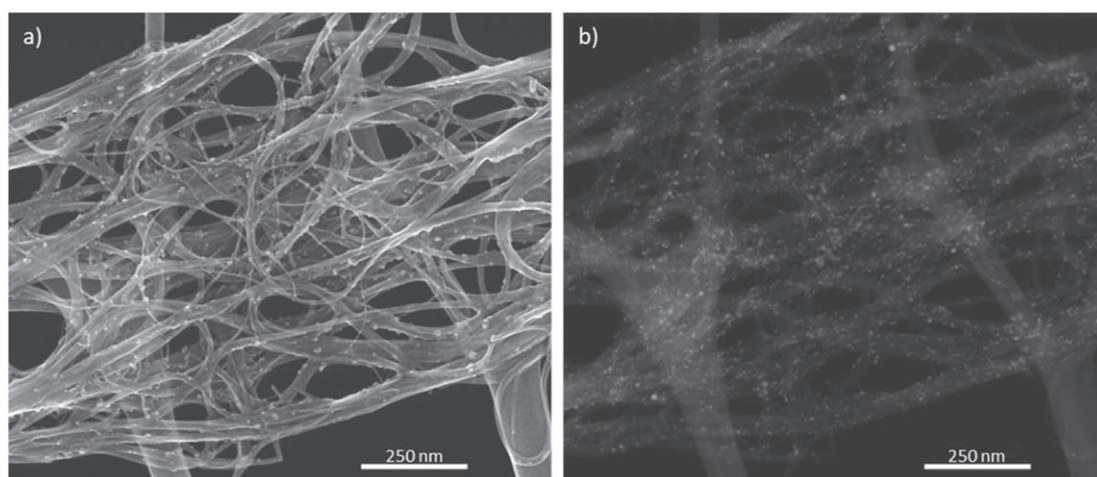
Figure 4. SEM micrographs of SWCNTs by (a) SE detector showing morphological details and (b) BSE detector, evidencing Iron homogeneous presence.

3.2. Morphological characterization by transmission and scanning electron microscopy

The surface and morphology of single-walled carbon nanotubes were observed by TEM and SEM. Figure 2(b) shows the TEM micrographs of the carbon nanotubes that allow to confirm that they are single wall type (SWCNTs) and particles onto their surface can be observed. Samples present rough surfaces and filaments of elongated and straight tubular or cylindrical shapes of a few nanometers (1.3–1.8 nm), with a distorted distribution. The diameter given by TEM is in good agreement with the value (1.4 nm) given by the supplier (see section 2.1).

In figure 3(b) spherical particles with a noticeably short size (3.0–10.0 nm) can be observed onto the tubes. Those particles may be attributed to the metal catalysts particles utilized to synthesize SWCNTs using CVD method. In addition, the elemental analysis of the chemical composition of the surface of SWCNTs was performed using Energy Dispersive Spectroscopy (EDS) coupled with TEM. Figure 3(a) shows the microanalysis by EDS in SWCNTs, the region of the chemical analysis is marked with the green square of the Figure 3(b). The analysis revealed elements as Carbon (89.87%), followed by Oxygen (5.81%), and in small proportions Iron (4.15%) and Sulphur (0.21%). The presence of Copper and Silicon is attributed to the secondary signals generated by the grid used to support the sample. The intensity of the sulfur peak is relatively too low (almost

Figure 5. SEM micrographs of SWCNTs by (a) SE detector, indicating in the green rectangle the (b) microanalysis by EDS and the respective BSE micrograph.

Figure 6. Adsorption capacity of SWCNTs for the removal of K^+ from aqueous solution.
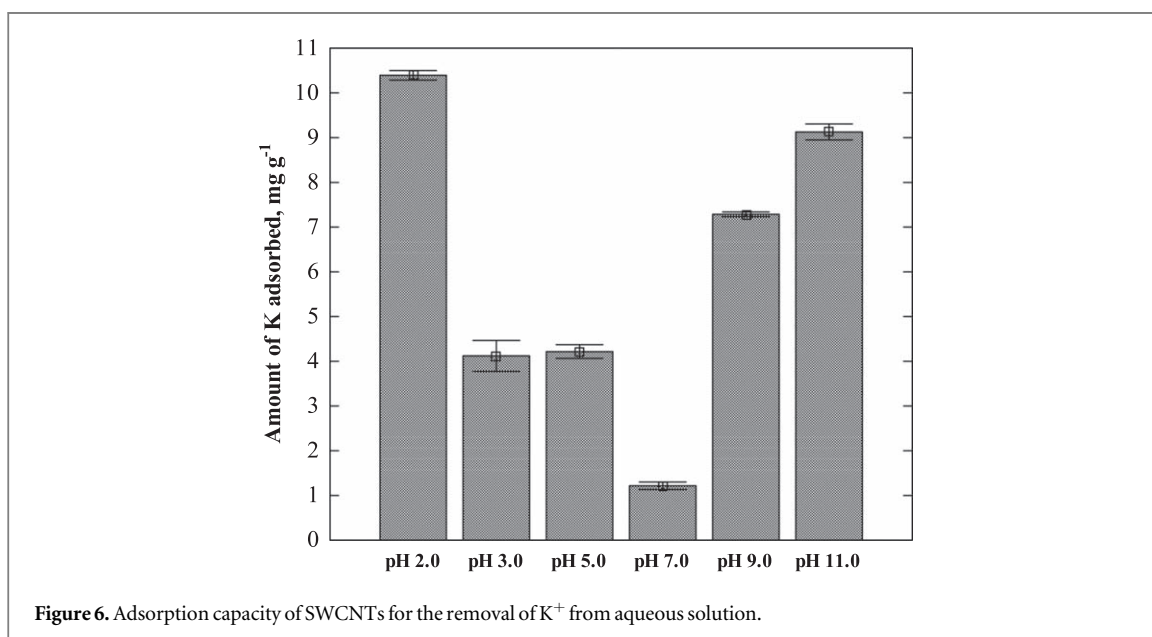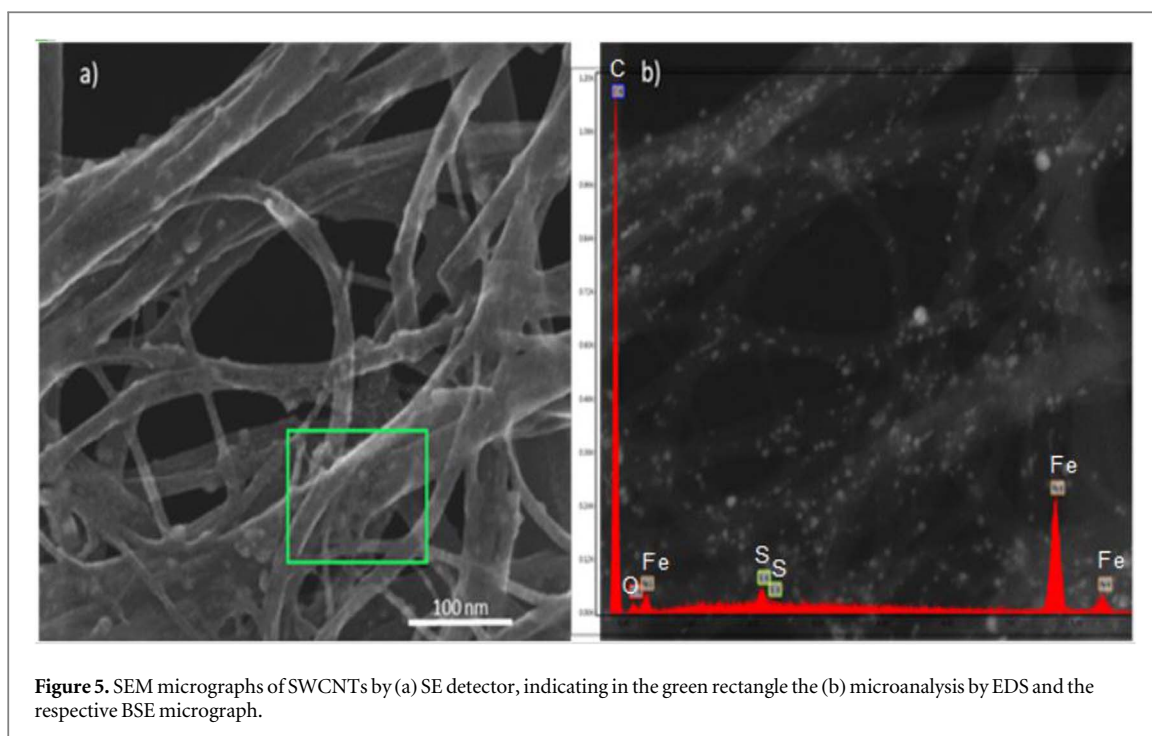
non visible) in the EDS spectrum because of its very low concentration. This can be explained by the weaker interaction between SWCNTs wall with the sulfur. Our findings are complemented by the results of Li *et al* [22] who reported that for the SWCNTs synthetised by Electric Arc (EA) denoted as S@EA-SWCNTs, the response of the Raman spectra to the presence of encapsulated sulfur is relatively modest. Thus, to provide direct information on the effect of sulfur incorporation on the electronic structure of the SWNTs, Li *et al* [22] have also examined the near-infrared and Visible (NIR/VIS) spectra of the samples and the results show that the features due to the SWCNT interband electronic transition regions have little change in the NIR/VIS spectrum of S@EA-SWCNTs.

The presence of iron can be justified by the CVD growth method used to produce the SWCNTs. In this method, metallic particles such as iron, cobalt, copper, etc, are generally used as catalysts during the synthesis procedure. Thus, some residue might remain on the surface or inside the tubes during the growth of the SWCNTs.

SEM was performed as well to enrich the SWCNTs surface characterization. Figure 4 shows a general area of the sample using SE and BSE. In figure 4(a), an aleatory arrangement can be observed as well as the presence of
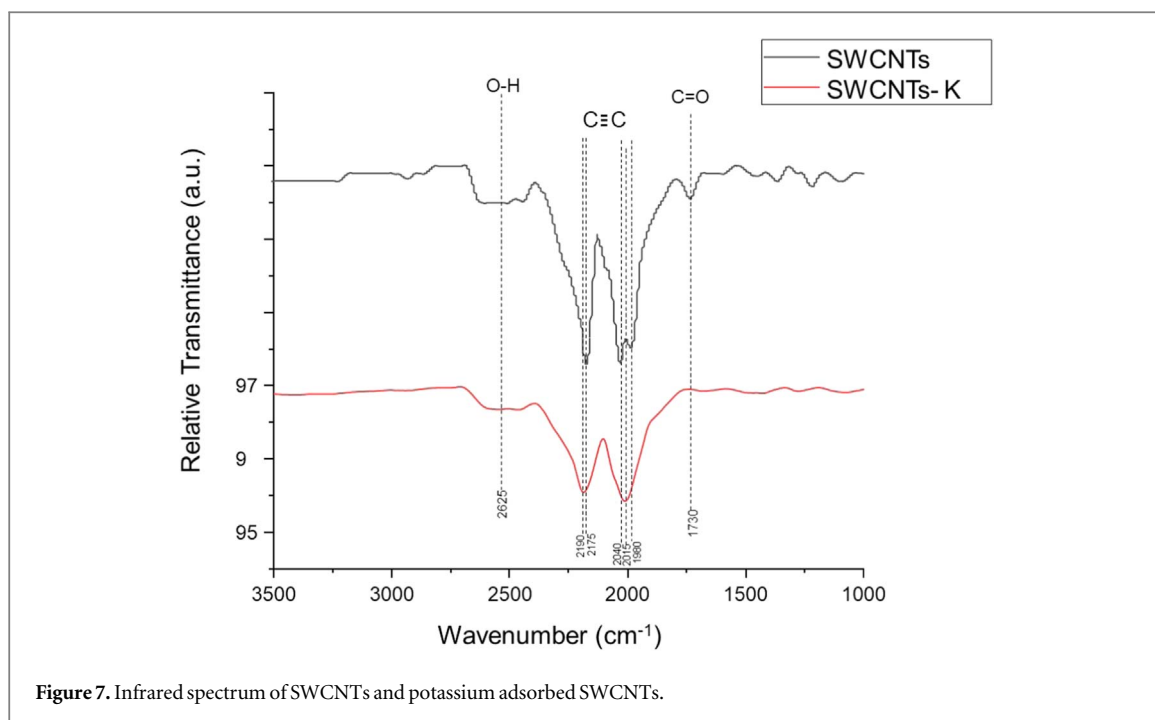
Figure 7. Infrared spectrum of SWCNTs and potassium adsorbed SWCNTs.

the spherical iron particles along carbon nanotubes. Figure 4(b) was acquired with BSE detector where the Iron particles high contrast can be appreciated, denoting a homogeneous distribution of iron.

EDS coupled with SEM was carried out in a bulk sample to confirm the elements detected by TEM-EDS. Figure 5(b) shows the microanalysis spectrum of the region marked with the green rectangle of figure 5(a). The analyses done by quintupled revealed the same elements reported previously: Carbon (87.89%), Oxygen (6.72%), Iron (5.15%) and Sulphur (0.24%), averaged values.

3.3. Adsorption capacity of K^+ contaminant with SWCNTs

The adsorption capacities of the contaminants studied at $C_0 = 100$ mg l^{-1}, and 0.01 g of SWCNTs adsorbent at different pH (2, 3, 5, 7, 9, 10, and 11) were obtained by triplicate and are shown in figure 6. The results revealed that the experiments using potassium as a contaminant lead to considerable adsorption capacity at the lowest and highest pH taken from the acidic and basic regions. The highest value 10.35 mg g^{-1} is obtained at pH 2. On the contrary, the adsorption capacity corresponding to neutral pH 7 was minimal. These results suggest that SWCNTs have a great capacity to remove potassium in the lower acidic pH and basic region. The adsorbent surface is known to be positively charged at pH $<$ pH$_{ZPC}$ [20, 21], favoring electrostatic attraction with anions on the adsorbent surface. In contrast, the electrostatic repulsion of anions is dominant at pH $>$ pH$_{ZPC}$, where the adsorbent surface is negatively charged. Potassium in an aqueous solution is a cation and its adsorption on SWCNTs could be decreased at pH $<$ pH$_{ZPC}$ if the predominant mechanism was by electrostatic attraction; however, the maximum adsorption capacity is obtained at pH 2. This can be explained by considering that K^+ could be exchanged with another cation such as Fe^{2+} on the surface of SWCNTs. The EDS analysis shown in figures 3(a) and 5(b) reveals the presence of Fe on the surface of SWCNTs so that the ion exchange mechanism can be considered. According to Yueh *et al* [23], Fe in carbon nanotubes exits in the forms of clusters and a thin layer and presented two kinds of Fe–C bonding. The bonding between the Fe cluster and the C atoms on the tube wall will be more like that of iron carbide with strong chemical bonds. While the bonding between the Fe thin layer and the graphite sheet is more like bonding between two metallic layers. Thus, the Fe cluster should interact strongly with the carbon tube.

On the other hand, the increase in K^+ adsorption capacity at pH $>$ pH$_{ZPC}$ can be attributed to the increase in the negative charge of the surface with increasing solution pH. Thus, it can be considered that K^+ is adsorbed by a mechanism of ion exchange and surface electrostatic attractions depending on the pH of the solution.

3.4. Functional groups by infrared spectroscopy analysis

Figure 7 shows the infrared spectra of SWCNTs samples compared to the potassium adsorbed SWCNTs spectra (SWCNTs-K). In these spectra, are distinguished the specific peaks corresponding to the vibrations of the OH$^-$ group which are between the bands 2475 to 2625 cm^{-1} [24]. The Li$^+$ ion solvation structures in the electrolytes were characterized with electrospray ionization mass spectrometry (ESI-MS) [25]. The authors show that the
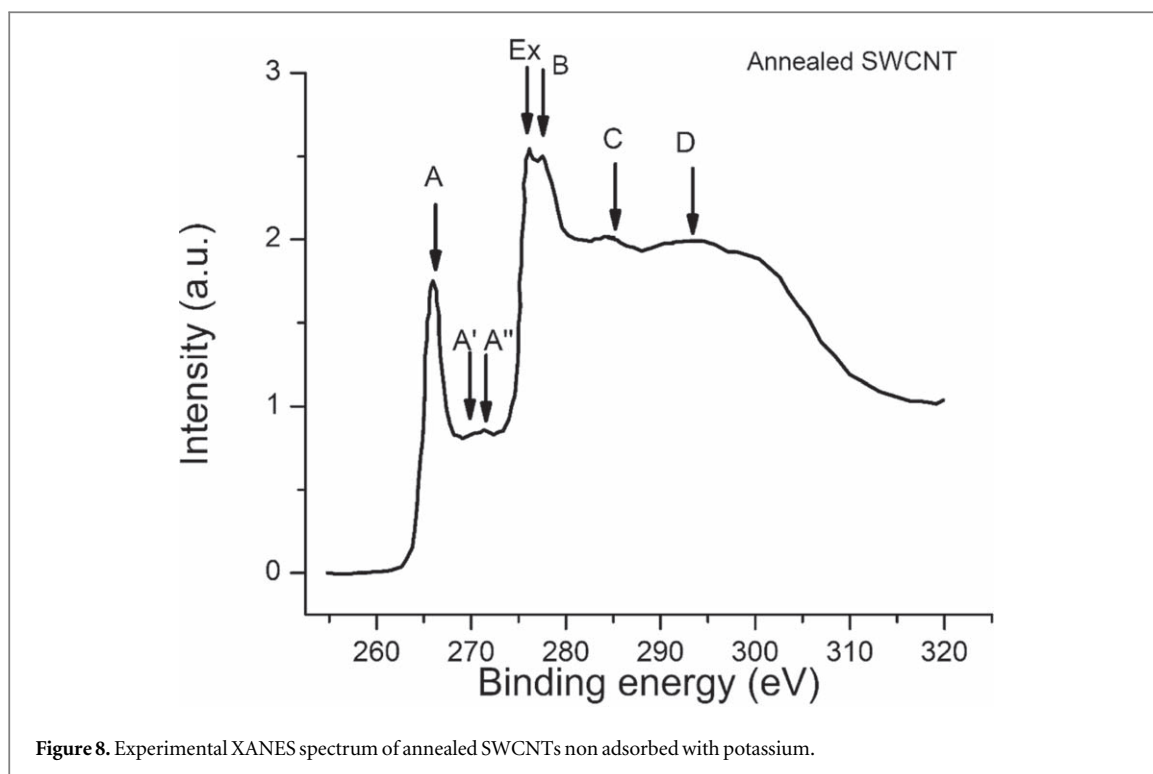
Figure 8. Experimental XANES spectrum of annealed SWCNTs non adsorbed with potassium.

Table 3. XANES adsorbates parameters for annealed SWCNTs non adsorbed with potassium. The intensity is in units of counts per second. BE stands for binding energy.

Peaks	BE (eV)	Intensity (c s^{-1})	Final states
A$'$	269.69	0.82	π^*C=C-OH/-(C= -π^*C=O)-
A$''$	271.34	0.86	π^*C=O

small peaks in the spectra can be attributed to the small amount of impurities with one -OH group instead of H in the solvent molecules. In addition, the peaks of 1980, 2015, 2040, 2175, and 2190 cm^{-1} bands are attributed to C≡C. As well, the peak 1730 cm^{-1} is assigned to the C=O band. It can be observed that in the adsorbed samples, the bands corresponding to C=O and C≡C are attenuated while that of OH–is almost identical. This may suggest that the bands C=O and C≡C are those mostly interfering in the adsorption process. The work of [25] using the *operand* Raman spectra near the radial breathing mode (RBM) show that peak diminishment in EA-SWCNTs resulting in bleaching of the optical interband transitions in the SWCNTs and suppressing the resonance character of the Raman scattering. Otherwise, the *ex situ* XPS C 1 s spectra of the lithiated and delithiated S@EA of the pristine indicate the existence of C–C bond, C–O, and isolated carbonyl C=O bonds. The latter two may arise from the impurity of the pristine SWCNTs or impurities introduced during the sulfur encapsulation. During lithiation, both C–O and C=O peaks become much more pronounced [25].

3.5. XANES results of potassium adsorbed SWCNTs

Figure 8 sketches the XANES spectrum at the carbon K (C(K))-edge of annealed SWCNTs non adsorbed with potassium and the assignment of the resolved peaks. The energies and assignments of the main peaks in the C(K) edge of annealed SWCNTs non adsorbed with potassium are summarized in table 3.

The effect of the gaseous environment on the electronic properties of CNTs has recently attracted a lot of attention [22, 26]. Because the adsorption of molecules constitutes another type of doping of CNTs. It is good to remind that the identified intrinsic adsorbates H_2O, CO, CO_2, O_2, are impurities specific to the surface of the CNTs [15, 27]. Most molecules adsorb weakly on SWCNTs and can be either charge donors or acceptors [23]. Charge donor molecules (H_2O, CO_2) interaction between the nanotubes is weak and does not have a significant influence on the electronic structures of SWCNTs [23]. Santucci *et al* [28] have proven both by theoretical and experimental methods that CO adsorb weakly on the tube wall with essentially no charge transfer between the tube and molecule. Moreover, Sankar *et al* [25] performed first-principle density functional theory (DFT) studies on the adsorption of gas molecules on (10, 0) SWCNT. Their results showed that for the adsorbed molecules (H_2O and CO), no charge transfer exists between the tube and molecule. This can also be correlated
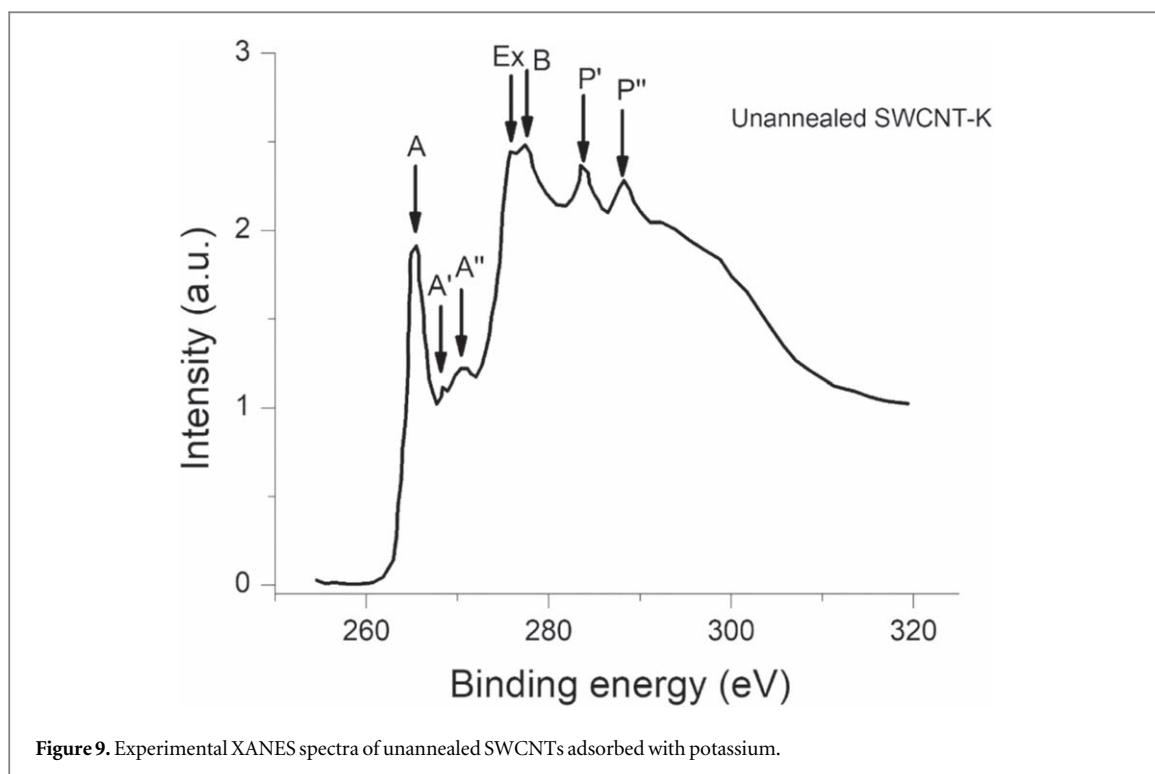
Figure 9. Experimental XANES spectra of unannealed SWCNTs adsorbed with potassium.
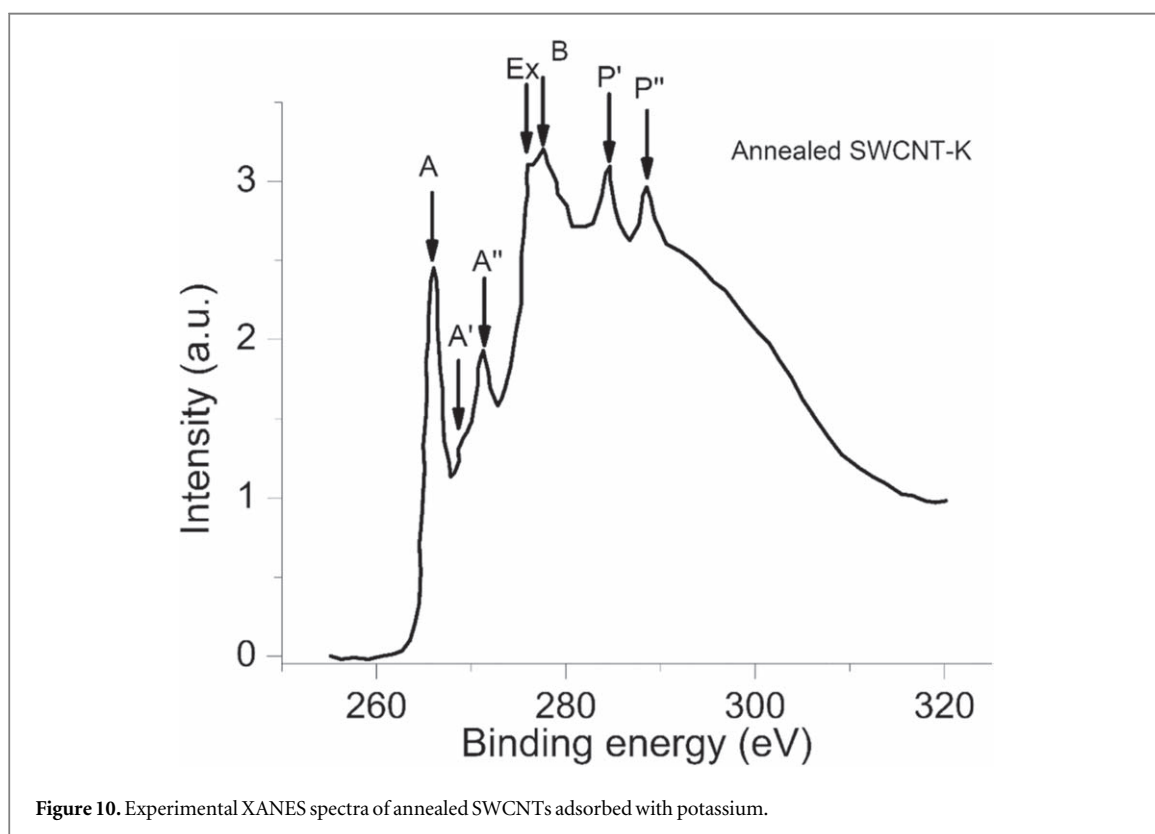
Figure 10. Experimental XANES spectra of annealed SWCNTs adsorbed with potassium.

with the adsorbate A′ in figure 8, which corresponds to the final states π^*C=C–OH/–(C=C–π^*C=O)– and is due to water molecules. It is not also sensitive enough to the thermal treatment suggesting the negligible charge transfer between the surface of CNTs and water molecules. The charge transfer is not negligible for O_2 and NO_2 which are both charge acceptors [23]. The bond length of C–C after adsorption of oxygen molecule on the external surface of nanotube increases since oxygen is more electronegative than carbon [29]. The interaction between O_2 molecules and SWCNT is much more pronounced, and SWCNT can be turned into a p-type conductor after NO_2 or O_2 adsorption [23] as it can be observed for the adsorbate A″ (π^*C=O) affected mainly

Table 4. XANES adsorbates parameters for unannealed SWCNTs adsorbed by potassium. The intensity is in units of counts per second. BE stands for Binding energy.

Peaks	BE (eV)	Intensity (c s^{-1})	Final states
A′	268.36	1.12	π^*C=C–OH/–(C=C–π^*C=O)–
A′	270.37	1.22	π^*C=O
P′	283.48	2.37	Potassium L$_2$-L$_1$
P′	288.21	2.28	Potassium L$_2$

Table 5. XANES adsorbates parameters for annealed SWCNTs adsorbed by potassium. The intensity is in units of counts per second. BE stands for Binding energy.

Peaks	BE (eV)	Intensity (c s^{-1})	Final states
A′	268.64	1.31	π^*C=C–OH/–(C=C–π^*C=O)–
A′	271.26	1.93	π^*C=O
P′	284.66	3.09	Potassium L$_2$–L$_1$
P′	288.52	2.97	Potassium L$_2$

by thermal annealing. This suggests that the curvature affects the physical, electronic, and chemical properties of the CNTs and has a significant effect on the desorption process [23, 30, 31]. It is revealed that the contribution of gas molecules is 23.7% in SWCNTs. This observation can be assigned to the electronic behavior of gas molecules and especially to the strong interaction of O$_2$ with the surface of CNTs. This can be correlated with some results, including nuclear magnetic resonance (NMR), which proved the increase of density of states at the Fermi level of SWCNTs after exposure to oxygen [32]. More to that, Collins *et al* [26] found that oxygen gas has dramatic effects on conductivity. The FTIR also showed that the functional groups at the surface of SWCNTs are principally OH$^-$, C=O and C≡C.

According to our previous results [10, 15], the two dominant peaks near 265.94 eV (A) and 277.54 eV (B) were associated with an unoccupied π^* and σ^* band, respectively. The features corresponding to C and D respectively at 284,43 eV and 293.05 eV were associated with σ-symmetry while Ex. at 276.14 eV was correlated to σ^* exciton (C–H* bond resonance).

Similar dominant peaks (A) and (B) are observed in the work of Zhong *et al* [33] on a SWCNT treated with the LiOH water. After a fitting process of their data (using the Igor package), they obtained two other picks like A′ and A″ of the present work. According to the reported XANES data, the first one A′ has been assigned to π^* (C–OH) and the second one A″ to π^* (C = O). Zhong *et al* [33] have also found a third pick attributed to σ^* (C–O) when the SWCNT material was treated by immersion in a 1 M LiOH water solution at pH = 12 for five days. Of all the above, the appearance of the peaks A′ and A″ clearly demonstrates the involvement of functional groups in the adsorption process; which will affect the atomic and electronic structures of SWCNTs. Let us stress that the heat exchange through the annealed process has been shown to cause changes in the binding energy and the intensity of the adsorbates. Compared to our previous results [10, 15], we note that the peaks A‴, A⁗ and P are not observed in our present spectra due to their extremely low resolution. Thus, we will focus only on the visible peaks in the following.

Figures 8 and 9 show XANES spectra of the carbon K (C(K)) edge of unannealed and annealed SWCNTs adsorbed with potassium and the assignment of the resolved peaks. The energies and assignments of the main peaks in the C(K) edge of unannealed and annealed SWCNTs adsorbed with potassium are summarized in tables 4 and 5. It is observed that the intensities of different adsorbates are superior for the annealed samples suggesting that the thermal treatment can affect the adsorbates whatever their origin. For annealed samples, the disappearance of peak A′ and the resolution of peak A″ can be noticed. The increase in the peaks P′ and P″ can also be seen. However, no change is seen in the shape of the peaks P′ and P″. These results showed that in the SWCNTs, the intrinsic adsorbates are less sensitive than the extrinsic adsorbates. Thus, the hybridization of the nanotubes can be affected.

Concerning the non adsorbed (figure 8 and table 3) and the adsorbed annealed samples (figure 10 and table 5), one can observe that the labeled main peaks in the spectrum of the latter are better resolved. Peak A′ is sharper and peak A″ is more intense in the adsorbed annealed samples (figure 10). The two intense peaks P′ and P″ which are due to potassium are in the position of peaks C and D in the non adsorbed spectrum. The adsorption process has brought a great change in the spectrum suggesting that the electronic properties of the

samples as well as the hybridization, can be modified by means of adsorption or doping. They can vary depending on the nature and the type of adsorbates utilized to remove the pollutants when using SWCNTs.

Our results also show that the conductivity of the SWCNTs is first modified and then improved by 75%. After thermal annealing, 41% of gas molecules still adsorbed against 75% of potassium. In addition, for 75% of the potassium adsorbates on the surface of SWCNTs, the contribution of the adsorbates gas molecules increases by 17.3%. Thus, the performance of SWCNTs depends on a better understanding of the functionalities at the CNTs's surface. The tube molecules' interaction may substantially affect the carbon nanotubes and lead to the applications like chemical sensors.

Intensities of adsorbates are directly correlated to carbon hybridization since the reactivity is connected to the diameter and type of hybridization in CNTs. It is seen that the values of the binding energy change from unannealed to annealed samples due to the thermal annealing treatment. The intensities of all adsorbates are decreasing from unannealed to annealed samples in SWCNTs. These results suggest that the binding energy, as well as the intensity of the intrinsic adsorbates, strongly depend on the diameter (curvature) of the CNTs. It can be understood that the adsorbates bonding can be affected by the thermal annealing process. They can either be shrunk or lengthened depending on the degree of thermal treatment. This could somehow affect the hybridization of the CNTs. The results are in good agreement with Ref. [34], where the SWCNTs are stated to be more reactive than multi walled CNTs (MWCNTs). Indeed, the great chemical reactivity of the SWCNTs is the consequence of the external arrangement of the pyramidized carbon atoms sp^2 arranged correctly for the formation of chemical bonds with the reactive species. Thus, CNTs having large curvature require less geometric deformation and hybridization change to accept an adsorbate. In addition, the effects of heat exchange have been shown to cause changes in the binding energy and the intensity of the adsorbates.

As shown earlier, the adsorbates are more sensitive in SWCNTs. The intensity of adsorbates A′ corresponding to the final states $\pi^*C=O$ is strongly affected in SWCNTs by thermal annealing treatment, as well as that of peaks P′ and P″ which are assigned to the final potassium states L2-L1 and L2. This suggests that the height of these adsorbates can be considerably reduced by heat treatment. This can be explained since it is known that one of the main objectives of thermal annealing is to minimize impurities. Other adsorbates are less sensitive to thermal treatment. All adsorbates are affected differently by interaction with each CNT's surface, creating a different environment that can alter molecular reactivity. These results show that the adsorbates are influenced by thermal annealing leading to the changes in the curvature and hybridization in SWCNTs nanomaterials. A thorough XANES study needs to be done to understand the process better.

4. Conclusion

In this paper, the electronic structure of potassium adsorbed single-walled carbon nanotubes has been investigated by x-ray near edge structure spectroscopy. We noticed that: the highest adsorption capacity for the removal of potassium by SWCNTs is obtained at pH 2 suggesting that the ion exchange can be assigned to the adsorption mechanism. Also, electrostatic attractions are involved during the potassium adsorption, mainly at pH > pH_{PZC}. TEM and SEM micrographs confirmed the single wall type of carbon nanotubes and an aleatory arrangement of SWCNTs, as well as the presence of the spherical iron particles along carbon nanotubes. The Carbon, Oxygen, Iron, and Sulphur elements are detected at the surface of SWCNTs and Iron may be attributed to the metal catalysts particles used during the synthesis. The infrared spectroscopy shows that the functional groups involved in the adsorption process are OH^-, C=O and C≡C. XANES spectroscopy has identified two intrinsic peaks corresponding respectively to the adsorbates associated to the $\pi^*C=C–OH/–(C=C–\pi^*C=O)$ and $\pi^*C=O$. The non-intrinsics peaks are attributed to potassium L2-L1 and L2 bands. XANES spectra show the difference between the adsorbates of non adsorbed and potassium adsorbed SWCNTs, suggesting that the sample's surface has been modified due to the adsorption process. The effect of thermal annealing on the interaction between adsorbates and SWCNTs was investigated. The conductivity of SWCNTs is increasing by 62.7%. The oxygen molecule has a significant effect on the conductivity of SWCNTs. The adsorbates are affected by thermal annealing treatment leading to the changes in curvature and hybridization in CNTs.

Acknowledgments

Data availability statement

The data that support the findings of this study are available upon reasonable request from the authors.

Conflict of interest

The authors declare that they have no conflict of interest.

ORCID iDs

Bridinette Thiodjio Sendja ⬤ https://orcid.org/0000-0003-1421-8388
Marius Silenou Mengoue ⬤ https://orcid.org/0000-0001-6192-2402

References

[1] Iijima S 1991 Helical microtubules of graphitic carbon *Nature* **354** 56–8

[2] Bernholc J, Brenner D, Buongiorno Nardelli M, Meunier V and Roland C 2002 Mechanical and electrical properties of nanotubes *Annu. Rev. Mater. Res.* **32** 347–75

[3] Park S, Srivastava D and Cho K 2001 External chemical reactivity of fullerenes and nanotubes *Mat. Res. Soc. Symp. Proc.* **675** 151

[4] Harris P J F 1999 *Carbon Nanotubes and Related Structure* (Cambridge: Cambridge University Press) pp 65–6 (http://assets. cambridge.org)

[5] Yu O, Jing-Cui P, Hui W and Zhi-Hua P 2008 The rehybridization of electronic orbitals in carbon nanotubes *Chin. Phys. B* **17** 3123–9

[6] Soni S, Salhotra A and Suar M 2014 *Handbook of Research on Diverse Applications of Nanotechnology in Biomedicine, Chemistry, and Engineering* (USA: Engineering Science Reference) p 820

[7] Ding Y, Yang X-B and Ni J 2006 Adsorption on the carbon nanotubes *Front. Phys. China* **3** 317–22

[8] Blanco A A G, Rocha J V, Múnera J F, Nazzarro M, Zgrablich G and Sapag K 2011 A study of the adsorption properties of single walled carbon nanotubes treated with nitric acid *Ads. Sci. Tech.* **29** 705–22

[9] Salam M A, Al-Zhrani G and Kosa S A 2014 Removal of heavy metal ions from aqueous solution by multi-walled carbon nanotubes modified with 8-hydroxyquinoline: Kinetic study *J. Ind. Eng. Chem.* **20** 572–80

[10] Tchenguem Kamto C R, Thiodjio Sendja B, Mane and Mane J 2019 Adsorption and desorption phenomena on thermally annealed multi-walled carbon nanotubes by XANES study *Chin.Phys. B.* **28** 093101

[11] Georgakilas V, Kordatos K, Prato M, Guldi D M, Holzinger M and Hirsch A 2002 Organic functionalization of carbon nanotubes *J. Am. Chem. Soc.* **124** 760–1

[12] 2010 Statistics on Water in Mexico, 2010 edition published by National Water Commission of Mexico Edited by Ministry of Environment and Natural Resources, Mexico www.conagua.gob.mx

[13] Hebard A F, Rosseinsky M J, Haddon R C, Murphy D W, Glarum S H, Palstra T T M, Ramirez A P and Kortan A R 1991 Superconductivity at 18 K in potassium-doped C60 *Nature* **350** 600–1

[14] Hannay N B, Geballe T H, Matthias B T, Andres K, Schmidt P and MacNair D 1965 Superconductivity in graphitic compounds *Phys. Rev. Lett.* **14** 225

[15] Mane Mane J, Thiodjio Sendja B and Eba Medjo R 2015 Contribution of carbon nanotubes cap to XAS signal: a review *J. Mater. Sci. Appl.* **1** 195–220 (http://www.aascit.org/journal/jmsa)

[16] Medellin-Castillo N A *et al* 2007 Adsorption of fluoride from water solution on bone char *Ind. Eng. Chem. Res.* **46** 9205–12

[17] Eba Medjo R, Thiodjio Sendja B and Mane Mane J 2014 Curvature, hybridization and contamination of carbon nanostructures analysis using electron microscopy and XANES spectroscopy *Materials Sciences and Applications* **5** 95–103

[18] Dehghani M H, Taher M M, Bajpai A K, Heibati B, Tyagi, Asif M and Gupta V K 2015 Removal of noxious Cr (VI) ions using single-walled carbon nanotubes and multi-walled carbon nanotubes *Chem. Eng. J.* **279** 344–52

[19] Pan B and Xing B 2008 Adsorption mechanisms of organic chemicals oncarbon nanotubes *Environ. Sci. Technol* **42** 9005–13

[20] Wang S G, Liu X W, Gong W X, Nie W, Gao B Y and Yue Q Y 2007 Adsorptionoffulvicacidsfrom aqueous solutions by carbonnanotubes *J. Chem. Technol. Biotechnol.* **82** 698–704

[21] Lu C Y and Su F S 2007 Adsorption of natural organic matter by carbonnanotubes *Sep. Purif. Technol.* **58** 113–21

[22] Li G *et al* 2015 Giant raman response to the encapsulation of sulfur in narrow diameter single-walled carbon nanotubes *J. Am. Chem. Soc.* **138** 40–3

[23] Yueh C L *et al* 2001 Electronic structure of the Fe-layercatalyzed carbon nanotubes studied by xray-absorption spectroscopy *Appl. Phys. Lett.* **79** 3179

[24] McPhail M R, Sells J A, He Z and Chusuei C C 2009 Charging nanowalls: adjusting the carbon nanotube isoelectric point via surface functionalization *J. Phys. Chem. C* **113** 14102–9

[25] Fu C *et al* 2018 Confined lithium-sulfur reactions in narrow-diameter carbon nanotubes reveal enhanced electrochemical reactivity *ACS. Nano.* **12** 9775–84

[26] Medellin-Castillo N A, Leyva-Ramos R, Padilla-Ortega E, Ocampo P R, Flores Cano J V and Berber-Mendoza M S 2014 Adsorption capacity of bone char for removing fluoride from water solution. Role of hydroxyapatite content, adsorption mechanism and competing anions *J. Ind. Eng. Chem.* **20** 4014–21

[27] Yang Y, Ling Y and Chen J P 2015 Adsorption of fluoride by Fe–Mg–La triple-metal composite: Adsorbent preparation, illustration of performance and study of mechanisms *Chem. Eng. J.* **262** 839–46

[28] Santucci S, Picozzi S, Di Gregorie F, Lozzi L, Cantalini C, Valentini J M L and Delley B K 2003 NO2 and CO gas adsorption on carbon nanotubes; Experiment and theory *J. Chem. Phys.* **119** 10904–10

[29] Collins P G, Bradley K, Ishigami M and Zettl A 1801 Extreme oxygen sensitivity of electronic properties of carbon nanotubes *Sci.* **287** 1801–4

[30] Mintmire J W, Dunlap B I and White C T 1992 Electronic and structural properties of carbon nanotubes *Phys. Rev. Lett.* **68** 631

[31] Blasé X, Benedict L X, Shirley E L and Louie S G 1994 Hybridization effects and metallicity in small radius carbon nanotubes *Phys. Rev. Lett.* **72** 1878

[32] Thiodjio Sendja B, Eba Medjo R, Mane Mane J, Ben-Bolie G H and Owono A P 2015 Theoretical investigation of x-ray absorption near edge spectroscopy (XANES) angular dependence of aligned carbon nanotubes grown by DC HF CVD process *Materials Sciences and Applications* **6** 373–90

[33] Zhong J, Song L, Chiou J, Dong C, Liang X and Wu Z 2010 Electronic structure study of modified single-walled carbon nanotubes by soft-x-ray absorption and resonant emission spectroscopy *Appl. Phys. Lett.* **96** 213112

[34] Zhao J, Buldum A, Han J and Lu J P 2002 Gas molecule adsorption in carbon nanotubes and nanotube bundles *Nanotech.* **13** 195–200

[35] Gowri Sankar P A and Udhayakumar K 2013 Electronic properties of boron and silicon doped (10, 0) zigzag single-walled carbon nanotube upon gas molecular adsorption: a DFT comparative study *J. Nanomaterial* 1–12

Adsorption and desorption phenomena on thermally annealed multi-walled carbon nanotubes by XANES study

Camile Rodolphe Tchenguem Kamto[1], Bridinette Thiodjio Sendja[2,†], and Jeannot Mane Mane[2,3]

[1] *University of Yaounde I, Faculty of Science, Department of Physics, Yaounde, Cameroon*

[2] *University of Yaounde I, National Advanced School of Engineering, Department of Mathematic and Physical Science, Yaounde, Cameroon*

[3] *University of Dschang, Dschang, Cameroon*

The multi-walled carbon nanotubes (MWCNTs) studied in this work were synthesized by the catalytic chemical vapor deposition (CCVD) process, and were thermally annealed by the hot filament plasma enhanced (HF PE) method at 550 °C for two hours. The x-ray absorption near edge structure (XANES) technique was used to investigate the adsorption and desorption phenomena of the MWCNTs at normal and grazing incidence angles. The adsorbates were found to have different sensitivities to the thermal annealing. The geometry of the incident beam consistently gave information about the adsorption and desorption phenomena. In addition, the adsorption of non-intrinsic potassium quantitatively affected the intrinsic adsorbates and contributed to increase the conductivity of the MWCNTs. The desorption of potassium was almost 70% greater after the thermal annealing. The potassium non-intrinsic adsorbates are from a physisorption mechanism whereas the intrinsic adsorbates result from chemisorption.

Keywords: multi-walled carbon nanotubes, thermal annealing, adsorption, desorption

PACS: 31.10.+z, 31.15.ae, 32.30.Rj, 82.80.Dx　　　　　　**DOI:** 10.1088/1674-1056/ab3437

1. Introduction

The theoretical and experimental knowledge of the structure of a system is required to elucidate new materials with novel properties. Carbon nanotubes (CNTs) have intensively undergone theoretical and experimental studies because of their versatilities. During the first decade of the discovery of CNTs by Sumio Iijima, they were usually obtained at high temperature (about 3500 °C) using graphite electrodes by the electric discharge process.[1] Nowadays, they are produced in industries at intermediate temperatures (between 700–950 °C) by the well-known catalytic chemical vapor deposition (CCVD) process,[2,3] electric discharge,[1] or laser ablation.[4] Among these, CCVD is one of the most suitable methods for synthesizing aligned CNTs since it can be carried out at low temperatures and pressures.[5] However, CCVD synthesized CNTs usually contain catalytic metallics and impurities whose nature and proportion depend on the synthesis parameters. The presence of impurities can significantly affect the properties of CNTs and consequently the global behavior of these materials.[6] The samples studied herein are multi-walled CNTs (MWCNTs) synthesized by the hot filament plasma enhanced catalytic chemical vapor deposition (HF PE CCVD) process fully described in Ref. [7]. CNTs are mostly characterized by scanning electron microscopy (SEM)[8] and transmission electron microscopy (TEM),[9] which are both qualitative methods. These techniques do not give enough information about the electronic and structural properties of the CNTs. The x-ray absorption near edge structure (XANES)

technique on the contrary is a powerful tool that provides the structural and electronic information on the local environment around the absorber atom in the medium range order due to its angular dependence of the absorption transition.[7] This technique is sensitive to the chemical adsorption and impurities, defects, and orbital rehybridization.[7] MWCNTs with large diameter are advantageous for various applications like molecular compounds for instance, in organic solar cells,[10] infrared detectors,[11] and biological systems.[12] The adsorption and desorption phenomena of the MWCNTs are of great interest since they provide a full understanding of the performance for water and wastewater treatment applications.

In this study, through XANES technique, we investigate the adsorption and desorption phenomena of MWCNTs grown by CCVD process and thermally annealed at 550 °C. The XANES spectra are collected at normal incidence (NI) and grazing incidence (GI) angles to evaluate the adsorption percentage.

2. Theory

MWCNT is made up of a bundle of single walled CNTs (SWCNT) arranged such that they all have the same vertical axis. The external diameter of the MWCNT depends on the growth process. By the electric arc discharge, the external diameter is about 20 nm, whereas it can reach 100 nm with the CCVD process.[2] In general, as a consequence of the synthesis process, the surfaces of the CNTs are usually covered by some adsorbates mostly considered as impurities.[13] These

---

adsorbates can affect, in different ways, the structure of the surfaces since they can be linked physically by van der Waals forces or chemical covalent bonds.[13] The former is named physisorption mechanism while the latter is chemisorption. If the free bonds are saturated, the strongly linked adsorbates can either eliminate or favor the restructuring of the free surface, which thus may or may not affect the properties of the surface.[13] It has been established that the Lennard–Jones interactions prevail in the adsorption mechanism,[14] suggesting that the interaction potential V between two species with a distance r can be written as a sum of the terms of the repulsion and attraction contributions, as follows:

$$V = \varepsilon \left[\left(\frac{r_0}{r} \right)^{12} - 2 \left(\frac{r_0}{r} \right)^6 \right], \quad (1)$$

where ε and r_0 are the Lennard–Jones parameters for each couple of species at the equilibrium distance.

Chemisorption is a dominant process in SWCNTs.[15] On the contrary, physisorption, which is a characteristic of MWCNTs, is a reversible process that can occur at low temperatures.[15] Adsorption capacity depends on the specific surface area and the number of walls in the MWCNT. The specific surface area reduces with an increase in diameter and in the number of walls.[16] The average specific surface area of the MWCNTs is between 30 m²/g and 400 m²/g depending on the mean diameter and the number of walls.[16] The specific surface area S of a MWCNT is given by[16]

$$S = \frac{2}{\rho(R_1 - R_2)} = \frac{2630}{n} \quad [\text{m}^2/\text{g}], \quad (2)$$

where R_1 and R_2 are the external and internal radii, respectively, and n is the number of walls. In the above formula, the density $\rho = 2.26$ g/cm³ and $R_1 - R_2$ is 3.36 Å, which correspond to those of graphite. Physisorption offers the possibility to modify the electronic properties of the substrate. The adsorbate species can leave the surface, leading to desorption, their speciation and the determination of their characteristics

can allow to extract valuable information on the desorption process. This can be done by breaking the chemical or physical bonds existing on the surface. XANES spectroscopy is a powerful tool that can give structural and electronic information on the atoms and molecules as well as the local chemical functionalities.[17] The experimental details and the CCVD growth process of our studied MWCNTs have been fully described elsewhere.[7,18]

3. Results and discussion

The XANES spectra collected at the carbon K edge are shown in Figs. 1 and 2. The data have been collected at normal incidence angle ($\theta = 0°$ with $\boldsymbol{E}$ parallel to the surface) (Figs. 1(a) and 2(a)) and at grazing incidence angle ($\theta = 90°$ with $\boldsymbol{E}$ normal to the surface) (Figs. 1(b) and 2(b)). Note that θ is the angle between the axis of the sample and the direction of the electric field vector $\boldsymbol{E}$ of the x-ray incident beam. The XANES spectra can be divided into three main regions as described in Ref. [18]. The first region located at 285.5 eV corresponds to peak A. The second region between 286.5 eV and 290.5 eV is assigned to the free electron like interlayer (FELI) states and the adsorbed or chemisorbed molecular states. The third region, corresponding to the transitions towards the σ^* and π^* empty states is above 291.8 eV. From our XANES spectra, the intrinsic and non-intrinsic adsorbates can be distinguished. The intrinsic adsorbates, namely, A′, A″, A‴, and A⁗ are the results of the gas, atomic, and/or molecular adsorption of different species such as oxygen (O_2), water (H_2O), and transition metals (TM) during the synthesis process.[7,19] The non-intrinsic adsorbate observed in our XANES spectra (Fig. 2) is attributed to the potassium element which appears accidentally during the synthesis process.[18]

Tables 1 and 2 show the intrinsic and non-intrinsic adsorbates with their corresponding intensities and final states in the Brilouin zone, for annealed and un-annealed samples contaminated with potassium, respectively.
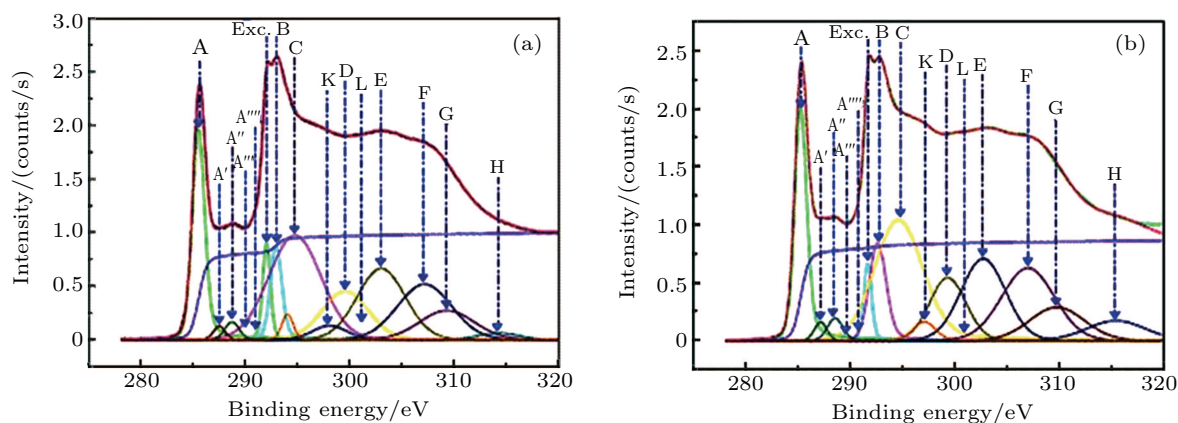
Fig. 1. Experimental and simulated XANES spectra of MWCNTs annealed and without contaminants at (a) normal and (b) grazing incidences.
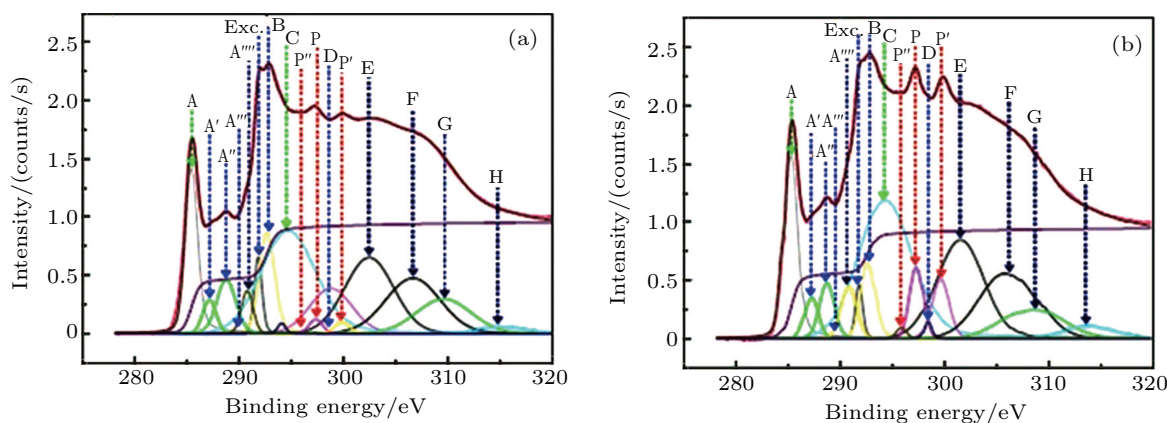
Fig. 2. Experimental and simulated XANES spectra of MWCNTs annealed and contaminated with potassium at (a) normal and (b) grazing incidences.

Table 1. Main feature parameters for annealed and potassium-contaminated MWCNTs from XANES spectra at normal and grazing incidence angles. The intensity is in units of counts per second.

Adsorbates	Energy/eV	Intensity at NI	Intensity at GI	Final-state band and Brillouin-zone
A′	286.53	0.46	0.46	free-electron-like interlayer states + adsorption
A″	288.40	1.10	1.02	free-electron-like interlayer states + adsorption
A‴	288.70	0.0	0.0	free-electron-like interlayer states + adsorption
A⁗	290.70	0.52	0.63	free-electron-like interlayer states + adsorption
P″	297.51	0.0	0.0	potassium L_2 level
P	296.60	0.19	0.17	potassium L_2, L_3 level
P′	299.83	0.17	0.20	potassium L_2–L_1 levels

Table 2. Main feature parameters for unannealed and potassium-contaminated MWCNTs from XANES spectra at grazing and normal incidence angles. The intensity is in units of counts per second.

Adsorbates	Energy/eV	Intensity at NI	Intensity at GI	Final-state band and Brillouin-zone
A′	286.53	0.67	0.86	free-electron-like interlayer states + adsorption
A″	288.40	1.57	1.90	free-electron-like interlayer states + adsorption
A‴	288.70	0.0	0.29	free-electron-like interlayer states + adsorption
A⁗	290.70	0.85	1.10	free-electron-like interlayer states + adsorption
P″	297.51	0.03	0.03	potassium L_2 level
P	296.60	1.02	1.39	potassium L_2, L_3 level
P′	299.83	1.39	1.55	potassium L_2–L_1 levels

Each adsorbate corresponds to a specific electronic transition which is assigned to peaks A′, A″, A‴, and A⁗ or P, P′, and P″. These peaks are strongly linked to the height of the adsorbates. Also, the probability for a chemical species to be adsorbed depends on the nature of the surface. The types of bonds and the associated physical properties considerably depend on the types of the adsorbed atoms.[22] The quantity of the adsorbates on the surface varies as a function of the curvature radius of the CNTs since the adsorption strongly depends on the specific surface area.[19]

The individual contributions of the adsorbates present in our samples exhibit significant differences at normal and grazing incidence angles. During the adsorption process, rehybridization can occur in which the sp^2 and sp^3 orbitals are mixed leading to two free hybrid orbitals. Such that, if the contribution of sp^3 increases, this will lead to the presence of more free bonds, resulting in the increase of the reactivity.

Figure 3 presents a comparison of the histogram of the

intensities of the contaminated MWCNTs un-annealed and annealed for different adsorbates at normal and grazing incidence angles respectively.
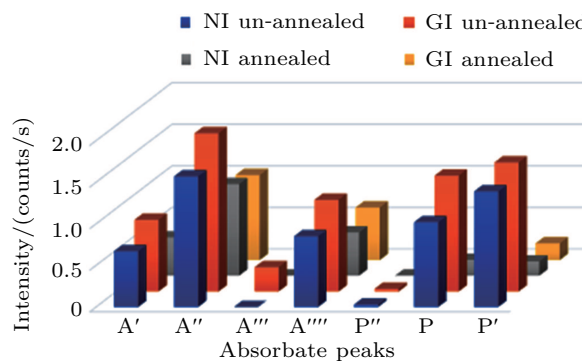
Fig. 3. The trend of the intensities of the adsorbates for the contaminated un-annealed and annealed MWCNTs at normal and grazing incidence angles.

Comparing the intensities of the annealed and unannealed contaminated MWCNTs shows that the non-intrinsic

adsorbates A′ and A‴ almost disappear in the presence of potassium adsorbates in the two studied angles. The quantity of the intrinsic adsorbates considerably reduces after the thermal annealing process at normal and grazing incidences. It can also be seen that the non-intrinsic adsorbates are less sensitive to the thermal treatment. However, it is shown that when the potassium is adsorbed at 12%, the intrinsic adsorbates increase by 2.12 and 1.64 times at normal and grazing incidence angles, respectively. At normal incidence, the x-ray beam is parallel to the surface of the sample, hence the π states are excited to π^* and some adsorbed chemical species are masked by others. On the contrary, at grazing incidence where the x-ray beam is perpendicular to the surface, the σ states are excited to σ^*. These findings show that the adsorption process is also affected by the direction of the x-ray beam as demonstrated by Huang *et al.*[6] It can be understood that the adsorbates are either affected or desorbed with different sensitivities. This can be explained by the types of bonds that are formed on the surface and/or the temperature of the annealing process (which might not be sufficient). Quantification of the sensitivity of the adsorbates can provide information on the purification method. Thus, the desorption yield of the adsorbates can be expressed as

$$R\mathrm{d}t = \frac{I_{\text{initial}} - I_{\text{final}}}{I_{\text{initial}}} \times 100\%, \tag{3}$$

where I_{initial} and I_{final} are the intensities of the adsorbates before and after thermal annealing, respectively. The histogram representing the desorption yield of the adsorbates evaluated from XANES results is shown in Fig. 4 at normal incidence and grazing incidence angles.
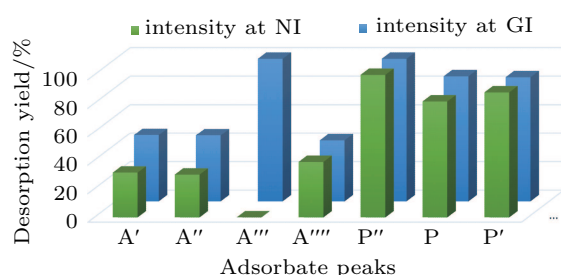
Fig. 4. Desorption yield of the adsorbates at normal incidence and grazing incidence angles.

It can be observed that potassium adsorbates (P, P′, and P″) are more sensitive to thermal annealing compared to the intrinsic adsorbates (A′, A″, A‴, and A⁗). Also, the geometry at grazing incidence angle is favorable to the desorption process. On the one hand, the high sensitivity of potassium adsorbates to the thermal annealing demonstrates that the physical bonds are established on the surface, leading to the physisorption mechanism. On the other hand, since the intrinsic adsorbates are not sensitive enough to the thermal annealing, suggesting the existence of chemical bonds on the surface, the chemisorption mechanism can be attributed to these types of

adsorbates. Chemical bonds are more difficult to break. Incidentally, the potassium donor species can easily be used to dope the MWCNTs. Ding *et al.*[23] and Dresselhaus *et al.*[24] showed that doping the SWCNTs with potassium can improve the conductivity and Fermi energy. The conductivity of our MWCNT is modified in the presence of potassium and is increased by about 12% after thermal annealing.

4. Conclusion

The characterization of the carbon nanostructures after synthesis is mandatory since the properties of these materials can be well understood for applications related to adsorption and desorption. These nanostructures can then be applied to solve problems of water, air, and soil purification. XANES spectroscopy was used to qualitatively and quantitatively evaluate the adsorbed species on the MWCNTs. We observed that the quantity adsorbed on the surface is proportional to the diameter of the multi-walls. In addition, the incident angle of the incoming beam plays a key role in understanding the adsorption phenomenon. The results showed that the potassium non-intrinsic adsorbates are resulted from the physisorption mechanism whereas the intrinsic adsorbates are from chemisorption. Also, the intrinsic adsorbates are less sensitive to the thermal treatment compared to the non-intrinsic potassium adsorbates. In addition, it is seen that the presence of potassium increases the conductivity of the MWCNTs after thermal treatment, and the desorption process is mostly affected at grazing incidence. It is worth noting that the adsorbates are useful for non-covalent functionalization with potential applications in electronic, biologic, water treatment, and environmental protection. Moreover, thermal annealing is one of the efficient methods for the purification and controlling the conductivity of the MWCNTs.

References

[1] Iijima S 1991 *Nature* **354** 56
[2] Dresselhaus M S, Dresselhaus G and Avouris P 2001 *Carbon Nanotubes: Synthesis, Structure, Properties And Applications* (Berlin: Springer) p. 29
[3] Cojocaru C S 2003 (Ph. D Thesis) (Université Louis Pasteur, Strasbourg I)
[4] Thess A, Lee R, Nikolaev P, Dai H, Petit P, Robert J, Xu C, Lee Y H, Kim S G, Rinzler A G, Colbert D T, Scuseria G E, Tomanek D, Fischer J E and Smalley R E 1996 *Science* **273** 483
[5] Lin K S, Mai Y J, Li S R, Shu C W and Wang C H 2012 *J. Nanomater* 939683
[6] Huang W, Wang Y, Luo G and Wie F 2003 *Carbon* **41** 2585
[7] Eba Medjo R, Thiodjio Sendja B, Mane Mane J and Owono Ateba P 2009 *Phys. Scr.* **80** 045601
[8] Cojocaru C S and Le Normand F 2006 *Thin Solid Films* **515** 53
[9] Taschner C, Pacal F, Leonhardt A, Spatenka P, Bartsch K, Graff A and Kaltofen R 2003 *Surf. Coat. Technol.* **174–175** 81

[10] Hatton R A, Blanchard N P, Miller A J and Silva S R P 2007 *Physica E* **37** 124

[11] Varghese O K, Kichambre P D, Gong D, Ong K G, Dickey E C and Grimes G A 2001 *Sens. Actuators B Chem.* **81** 32

[12] Zhu L, Chang D W, Dai L and Hong Y 2007 *Nano Lett.* **7** 3592

[13] Ibach H 2006 *Physics of Surfaces and Interfaces* (Berlin: Springer-Verlag) p. 30

[14] Lennard-Jones J E 1932 *Trans. Faraday Soc.* **28** 333

[15] Dabrowski A 2001 *Adv. Colloid Interface Sci.* **93** 135

[16] Peigney A, Laurent C, Flahaut E, Bacsa R R and Rousset A 2001 *Carbon* **39** 507

[17] Kuznetsova A, Popova I, Yates J T, Bronikowski M J, Huffman C B, Liu J, Smalley R E, Hwu H H and Chen J G 2001 *J. Am. Chem. Soc.* **123** 10699

[18] Eba Medjo R, Thiodjio Sendja B and Mane Mane J 2014 *Mater. Sci. Appl.* **5** 95

[19] Jun Z and Chang L 2005 *Xanes Study of Carbon Based Nanotubes* **29** *Conference proceedings*

[20] Eba Medjo R 2015 *Contamination in Manufacturing of Carbon Nanostructures*

[21] Rosenberg R A, Love P J and Rehn V 1986 *Phys. Rev. B* **33** 4034

[22] Durgun E, Dag S, Bagci V M K, *et al.* 2003 *Phys. Rev. B* **67** 201401(R)

[23] Ding Y, Yang X B and Ni J 2006 *Front. Phys. Chin.* **1** 317

[24] Dresselhaus M S, Williams K A and Eklund P C 1999 *MRS Bull.* **24** 45